APPLIED COMPUTATIONAL ELECTROMAGNETICS SOCIETY JOURNAL

October 2019
Vol. 34 No. 10
ISSN 1054-4887

The ACES Journal is abstracted in INSPEC, in Engineering Index, DTIC, Science Citation Index Expanded, the Research Alert, and to Current Contents/Engineering, Computing & Technology.

The illustrations on the front cover have been obtained from the research groups at the Department of Electrical Engineering, The University of Mississippi.

OCTOBER 2019 REVIEWERS: REGULAR PAPERS

Marco Arjona
Mehmet Belen
Toni Björninen
Ali Çetin
Chien-Hung Chen
Jie Chen
Dajun Cheng
Klaus Debes
Chonghua Fang
Bernhard Hoenders
Ahmad Hosseinbeig
Yong Mao Huang
Zhixiang Huang
Shian Hwu
Taha Imeci
Matthew Inman
Tianqi Jiao
Rostom Khalef
Ashok Kumar
Wang-Sang Lee
Lilin Li
Long Li
Tuan Li
Yan Li
Yixin Li
Chia-Hsien Lin
Haiwen Liu
Shengyuan Luo
Omid Manoochehri
Adam Mehrabani
Nasser Ojaroudi
V.A.Sankar Ponnapalli
Lingyun Ren
Qiang Ren
Kamalesh Sainath
Nitin Saluja
Suganthi Santhanam
Omar Saraereh
Kapil Sharma
Jan Sikora
Sellakkutti Suganthi
Wanchun Tang
Junwu Tao
Christopher Trueman
Wei-Chung Weng
Yuancheng Xu
Binbin Yang
Ferdows Zarrabi
Yuanguo Zhou

OCTOBER 2019 REVIEWERS: EXPRESS PAPERS

Nurhan Turker Tokan
Christopher Trueman
Mustafa H. B. Ucar

THE APPLIED COMPUTATIONAL ELECTROMAGNETICS SOCIETY JOURNAL

Vol. 34 No. 10 October 2019

TABLE OF CONTENTS – REGULAR PAPERS

TABLE OF CONTENTS – EXPRESS PAPERS

A Compact Finite-Difference Frequency-Domain Method for Analysis of Microwave Transmission Lines with Rough Surface

Binke Huang and Xubing Wang

Department of Information and Telecommunication Engineering
Xi'an Jiaotong University, Xi'an 710049, China
bkhuang@mail.xjtu.edu.cn

Abstract ─ Accurate modeling of microwave transmission lines is very important in microwave communication and radar systems, especially at high frequencies. A compact finite-difference frequency-domain method (FDFD) is presented to analyze the propagation characteristics of microwave transmission lines with rough conductor surface. Equations in the Maxwell system are discretized with difference method in the cross-section of the microwave transmission line, and rough surface of microwave transmission lines is replaced by complex surface impedance from the conductivity Gradient Model. The eigen equations of the electromagnetic field components are formed and solved to obtain the propagation constants for a given frequency. The presented method reduces the computer storage effectively in ensuring simulation accuracy without the direct modeling for surface roughness, which can be applied in the modeling of complex microwave circuits.

Index Terms ─ Conductor surface roughness, Finite-Difference Frequency-Domain (FDFD), surface impedance boundary conditions, transmission lines.

I. INTRODUCTION

The surface roughness is necessary in manufacture to add the adhesion between the conductor trace and dielectric substrate for planar transmission lines, which will increase transmission loss further. Therefore, accurate characterization the effect of surface roughness in microwave transmission lines is beneficial in analysis and design of microwave circuits, in particular at high frequencies, such as in millimeter waves.

In 1993, Detlev Hollmann computed the transmission loss in full-waves with finite-difference time-domain (FDTD) method [1], and the conductor loss as well as the loss from the conductor rough surface are considered. The FDTD approaches required large memory space and high CPU time, and the phase constants need to be set as an input parameter and the eigen frequencies of interest need to be found via discrete Fourier transform. A 2-D full-wave finite-difference frequency-domain (FDFD) method combined with the surface impedance boundary condition has been applied for the analysis of dispersion characteristics of lossy metal waveguides [2],[3]. For quasi-TEM applications to a wide variety of transmission line structures, a FDFD solver provides an efficient solution for conductor current distributions involving both skin effect and proximity effect [4]. However, all the six field components need to be calculated to yield an eigenvalue equation. Other than the FDFD method which uses a six field matrix, the compact 2-D full-wave finite-difference frequency-domain method is much more efficient to calculate the propagation constants of microwave transmission lines [5],[6], which only involves four transverse field components.

A compact 2-D finite difference frequency domain with surface impedance boundary condition has been applied to analyze the propagation characteristics of surface smooth conductor with finite conductivity [7],[8], however, the propagation characteristics of microwave transmission line with rough surface has not been demonstrated accurately yet. In this paper, a compact finite-difference frequency-domain approach combined with a complex surface impedance of the conductivity Gradient Model is presented to analyze the propagation characteristics of waveguide and microstrip line with rough conductor surfaces.

II. THEORIES

A. Surface impedance for rough surface

For a rough surface in *y*-*z*-plane, a continuous transition of macroscopic conductivity $\sigma(x)$ from 0 to σ_{bulk} perpendicular to the surface can be utilized to model surface roughness in the Gradient Model [9]. Taking this Gradient Model approach, the field distributions and the skin effect in rough conductor surfaces can be deduced from Maxwell's equation with the location dependent conductivity, and this results in a differential equation in one dimension for magnetic field component $B_y(x)$ only [10]. Without loss of generality, the solution for the magnetic field B_y distribution for a given RMS-roughness R_q=1μm and a frequency f=1GHz is shown in Fig. 1 in comparison to the magnetic field for an ideally

Submitted On: December 29, 2018
Accepted On: July 10, 2019

smooth surface at position x=0. Moreover, the current density distribution $J_z(x)$ can be calculated from $B_y(x)$ using Ampère's law. The magnitude of the current density for a rough surface and a perfect smooth surface are also shown in Fig. 1. The current density shows an abrupt step to its maximum value and declines in the conductor for a smooth surface, while the current density for a rough surface delivers a smooth response between dielectric and conductor [11].

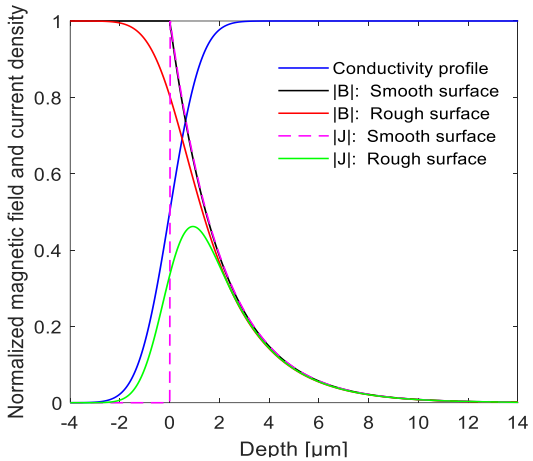

Fig. 1. Magnitude of magnetic field and current density for an ideal smooth surface and a rough surface.

The surface impedance with smooth non-ideal conductor is [12]:

$$Z_{\text{smooth}} = R_s + jX_s = -\mu_0 \frac{E_z}{B_y} = \frac{1+j}{\sigma\delta}, \tag{1}$$

where σ and δ are the intrinsic conductivity and skin-effect depth, respectively. We can see from (1) that $X_s = R_s$ for conductors with smooth surface, as B_y and J_z show the same x-dependency in Fig. 1.

For conductor with rough surface, however, real and imaginary part will not be equal ($X_s \neq R_s$), as B_y and J_z do not show the same x-dependency (Fig. 1). The ratio of E_z and B_y in (1) must therefore be expressed by the responses of B_y and J_z obtained with the conductivity Gradient Model [11].

With the Maxwell equations, we have:

$$(\nabla \times \bar{E})_y = -\frac{\partial E_z}{\partial x} = -j\omega B_y \rightarrow E_z = j\omega \int B_y dx, \tag{2}$$

$$(\nabla \times \bar{B})_z = \frac{\partial B_y}{\partial x} = \mu_0 J_z \rightarrow B_y = \mu_0 \int J_z dx. \tag{3}$$

The surface impedance for conductor with rough surface can be derived directly [11]:

$$Z_{\text{rough}} = -j\omega \frac{\int B_y dx}{\int J_z dx}. \tag{4}$$

Figure 2 shows typical frequency responses of its real and imaginary part in comparison to those of a smooth surface.

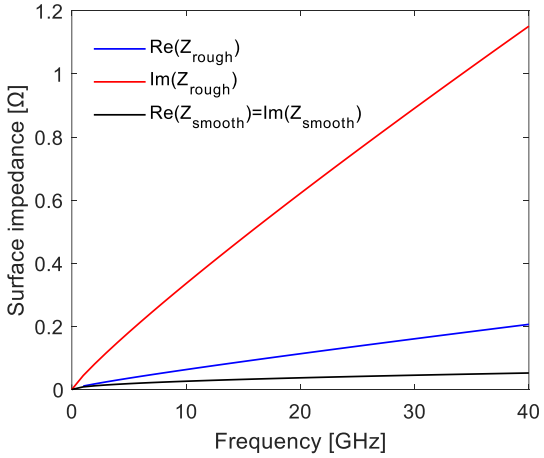

Fig. 2. Real and imaginary part of the surface impedance of copper for a rough surface with 1um RMS-roughness and a smooth surface.

With a series derivation for B_y and J_z [13], the surface impedance condition with rough conductor surface can be obtained, which can be convenient incorporated into conductor boundary condition in the FDFD method to characterize the effects of rough surface for microwave transmission lines.

B. A compact 2-D full-wave finite-difference frequency-domain method

Inside the transmission lines, the transverse field components can be expressed by eliminating the longitudinal components from the Maxwell curl discrete equation as follows [5]:

$$\begin{aligned} &-j\frac{\gamma}{k}E_x(i,j) \\ &= -\frac{1}{k^2\Delta x\Delta y}[H_x(i,j-1)] - H_x(i+1,j-1) - H_x(i,j) + H_x(i+1,j)] \\ &+ \frac{1}{k^2\Delta x^2}H_y(i-1,j) + (1-\frac{2}{k^2\Delta x^2})H_y(i,j) + \frac{1}{k^2\Delta x^2}H_y(i+1,j), \end{aligned} \tag{5a}$$

$$\begin{aligned} &-j\frac{\gamma}{k}E_y(i,j) \\ &= \frac{1}{k^2\Delta x\Delta y}[H_y(i-1,j)] - H_y(i-1,j+1) - H_y(i,j) + H_y(i,j+1)] \\ &- \frac{1}{k^2\Delta y^2}H_x(i,j-1) - (1-\frac{2}{k^2\Delta y^2})H_x(i,j) - \frac{1}{k^2\Delta y^2}H_x(i,j+1), \end{aligned} \tag{5b}$$

$$\begin{aligned} &-j\frac{\gamma}{k}H_x(i,j) \\ &= \frac{1}{k^2\Delta x\Delta y}[E_x(i-1,j)] - E_x(i-1,j+1) - E_x(i,j) + E_x(i,j+1)] \\ &- \frac{1}{k^2\Delta x^2}E_y(i-1,j) - (1-\frac{2}{k^2\Delta x^2})E_y(i,j) - \frac{1}{k^2\Delta x^2}E_y(i+1,j), \end{aligned} \tag{5c}$$

$$-j\frac{\gamma}{k}H_y(i,j)$$
$$=-\frac{1}{k^2\Delta x\Delta y}[E_y(i,j-1)]-E_y(i+1,j-1)-E_y(i,j)+E_y(i+1,j)]$$
$$+\frac{1}{k^2\Delta y^2}E_x(i,j-1)+(1-\frac{2}{k^2\Delta y^2})E_x(i,j)+\frac{1}{k^2\Delta y^2}E_x(i,j+1), \quad (5d)$$

where γ is the propagation constant and k is the wave number in the free space, Δx and Δy are the mesh sizes in x- and y-direction, respectively.

Equation (5) shows that one component of E (or H) field can be represented by seven components of neighbor H (or E) field. Equation (5) is not applicable to deal the components on the non-ideal conductor boundary. The fields on the boundary must be computed with special boundary conditions.

Considering the finite conductivity of non-ideal conductor, the relationship between the tangential electric field and the tangential magnetic field on the boundary is related with the surface impedance boundary conditions (SIBCs):

$$\bar{E}_{\tan}=Z_s\hat{n}\times\bar{H}_{\tan}. \quad (6)$$

For conductor with smooth surface, the surface impedance Z_s is determined through formula (1). If at high frequencies, the conductor surface roughness need to be considered, the surface impedance for rough surfaces can be calculated with formula (4).

With the SIBCs and eliminating the longitudinal components from the applied Maxwell discrete equations, as shown in Fig. 3 (a), $E_x(i,j)$, $E_y(i,j)$ and $H_y(i,j)$ on the lower boundary satisfy the following formula:

$$-j\frac{\gamma}{k}E_x(i,1)=j\frac{Z_s}{k\Delta x}H_x(i,1)-j\frac{Z_s}{k\Delta x}H_x(i+1,1)$$
$$+j\frac{Z_s}{k\Delta y}H_y(i,1)-j\frac{Z_s}{k\Delta y}H_y(i,2), \quad (7a)$$

$$-j\frac{\gamma}{k}E_y(i,1)$$
$$=(j\frac{Z_s}{k\Delta y}-1+\frac{1}{k^2\Delta y^2})H_x(i,1)+\frac{1}{k^2\Delta y^2}H_x(i,2) \quad (7b)$$
$$-\frac{1}{k^2\Delta x\Delta y}H_y(i-1,2)+\frac{1}{k^2\Delta x\Delta y}H_y(i,2),$$

$$-j\frac{\gamma}{k}H_y(i,1)=\frac{-jZ_s}{k\Delta y-jZ_S}[-j\frac{\gamma}{k}H_y(i,2)]. \quad (7c)$$

In Fig. 3 (b), applying the SIBC on the left boundary with the non-ideal conductor, we have:

$$-j\frac{\gamma}{k}E_x(1,j)$$
$$=\frac{1}{k^2\Delta x\Delta y}H_x(2,j-1)-\frac{1}{k^2\Delta x\Delta y}H_x(2,j) \quad (8a)$$
$$+(1-\frac{1}{k^2\Delta x^2}-j\frac{Z_s}{k\Delta x})H_y(1,j)+\frac{1}{k^2\Delta x^2}H_y(2,j),$$

$$-j\frac{\gamma}{k}E_y(1,j)=-j\frac{Z_s}{k\Delta x}H_x(1,j)+j\frac{Z_s}{k\Delta x}H_x(2,j)$$
$$-j\frac{Z_s}{k\Delta y}H_y(1,j)+j\frac{Z_s}{k\Delta y}H_y(1,j+1), \quad (8b)$$

$$-j\frac{\gamma}{k}H_x(1,j)=\frac{-jZ_s}{k\Delta x-jZ_S}[-j\frac{\gamma}{k}H_x(2,j)]. \quad (8c)$$

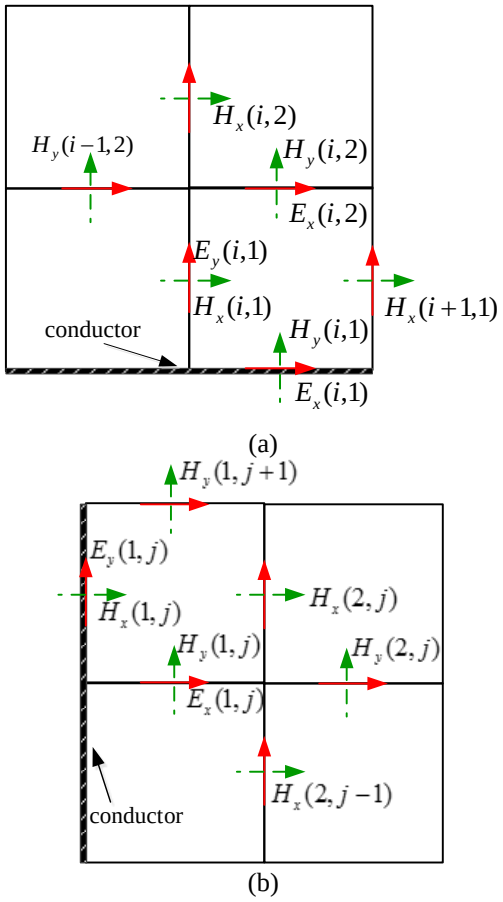

Fig. 3. Transverse field components on boundary surface: (a) E_x, E_y, and H_y on lower boundary, and (b) E_x, E_y, and H_x on left boundary.

Similarly, the field components on the top boundary and the right boundary can be obtained by applying the SIBCs directly.

From the equations for inner nodes and surface nodes, we can conclude an eigenvalue problem as:

$$[A][X]=\lambda[X], \quad (9)$$

where $[X]=[E_x,E_y,H_x,H_y]^T$, $\lambda=-j\frac{\gamma}{k}=\frac{\beta-j\alpha}{k}$, β is the phase constant, and α is the attenuation constant caused by the mental loss. $[A]$ is a sparse coefficient matrix, and the eigen solution of $[A]$ delivers the propagation constant.

III. NUMERICAL RESULTS

In this section, a waveguide and a shielded microstrip line are provided to illustrate the efficiency of the proposed method.

A. Waveguide

With the FDFD method, the propagation constants for waveguide in different frequencies can be obtained. The waveguide is an empty rectangular copper waveguide with the size of $a \times b$=19.05mm×9mm, and with the conductivity σ=5.8×10^{7}S/m. The computational domain for the cross section of waveguide comprises a grid of 10×5 cells in the FDFD simulation. The computed results of propagation constant for TE_{10} mode of waveguide with smooth surface are compared with the analytical perturbation method [12] with good correction as shown in Fig. 4.

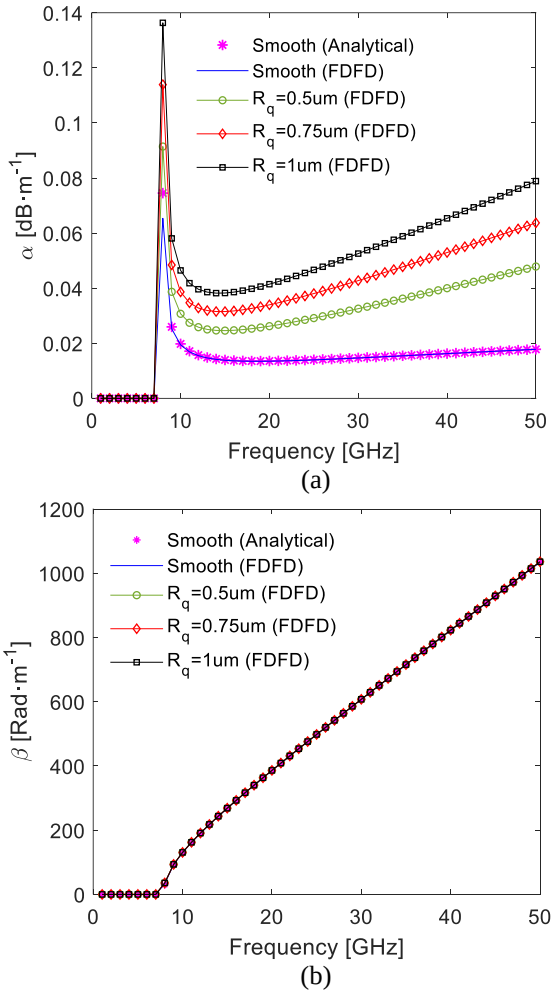

Fig. 4. The propagation of waveguide considering conductor surface roughness: (a) attenuation constant, and (b) phase constant.

As shown in Fig. 4 (a), under other parameters invariably, attenuation constant tends to 0 when the frequency is below cutoff frequency, and as the frequency increases, attenuation constant keeps decreasing in the cutoff region when f tends to f_{min} [14]. The surface impedance is dominant when f>f_{min}, so attenuation constant increases as frequency increases. Under other parameters invariably, the attenuation constant monotonically rises as the surface roughness increases in Fig. 4 (a). As shown in Fig. 4 (b), the differences between phase constants of waveguide with smooth surface and roughness surface are negligible.

B. Shielded microstrip line

Consider a shielded microstrip line as defined in Fig. 5 with a trace width w=3.81mm on top of a dielectric layer with ε_r=2.2, tanδ=0, and the height h=2.7mm. The conductor of trace and ground plane is with a conductivity σ=5.8×10^{7}S/m and the thickness is negligible. The width and height for the shielded metallic box are a=9.525mm and b=4.5mm, respectively. The cross section of the shielded microstrip line is meshed with total 10×5 cells in the FDFD simulation. The computed results obtained by our proposed method are given in Fig. 6. Numerical results of propagation constant of microstrip line with smooth surface are compared with the results of CST Microwave Studio and a good agreement is achieved. Under other parameters invariably, the attenuation constant monotonically rises as the frequency increases in Fig. 6 (a), and the roughness of surface increases from 0 to 1um, the value of attenuation constants increase, especially at higher frequencies. As shown in Fig. 6 (b), the differences between phase constant of shielded microstrip with line smooth surface and roughness surfaces are too small to be distinguished.

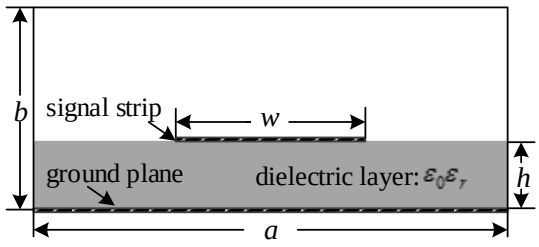

Fig. 5. The cross section of a shielded microstrip line.

Compared to the 2-D FDFD with six components in [3], the dimension of the coefficient matrix [A] in (9) is reduced to two thirds, because only four transverse field components are contained in the compact 2-D FDFD. The comparison of efficiency in calculation the propagation constants for the shielded microstrip line [Fig. 5] are shown in Table 1. The calculations are carried out on Intel (R) I7 2.7GHz laptop using Matlab R2017b.

We can see that the CPU time can be reduced considerably as compared to the case in which six field components are comprised, since the cutting down order of the coefficient matrix largely for solving the eigenvalue problem in the proposed method.

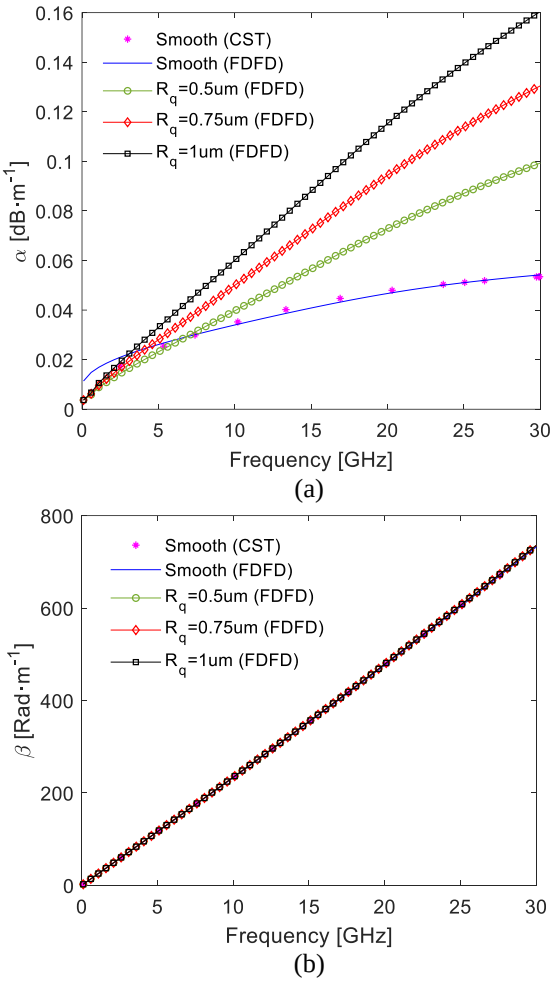

Fig. 6. The propagation of a shielded microstrip line considering conductor surface roughness: (a) attenuation constant, and (b) phase constant.

Table 1: Comparison of this method and the method in [3] for the second example

	This Method	Method in [3]
Dimension of matrix	236	354
Number of non-zero elements	1222	883
CPU time (s)	1.54	6.40

IV. CONCLUSION

In the paper, a compact 2D full-wave FDFD method combined with complex surface impedance of the conductivity Gradient Model has been applied for the dispersion characteristics of microwave transmission lines with roughness surface. Accurate results of attenuation constants and phase constants of waveguide and shielded microstrip line with roughness surface have been obtained by using the proposed method. The proposed method will be a powerful tool to calculate the propagation constants for microwave transmission lines with roughness surface, especially at high frequencies.

ACKNOWLEDGMENT

This work was supported by the National Nature Science Foundation of China (Grant No. 61471293) and the China Scholarship Council (Grant No. 201706285142).

REFERENCES

[1] D. Hollmann, S. Haffa, F. Rostan, and W. Wiesbeck, "The introduction of surface resistance in the three-dimensional finite-difference method in frequency domain," *IEEE Transactions on Microwave Theory and Techniques*, vol. 41, no. 5, pp. 893-895, 1993.

[2] B. Z. Wang, X. H. Wang, and W. Shao, "2D full-wave finite-difference frequency-domain method for lossy metal waveguide," *Microwave and Optical Technology Letters*, vol. 42, no. 2, pp. 158-161, 2004.

[3] B. K. Huang and C. F. Zhao, "Propagation characteristics of rectangular waveguides at tera-hertz frequencies with finite-difference frequency-domain method," *Frequenz*, vol. 68, no. 1-2, pp. 43-49, 2014.

[4] J. P. Donohoe, "A Finite-difference frequency domain solver for quasi-TEM applications," *ACES Journal*, vol. 33, no. 10, pp. 1093-1095, 2018.

[5] Y. J. Zhao, K. L. Wu, and K. K. M. Cheng, "A compact 2-D full-wave finite-difference frequency-domain method for general guided wave structures," *IEEE Transactions on Microwave Theory and Techniques*, vol. 50, no. 7, pp. 1844-1848, 2002.

[6] Q. Li, W. Zhao, Y. J. Zhao, and W. S. Jiang, "Dispersive characteristics analysis of lossy microstrip with 4-component 2-D CFDFD method," *Proceedings-2009 3rd IEEE International Symposium on Microwave, Antenna, Propagation and EMC Technologies for Wireless Communications, MAPE 2009*, Beijing China, pp. 588-592, Oct. 2009.

[7] W. Zhao, H. W. Deng, and Y. J. Zhao, "Dispersion characteristics analysis of lossy coaxial metal waveguide with 4-component compact 2-D FDFD method," *ISAPE 2008-The 8th International Symposium on Antennas, Propagation and EM Theory Proceedings*, Kunming, China, pp. 851-854, Nov. 2008.

[8] W. Zhao, H. W. Deng, and Y. J. Zhao, "Application of 4-component compact 2-D FDFD method in analysis of lossy circular metal waveguide," *Journal of Electromagnetic Waves & Applications*,

vol. 22, no. 17-18, pp. 2297-2308, 2008.

[9] G. Gold and K. Helmreich, "A physical model for skin effect in rough surfaces. *Proceedings of the 7th European Microwave Integrated Circuits Conference*, Amsterdam, The Netherlands, pp. 631-634, Oct. 2012.

[10] G. Gold and K. Helmreich, "Effective conductivity concept for modeling conductor surface roughness," *DesignCon 2014: Where the Chip Meets the Board*, Santa Clara, CA, USA, Jan. 2014.

[11] G. Gold and K. Helmreich, "Surface impedance concept for modeling conductor roughness," *2015. IEEE MTT-S International Microwave Symposium, IMS 2015*, Phoenix, AZ, USA, May 2015.

[12] R. F. Harrington, *Time-harmonic Electromagnetic Fields*. New York: McGraw-Hill, 1961.

[13] B. K. Huang and Q. Jia, "A method to extract dielectric parameters from transmission lines with conductor surface roughness at microwave frequencies," *Progress in Electromagnetics Research M*, vol. 48, pp. 1-8, 2016.

[14] S. Ramo and J. R. Whinnery, *Fields and Waves in Modern Radio*. 2nd Ed., New York: Wiley, 1953.

A Design Method for Synthesizing a Dual-Passband FSS for Wi-Fi Using Equivalent Circuit Model

Yuan Xu and Mang He

School of Information and Electronics
Beijing Institute of Technology, Beijing, 100081, China
hemang@bit.edu.cn

Abstract ─ In this letter, a dual-passband frequency selective surface (FSS) at Wi-Fi operation bands is presented. The proposed structure is implemented by two-dimensional periodic array of double square slots on single dielectric layer, which can be used to isolate the intensive care rooms of hospitals from insignificant signals, but supports Wi-Fi features, enabling doctors to acquire the patients' health condition at any time. The design procedure is based on the equivalent circuit method (ECM) combined with the genetic algorithm (GA) curve-fitting, which aims at providing the initial dimension parameters of FSS. Ultimately, the calculated results from the ECM are compared with the numerical results of the HFSS optimization, and the measured frequency response of the fabricated FSS covers all the Wi-Fi frequency bands, which verify the reliability of this design.

Index Terms ─ Equivalent circuit method, frequency selective surface, genetic algorithm, Wi-Fi.

I. INTRODUCTION

Nowadays, Wi-Fi has brought mobility and flexibility to our lives by different kinds of wireless devices. For example, the devices in Intensive Care Units (ICUs) of hospital use Wi-Fi to support the communication of the patients' health condition to doctors outside the rooms [1]. However, the distraction of other insignificant signals should be isolated from the rooms to minimize the impact on the precision equipment.

Frequency selective surfaces (FSSs) have been an important subject for their widespread applications as spatial filters for decades of years [2]. The feature of transmission at resonant frequency allows FSS to perform like a bandpass filter in Wi-Fi applications to improve transmission of RF/MW signals through shell [3-5]. Motivated by the ICUs' requirement, the bandpass FSS designed in this paper is applied as the shielding screen between ICUs and the outside world to isolate the rooms from the impact of insignificant signals, yet to allow Wi-Fi frequencies to pass through. According to the standard of IEEE 802.11n, the frequency band of the fourth generation Wi-Fi contains two parts: 2.4 GHz - 2.4835 GHz, and 5.15 GHz - 5.850 GHz. It is important to guarantee the transmission of electromagnetic (EM) wave at these two bands in the screen design.

Commonly, the design of FSS mainly relies on the full-wave numerical software [6-8], and the parametric sweep is an indispensable process. However, although the numerical simulations yield accurate frequency response for a given FSS structure, they cannot provide adequate information of how to start an FSS design and how to initialize the geometrical sizes of the design to fulfill the expected frequency response in a general form. In this letter, the equivalent circuit method is introduced to provide the initial design parameters of an FSS from the desired frequency response. For the dual-band design in Wi-Fi bands, we use the periodic elements of square slot (SS) and square loop (SL) [9], whose surface impedances in both the normal- and oblique-incidence situations [10-13] are studied in detail, to present band-pass and band-stop performances. In the synthesizing process [14, 15], equivalent circuit (EC) parameters and then the geometrical sizes of the structure can be obtained from a few typical *S*-parameter (S_{11}/S_{21}) samplings of the desired response curves via the genetic algorithm (GA) curve-fitting technique [16-18].

Ultimately, the dual-passband FSS designed by ECM, works well at Wi-Fi bands with the stability for different incident angles. Compared with the existing structure [1, 3-5, 19], this design has a simple structure and covers all the Wi-Fi operation frequency bands at normal and oblique incidence. For the sake of demonstration, a prototype of the FSS was fabricated and measured.

II. STRUCTURE DESCRIPTION AND OPERATING PRINCIPLES

A. Structure description

As mentioned in [2], the FSS composed of the SS elements is a bandpass filter. To obtain the two passbands for Wi-Fi application, the structure of double square slots can be chosen to construct the desired FSS. Figure 1 (a) shows the geometrical structure of this single-

Submitted On: March 21, 2019
Accepted On: May 12, 2019

layer FSS element. The metal part is printed on the top side of support dielectric medium whose thickness is d (the relative permittivity is ε_r, and the length of period element period is D). The length of the larger loop is l_1, and the width is w_1. The length of the smaller loop is l_2, and the width is w_2.

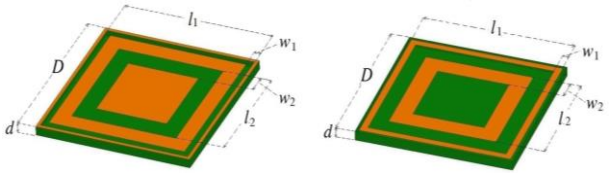

(a) (b)

Fig. 1. (a) The element of double square slots FSS (dual-passband), and (b) the element of double square loops FSS (dual-stopband). The structure in (b) is complementary to the structure in (a). The metal part is orange in color.

B. Design procedure

To determine the dimensions of the proposed structure, the design procedure contains:

Step 1. Obtain the equivalent circuit model of the FSS;

Step 2. Derive the impedance of metal layer;

Step 3. Build the transmission matrix based on the transmission line principle;

Step 4. Synthesize the EC parameters and then the geometrical sizes of the structure from a few typical S-parameter (S11/S21) samplings of the desired response curves via GA curve-fitting process;

Step 5. Optimize the FSS parameters based on the ECM data.

In step 1, it's difficult to judge whether the equivalent circuit of two square slots in Fig. 1 (a) are serial or parallel connected. However, the complementary structure of slots - double square loops (see Fig. 1 (b)) whose frequency response is dual stopband, has been studied in [20, 21], and its equivalent circuit is shown in Fig. 2, where the slots between loops present equivalent capacitance, and the strips represent the inductance. So, there are two serial LC resonators (L_1 - C_1 and L_2 - C_2) in the patch structure. Consequently, in this letter, we choose to pay attention to the square loops first, to simplify the equivalent circuit model. Later, using the Babinet's principle, it is easy to obtain the impedance of slots structure.

In step 2, as mentioned above, to obtain the impedance of the double square slots FSS layer, we should achieve the impedance of its complementary structure (SL). As shown in Fig. 2, the impedance of the patch FSS in different polarization can be depicted as:

$$Z_{SL}^{TE} = (j\omega L_1 + 1/\ j\omega C_1) \| (j\omega L_2 + 1/\ j\omega C_2) / \xi\,, \quad (1)$$

$$Z_{SL}^{TM} = (j\omega L_1 + 1/\ j\omega C_1) \| (j\omega L_2 + 1/\ j\omega C_2)\,, \quad (2)$$

where, $\xi = 1 - sin^2\theta / 2\varepsilon_{eff}$ is the influence factor of the incident angle θ [10]. Based on the equations in [10, 22], the circuit parameters in Fig. 2 can be derived as:

$$L_1 = \frac{\mu_0 l_1}{2\pi} \ln(1/\sin\frac{\pi w_1}{2D})\,, \quad (3)$$

$$C_1 = \varepsilon_0 \varepsilon_{eff} \frac{2l_1}{\pi} \ln[1/\sin\frac{\pi(D-l_1)}{2D}]\,, \quad (4)$$

$$L_2 = \frac{\mu_0 l_2}{2\pi} \ln(1/\sin\frac{\pi w_2}{2D})\,, \quad (5)$$

$$C_2 = \varepsilon_0 \varepsilon_{eff} \frac{l_2}{\pi} \ln[1/\sin\frac{\pi(l_1 - l_2 - 2w_1)/2}{2D}]\,, \quad (6)$$

the geometrical parameters are determined in Fig. 1, and ε_0 and μ_0 are the electromagnetic parameters of free space. The effective permittivity ε_{eff} of single layer FSS here is defined as:

$$\varepsilon_{eff} = \frac{\varepsilon_r + 1}{2} - \frac{\varepsilon_r - 1}{2} \exp[(-700d)^3]\,, \quad (7)$$

where, d and ε_r are the thickness and permittivity of the dielectric medium.

Then, applying the Babinet's principle:

$$Z_{SL}^{TE} Z_{SS}^{TM} = \frac{\eta_{eff}^2}{4}\,, \quad (8)$$

$$Z_{SL}^{TM} Z_{SS}^{TE} = \frac{\eta_{eff}^2}{4}\,, \quad (9)$$

where $\eta_{eff} = \sqrt{\mu_0 / (\varepsilon_0 \varepsilon_{eff})}$ is the effective wave impedance, we can obtain the impedance of double square slots $Z_{SS}^{TE,TM}$.

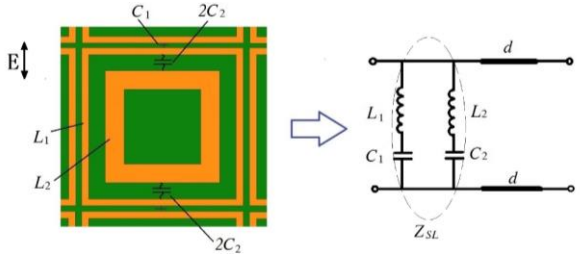

Fig. 2. The equivalent circuit of double square loops FSS.

In step 3, the medium below the metal patches can be regarded as a short transmission line in the circuit. So, the analytical transmission coefficients S_{21} for TE/TM polarization can be obtained from [23]:

$$S_{21} = \frac{2}{(A + B/Z_0^{TE,TM}) + (Z_0^{TE,TM} C + D)}\,, \quad (10)$$

$$Z_0^{TE} = Z_0 / \cos(\theta), Z_0^{TM} = Z_0 \cos(\theta)\,, \quad (11)$$

where, Z_0 is the intrinsic wave impedance in free space. According to the equivalent circuit shown in Fig. 2, the ABCD matrix can be written as the product of two cascade matrices:

$$\begin{bmatrix} A & B \\ C & D \end{bmatrix} = \begin{bmatrix} 1 & 0 \\ 1/Z_{SS}^{TE,TM} & 1 \end{bmatrix} \begin{bmatrix} \cosh(j\theta_1) & Z_1 \sinh(j\theta_1) \\ Y_1 \sinh(j\theta_1) & \cosh(j\theta_1) \end{bmatrix}, \quad (12)$$

where the parameters are as follows,

$$Z_1^{TE} = \omega\mu_0 / \beta_1, Z_1^{TM} = \beta_1 / \omega\varepsilon_0\varepsilon_r,$$

$$Y_1 = 1/Z_1, \theta_1 = \beta_1 d,$$

$$\beta_1 = \sqrt{k_1^2 - k_t^2}, k_t = k_0 \sin(\theta), k_1 = k_0\sqrt{\varepsilon_r}, \quad (13)$$

where k_t is the transverse vector, k_1 is the propagation constant in the substrate, and k_0 is the wave number in free space.

In step 4, we determine the dielectric substrate has a thickness of 1.27 mm and the relative permittivity of 2.2. To synthesize the unknown geometrical parameters: l_1, w_1, l_2, w_2, and D, we apply the GA curve-fitting method on the samplings from the desired S_{21} curve. Here, several sampling frequencies and the corresponding values of $|S_{21}|$ are listed in Table 1, which manifest the main property of the dual passbands. In this method, to ensure the good transmission properties of the FSS in different incident angles and different polarizations, we introduce different weighting factors to the adaptive function:

$$fun = \sum_{r=1}^{2}\sum_{m=1}^{M}\sum_{n=1}^{N} W_n \left\{ W^{TE,TM} \left[\left| S_{21}^{TE,TM} \right|(m,n) - \left| S_{21}^{0} \right|(m) \right] \right\}, \quad (14)$$

where, r indicates the TE and TM polarization, m indicates the number of frequency points, and n indicates the number of angle points. $W^{TE,TM}$ is the weighting factor of TE/TM polarization, and W_n is the weighting factor of different incident angles. $\left|S_{21}^{TE,TM}\right|(m,n)$ is the magnitude of transmission coefficients at different frequencies and angles, which has been derived in step. 3, and $\left|S_{21}^{0}\right|(m)$ is the sampling points from the desired $|S_{21}|$ curve at different frequencies (in Table 1).

Table 1: Samples from the desired frequency response of $|S_{21}|$

Sampling Frequencies (GHz)	1.0	2.4	2.5	4.0	5.1
$\left\|S_{21}^{0}\right\|$ **(dB)**	-5.0	-0.5	-0.5	-15	-0.5
Sampling Frequencies (GHz)	5.3	5.5	5.7	5.9	
$\left\|S_{21}^{0}\right\|$ **(dB)**	0	0	0	-0.5	

In this design, we define: $W^{TE} = W^{TM} = 1$ (ensure the property for both TE and TM polarization), W_n = 1 ($\theta \le 45^\circ$) and W_n = 0.1 ($\theta > 45^\circ$) (ensure the property of oblique incidence θ = 0~45°). In the GA algorithm, FSS structural parameters are chosen as the parameters to be optimized, and seaching ranges are set to be: $15\ mm \le l_2 < l_1 < D \le 30\ mm, 0.1\ mm \le w_{1,2} \le 3\ mm$. Also the stopping criteria of GA is defined [24, 25]: the population size is 100, the number of max generations is 100, the number of stall generations is 50, the crossover fraction is 0.75, and the function tolerance is 1e-6. Using the GA optimization to minimize the adaptive function (14), the optimal unknown geometrical parameters can be obtained (see Table 2).

Table 2: Geometrical parameters calculated by the ECM and HFSS

	l_1 (mm)	w_1 (mm)	l_2 (mm)	w_2 (mm)	D (mm)
Optimal Values by ECM and GA	23.5	1.5	16.6	2.3	24.6
Optimal Values by HFSS' Parameter-Sweep	24.0	1.0	17.0	2.8	25.0

Then in step 5, the ECM data achieved from step 4 are used as the initial values in the parameter-sweep process in the ANSYS HFSS for fine tuning. The optimization results are compared with the ECM data in Table 2. It can be seen that the ECM data are close to the optimized structure dimensions, which will save lots of time for starting an FSS design. In addition, the effect of different dimension parameters can be easily achieved from the ECM equations, which offers many conveniences to the HFSS optimization. Based on this principle, it can be obtained that increasing the parameter w_2 properly will achieve the wide band in 5.15 GHz - 5.850 GHz.

III. SIMULATION AND EXPERIMENTAL VERIFICATION

A. ECM results and simulated results

Here, the optimization range of incident angle is 0°~45° as defined in step 4. Based on the analysis in Section II, the computed transmission coefficient $|S_{21}|$ (θ = 0° and 45°) with the structure sizes obtained by ECM is plotted in Fig. 3 (a), compared with the sampling points in Table 1. It's seen that the resonant frequencies of the response are close to the desired sampling points, which means the results of ECM almost presents the expected dual bands response.

The simulated $|S_{21}|$ (θ = 0° and 45°) from HFSS with the optimization sizes in Table 2 from step 5 is shown in Fig. 3 (b), as well as the results of TE- and TM-polarization. The results in Fig. 3 (b) present that the FSS we design can guarantee the transmission of EM wave (transmission efficiency is more than 80%) even the incident angle is up to 45° in both Wi-Fi bands: 2.4 GHz - 2.4835 GHz, and 5.15 GHz - 5.850 GHz. In addition,

the optimal values by HFSS are in close proximity to the calculated sizes given by the proposed ECM. The good simulated results indicate this design of FSS is qualified to the Wi-Fi application.

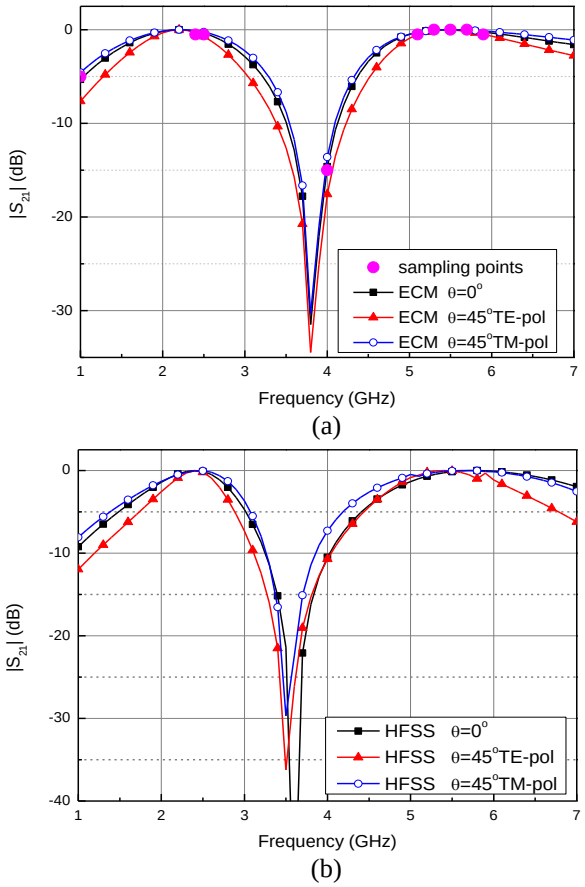

Fig. 3. (a) $|S_{21}|$ of FSS with the synthesized sizes by ECM calculation, and (b) $|S_{21}|$ of the FSS with optimal sizes fine-tuned by HFSS simulations.

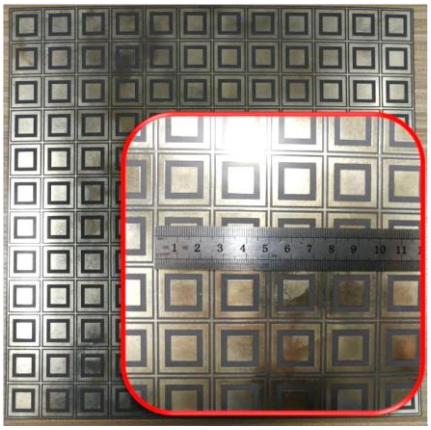

Fig. 4. The top view photo of the fabricated FSS.

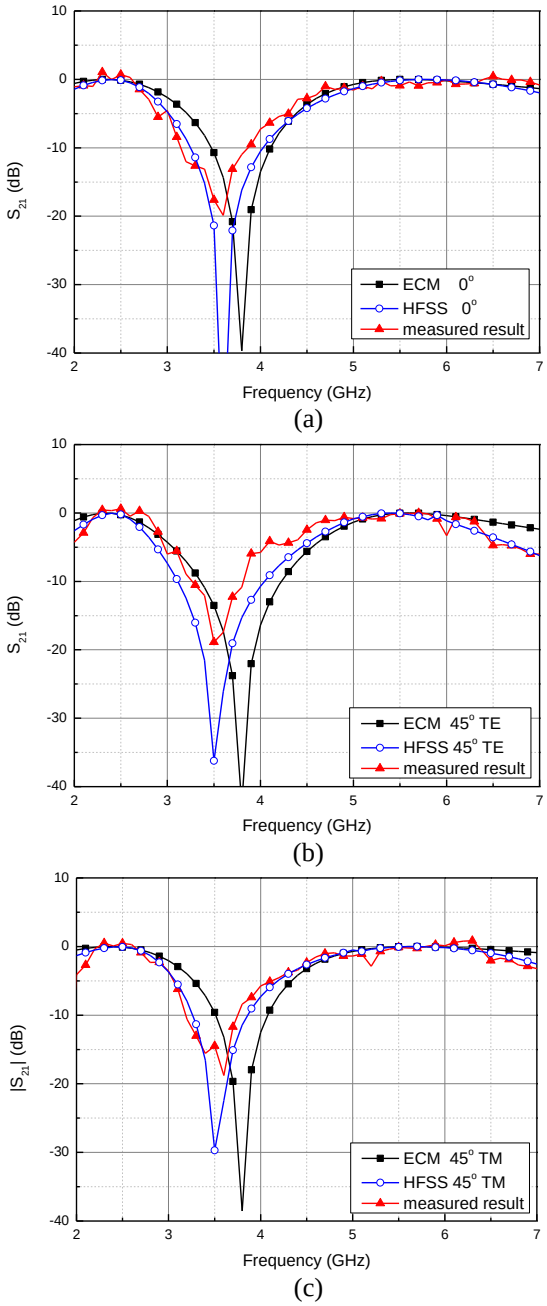

Fig. 5. Measured results compared with the calculated results from ECM and HFSS: (a) $|S_{21}|$ of normal incidence, (b) $|S_{21}|$ of oblique incidence θ = 45° for TE-polarization, and (c) $|S_{21}|$ of oblique incidence θ = 45° for TM-polarization.

B. Experimental verification

To validate the performance of the proposed FSS, a proto-type is fabricated and measured. The prototype is fabricated on Arlon DiClad 880 dielectric substrate (see Fig. 4), of which the permittivity is 2.2, loss tangent is

0.0009, and the thickness is 1.27 mm. The dimensions of FSS elements follow the final optimized data by HFSS in Table 2. The physical dimensions of the FSS arrays are 30.00 cm × 30.00 cm, which means the number of elements is 12 × 12. Then, the measurement was performed with the setup consisting of two broadband horn antennas for transmitting and receiving EM wave, respectively. During the measurement of the transmission coefficient of the FSS, we first need to measure the $|S_{21}|$ between the horn antennas without the FSS as the calibration data, and then we measure again the $|S_{21}|$ between the two horns when the FSS under test is present. Finally, the $|S_{21}|$ of the FSS itself is obtained by normalizing the $|S_{21}|$ measured in the second time to the calibration data.

Limited by the experiment conditions, the measurement starts from the frequency of 2 GHz to 7 GHz. The measured results of $|S_{21}|$ are compared with the numerical results by ECM and HFSS using the same structure parameters in Fig. 5, when the angle and polarization of incidence varies. As can be seen, the measured results agree well with the simulated ones from HFSS, indicating two passbands: 2.4 GHz - 2.4835 GHz, and 5.15 GHz - 5.850 GHz, with $|S_{21}| \geq$ -1.5 dB, and a stopband at 3.6 GHz, with $|S_{21}| \leq$ -15 dB. In addition, the FSS works stably when the angle of incidence increases up to 45°. At the same time, it is found in Fig. 5 that the measured frequency responses have small ripples over the frequency range, which is possibly caused by truncation and assembly errors between the transmit and receive antennas. As well, ECM results show similar properties except for a slight difference, which is caused by the accuracy of the equivalent circuit formulations is less than the full-wave simulation, and we'll improve it in our future work. Nevertheless, the fabricated prototype meets the desired requirements quite well, which indicates that the proposed design procedure using ECM is feasible and effective.

IV. CONCLUSION

This letter proposes a dual-passband single-layer FSS based on the classic structure of double square slots used in the ICUs to allow the Wi-Fi signals to pass through, and to isolate the insignificant signals. The design procedure applies the method of equivalent circuit and genetic algorithm to determine the FSS's geometrical parameters. To reduce the difficulty in analyzing slots structure, we put forward the approach of introducing complementary structure and obtaining the impedance of slots by Babinet's principle afterwards. The synthesized geometrical sizes given by the proposed ECM are in close proximity to the optimized values by HFSS, which means the ECM is qualified to start an FSS design. This design method provides a convenient way to realize the dimension estimation of the desired FSS, which will save much time in the design process. Besides, the measured results of fabrication cover all the Wi-Fi working bands both in normal- and oblique-incidence situation, which validate the reliability of this design method.

REFERENCES

[1] S. I. Sohail, "Wi-Fi transmission and multi-band shielding using single-layer frequency selective surface," *2016 IEEE International Symposium on Antennas and Propagation (APSURSI)*, Fajardo, pp. 963-964, 2016.

[2] B. A. Munk, *Frequency Selective Surface: Theory and Design*. New York: Wiley-Interscience, pp. 1-22, 2000.

[3] D. Hamzaoui, T. P. Vuong, F. Djahli, and G. I. Kiani, "Novel compact dual-band artificial magnetic conductors for Wi-Fi applications," *The 8th European Conference on Antennas and Propagation (EuCAP 2014)*, The Hague, pp. 2397-2400, 2014.

[4] I. Ullah, X. Zhao, D. Habibi, and G. Kiani, "Transmission improvement of UMTS and Wi-Fi signals through energy saving glass using FSS," *WAMICON 2011 Conference Proceedings*, Clear-water Beach, FL, pp. 1-5, 2011.

[5] D. Ferreira, I. Cuinas, and R. F. S. Caldeirinha, "Dual-band single-layer quarter ring frequency selective surface for Wi-Fi applications," *IET Microw. Antennas Propag*., vol. 10, pp. 435-441, 2016.

[6] X. Sheng, J. Fan, N. Liu, and C. Zhang, "A miniaturized dual-band FSS with controllable frequency resonances," *IEEE Microwave and Wireless Components Lett.*, vol. 27, no. 10, pp. 915-917, Oct. 2017.

[7] S. Ünaldı, S. Çimen, G. Çakır, and U. E. Ayten, "A novel dual-band ultrathin FSS with closely settled frequency response," *IEEE Antennas and Wireless Propag. Lett.*, vol. 16, pp. 1381-1384, 2017.

[8] M. Z. Joozdani and M. K. Amirhosseini, "Equivalent circuit model for the frequency-selective surface embedded in a layer with constant conductivity," *IEEE Trans. Antennas and Propag.*, vol. 65, no. 2, pp. 705-712, Feb. 2017.

[9] D. Ferreira, R. F. S. Caldeirinha, I. Cuiñas, and T. R. Fernandes, "Square loop and slot frequency selective surfaces study for equivalent circuit model optimization," *IEEE Trans. Antennas and Propag.*, vol. 63, no. 9, pp. 3947-3955, Sept. 2015.

[10] O. Luukkonen and C. Simovski, "Simple and accurate analytical model of planar grids and high-impedance surfaces comprising metal strips or patches," *IEEE Trans. Antennas and Propag.*, vol. 56, no. 6, pp. 1624-1632, June 2008.

[11] R. J. Langley and E. A. Parker, "Equivalent circuit model for arrays of square loops," in *Electronics Letters*, vol. 18, no. 7, pp. 294-296, 1 Apr. 1982.

[12] C. K. Lee and R. J. Langley, "Equivalent-circuit models for frequency-selective surfaces at oblique angles of incidence," in *IEE Proceedings H - Microwaves, Antennas and Propagation*, vol. 132, no. 6, pp. 395-399, Oct. 1985.

[13] G. H. Sung, K. W. Sowerby, M. J. Neve, and A. G. Williamson, "A frequency-selective wall for interference reduction in wireless indoor environments," in *IEEE Antennas and Propagation Magazine*, vol. 48, no. 5, pp. 29-37, Oct. 2006.

[14] N. Liu, X. Sheng, C. Zhang, and D. Guo, "Design of frequency selective surface structure with high angular stability for radome application," *IEEE Antennas Wireless Propag. Lett.*, vol. 17, no. 1, pp. 138-141, Jan. 2018.

[15] N. Liu, X. Sheng, C. Zhang, J. Fan, and D. Guo, "A design method for synthesizing wideband band-stop FSS via its equivalent circuit model," *IEEE Antennas Wireless Propag. Lett.*, vol. 16, pp. 2721-2725, 2017.

[16] G. Manara, A. Monorchio, and R. Mittra, "Frequency selective surface design based on genetic algorithm," *Electronics Letters*, vol. 35, pp. 1400-1401, 1999.

[17] E. F. Kent, B. Doken, and M. Kartel, "A new equivalent circuit based FSS design method by using genetic algorithm," *International Conference on Engineering Optimization*, pp. 1-4, 2010.

[18] Z. Li, P. Y. Papalambros, and J. L. Volakis, "Frequency selective surface design by integrating optimization algorithms with fast full wave numerical methods," *IEE Proc. Microw. Antennas Propag.*, vol. 149, no. 3, pp. 175-180, 2002.

[19] X. Xiong, W. Hong, Z. Zhao, L. Deng, and S. Li, "Wi-Fi band-stop FSS for increased privacy protection in smart building," *2015 IEEE 6th International Symposium on Microwave, Antenna, Propagation, and EMC Technologies (MAPE)*, Shanghai, pp. 826-828, 2015.

[20] R. J. Langley and E. A. Parker, "Double-square frequency-selective surfaces and their equivalent circuit," *Electronics Letters*, vol. 19, no. 17, pp. 675-677, 18 Aug. 1983.

[21] M. Yan, J. Wang, and H. Ma, "A tri-band, highly selective, bandpass FSS using cascaded multilayer loop arrays," *IEEE Trans. Antennas and Propag.*, vol. 64, no. 5, pp. 2046-2049, May 2016.

[22] F. Costa, A. Monorchio, and G. Manara, "An overview of equivalent circuit modeling techniques of frequency selective surfaces and metasurfaces," *Applied Computational Electromagnetics Society Journal*, no. 29, pp. 960, 2014.

[23] H. Li, Q. Cao, C. Yang, and Y. Wang, "Design and analysis of a frequency selective radome (FSR) with wideband absorbing properties," *2016 IEEE International Workshop on Electromagnetics: Applications and Student Innovation Competition (iWEM)*, Nanjing, pp. 1-3, 2016.

[24] A. J. Chipperfield and P. J. Fleming, "The MATLAB genetic algorithm toolbox," *IEE Colloquium on Applied Control Techniques Using MATLAB*, London, UK, pp. 10/1-10/4, 1995.

[25] Y. Rahmat-Samii, *Electromagnetic Optimization by Genetic Algorithms*. Wiley Series in Microwave and Optical Engineering, 1999.

An Efficient Numerical Model for the Radiation Analysis of Microstrip Patch Antennas

Lu Liu and Zaiping Nie

School of Electrical Science and Engineering
University of Electronic Science and Technology of China, Chengdu, Sichuan, 610054, China
liulu1412@163.com, zpnie@uestc.edu.cn

Abstract ─ An accurate integral equation method based on quasi-static relationship (QSR), thin dielectric sheet (TDS) method and high-order hierarchical Legendre (HOHL) basis function is proposed in this paper for fast analysis of microstrip antennas radiation problems. This technique employs the QSR of the current on the parallel plate capacitor to describe the field continuity boundary condition and to embody the tight coupling between the radiation patch, the ground plane and the substrate of microstrip antenna. The frequency offset problem of conventional VSIE can be effectively eliminated. Moreover, combined with the TDS and the HOHL basis function, the proposed model can provide high accuracy in input impedance and far-field performance with faster convergence speed and lower computational cost. Numerical results are presented to show the accuracy and efficiency of the proposed method.

Index Terms ─ Microstrip antenna and array, numerical modelling, radiation analysis, quasi-static relationship, thin dielectric sheet method.

I. INTRODUCTION

Integral equation methods (IEM) and their numerical solutions have been widely used for simulating electromagnetic scattering and radiation problems [1-3]. However, when IEMs are used for modelling the radiation performance of metal-dielectric composite structures (microstrip patch antennas, for example), the number of the unknowns to be solved, iteration convergence and the accuracy of the solution are still challenging due to complex excitations, multi-scale structures and strong mutual coupling. Uniform plane wave is commonly employed as the excitation condition for the scattering target. Conversely, a forced voltage or current is typically used as the excitation at the feed port of the radiation problem, resulting in a strong and complex field distribution near the feed port. Due to the complex field distribution and strong mutual coupling, the modelling of radiation problems is more difficult than scattering problems. Therefore, constraint conditions describing the physical mechanisms of radiation structures may be very helpful for efficient modelling of radiation problems.

The volume-surface integral equation (VSIE) [1,4] is particularly convenient for modelling microstrip antennas because it is more accurate for modelling the thin dielectric, corners and edges than the commonly used surface integral equation (SIE) [5]. However, the traditional VSIE numerical solution has two major drawbacks that prevent its application to the radiation analysis of microstrip antennas. First, the convergence is very slow, and a significant shifting of the resonant frequency can be observed in the numerical solution. In addition, most existing VSIE models apply low-order and sub-domain basis functions to expand the unknown current [6-9], and geometrically model the detailed structure of the antenna by means of many electrically small elements to match the structure precisely, all leading to a large number of unknowns and huge computational costs, especially for antenna arrays.

Makarov et al. [6] first proposed that the failure description of the boundary condition on the interface between metal and dielectric is the main reason for the resonant frequency shifting problem of the VSIE model. They enforced an explicit boundary condition for the volume bases in contact with the metal surface to address this issue successfully. According to this idea, Zhang et al. [8] proposed a new hybrid basis function to explicitly enforce the boundary condition at the interface. A coupled surface-volume integral equation approach proposed by Lu and Chew [3] used the current continuity equation $\hat{n} \cdot \vec{D} = \nabla \cdot \vec{J}_s / i\omega$ as a boundary condition to formulate the relationship between the current $\vec{J}_s$ on the metal side of the interface and the electric flux density $\vec{D}$ on the dielectric side. This formulation is valid for composite objects with three-dimensional metal body. However, it may not be accurate for the metal sheet with "zero-thickness", such as the antenna patch and its ground plane.

To reduce the number of unknowns and memory requirements, Cai [10] used curved tetrahedral/triangular elements for geometric modelling and the higher order

Submitted On: March 22, 2019
Accepted On: June 6, 2019

hierarchical vector basis functions for the volume/ surface current modelling. The entire domain basis function with high-precision edge condition has been used in [11] to represent the surface current distribution on the patch to reduce computational requirements and achieve the fast analysis of microstrip antennas. However, it is not convenient for the analysis of strongly coupled environments, such as arrays. Thin dielectric sheet (TDS) approximation is also an effective and reliable method for reducing unknowns when VSIE is used to deal with thin dielectric problems [12-14]. The coupled PEC-TDS approach proposed in [13] has been used to analyze the radiation of the patch antenna, and high efficiency has been observed. However, the total number of unknowns is still large because this approach is based on low-order basis functions, and the unknowns for the volume are required.

In order to eliminate the frequency offset problem, improve the convergence performance, and reduce the unknowns simultaneously, an efficient numerical technique based on the quasi-static relationship (QSR) of the current on the parallel plate capacitor in conjunction with TDS approach is proposed for the fast analysis of radiation problems of microstrip antennas in this work. QSR is employed to embody the tight coupling properties and describe the current continuity condition between two sides of the metal-dielectric interface, thereby improving the accuracy of the numerical solution. Besides, by combining the TDS approach with the QSR formulation, the need to solve for $\vec{D}$ in the substrate is removed. Therefore, the unknowns can be greatly reduced and only exist on the metal surface. Moreover, the unknowns can be further reduced by using higher order hierarchical legendre (HOHL) basis function to expand the current. Furthermore, since the direction of HOHL basis function is consistent with the edge of the patch, the edge singular current on the patch can be well described, and the convergence property can be significantly improved compared to the commonly used RWG basis functions. In general, when dealing with the radiation problems of microstrip patch antennas, arrays and electrically large antennas, the new model proposed in this work provides less error in resonant frequency with fewer unknowns and faster convergence speed compared with the traditional VSIE model.

II. FORMULATION

The following VSIE model is commonly used to describe the electromagnetic properties of microstrip patch antenna with a thin finite dielectric substrate as shown in Fig. 1:

$$\begin{aligned} &\vec{E}^i(\vec{r}) + \vec{E}^s(\vec{r})\,|_{\tan} = 0 \qquad (\vec{r} \in S) \\ &\vec{E}^i(\vec{r}) + \vec{E}^s(\vec{r}) = \vec{E}(\vec{r}) \qquad (\vec{r} \in V), \end{aligned} \tag{1}$$

where V is the dielectric volume, S denotes the metal surface, $\vec{E}^i$ represents the incident electric field due to the applied source and $\vec{E}^s$ is the total scattered field.

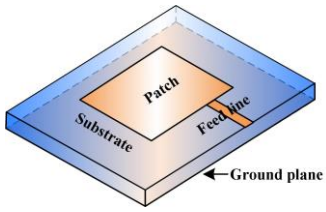

Fig. 1. Microstrip patch antenna model.

The scattered field produced by the surface current on the conducting patch $\vec{J}_s$ and the equivalent volume current in V are given by:

$$\vec{E}^s_{pec}(\vec{r}) = ik_0\eta_0 \int_S [\vec{J}_s(\vec{r}') + \frac{1}{k_0^2}\nabla\nabla'\cdot\vec{J}_s(\vec{r}')]G(\vec{r},\vec{r}')d_{s'}, \tag{2}$$

and

$$\vec{E}^s_{die}(\vec{r}) = ik_0\eta_0 \int_V [i\omega\chi(\vec{r}')\vec{D}(\vec{r}') + \frac{i\omega}{k_0^2}\nabla\nabla'\cdot\chi(\vec{r}')\vec{D}(\vec{r}')]G(\vec{r},\vec{r}')d_{v'}, \tag{3}$$

respectively. Where $\vec{D}$ is the electric flux density in V and η_0 is the wave impedance in free space. The contrast ratio χ is defined as $\chi(\vec{r}) = [\varepsilon(\vec{r}) - \varepsilon_0]/\varepsilon(\vec{r})$. The harmonic time convention e^{-iwt} is adopted in this work.

In the above VSIE model, the metals and dielectrics are considered to be independent of each other. Field continuity boundary condition on the metal-dielectric interface may not be satisfied if the commonly used SWG basis functions are employed to expand the electric flux density [6]. It may cause problems of resonant frequency offset and poor convergence when it is used in radiation analysis.

Based on the cavity model proposed by Lo [15], the electric field within each volume element can be assumed to have only one significant vertical component for a microstrip patch antenna with a thin dielectric substrate. In this work, the vertical component of the electric flux density in substrate is described by the surface currents at the top patch and the ground plane by using the parallel plate capacitor QSR shown in Fig. 2. The QSR formula [16] can be written as:

$$\vec{D}_n = \begin{cases} \hat{z}\dfrac{1}{2i\omega}(\nabla\cdot\vec{J}_s^- - \nabla\cdot\vec{J}_s^+) \text{ between ground plane and patch} \\ \hat{z}\dfrac{1}{2i\omega}(\nabla\cdot\vec{J}_s^- - 0) \text{ between ground plane and vacuum} \end{cases}, \tag{4}$$

where $\vec{J}_s^+$ and $\vec{J}_s^-$ are the surface current density on the metal radiation patch and the metal ground plane respectively. In more detail, the electric flux density $\vec{D}$ in the dielectric is modelled by the currents on the radiation patch and the ground plane. Therefore, the field

continuity and the tight coupling between the radiation patch, the ground plane and the substrate can be described.

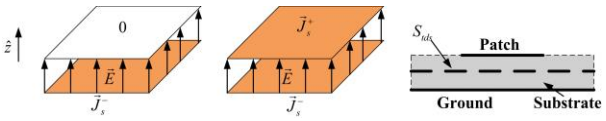

Fig. 2. Quasi-static electric field distribution in dielectric substrate.

When the thickness of the substrate τ is very small compared to the wavelength, the volume integral in (3) can be approximated by surface integral $d_{V'} \approx \tau d_{S'}$ to reduce the requirement of the computational resources, according to the idea of TDS approach [17]. The scattering field (3) introduced by the volume equivalent current can be calculated by surface integral and can be written as:

$$\vec{E}^s_{die}(\vec{r}) = ik_0\eta_0 \left\{ \int_{S_{tds}} i\omega\chi\tau(\vec{r}')\vec{D}_n(\vec{r}')G(\vec{r},\vec{r}')d_{s'} - \frac{i\omega}{k_0^2}\int_S \chi(\vec{r}')\vec{D}_n(\vec{r}')\nabla[G_\tau(\vec{r},\vec{r}') - G(\vec{r},\vec{r}')]d_{s'} \right\}, \quad (5)$$

where S_{tds} is the middle surface between the top patch and the ground plane as shown in Fig. 2, and $G_\tau(\vec{r},\vec{r}') = G(\vec{r},\vec{r}' + \tau\hat{n})$. Combined with (4), equation (5) can be further expressed as:

$$\vec{E}^s_{die}(\vec{r}) = ik_0\eta_0 \left\{ \int_{S_{tds}} \frac{\tau\chi(\vec{r}')}{2}\cdot\hat{n}\cdot[\nabla\cdot\vec{J}_s^- - \nabla\cdot\vec{J}_s^+]G(\vec{r},\vec{r}')d_{s'} - \frac{1}{k_0^2}\int_S \frac{\chi(\vec{r}')}{2}[\nabla\cdot\vec{J}_s^- - \nabla\cdot\vec{J}_s^+]\cdot\nabla[G_\tau(\vec{r},\vec{r}') - G(\vec{r},\vec{r}')]d_{s'} \right\}. \quad (6)$$

The above equation indicates that the field continuity condition and tight coupling can be rigorously embedded by expressing $\vec{D}$ in the substrate using the current on the radiation patch and ground plane. Moreover, as the unknowns only exist on the metal surface and no volume unknown is required in this model, the number of total unknowns can be significantly reduced. Since QSR and TDS are used in this model, it is suitable for planar microstrip antennas with thin dielectric substrates, and may lose accuracy when processing conformal microstrip antennas with high curvature.

RWG basis function is typically used in VSIE method to expand the current on the metal surface. RWG is a zeroth-order basis function, and the direction of the basis function is perpendicular to the common side of the adjacent elements. When the microstrip antenna operates at the resonant frequency, there are two singular edge currents parallel to the two edges of the radiating patch. Therefore, the mesh size of the RWG basis function needs to be small enough to accurately describe the edge current on the radiating patch, which results in a large number of unknowns. In this work, HOHL basis function [18] is used to describe the surface current because the direction of the HOHL basis function is consistent with the edge of the radiating patch, which can well describe the singular edge currents on the radiating patch and improve the convergence characteristics of the system. In addition, the mesh size of the HOHL basis function is always much larger than the RWG basis function, therefore the unknowns and memory costs can be further reduced. The HOHL basis function is defined as:

$$\vec{J}_s = \vec{J}_s^u\vec{a}_u + \vec{J}_s^v\vec{a}_v, \quad (7)$$

where $\vec{a}_u$ and $\vec{a}_v$ are the co-variant unitary vectors. The definition of u-directed current $\vec{J}_s^u$ or v-directed current $\vec{J}_s^v$ can be found in [18].

III. NUMERICAL RESULTS

A. Microstrip patch antenna radiation analysis

Consider a microstrip patch antenna excited by a transmission line as shown in Fig. 3. A rectangular patch is placed over a dielectric substrate with $\varepsilon_r = 2.2$. The bottom plane of the substrate is covered by a finite ground plane. Finite-width feeding model [19] is employed in this section to improve convergence and accuracy. The input impedance performances obtained by the proposed approach and the VSIE model described in equation (1) (discretized by RWG and SWG) are shown in Fig. 4 (a). The Ansoft HFSS finite element (FEM) simulation results are also given as a reference. A significant positive frequency offset (about 3%) of the traditional VSIE solution can be observed, which is consistent with the result described in [6]. However, both the real and imaginary part of the input impedance calculated by the proposed approach over 7.0GHz to 9.0GHz are in good agreement with the FEM solutions. Only a frequency shift of 0.087% is observed, which indicates that the frequency offset can be effectively eliminated by the proposed approach. The comparison of the radiation gain pattern at the phi=0° plane computed by the proposed model and the FEM is shown in Fig. 4 (b). Although a difference of 2dB exists in the back lobe of the pattern, excellent agreement can be observed.

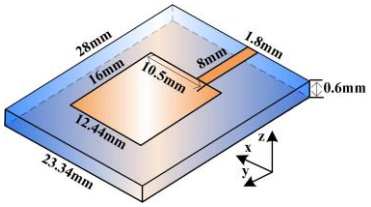

Fig. 3. The geometry of a microstrip patch antenna working at X band.

The computational details of both the proposed approach and traditional VSIE model under the same computing platform are listed in Table 1. For the VSIE model, the patch antenna requires 499 triangles for conductive plates and 1391 tetrahedrons for dielectric substrate modelling, resulting in 3990 unknowns in total. However, the proposed model consists of 34 quadrilateral elements and results in 238 unknowns in total when 2 order HOHL basis functions are used. The memory of the impedance matrix is reduced from 12.1MB to 0.43MB and the total CUP time is reduced from 1185s to 27s. In addition, the convergence properties of the proposed model and VSIE model are represented by the red and black line, respectively, in Fig. 5. The proposed approach converges much faster than the traditional VSIE. Both equations are solved by the GMRES iterative method and no preconditioned method is employed. As a consequence, the proposed approach provides higher accuracy and requires fewer computational resources than traditional VSIE model, when analyzing the radiation problem of the microstrip antenna.

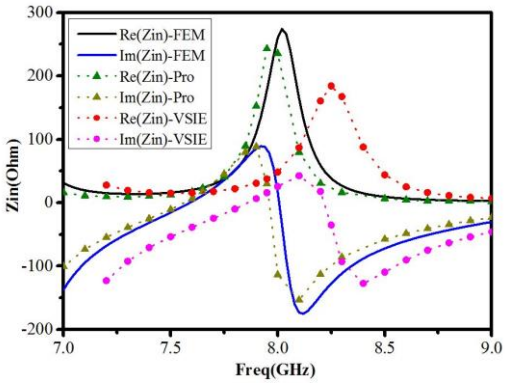

(a)

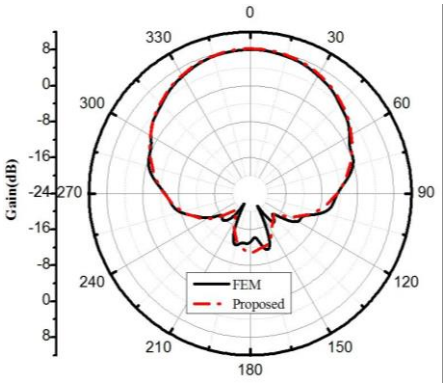

(b)

Fig. 4. Input impedance and far-field radiation performance. (a) Comparison of the input impedance calculated by FEM, VSIE and the proposed model. (b) Comparison of the radiation patterns obtained by FEM and proposed model at 7.75GHz, phi=0°.

Table 1: Comparison of CPU time and memory requirement of the proposed model and the traditional model

	Number of Unknowns	Memory of Impedance Matrix (MB)	Total CPU Time (s)
Traditional VSIE	3990	121.46	1184
Proposed model	238	0.43	27

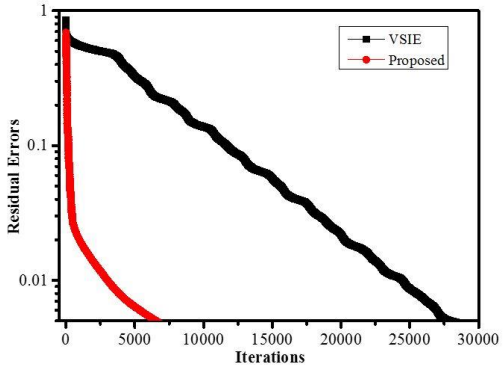

Fig. 5. The convergence properties of the proposed model and traditional VSIE.

B. Reflector antenna with a patch antenna as feed

The proposed approach is also a good choice for the EM modelling of electrically large antennas, such as the reflector antenna with a patch antenna as the feed. The geometries and dimensions of the reflector and patch antenna are shown in Fig. 6 (a). The dielectric constant of the patch antenna substrate is 3.5. FEM is very efficient for analyzing electrically small antenna. However, it is not suitable for analyzing electrically large antennas due to the large number of unknowns generated by the bounding box. VSIE model with low-order basis functions is also not a good choice because of the frequency shift problem and the large number of unknowns. VSIE needs more than 20196 unknowns to describe this example and takes more than two hours of solving time when MLFMA and Block-Diagonal precondition are used for acceleration. However, only 2658 unknowns is required for the proposed method when 2 order HOHL basis function is selected, and the solving time can be reduced to 508s. The return loss (with respect to 50Ω) calculated by VSIE, the proposed method and FEM are compared in Fig. 6 (b). Similarly, a significant frequency shift of about 4.9% is observed for VSIE result, however, the S_{11} obtained from the proposed approach consists well with FEM solution. The comparison of radiation gain patterns is shown in Fig. 6 (c). Good agreement in the main lobe of the pattern is observed, although the side and back lobes are slightly different.

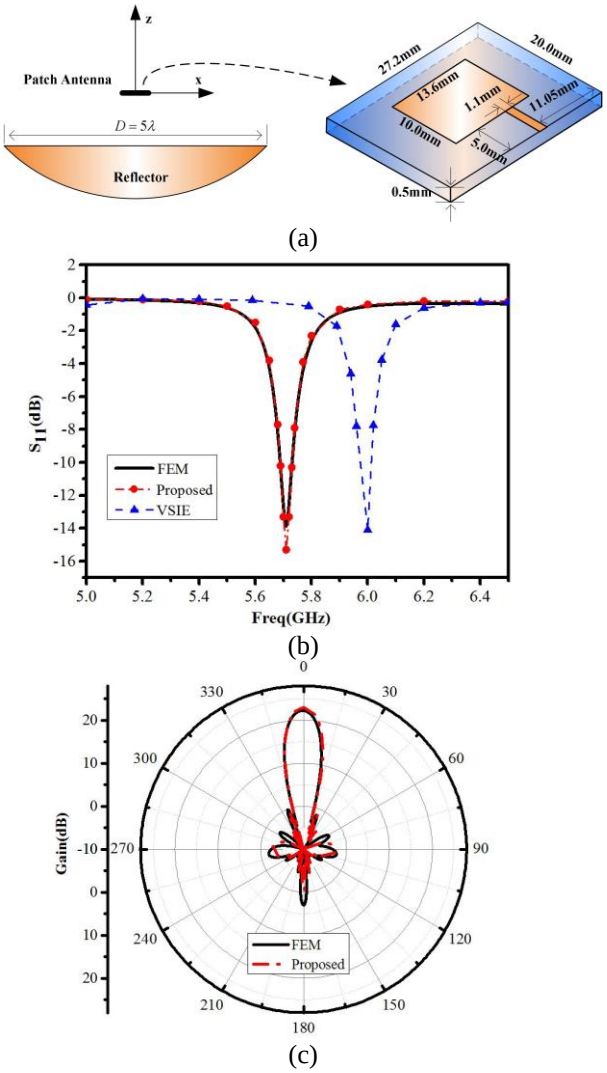

Fig. 6. Reflector antenna with a microstrip patch antenna as feed. (a) Geometry of the reflector antenna with $f/D = 0.38$ and the patch antenna at the focus plane. (b) Comparison of the return loss obtained by FEM, VSIE and the proposed mode, S_{11}. (c) Comparison of the radiation patterns obtained by FEM and the proposed model at 5.71GHz, phi=0°.

C. Microstrip patch antenna array

As the final example, a 3×4 two-dimensional patch array shown in Fig. 7 (a) is considered. The size of each antenna element and the dielectric constant of the substrate are the same as the patch antenna described in the second example. The distance between two adjacent elements is 20.4mm. The excitation voltages of each element is set as 1.0V. The proposed model contains a total of 3108 unknowns and takes 1851 seconds to solve this problem when MLFMA is employed. However, VSIE model requires 35678 unknowns and takes more than 10 hours of solving time due to its poor convergence. The radiation performance of this antenna array in phi=0° plane computed by the proposed model is compared with the result of FEM in Fig.7 (b). The main and side lobes are in good agreement, and a slight difference exists in the back lobe of the pattern. The results show that the proposed model has high accuracy and efficiency even when analyzing the strongly coupled antenna array radiation problems.

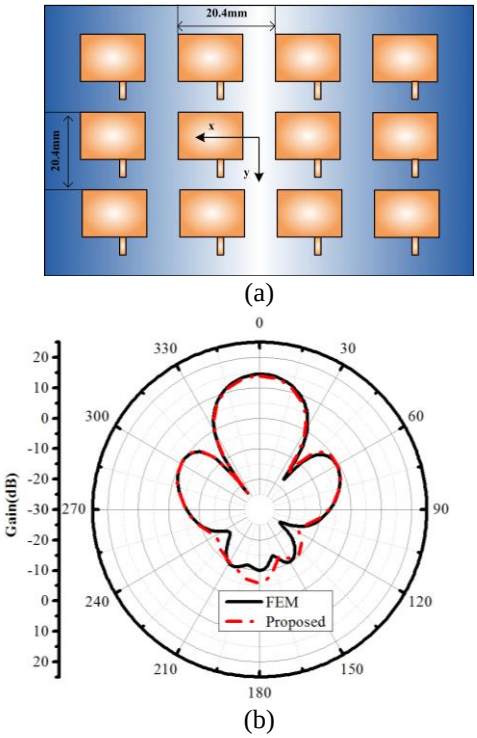

Fig. 7. 3×4 microstrip patch antenna array. (a) Geometry of the array. (b) Comparison of the radiation patterns obtained by FEM and the proposed model at 5.71GHz, phi=0°.

IV. CONCLUSION

Based on the physical properties of microstrip antennas, an effective numerical model is proposed for fast analyzing the radiation of planar microstrip patch antennas with thin dielectric substrates. In this model, the current on metal surface is described by the HOHL basis function. QSR formulation is applied to embody the physical properties of the microwave resonant structure. TDS method combined with QSR is employed to reduce computing resources and improve efficiency. Numerical examples have demonstrated that this model is able to remove the frequency shift problem, reduce the number of unknowns and speed up the iteration convergence significantly compared to traditional VSIE model. Since this model has fewer unknowns and can be easily combined with the existing fast algorithms, it is

promising for simulation of electrically large antennas and antenna arrays with big number of elements.

ACKNOWLEDGMENT

This work is supported by the Natural Science Foundation of China (NSFC) under Grant No. 61721001.

REFERENCES

[1] T. Sarkar and E. Arvas, "An integral equation approach to the analysis of finite microstrip antennas: Volume/surface formulation," *IEEE Trans. Antennas Propag*., vol. 38, no. 3, pp. 305-312, 1990.

[2] R. Zhao, Z. Huang, W. Huang, J. Hu, and X. Wu, "Multiple-traces surface integral equations for electro-magnetic scattering from complex micro-strip structures," *IEEE Trans. Antennas Propag*., vol. 66, no. 7, pp. 3804-3809, 2018.

[3] C. C. Lu and W. C. Chew, "A coupled surface-volume integral equation approach for the calculation of electromagnetic scattering from composite metallic and material Targets," *IEEE Trans. Antennas Propag*., vol. 48, no. 12, pp. 1866-1868, 2000.

[4] K. Xiao, Y. Lin, F. Zhao, S. Chai, and J. Mao, "Analysis of microstrip antennas using the volume surface integral equation formulation and the pre-corrected fast fourier transform method," *ACES Journal*, vol. 26, no. 11, pp. 922-929, Nov. 2011.

[5] S. Rao, T. Sarkar, P. Midya, and A. Djordevic, "Electromagnetic radiation and scattering from finite conducting and dielectric structures: Surface/ surface formulation," *IEEE Trans. Antennas Propag*., vol. 39, no. 3, pp. 1034-1037, 1991.

[6] S. Makarov, S. Kulkarni, A. Marut, and L. Kempel, "Method of moments solution for a printed patch/ slot antenna on a thin finite dielectric substrate using the volume integral equation," *IEEE Trans. Antennas Propag*., vol. 54, no. 4, pp. 1174-1184, 2007.

[7] K. Xiao, S. Chai, and L. Li, "Comparisons of coupled VSIE and noncoupled VSIE formulations," *J. Electromagnetic Waves Appl*., vol. 25, no. 10, pp. 1341-1351, 2011.

[8] K. Zhang, M. He, X. Xu, and H. Sun, "An efficient solution of the volume-surface integral equation for electromagnetic scattering and radiation of the composite dielectric-conductor objects with reduced number of unknowns," *IEEE Trans. Antennas Propag*., vol. 61, no. 2, pp. 798-809, 2013.

[9] J. Chen, S. Li, F. Zhao, and Y. Song, "Analysis of electromagnetic scattering problems by means of a VSIE-ODDM-MLFMA method," *ACES Journal*, vol. 27, no. 8, pp. 660-667, Aug. 201.

[10] Q. Cai, Y. Zhao, W. Huang, Y. Zheng, Z. Zhang, Z. Nie, and Q. Liu, "Volume surface integral equation method based on higher order hierarchical vector basis functions for EM scattering and radiation from composite metallic and dielectric structures," *IEEE Trans. Antennas Propag*., vol. 64, no. 12, pp. 5359-5372, 2016.

[11] R. Ribeiro, V. Marcos, and F. Alexis, "Entire domain basis function with accurate edge condition for rectangular microstrip antennas," *IEEE Antennas and Wireless Propagation Letters*, vol. 68, no. 1, pp. 123-127, 2019.

[12] I. T. Chiang and W. C. Chew, "Thin dielectric sheet simulation by surface integral equation using modified RWG and pulse bases," *IEEE Trans. Antennas Propag*., vol. 54, no. 7, pp. 1927-1934, 2006.

[13] I. T. Chiang and W. C. Chew, "A coupled PEC-TDS surface integral equation approach for electro-magnetic scattering and radiation from composite metallic and thin dielectric objects," *IEEE Trans. Antennas Propag*., vol. 54, no. 11, pp. 3511-3516, 2006.

[14] C. P. Davis and W. C. Chew, "An alternative to impedance boundary conditions for dielectric-coated PEC surfaces," *IEEE AP-S Int. Symp.*, Honolulu, HI, pp. 2785-2788, June 2007.

[15] Y. T. Lo, D. Solomon, and F. Richards "Theory and experiment on microstrip antennas," *IEEE Trans. Antennas Propag*., vol. 27, no. 2, pp. 137-145, 1979.

[16] S. Makarov, *Antenna and EM Modeling with MATLAB*. New York, 2002.

[17] X. Niu, Z. Nie, S. He, and X. Que, "Improved multilayer thin dielectric sheet approximation for scattering from electrically large dielectric sheets," *IEEE Antennas and Wireless Propagation Letters*, vol. 14, pp. 779-782, 2015.

[18] E. Jorgensen, J. L. Volakis, P. Meincke, and O. Breinbjerg, "Higher order hierarchical legendre basis functions for electromagnetic modeling," *IEEE Trans. Antennas Propag*., vol. 52, no. 11, pp. 2985-2996, 2004.

[19] Y. Lo, L. Jiang, and W. Chew, "Finite-width feed and load models," *IEEE Trans. Antennas Propag*., vol. 61, no. 1, pp. 281-289, 2013.

High Power Dielectric Reflectarray Antenna using 3D Printing Technology

Binke Huang [1], Qiwen Qiang [1], and Guy A. E. Vandenbosch [2]

[1] Department of Information and Telecommunication Engineering
Xi'an Jiaotong University, Xi'an 710049, China
bkhuang@mail.xjtu.edu.cn, foreverfree2@sina.com

[2] Department of Electrical Engineering, Division ESAT-TELEMIC
KU Leuven, B-3001 Leuven, Belgium
guy.vandenbosch@esat.kuleuven.be

Abstract ─ A high power dielectric reflectarray with a continuous variation of the effective permittivity of a dielectric slab is proposed, based on a cross-shaped element implemented in the slab. The improved method used to retrieve the effective permittivity from the S parameters shows that a continuously changing effective relative permittivity from 1.25 to 3.4 can be reached by adjusting the notch width of the cross-shape, yielding a full 360° range of phase shifts at 9.3GHz. An array of 10×10 elements is designed to verify the radiation properties.Simulation results show that a main beam direction of 25° and a maximum gain of 19.5dB can be realized at the 9.3GHz center frequency. The power capacity of the element reaches 371kW, opening the possibility of high power applications. Fused Deposition Modelling (FDM), a specific approach in 3D printing, was employed for the fabrication of a prototype. This technology significantly reduces material cost and manufacturing time.

Index Terms ─ Dielectric reflectarray, Fused Deposition Modeling (FDM), high power.

I. INTRODUCTION

The reflectarray antenna is regarded as a good alternative for traditional parabolic antennas and array antennas because of its low profile, high gain, beam steering possibilities and simple horn feeding [1-2]. A reflectarray can be achieved by dividing the reflector surface into a sub-wavelength grid of individual metamaterial unit cells, each with a variable reflection phase. However, since periodic unit cells may exhibit dielectric breakdown at high powers [3], which would change the radiation properties of the antenna and introduce irreversible damage, care must be taken so that neither dielectric nor air breakdown occurs under operating conditions.

In recent years, in order to improve the mobility of high power parabolic antennas equipped on vehicles, the reflectarray is considered as a promising alternative to the bulky conventional parabolic antenna in many high power applications. In 2015, Zhao *et al.* proposed an element of double square rings covered with a PTFE layer for an X-band high power reflectarray antenna [4]. In 2017, Gregory *et al.* proposed a shorted circular element unit cell for implementing steerable high power reflectarray [5]. In 2018, Gregory *et al.* proposed metamaterial-based unit cells usable in reflectarrays. They are comprised of end-loaded dipoles with capacitive lumped elements, round edges, and approximate high voltage capacitors as loads to mitigate field enhancement [6-7]. However, all these designs are complex in processing and the power capacity is unable to reach the GW/m^2 regime.

In this paper, we present a kind of dielectric reflectarray element that is feasible to be fabricated by FDM 3D printing technology to replace the traditional microstrip element for power capacity enhancement. The element is composed of a conductive ground and a dielectric block of changing effective permittivity to regulate the reflection phase. An improved method is used to retrieve the effective permittivity of the cross-shaped element based metamaterial slab with periodic boundary from its S parameters. By varying the notch width of the slab, a continuous effective relative permittivity is successfully achieved. This variation in the relative permittivity is used to obtain the required reflection phase shifts in the reflectarray. The power capacity is investigated. A complete reflectarray antenna with 10×10 elements is designed with the full-wave simulation software CST Microwave Studio® [8] to validate the radiation properties, and a 10×10 array is prototyped with 3D printing technology.

II. ELEMENT DESIGN

A. Homogeneous slab of dielectric

Consider a homogeneous dielectric slab backed by a conductive ground. The thickness of the slab is *h*, its

Submitted On: January 24, 2019
Accepted On: April 6, 2019

permittivity is ε, and its loss tangent is tanδ. Assume a normally incident plane wave. Fig. 1 shows the phase and the magnitude of the reflection coefficient versus the relative permittivity of the slab for the case h=25 mm (0.775λ for f=9.3GHz), ε_r=1.0 to 3.5, and tanδ=5.1×10-3 at f=9.1GHz, 9.3GHz and 9.5GHz. The dielectric is inspired by [9] and the height is considerable in order to get sufficient phase shift. It can be seen that when the bulk relative permittivity changes from 1.0 to 3.5, the reflection phase shifts indicate a range of more than 360°. The reflection phase curves are quasi-parallel for the three frequencies. The reflection magnitude varies in between -0.20 and -0.60 dB.

B. The cross-shaped block

Replace the continuous slab by an array of cross-shaped dielectric blocks, as depicted in Fig. 2. The bulk relative permittivity of the dielectric is 3.4. The element spacing is P=16 mm (0.5 λ) to avoid grating lobes. The dimensions of the cross-shaped dielectric blocks are listed in Table 1.

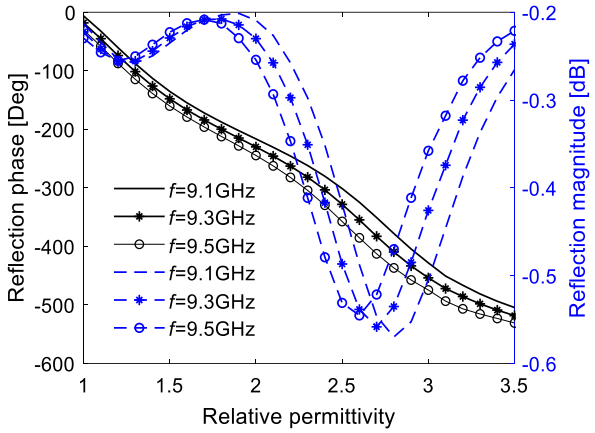

Fig. 1. Reflection coefficient versus relative permittivity of the slab.

Characterizing this block array as an effective homogeneous dielectric slab, we need to remove the ground and retrieve the effective permittivity and permeability from the reflection (S_{11}) and transmission (S_{21}) coefficients for a normally incident plane wave. The S parameters are related to the refractive index n of this effective slab and the free space wave impedance Z by [10]:

$$n = \{\arccos[(1-S_{11}^2+S_{21}^2)/(2S_{21})]\}/(k_0 h), \quad (1)$$

$$Z = \sqrt{[(1+S_{11})^2 - S_{21}^2]/[(1-S_{11})^2 - S_{21}^2]}, \quad (2)$$

where k_0 denotes the wave number. The permittivity ε and permeability μ are then directly calculated from ε=nZ and μ=n/Z. Figure 3 shows that for the example considered with h=2 mm the retrieved effective permittivity varies with the size of the corner notch w. We can see that an effective relative permittivity from 1.25 to 3.4 can be achieved by properly choosing w. Moreover, the effective relative permittivity is quite stable with a maximum variation of no more than 0.2 for the three different frequencies depicted. This guarantees the desired phase shifts in the frequency band of interest.

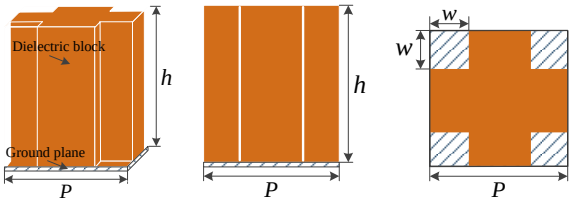

Fig. 2. Element structure with cross-shaped dielectric block: (a) perspective view, (b) front view, and (c) top view.

Table 1: Parameters of cross-shaped dielectric block

Name	Description	Value
H	Height of slab	2 mm
P	Element spacing	16 mm
w	Size of notch	0.5~7.5 mm
ε_r	Effective relative permittivity	3.4
tanδ	Loss tangent	5.1×10^{-3}

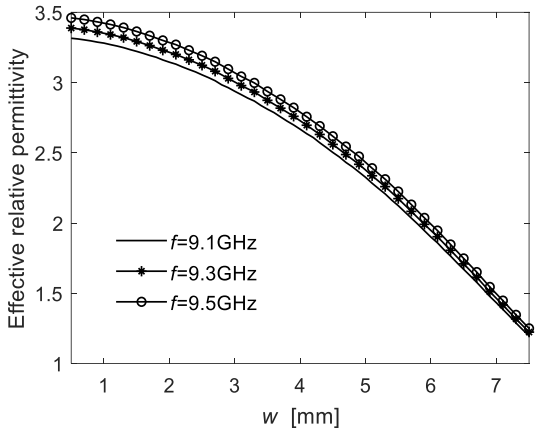

Fig. 3. Retrieved effective relative permittivity versus notch size w, all for h =2 mm.

The height of the cross-shaped block h=2 mm is adopted for achieving a high accuracy when retrieving its effective permittivity from (1). Now the thickness is increased to the original 25 mm, the ground is added again, and the resulting topology is simulated using Ansys HFSS™ with periodic boundaries [11]. Figure 4 shows the resulting phase and magnitude of the reflection coefficient versus the notch size w for normal incidence at f=9.1 GHz, 9.3 GHz and 9.5 GHz. It can be seen that the reflection phase possesses a good linearity and a

similar flatness as for the original homogeneous slab (See Fig. 1). The phase shift is smooth and the ranges for the three different frequencies are all more than 360°. The reflection magnitude for the different frequencies and notch sizes *w* is better than -0.55 dB (0.94), indicating a fairly efficient reflector performance.

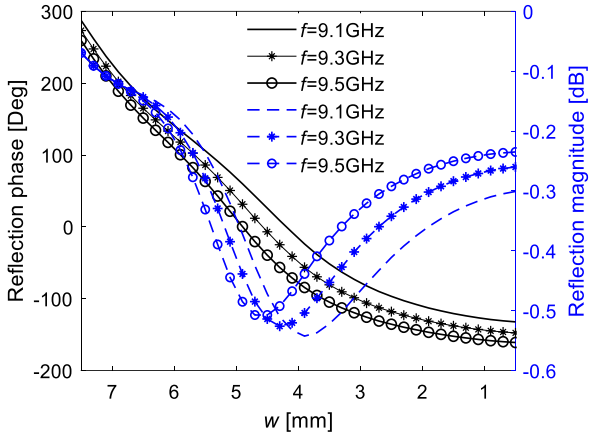

Fig. 4. Reflection coefficient versus notch size *w* simulated with HFSS.

III. REFLECTARRAY DESIGN

A complete dielectric reflectarray antenna is designed in this section. The idea is to generate a transversally changing permittivity by changing the size of the corner notch *w* from block to block and this in such a way that it yields the correct transversally changing reflection phase needed in the reflectarray. The required phase shift for each element (*m*,*n*) located at (x_m, y_n, 0) can be calculated as follows [1]:

$$k_0(r_{mn} - \bar{R}_{mn} \cdot \hat{r}_b) - \Delta\Phi_{mn} = 2\pi N, \quad (3)$$

$$r_{mn} = \sqrt{(x_F - x_m)^2 + (y_F - y_n)^2 + z_F^2}, \quad (4)$$

where k_0 denotes the wave number, $\bar{r}_{mn}$ is the position vector of the mn^{th} element relative to the feed point at (x_F, y_F, z_F) = (0, 0, z_F). $\bar{R}_{mn}$ is the position vector of mn^{th} element relative to (0, 0, 0), $\hat{r}_b$ is the direction vector of the desired pencil beam with (θ_b, φ_b) in a spherical coordinate system, N=1, 2, 3, …, and $\Delta\Phi_{mn}$ is the phase shift introduced by the element of the reflectarray in the reflected wave relative to the incident wave.

The reflectarray topology is illustrated in Fig. 5. The resulting design is an array of 10×10 element blocks with an aperture size of 160mm×160mm, operating at 9.3GHz and fed by a centered pyramid horn. It's phase center is located at a distance F=100 mm from the reflectarray. The desired main beam direction (θ_b, φ_b) is set as (25°, 0°). F corresponds to the focal length of the reflectarray. It is calculated as:

$$F = D/(2\tan\theta_e), \quad (5)$$

where D is the size of the reflector aperture, and θ_e is half the beamwidth where the gain of the feed horn drops by less than 10 dB compared to the broadside maximum. A pyramidal horn antenna with a θ_e of 38° and a standard waveguide WR90 as feeding port was selected [11].

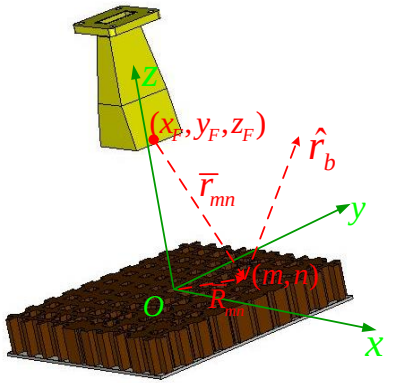

Fig. 5. The designed complete reflectarray.

The simulated radiation pattern in *x*-*z* plane for co-polarization (φ=0°) and in *y*-*z* plane for cross-polarization (φ=90°) at f = 9.3GHz are shown in Fig. 6. The reflected pencil beam is observed at 25 degrees, the maximum gain is 19.5dBi, and the 3dB beamwidth is 14°. The sidelobes are more than 10.5dB lower than the main lobe and the cross-polarization level is 18.2dB below the co-polarization level.

IV. POWER CAPACITY ANALYSIS

The limiting factor in power peak handling is the breakdown strength of the air around the cross-shaped block, which is approximately 3MV/m [7]. This is because, usually, the high power pulse is modulated with a sinusoidal signal and the duty cycle is sufficiently low so that thermal effects can be ignored. The key idea is thus to make a design with a low peak value of the electric field around the element, for a fixed input power. It is obvious that the variation of the notch size *w* leads to a variation of the *E*-field strength distribution. Simulations show that the maximum field distribution for the element occurs at resonance with the reflection phase equaling zero, since the reflected wave and the incident wave are in phase addition. This is for a normally incident plane wave from the positive *z*-direction. In our design this means for w = 4 mm at 9.3 GHz. For a feeding power density p_{in} of the structure of 1W/(0.016m)^2=3.906kW/m^2, the maximum *E*-field strength is 4926 V/m. Figure 7 shows how the maximum absolute value of the total *E*-field varies with the notch size *w* at 9.3 GHz. The maximum power density of the exciting plane wave can be calculated as follows [4]:

$$p_{\max} = [E_b / \max(E_{pin})]^2 p_{in}, \quad (6)$$

where max(E_{pin}) indicates the maximum *E*-field strength

in the structure fed with a power density p_{in} and E_b=3MV/m represents the breakdown *E*-field strength of air. The maximum power density for the incident plane wave is thus calculated as $p_{max}=(3\times10^6/4926)\times3.906$ kW/m$^2\approx1.45$GW/m^2.Assuming that the input power of every element is uniform, the power capacity of an element can go up to 1.45GW/m$^2\times0.016$m^2 =371kW. However, note that this is only an estimate of the order of magnitude since in reality there are different oblique incident angles for the different elements on the reflector, and thus the input power of the different elements is non-uniform.

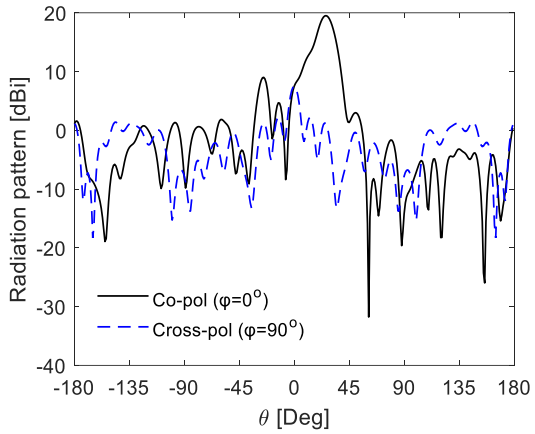

Fig. 6. Radiation pattern of the designed reflectarray at 9.3GHz: co-polar component in *H* plane (φ=0º) and cross-polar component in *E* plane (φ=90º).

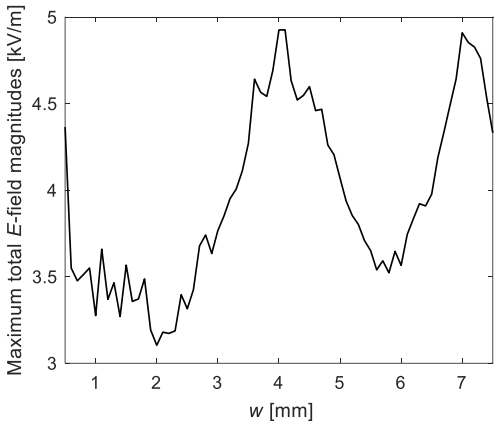

Fig. 7. Maximum total *E*-field magnitudes in the structure versus *w*.

Note that the power capacity of the structure with double square ring element covered with a polytetrafluoroethylene (PTFE) layer, as proposed in [4], is just 162kW, and the one of the structure with end-loaded dipoles, as proposed in [8], is just 150kW. The dielectric element proposed in this paper is obviously superior to the printed metallic elements for high power handling in reflectarrays as available in literature.

V. MEASUREMENTS

To verify the operational principle of our reflectarray design, a prototype of 10×10 elements was fabricated using low-cost FDM 3D printing technology. The dielectric material used is DSM's Somos® Imagine 8000 with the relative permittivity ε_r=3.4 at 1 MHz and unknown loss tangent, and a copper plate is used as ground. Figure 8 (a) shows the prototype of the reflector. The chosen feed horn was an HD-100HAT9 from HD Microwave Studio working in X-band [12]. For this horn, θ_e=38º, so that for the 10×10 array with *D*=160 mm the focal distance becomes *F*=102mm. In the actual prototype, the approximating value *F*=100mm was used, both in simulations and measurements. An Agilent E8257D signal generator (10MHz-40GHz) was used as source. A similar horn antenna was used as receiving antenna. The measurement set-up is shown in Fig. 8 (b).

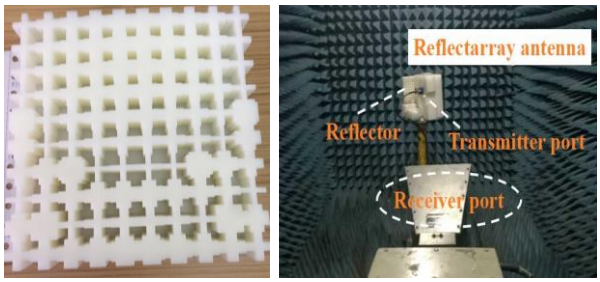

(a) (b)

Fig. 8. Photograph of the fabricated reflectarray under test in anechoic chamber. (a) Prototype of reflector, and (b) measurement set-up.

Figure 9 shows the radiation patterns at 9.3GHz, both the measured one and the ones simulated for relative permittivities ε_r=3.4 and ε_r=2.5, respectively, and an assumed loss tangent of 5.1×10^{-3} for the dielectric material. The measured gain is 15.8dBi in the direction of 20.4°. The simulated gain is 17.2dBi in the direction of 23° with ε_r=2.5, and 19.5dBi in the direction of 25° with ε_r=3.4. Comparing the measurements and simulations, the gain difference and the beam direction offset are 1.4dB and 2.6° for ε_r=2.5, while they are 3.7 dB and 4.6° for ε_r=3.4, respectively. The main reason for the observed discrepancies is the fact that the relative permittivity ε_r is actually less than 3.4 and decreases gradually with an increase of frequency. In fact, the material DSM's Somos® Imagine 8000 used in FDM 3D printing is similar as an acrylonitrile butadiene styrene (ABS) and its relative permittivity ε_r approaches 2.5 at 9.3GHz [9]. This explains the reasonable agreement between measurements and simulations with ε_r=2.5 at 9.3GHz. Second, the surface fabrication error for the reflector when using

FDM technology according to the vendor is ±0.2mm, which is larger than for traditional manufacturing techniques. This may also introduce phase compensation errors compared with the design, resulting in a beam direction shift and gain reduction.

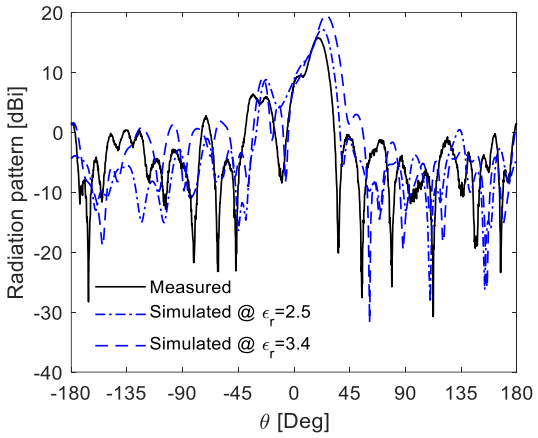

Fig. 9. Radiation pattern of the prototype reflectarray at 9.3GHz in *H* plane.

The simulated and measured gains as a function of frequency from 8.5GHz to 10GHz are given in Fig. 10. The relative permittivity ε_r=2.5 is used in the simulation. The gains increase with increasing frequency. The maximum gain difference between measurements and simulations is less than 1.4dB in this bandwidth. The proposed reflectarray satisfies the requirement of reaching a 100MHz bandwidth centered at 9.3GHz. The simulated aperture efficiency is 17.0% at 9.3GHz, 18.5% at 10GHz when ε_r=2.5, and the measured aperture efficiency is 12.3% and 16.5% at 9.3GHz and 10GHz, respectively.

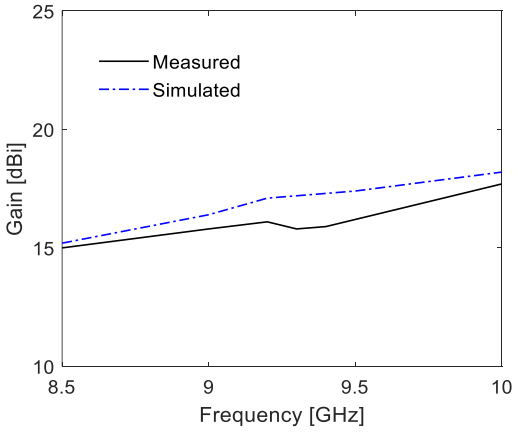

Fig. 10. Gain of dielectric reflectarray in *H* plane.

VI. CONCLUSION

A new dielectric cross-shaped reflectarray element is proposed that allows to continuously changing the effective relative permittivity in order to realize a correct reflection phase shift for reflectarray purposes. The new element provides a simple and effective method for implementing high power reflectarrays. A prototype antenna based on the element has been fabricated with 3D printing technology. A good qualitative agreement between simulated and measured results has been realized.

ACKNOWLEDGMENT

This work was supported in part by the National Natural Science Foundation of China under Grant 61471293 and the China Scholarship Council under Grant 201706285142.

REFERENCES

[1] J. Huang and J. A. Encinar, *Reflectionarray Antennas*. Hoboken-Piscataway, NJ, USA: Wiley-IEEE Press, 2007.

[2] S. H. Zainud-Deen, S. M. Gaber, A. M. Abd-Elhady, et al., "Perforated dielectric resonator antenna reflectarray," *Applied Computational Electromagnetics Society Journal*, vol. 26, no. 10, pp. 848-855, 2011.

[3] J. A. Bossard, C. P. Scarborough, Q. Wu, et al., "High-power considerations in metamaterial antennas," *Proc. IEEE Antennas Propag. Soc. Int. Symp.*, pp. 539-540, July 2014.

[4] J. Zhao, H. Li, and T. Li, "Design of a double square rings element for high-power X-band reflectarray antenna," *Proc. IEEE International Vacuum Electronics Conference*, Beijing, China, pp. 1-2, Apr. 2015.

[5] M. D. Gregory, J. D. Binion, D. Z. Zhu, et al., "High power metasurface reflectarray antennas using switched shorted circular elements," *IEEE International Symposium on Antennas and Propagation & USNC/URSI National Radio Science Meeting*, San Diego, CA, USA, pp. 1037-1038, July 2017.

[6] M. D. Gregory, J. A. Bossard, Z. C. P. O. Morgan, et al., "Metamaterials for high power reflectarray design," *IEEE/ACES International Conference on Wireless Information Technology & Systems*, Honolulu, HI, USA, pp. 1-2, Mar. 2016.

[7] M. D. Gregory, J. A. Bossard, Z. C. P. O. Morgan, et al., "A low cost and highly efficient meta-material reflector antenna," *IEEE Transactions on Antennas & Propagation*, vol. 66, no. 3, pp. 1545-1548, 2018.

[8] CST Microwave Studio, ver. 2014, Computer Simulation Technology, Framingham, MA, 2014.

[9] D. V. Isakov, Q. Lei, F. Castles, et al., "3D printed anisotropic dielectric composite with metamaterial features," *Mater. Design*, vol. 93, pp. 423-430, Mar. 2016.

[10] X. Chen, T. M. Grezegorczyk, B. I. Wu, et al., "Robust method to retrieve the constitutive effective parameters of metamaterials," *Phys. Review E*, vol. 70, no. 2, 2004.

[11] Ansoft High Frequency Structure Simulation (HFSS), ver. 15, Ansoft Corporation, Pittsburgh, PA, 2015.

[12] H. D. Wu, "HD Microwave User's Manual," 8th ed., 2017. [Online] Available: http://www.hengdamw.com/microwave-millimeterwave-antennas/standard-gain-horn-antenna.html

Optical Crosstalk Improvement in Ring Resonator Based Add/Drop Multiplexers Using Controllable Reflectivity

Riyadh D. Mansoor [1] and Alistair P. Duffy [2]

[1] Engineering College
Al-Muthanna University, Samawa, Iraq
riyadhdmu@mu.edu.iq

[2] School of Engineering and Sustainable Development
De Montfort University, Leicester, UK
apd@dmu.ac.uk

Abstract ─ In this paper, the topic of optical signal integrity is approached by studying crosstalk suppression in ring resonator based optical Add/Drop Multiplexers (OADM). The resonance splitting induced by surface corrugation is exploited to enhance signal integrity by increasing the crosstalk suppression bandwidth compared to that of a smooth-walled resonator. Sidewall roughness in silicon-on-insulator waveguides is studied using Coupled Mode Theory (time and space domain CMT). An analytical model of a corrugated ring resonator is presented, which is then exploited to estimate the spectral response of the different ports. Verification against results generated from full-wave electromagnetic numerical modeling of a randomized corrugated ring is performed. The analysis then examines the performance of an OADM with controllable reflectivity resulting from a predefined corrugation of sidewall. Gratings have been successfully used in optical filters; this paper proposes the use of a grating in an OADM, giving more controlled roughness. A grating-assisted design of a single ring OADM with 28 GHz crosstalk suppression bandwidth is presented. This bandwidth supports the dropping of 10 Gbps signals with mitigated crosstalk levels and improved signal integrity.

Index Terms ─ Back reflection, crosstalk, grating reflectivity, ring resonators, sidewall roughness.

I. INTRODUCTION

Signal integrity issues in all optical networks are of increasing interest due to the closer proximity of waveguides and optical components as integration density increases. The distinction between RF and optical communications frequencies is diminishing, making true on the claim that Electromagnetic compatibility (EMC) is "a DC to light phenomenon". Silicon-On-Insulator (SOI) is a promising technology to increase the integration density of all optical networks [1], [2]. SOI waveguides provide high confinement of light in devices of small dimensions and allow for large-scale integration in planar light wave circuits [3]. In this technology the propagation loss is relatively low [4]. However, the back-reflection effect due to sidewall roughness is of great importance [5], [6]. In rough-walled ring resonators, back reflection is a well-known cause of resonance splitting due to the interference between forward and counter-directional modes [7]-[9]. This effect has been exploited to increase the extinction ratio by enhancing the depth of the through port response at resonance [7]. In this paper, the resonance splitting resulting from a periodic perturbation of the sidewall roughness is exploited to improve the crosstalk performance of optical add/drop multiplexers OADMs in wavelength division multiplexed (WDM) networks by increasing the crosstalk suppression bandwidth [10].

Back reflection is a frequency dependent phenomenon that manifests as a variation of the response at each resonant frequency. The existence of resonance splitting relies on the relation between coupling coefficients and reflectivity. To extract the coupling and loss coefficients from experimental or numerical results, the back-reflection effect should be considered to produce an accurate analysis of OADMs. A coherent backscattering measuring system [11] and a fully analytical model [4] have been proposed to characterize all parameters of the ring including back reflection.

The sidewall roughness was created using semi-periodic gratings as reported, experimentally, in [12]. A set of ridges having identical length and period was shown to act as a wall corrugation. Therefore, it was studied as a quasi-grating and the reflectivity was measured as a function of frequency. Controlling the backscattering by predefining the dimensions of a quasi-grating during the fabrication introduces a new field of applications using grating-assisted resonators [13], [14]. Using Bragg grating calculations [15], the back-reflection

Submitted On: January 18, 2019
Accepted On: May 6, 2019

effect can be controlled by changing the grating dimensions (number, period and lengths of gratings). The dual-mode filter model has been used recently in photonic integrated platforms [16] in a similar manner to that in microwave circuits. Using a partial reflector inside a single ring resonator will result in a second order response. This effect has been exploited to enhance filter performance [9] and maximize the bandwidth of crosstalk suppression [17].

In this paper, controllable levels of back-reflection induced by a periodic surface corrugation are exploited to improve the crosstalk suppression bandwidth. This bandwidth of crosstalk suppression is defined as the bandwidth over which the suppression of intra-band crosstalk is maintained above 20 dB [18]. To achieve this aim, the research presented in this paper is arranged as follows:

1. Time domain Coupled Mode Theory (CMT) [19], [20] is exploited to propose an analytical model. This model allows a complete characterization of all parameters of the ring including back reflection.

2. An equivalent model of the corrugated ring is presented. The back-reflection can be visualized as resulting from a virtual ring. The space domain calculation is used, where the sidewall roughness is treated as a single scattering point.

3. The validity of the proposed models is tested against an existing experimental result [4]. Time and space domain models allow for accurate characterization of the ring without the need for curve fitting calculations.

4. The spectral response of different ports is simulated numerically using a commercial full wave simulation tool, CST [21], and the controllable reflectivity induced by semi-periodic gratings is modelled and validated using the ASPIC design simulator [22].

This paper presents a general solution for rough-wall ring resonator modelling as well as a particular solution to maximize the crosstalk suppression bandwidth. It concludes with a design that provides a 28 GHz crosstalk bandwidth.

II. COUPLED MODE ANALYSIS

Mutual coupling between the back reflected mode (induced by surface corrugation) and the forward mode is modelled analytically using CMT (coupled mode theory), both in the time and space domains.

A. Time domain analysis

Starting with Fig. 1, $a(t)$ is the forward mode, while $b(t)$ refers to the back-reflection mode, which is related to $a(t)$ through the reflection coefficient *r*. No new channels at the add port were assumed.

Based on the analysis of the time domain CMT [7], [23], the stored energy in the ring (forward mode) behaves as described by eq. (1):

$$\frac{\mathrm{da(t)}}{\mathrm{dt}} = \left(\mathrm{j}\omega_0 - \frac{1}{\tau}\right)\cdot \mathrm{a(t)} - \mathrm{j}k_1 \cdot \mathrm{S_i} - \mathrm{ju}\cdot \mathrm{b(t)}. \quad (1)$$

Where $u = \sqrt{\mathrm{r}}\cdot\frac{\mathrm{V_g}}{\mathrm{l}}$, is the mutual coupling, l is the perimeter of resonator $(2\pi R)$, V_g is the group velocity and $\frac{1}{\tau}$ is the decay rate of energy inside the ring (which depends mainly on the losses and coupling coefficient inside the resonator). S_i and k_1 are the input field and the coupling coefficient, respectively.

Also, the energy of the back-reflection mode changes as in eq. (2):

$$\frac{\mathrm{db(t)}}{\mathrm{dt}} = \left(\mathrm{j}\omega_0 - \frac{1}{\tau}\right)\cdot \mathrm{b(t)} - \mathrm{ju}\cdot \mathrm{a(t)}. \quad (2)$$

Based on (1) and (2), *a(t)* and *b(t)* can be obtained as in (3), (4) and (5):

$$\mathrm{a(t)} = \frac{-\mathrm{j}k_1\cdot \mathrm{S_i} - \mathrm{ju}\cdot \mathrm{b(t)}}{\mathrm{A}}, \quad (3)$$

$$\mathrm{A} = \mathrm{j}(\omega - \omega_o) + \frac{1}{\tau}, \quad (4)$$

$$\mathrm{b(t)} = \frac{-\mathrm{ju}\cdot \mathrm{a(t)}}{\mathrm{A}}. \quad (5)$$

And from (3) and (5), equation (6) is obtained:

$$\mathrm{a(t)} = \frac{-\mathrm{j}\cdot k_1\cdot \mathrm{A}}{\mathrm{A^2} + \mathrm{u^2}}\cdot \mathrm{S_i}. \quad (6)$$

Considering that β is the propagation constant in a waveguide of length *l*; the response of each port is as follows [17]:

i. Through-port spectral response (equations (7) and (8)):

$$\mathrm{S_t} = \mathrm{e}^{\mathrm{j}\beta \mathrm{l}}\left(\mathrm{S_i} - \mathrm{j}\cdot k_1\cdot \mathrm{a(t)}\right), \quad (7)$$

$$\left|\frac{\mathrm{S_t}}{\mathrm{S_i}}\right|^2 = \left|1 - \frac{{k_1}^2\cdot \mathrm{A}}{\mathrm{A^2} + \mathrm{u^2}}\right|^2. \quad (8)$$

ii. Drop-port spectral response (equations (9) and (10)):

$$\mathrm{S_d} = -\mathrm{j}\cdot k_2\cdot \mathrm{a(t)}, \quad (9)$$

$$\left|\frac{\mathrm{S_d}}{\mathrm{S_i}}\right|^2 = \left|\frac{k_1 k_2\cdot \mathrm{A}}{\mathrm{A^2} + \mathrm{u^2}}\right|^2. \quad (10)$$

iii. Add-port response (reflectivity) (equations (11 – (13)):

$$\mathrm{S_a} = -\mathrm{j}\cdot k_2\cdot \mathrm{b(t)}, \quad (11)$$

$$\mathrm{S_a} = \frac{-k_1 k_2\cdot \mathrm{u}}{\mathrm{A}}\cdot \mathrm{a(t)}, \quad (12)$$

$$\left|\frac{\mathrm{S_a}}{\mathrm{S_i}}\right|^2 = \left|\frac{k_1 k_2\cdot \mathrm{u}}{\mathrm{A^2} + \mathrm{u^2}}\right|^2. \quad (13)$$

The behavior at resonance is given in equations (14), (15) and (16):

$$\left|\frac{S_t}{S_i}\right|^2 = \frac{\left[u^2 + \frac{1}{\tau^2} - \frac{{k_1}^2}{\tau}\right]^2}{\left[u^2 + \frac{1}{\tau^2}\right]^2}, \quad (14)$$

$$\left|\frac{S_d}{S_i}\right|^2 = \frac{\frac{{k_1}^2 {k_2}^2}{\tau^2}}{\left[u^2 + \frac{1}{\tau^2}\right]^2}, \quad (15)$$

and

$$\left|\frac{S_a}{S_i}\right|^2 = \frac{{k_1}^2 {k_2}^2 \cdot u^2}{\left[u^2 + \frac{1}{\tau^2}\right]^2}. \quad (16)$$

To obtain the scattering parameters,

$$Th_o = \left|\frac{S_t}{S_i}\right|^2, Dr_o = \left|\frac{S_d}{S_i}\right|^2, \text{and } Re_o = \left|\frac{S_a}{S_i}\right|^2,$$

where, Th_o, Dr_o and Re_o are the through, drop and back reflection values at resonance respectively.

From (15) and (16):

$$\frac{Dr_o}{Re_o} = \frac{1}{\tau^2 \cdot u^2}. \quad (17)$$

Then,

$$u^2 = \frac{1}{\tau^2} \cdot \frac{Re_o}{Dr_o}. \quad (18)$$

To obtain τ, the ratio of Eqs. (10) and (13) is taken at f_1 which is the frequency where $Re = \frac{1}{2} \cdot Re_o$. With some rearrangements, equation (19) results:

$$\tau = \frac{1}{\Delta\omega} \cdot \sqrt{\frac{2Dr}{Dro} - 1}. \quad (19)$$

Dr is the value of the drop response at f_1 and $\Delta\omega$ is the frequency difference between f_1 and the resonant frequency.

Given the value of τ, the back-reflection coefficient is expressed as in Equ. (20):

$$R = \frac{(\Delta\omega)^2 \cdot l^2}{vg^2} \cdot \frac{Dro \cdot Re_o}{\sqrt{2Dr - Dro}}. \quad (20)$$

Also, the coupling coefficients can be represented as in equations (21) and (22):

$${k_1}^2 = \frac{l}{v_g} \cdot \frac{1}{\tau} \cdot \frac{(R_{eo} + D_{eo})}{D_{eo}} \cdot \left[1 - \sqrt{Th_o}\right], \quad (21)$$

$${k_2}^2 = \frac{l}{v_g} \cdot \frac{1}{\tau} \cdot \frac{(R_{eo} + D_{eo})}{\left[1 - \sqrt{Th_o}\right]}. \quad (22)$$

Finally, the losses can be measured based on [24] as in equation (23):

$${k_p}^2 = \left[\frac{2 \cdot l}{v_g} \cdot \frac{1}{\tau}\right] - {k_1}^2 - {k_2}^2. \quad (23)$$

And the losses coefficient is given in equation (24):

$$\alpha = \frac{1}{l} \cdot [-10 \cdot \log(1 - {k_p}^2). \quad (24)$$

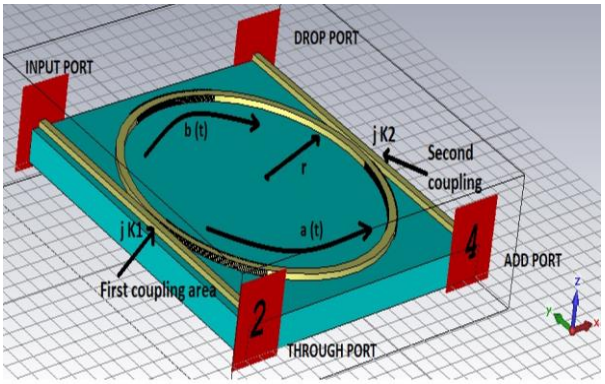

Fig. 1. Forward and back reflected modes in a rough-walled RR add/drop filter.

B. Space domain analysis

Although the scattering is distributed around the ring, it is helpful to think of it as an accumulated single scattering point [6] as shown in Fig. 2 (a). This point of scattering is characterized by $({K_r}^2)$ and $({t_r}^2)$, the back-reflection and transmission coefficient, respectively. The proposed equivalent structure is shown in Fig. 2 (b), where the reflection is assumed to be induced by a virtual ring.

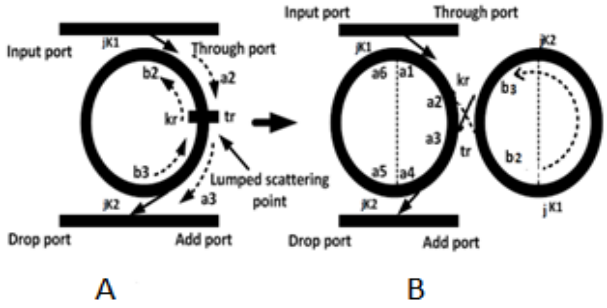

Fig. 2. The corrugated ring resonator (a), and (b) is the proposed virtual model.

The loop equations were written as in [17] to calculate the spectral responses of each port considering the existence of back reflection.

The drop port response is given in equation (25):

$$S_d = \frac{-k_1 k_2 \cdot \left[t_r - t_1 t_2 e^{-j\emptyset}\right] \cdot e^{-j\emptyset/2}}{1 - 2 \cdot t_1 t_2 \cdot t_r \cdot e^{-j\emptyset} + {t_1}^2 {t_2}^2 \cdot e^{-2j\emptyset}}, \quad (25)$$

where, $\emptyset = \alpha l + j\beta l$, is the propagation loss and phase change. k_1 and k_2 are the bus/ring power coupling coefficients, $t_r = \sqrt{1 - {k_r}^2}$ and l is the ring perimeter.

Also, the response of through port is given as in (26):

$$S_t = \frac{t - (t_1^2 - 1)t_r t_2 e^{-j\phi} + t_2^2 t_1 e^{-j\phi}}{1 - 2t_1 t_2 t_r e^{-j\phi} + (t_1 t_2)^4 e^{-2j\phi}}. \quad (26)$$

Finally, the induced back-reflected signal at the add port due to the counter directional propagated mode is as given in equation (27):

$$S_{back} = \frac{jk_r \cdot k_1 k_2 \cdot t_1 \cdot e^{-j3\phi/2}}{1 - 2 \cdot t_1 t_2 \cdot t_r \cdot e^{-j\phi} + {t_1}^2 {t_2}^2 \cdot e^{-2j\phi}}. \quad (27)$$

Equations (25) to (27) represent the frequency response of a corrugated ring OADM. These equations and equations (21)-(23) allow for complete modelling of corrugated ring resonators and provide an alternative solution to reproduce the experimental results without the need for curve fitting.

C. Validation

These models (in both the time and space domains) are examined first against the experimental outcomes published in [4].

1. The analytical model (time domain) represented by equations (20) to (23) is used to extract the coupling coefficients from the experimentally determined response presented in [4], as shown in Fig. 3 (b). The fitted parameters are: ${k_1}^2 = 4.8\%$, ${k_2}^2 = 1.76\%$, $t_r = 0.9991$ and the round-trip loss $e^{-\alpha l} = 0.9639$.

2. The space domain model was used to plot the spectral response and reproduce the experimental results using coupling coefficients (${K_1}^2$, ${K_2}^2$, t_r, and loss coefficient) calculated in step 1.

A comparison between Figs. 3 (a) and (b) shows the accuracy of the presented models and allows for the use of these equations for filter performance optimization in terms of crosstalk and signal integrity.

For further validation, a corrugated ring was modeled using CST MWS [21]. Figure 4 shows the CST model of a ring resonator based OADM.

In the electromagnetic model, the following parameters were used:

A substrate was silicon dioxide of 1 μm height with a 1.44 refractive index. Then the silicon waveguides were introduced above the substrate with 0.22 μm heights and 0.5 μm widths for single mode propagation [3]. A refractive index of 3.47 was used for the silicon waveguides [25]. The upper cladding was air. The corrugated ring was first modeled geometrically using Ruby code [26], and then moved into CST as a Wavefront.obj file. The ring radius was 8μm and the distances between the bus waveguides and the ring were 60 nm and 160 nm for the input and output bus waveguides, respectively. These values were taken to ensure the presence of resonance splitting. A hexahedral meshing in the transient CST solver was performed for simulation. The various spectral responses for the ports of a corrugated ring resonator are shown in Fig. 5. S_{21}, S_{31}, and S_{41} signify the output, drop and back reflection responses, respectively.

Equations (21) to (23) were used to calculate different parameters of the resonator from the simulation results. The modelled corrugated ring parameters (coupling, reflection, and loss coefficients) are calculated as: ${k_1}^2 = 10.774\%$, ${k_2}^2 = 1.422\%$, $t_r = 0.998$ and $e^{-\alpha l} = 0.986$.

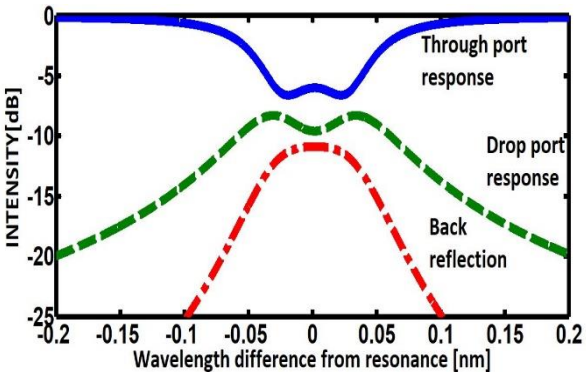

(a)

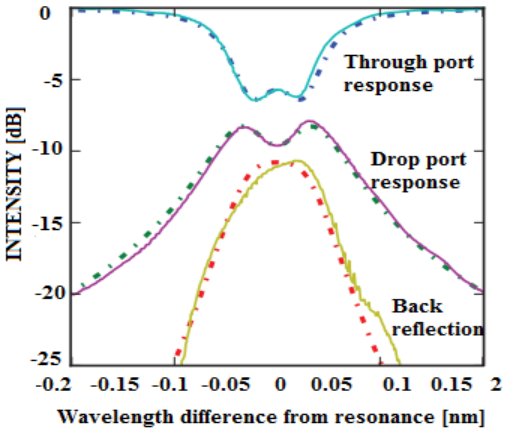

(b)

Fig. 3. (a) Spectral response of OADM based on time and space domain models. (b) Experimental results presented in [4].

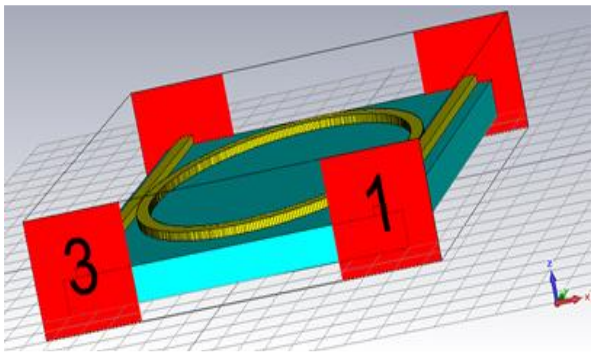

Fig. 4. CST model of a random sidewall roughness in a

corrugated single RR add /drop filter.

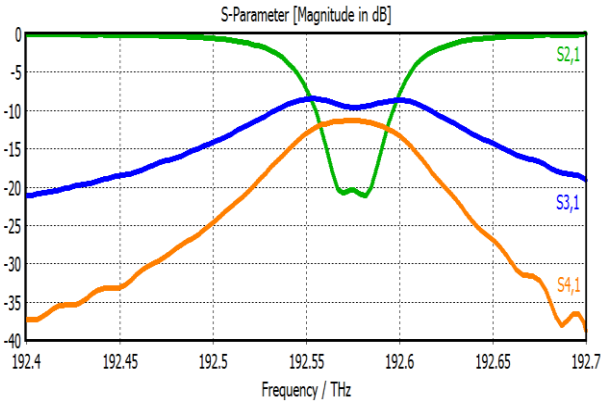

Fig. 5. CST spectral response of a corrugated ring.

These values were introduced into equations (25) - (27) to reproduce the spectral responses of different ports. Figure 6 shows a comparison between the analytically calculated port responses and that fitted using CST simulation. A good agreement between these results is clear. This provides additional validation for the derived equations and enables the application of them to study the effect of back-reflection on the crosstalk suppression bandwidth.

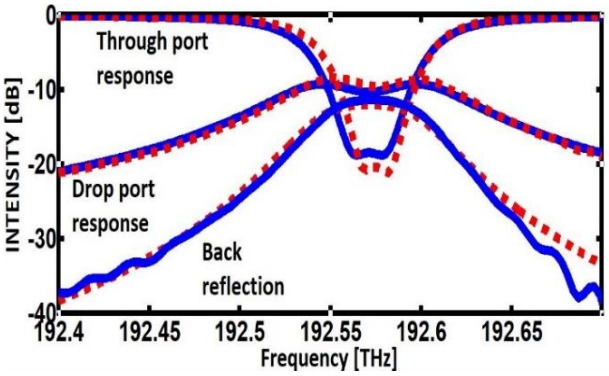

Fig. 6. Numerical (solid) and theoretical (dotted) modelled spectral response for a corrugated ring resonator.

Another advantage of the derived equations is in examining different values of the reflection coefficient (t_r) to show the effect of back-reflection on crosstalk suppression. Increasing the back-reflection coefficient, reducing t_r, leads to strong response splitting due to the mutual coupling between counter directional propagating modes, as shown in Fig. 7. Two minimums and a single maximum would exist in the output port response (S_{21}) of a single ring because of the back-reflection. Similarly, a double maximum and one minimum appears in the drop port response (S_{31}).

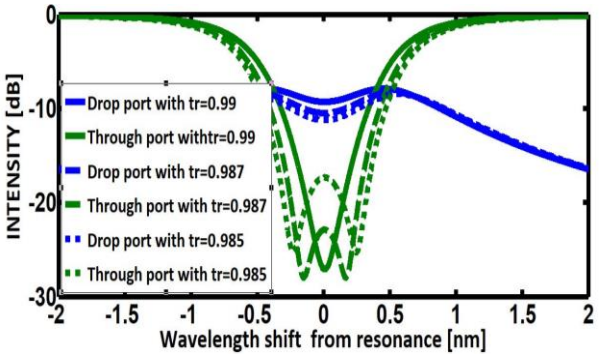

Fig. 7. The effect of reflection coefficient on the output and drop port response.

The difference between S31 (drop port response) and S21 (through port response) at each wavelength, represents the crosstalk suppression. It is required to be higher than |20| dB [27], for as wide a wavelength range as possible to increase the crosstalk suppression bandwidth to ensure high data rate channel dropping with improved signal integrity and mitigated crosstalk. This can be achieved by optimizing the reflectivity of the side-wall within the rough region, as discussed in the following sections.

III. CONTROLLABLE REFLECTIVITY

In this section, total reflectivity resulting from adding a number of reflectors is studied using the Bragg grating reflectivity model [15]. Single and double gratings are shown in Fig. 8.

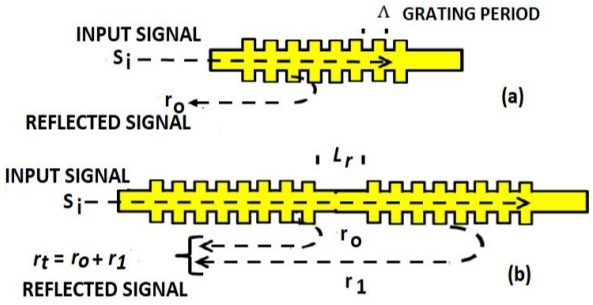

Fig. 8. (a) Single grating and (b) double gratings model.

The power back-reflection coefficient R is modelled as [28] and given in equation (28):

$$R = |r_0|^2 = \frac{k^2 \cdot \sinh^2(S \cdot L)}{\delta^2 \cdot \sinh^2(S \cdot L) + S^2 \cdot \cosh^2(S \cdot L)}, \quad (28)$$

where, r_0 is the reflection coefficient, $k = \frac{\pi \cdot \Delta n_{eff}}{\lambda}$ is the coupler coupling coefficient, and $\delta = \frac{2\pi n_{eff}}{\lambda} - \frac{\pi}{\Lambda}$, is the detuned propagation constant. n_{eff} is the effective refractive index, Λ is the period of the grating, L is the reflector length, and $S = \sqrt{k^2 - \delta^2}$. Equation (28) shows

a high dependency of the reflectivity on the change of n_{eff}, and grating parameters (L, and ʌ). Increasing the reflectivity by modifying various parameters is the main aim of this section. The refractive indices were 3.47 for Si and 1.44 for SiO_2 at the wavelengths around 1550 nm [3]. n_{eff} was 2.55, with a constant change over the grating as $\Delta n_{eff} = 0.5$. The effects of different parameters are examined as follows:

1. Reflector length (*L*): A 100 nm grating period and 50% duty cycle are considered first; these values were chosen to ensure high reflectivity around 1550 nm. Figure 9 shows that increasing L only influences a change of the reflectivity over the range of wavelengths around 1550 nm. Here, the range of wavelengths obtained was 1540-1560 nm and the best reflector length was 6500 nm (relatively high reflectivity) as shown in Fig. 9.

2. Grating period (ʌ): For $L = 6500$ nm and 50% duty cycle. Figure 10 shows an increase in the reflectivity with increasing grating period. Depending on the diffraction theory [12], the Bragg wavelength is ($\lambda_{Bragg} = 2 \cdot n \cdot \Lambda$). Therefore, increasing ʌ will increase the Bragg wavelength and shift it nearer to the required range.

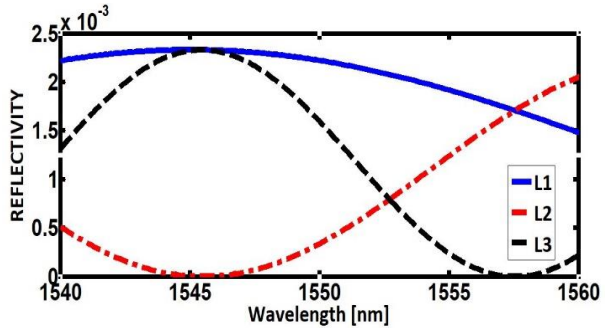

Fig. 9. The effect of ***L***. ***L*1**=6500 nm, L_2=13000 nm and L_3=19500 nm.

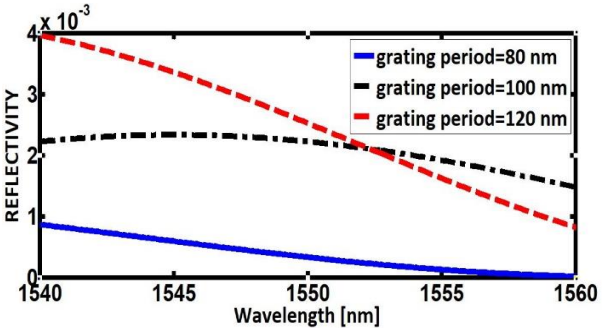

Fig. 10. The effect grating period.

3. Number of reflectors: Fig. 8 (b) shows the case of two groups of gratings, the total reflectivity of this model results from the contribution of each reflector. However, when adding r_0 and r_1, a locked loop needs to be considered between the reflectors. Based on Mason's rule [29], the total reflectivity of two reflectors is as given in equation (29):

$$r_0 + r_1 = \frac{r_0 + r_1 \cdot e^{-j2\beta L_r}}{1 + r_0 r_1 e^{-j\beta L_r}}. \quad (29)$$

For three groups of gratings, the total reflectivity will be greater due to the number of reflectors. The total reflectivity can be calculated as in equation (30):

$$r_0 + r_1 + r_2 = \frac{r_0 + r_1 e^{-j2\beta L_{r1}} + r_2 e^{-l2\beta(L_{r1}+L_{r2})} + r_0 r_1 r_2 e^{-j2\beta L_{r2}}}{1 + r_0 r_1 e^{-j2\beta L_{r1}} + r_1 r_2 e^{-j2\beta L_{r2}} + r_0 r_2 e^{-l2\beta(L_{r1}+L_{r2})}}, \quad (30)$$

where L_{r1} and L_{r2} are the separations between gratings. The reflectivity of one, two and three gratings is shown in Fig. 11.

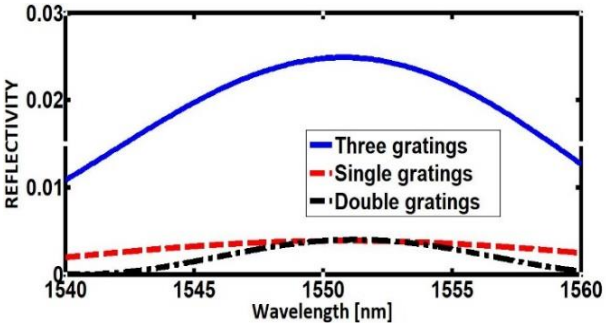

Fig. 11. Number of reflectors effect.

ASPIC design software [22] was used to validate equations (29) and (30), as shown in Fig. 12. ASPIC is a model-based simulation software and approaches simulation differently to the physically based CST MWS simulation software. The effect of using single, double and three gratings is simulated first. It is shown in Fig. 12 (b) that, increasing the number of gratings will result in an increase of back reflection as in [12]. Differences between analytical and ASPIC simulator results may be attributed to the change of the effective index with wavelength (material dispersion) [30].

4. Effect of *Lr*: to obtain high reflectivity, the distance between reflectors should ensure a π radian phase shift. The overall reflectivity is strongly affected by Lr as shown in Fig. 13. Therefore, the perimeter of the grating assisted ring needs to be optimized to maximize the reflection by ensuring a proper Lr.

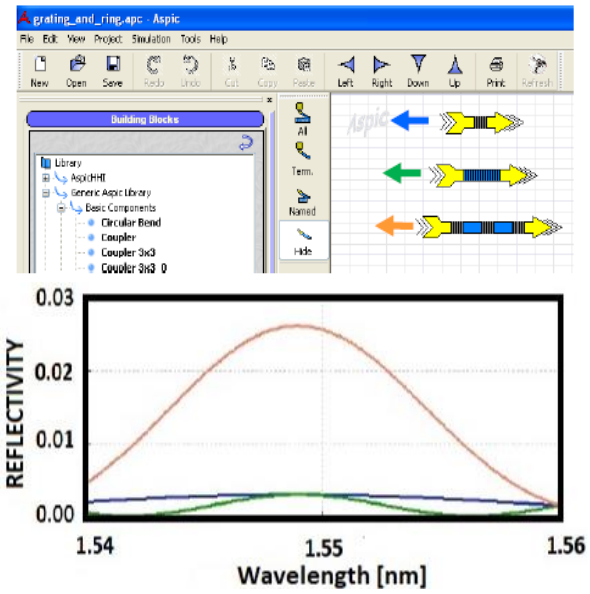

Fig. 12. Aspic model for three gratings (upper), and the reflectivity as a function of wavelength (lower) for single grating (blue), double grating (green) and three gratings (red).

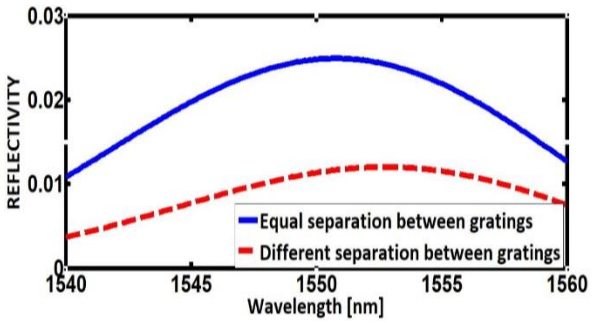

Fig. 13. The separation effect between three reflectors.

IV. GRATING ASSISTED SINGLE RING

This section aims to build on the above calculations to suggest a novel design of OADM that provides high crosstalk mitigation and ensure high integration density. The design steps are listed below:

Step 1: The goal-maximization algorithm is exploited to optimize the coupling and reflection coefficients that maximize the bandwidth of crosstalk suppression. Different parameters of an OADM with a corrugated ring are optimized based on Equations (25) and (26) to maximize the bandwidth of crosstalk suppression. Each time, a set of coupling coefficients (k_1, k_2 and tr) is used to calculate S_{31}-S_{21} and compare it with a |20| dB suppression threshold over the range of frequencies around one resonance.

Step 2: Not only k_1, k_2 and t_r need to be optimized, the ring radius needs to be chosen to match the resonance wavelength with the calculated value of tr.

Step 3: Three reflectors were used to ensure high reflectivity. The distance between the three reflectors was calculated as $(L_r = ((l - 3 \times L))/3)$, where l is the mean length of the ring. To maximize the reflectivity, the distance between reflectors was to be optimized.

Step 4: A model that combined all the parameters (coupling coefficients, ring radius, number of gratings, grating length, and grating period) was used. The optimization approach was performed for 100 and 120 mm grating period since these values provided increased reflectivity, as depicted in Fig. 10.

The optimized ring parameters for maximum crosstalk bandwidth in an asymmetric ring resonator were as follows: The power coupling coefficients ${K_1}^2 = 0.2258$, ${K_2}^2 = 0.0329$, and the back-reflection coefficient $t_r = 0.99$. The optimized value of back-reflection coefficient was used in equation (28) to calculate the length of reflectors inside the ring. A ring of 9.64 μm radius loaded with three reflectors each of 6.5μm length, separated by 13.7 μm is proposed. The period of ridges in each reflector is 0.1μm. A 28 GHz crosstalk suppression BW was obtained using these optimized parameters, as shown in Fig. 14. By comparison, an OADM made of a smooth surface ring with high coupling coefficient > 0.65 [18] is needed to obtain a similar crosstalk BW. Such a high coupling coefficient would affect the selectivity of the multiplexer (Q-factor) and allow for the adjacent channels to increase the inter-band crosstalk. Also, a double ring resonator can have a similar BW [18]. However, the integration density will be reduced due to the increased filter size.

To this extent it is shown analytically that a single ring with three reflectors provides high data-rate channel dropping compared to the smooth surface ring OADMs. To ensure the accuracy of the results, a numerical validation using ASPIC simulator for the proposed model was performed.

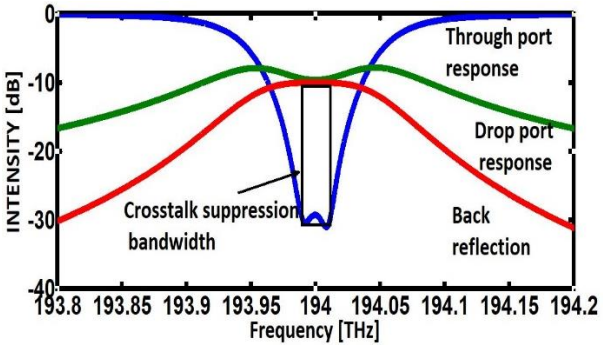

(a)

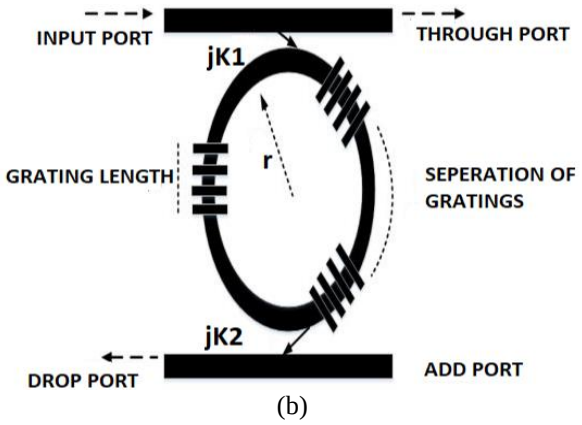

(b)

Fig. 14. (a) The single ring resonator spectral response, and (b) schematic of a grating-assisted OADM.

The ASPIC simulator results for a single ring resonator with three reflectors are shown in Fig. 15, which shows a good agreement with that of [17] (ASPIC simulation was performed for a 5 μm ring resonator model) where the resonance splitting is clear and |20| dB crosstalk suppression is maintained for a wide crosstalk suppression bandwidth.

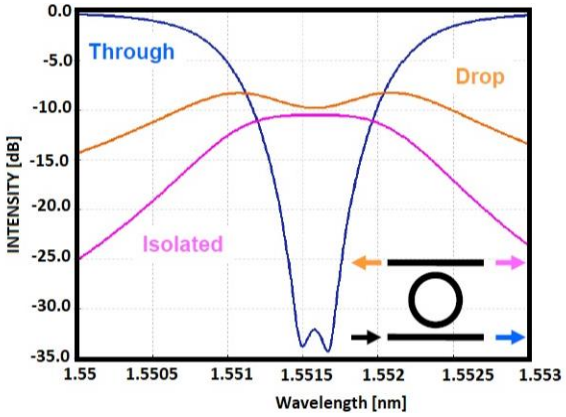

Fig. 15. The three-port response for a grating assisted ring resonator (Aspic simulated results).

V. CONCLUSION

Mitigating crosstalk effects and enhancing signal integrity in a small size ring resonator based OADM, by increasing the crosstalk suppression bandwidth, was the main aim of this paper. The objective of this work is to exploit the resonance splitting induced by silicon waveguide surface corrugation. To do that, a simple and direct approach to estimate all port responses without the need for curve fitting was presented. An equivalent model for the corrugated ring was proposed and examined against experimental published results. 3D simulation software was used for further validation. Analytical and numerical calculations were performed to ensure the accuracy of the proposed model. Finally, this model was used to obtain the optimized parameters of a ring resonator that maximize crosstalk suppression BW. A novel design, with more controllability during manufacture compared to a purely randomized corrugation, was proposed, and a 28 GHz crosstalk suppression BW was achieved. This bandwidth supports the dropping of 10 Gbps signals with mitigated crosstalk level and improved signal integrity.

REFERENCES

[1] A. Bianco, et al., "Crosstalk minimization in microring-based wavelength routing matrices," in *Global Telecommunications Conference (GLOBECOM), IEEE*, pp. 1-5, 2011.

[2] S. Koziel and S. Ogurtsov, "Simulation-driven optimization approach for fast design of integrated photonic components," in *30th Annual Review of Progress in Applied Computational Electromagnetic*, Jacksonville, FL, pp. 679-684, 2014.

[3] W. Bogaerts, et al., "Silicon microring resonators," *Laser & Photonics Reviews*, vol. 6, no. 1, pp. 47-73, 2012.

[4] G. Ballesteros, et al., "Characterizing and modeling backscattering in silicon microring resonators," *Optics Express*, vol. 19, no. 25, pp. 24980-24985, 2011.

[5] C. Sui, et al., "Analysis of microdisk/microring's surface roughness effect by orthogonal decomposition," *Optics and Photonics Journal*, vol. 3, pp. 288, 2013.

[6] B. E. Little, J. Laine, and S. T. Chu, "Surface-roughness-induced contradirectional coupling in ring and disk resonators," *Opt. Lett.*, vol. 22, no. 1, pp. 4-6, 1997.

[7] Z. Zhang, et al., "Resonance-splitting and enhanced notch depth in SOI ring resonators with mutual mode coupling," *Optics Express*, vol. 16, no. 7, pp. 4621-4630, 2008.

[8] G. T. Paloczi, J. Scheuer, and A. Yariv, "Compact microring-based wavelength-selective inline optical reflector," *IEEE Photonics Technology Letters*, vol. 17, no. 2, pp. 390-392, 2005.

[9] C. Alonso-Ramos, et al., "Dual-mode coupled-resonator integrated optical filters," *IEEE Photonics Technology Letters*, vol. 26, pp. 929-932, 2014.

[10] R. D. Mansoor, et al., "Estimation of the bandwidth of acceptable crosstalk of parallel coupled ring resonator add/drop filters," *IEEE Trans. Electromagn. Compat.*, vol. 57, no. 5, pp. 1005-1012, 2015.

[11] F. Morichetti, A. Canciamilla, and A. Melloni, "Statistics of backscattering in optical waveguides," *Opt. Lett.*, vol. 35, no. 11, pp. 1777-1779, 2010.

[12] T. Wang, et al., "Modeling of quasi-grating sidewall corrugation in SOI microring add-drop

filters," *Opt. Commun*., vol. 282, no. 17, pp. 3464-3467, 2009.
[13] Y. M. Kang, A. Arbabi, and L. L. Goddard, "Engineering the spectral reflectance of microring resonators with integrated reflective elements," *Optics Express*, vol. 18, no. 16, pp. 16813-16825, 2010.
[14] W. Shi, et al., "Grating-coupled silicon microring resonators," *Appl. Phys. Lett*., vol. 100, no. 12, pp. 121118-121118-4, 2012.
[15] K. O. Hill and G. Meltz, "Fiber Bragg grating technology fundamentals and overview," *J. Lightwave Technol*., vol. 15, no. 8, pp. 1263-1276, 1997.
[16] A. E. Atia and A. E. Williams, "Narrow-bandpass waveguide filters," *Microwave Theory and Techniques, IEEE Transactions On*, vol. 20, no. 4, pp. 258-265, 1972.
[17] R. Mansoor, et al., "Crosstalk bandwidth of grating-assisted ring resonator add/drop filter," *Opt. Quant. Electron*., vol. 47, pp. 1127-1137, 2015.
[18] R. D. Mansoor, et al., "Over coupled ring resonator based add/drop filters," *Quantum Electronics, IEEE Journal of*, vol. 50, no. 8, pp. 598-604, 2014.
[19] A. Yariv, "Coupled-mode theory for guided-wave optics," *Quantum Electronics, IEEE Journal of*, vol. 9, no. 9, pp. 919-933, 1973.
[20] O. Schwelb, "Microring resonator based photonic circuits: Analysis and design," in *Telecommunications in Modern Satellite, Cable and Broadcasting Services*, pp. 187-194, 2007.
[21] 3D Electromagnetic Simulation software, 2013. Available: www.cst.com.
[22] ASPIC design software, 2014. Available: www.aspicdesign.com.
[23] C. Manolatou, et al., "Coupling of modes analysis of resonant channel add-drop filters," *Quantum Electronics, IEEE Journal of*, vol. 35, no. 9, pp. 1322-1331, 1999.
[24] S. Xiao, et al., "Modeling and measurement of losses in silicon-on-insulator resonators and bends," *Optics Express*, vol. 15, no. 17, pp. 10553-10561, 2007.
[25] O. Schwelb, "Transmission, group delay, and dispersion in single-ring optical resonators and add/drop filters-a tutorial overview," *Lightwave Technology, Journal of*, vol. 22, no. 5, pp. 1380-1394, 2004.
[26] Ruby programming language. 2014. Available: https//:www.ruby-lang.org
[27] O. Schwelb, "Crosstalk and bandwidth of lossy microring add/drop multiplexers," *Opt. Commun*., vol. 265, no. 1, pp. 175-179, 2006.
[28] S. P. Ugale and V. Mishra, "Modeling and characterization of fiber Bragg grating for maximum reflectivity," *Optik-International Journal for Light and Electron Optics*, vol. 122, no. 22, pp. 1990-1993, 2011.
[29] S. J. Mason, *Feedback Theory: Further Properties of Signal Flow Graphs*. Research Laboratory of Electronics, Massachusetts Institute of Technology, 1956.
[30] H. Li, "Refractive index of silicon and germanium and its wavelength and temperature derivatives," *Journal of Physical and Chemical Reference Data*, vol. 9, no. 3, pp. 561-658, 1980.

Riyadh D. Mansoor received the B.Sc degree in Electrical and Electronic Engineering and the Master degree from the University of Basra, Iraq, in 1996 and 1998 respectively. He finished his Ph.D. in Optical Communication at De Montfort University, Leicester, UK, in 2015. He is currently working as a Senior Lecturer with the faculty of Engineering, Al-Muthanna University, Samawa, Iraq. His research interests include photonic circuits, optical communications, and Electromagnetic compatibility.

Alistair P. Duffy received the B.Eng. (Hons.) degree in Electrical and Electronic Engineering and the M.Eng. degree from University College, Cardiff, U.K., in 1988 and 1989, respectively. He received his Ph.D. degree from Nottingham University, Nottingham, U.K., in 1993 for his work on experimental validation of numerical modeling.

He is currently Professor of Electromagnetics and Director of the Institute of Engineering Sciences at De Montfort University, Leicester, U.K. He is also a Guest Professor at Harbin Institute of Technology, Harbin, China. He is the author of approximately 300 articles published in journals and presented at international symposia. His research interests include CEM validation, communications cabling, and technology management.

Duffy is a Fellow of the IEEE, the Institution of Engineering and Technology (IET) and the Royal Society for the Encouragement of Arts, Manufactures and Commerce (RSA). He is currently President Elect for the IEEE EMC Society. He is also Chair of the IEEE EMC Society Standards Development and Education Committee, along with a number of Standards working group officer roles. He is an Associate Editor of the IEEE Transactions on EMC Technology management.

Design of a Thin Broadband Metamaterial Absorber Based on Resistance Frequency Selective Surface

Peng Zhou [1], Qiulin Huang [1*], Lei Ji [2], and Xiaowei Shi [1]

[1] National Key Laboratory of Antennas and Microwave Technology
Xidian University, Xi'an, 710071, China
pengzhou@stu.xidian.edu.cn, *qiulhuang@mail.xidian.edu.cn, xwshi@mail.xidian.edu.cn

[2] School of Electronic Information and Electrical Engineering
Shanghai Jiao Tong University, Shanghai, 200240, China
jilei19940605@163.com

Abstract ─ A thin broadband metamaterial absorber with Resistive Frequency Selective Surface (RFSS) is presented. The absorber maintains a good performance over a broad operating frequency band with low profile. It is designed by a class of periodic artificial electromagnetic structures and the unit cell of the proposed absorber is composed of resistively loaded square loops with different sizes. By combining multiple resonant square loops (MRSL) of different geometries on a single layer structure, the absorption spectrum is greatly expanded. Simulation results show that the absorption coefficient is greater than 85% from 7.9GHz to 18.9GHz, while the thickness of the whole structure is 0.1λ (the free space wavelength) at the lowest operation frequency. A prototype was fabricated and measured in an anechoic chamber to validate the proposed design method. Favorable agreement among the full-wave simulation result and measurement result was achieved.

Index Terms ─ Broadband absorber, multiple resonant, resistive frequency selective surface.

I. INTRODUCTION

A lot of effort has been devoted in the last decades by technology research to realizing materials with absorb electromagnetic wave properties. One of the challenges at present is to improve the operation bandwidth of a structure at a lower profile so that a wider application. The dilemma of attaining both thin thickness and wide bandwidth on metal backed magnetodielectric absorbers simultaneously has been illustrated by the Razanov limitation [1]:

$$\Delta\lambda=\left(\lambda_{\max}-\lambda_{\min}\right)<\frac{2\pi^2\sum_i \mu_{s,i}^{'} d_i}{\left|\ln p_0\right|}, \qquad (1)$$

where d_i, $\mu_{s,i}^{'}$ are the thickness and the static permeability of *ith* layer of the multilayer slab. These materials are conventionally characterized by the thickness d_i and by the largest value of module of the voltage reflection coefficient ρ_0 within the operating waveband. There is an optimal bandwidth-thickness ratio (Δλ/t), because the absorption bandwidth (Δλ) is proportional to the effective total thickness ($t=\sum \mu_{s,i}^{'} d_i$). Hence, it is always a challenge for designers to develop technologies to approach this optimal ratio on microwave planar absorbers [2].

Based on the new properties of metamaterial, the metamaterial absorbers (MMA) are widely concerned by many researchers, especially in the optical band and microwave band. The first perfect MMA based on the theory of electromagnetic resonance was proposed by Landy et al. in 2008 [3]. However, owing to the facts that the absorber design principle is based on resonant properties, it inherently limits the absorption to a narrow spectrum. Since then, researchers proposed a variety of MMA that polarization-insensitive and wide incidence angle characteristics, but the absorption frequency spectrum is still narrow [4-9].

In order to achieve broadband absorption performance, the general method is to obtain multi-resonant modes by multi-scaled patterns or fractal structures [10-14]. To a certain extent, the spectrum of broadband absorption has improved, however, the multiple absorption spectra are discretely distributed.

To obtain continuous broadband absorption, several other bandwidth enhancement approaches including the lumped elements loading technology and the multi-layer resistive frequency selection surface (RFSS) absorber [15-18] are proposed. However, these methods have several limitations for the practical application, owing to the increased unit dimension, overall thickness of the absorber, and fabrication difficulty, which are not convenient for many practical applications. Therefore, the design of the low profile with the simple resonance structure, broadband absorption, and high absorption ratio becomes particularly urgent.

Submitted On: January 23, 2019
Accepted On: April 19, 2019

In this paper, a new multiple resonant broadband absorber is studied and presented, which consists of multi-sizes square loops in periodic. The design of the square loop structure based on the theory of resistive frequency selective surface. Simulation results of single and multiple resonances structure are presented, which allow a detailed explanation of the multi-resonant mechanism of the wideband absorber. By rationally designing the size of the multi-resonant square loops and appropriately optimizing the combined structure, continuous multi-resonance point absorption can be generated, which greatly expands the operation spectrum range of the microwave planar absorbers. The absorption coefficient of full-wave HFSS simulation is compared to verify the validation. Using this multi-resonant method, the multi-resonant planar absorbing structure is designed. This letter gives a brief introduction of the multi-resonant square loop absorber design method, which could be used in the wideband absorber design for RCS reduction application of the wideband antenna.

II. ABSORBER DESIGN

A. Single resonant square loop structure

A unit cell of the single resonant square loop (SRSL) absorber based on Resistive Frequency selective surface FSS is shown in Fig. 1. It consists of three layers: surface metal layer, dielectric layer and the PEC ground plane. Between the substrate and the ground plane, an air gap or a foam layer is usually applied to modify the resonant frequency band. Four resistors which can absorb the resonant power are welded in the middle of each edge. Such unit cell can be arranged in periodic to make up a resonant structure that have frequency selective characteristic, based on the theory of frequency selective surface FSS.

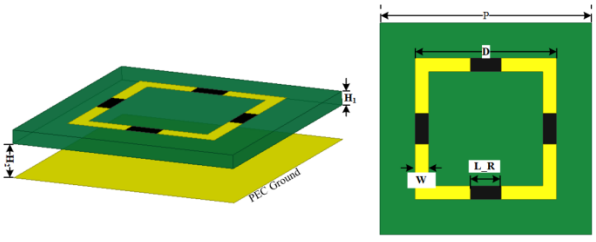

(a) (b)

Fig. 1. The structure of a SRSL: (a) 3D view and (b) top view.

B. Multi-resonant square loop structure

The schematic of the proposed Multi-resonant square loop (MRSL) absorber is shown in Fig. 2. As seen from Fig. 2 (a), the MRSL absorber is built up arranging the single square loops in a periodic structure and each unit cell has nine square loops which in five different sizes. Particularly, every square loop is welded with chip resistors of same resistance in the middle of each edge. Figure 2 (b) presents the 10×10 periodic structure model of the MRSL absorber. All the square loops are printed on a FR-4 substrate with the relative permittivity of 4.4 and thickness of 0.8mm.

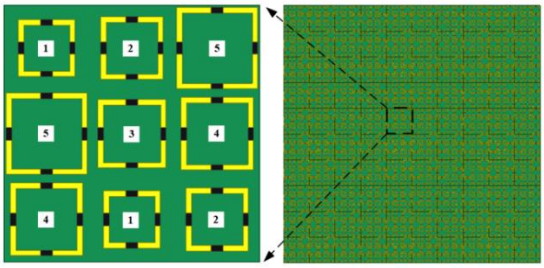

(a) (b)

Fig. 2. The proposed MRSL absorber: (a) a view of the unit cell in periodic structure model, and (b) a 10×10 periodic structure model.

Comparing with the single resonant square loop structure, the perimeter of the square loops at different positions are variable with five sizes, but the distance between any two adjacent square loop and the height of the air layer are remained. This change can connect the independent resonance points to produce a wideband frequency response.

III. SMULATION RESULTS

The unit cell was simulated by the electromagnetic full-wave simulator Ansys HFSS. Simulation schematic of parameters is given in Fig. 3. In the simulation, the unit cell placed in a waveguide, where each side of the waveguide is excited by a Floquet port. Master and slave boundaries are applied to the lateral walls of the waveguide to numerically realize an infinite array.

The absorption coefficient of the unit cell, $A(\omega)$, was computed as follows:

$$A(\omega)=1-R(\omega)-T(\omega), \quad (2)$$

$$R(\omega)=|S_{11}|^2, \quad (3)$$

$$T(\omega)=|S_{21}|^2. \quad (4)$$

Where $A(\omega)$ is absorption coefficient. $R(\omega)$ and $T(\omega)$ represent reflection coefficient and transmission coefficient, respectively. The transmission coefficient $T(\omega)$ is zero, due to the presence of the PEC ground plane. According to (2), (3), (4), absorption coefficient can be easily calculated.

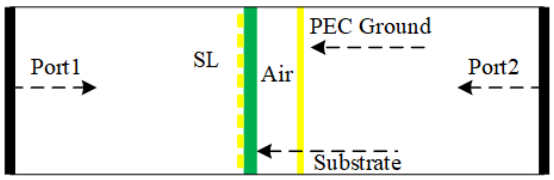

Fig. 3. Simulation schematic of the Floquet periodic boundary condition.

A. Simulation results of SRSL structure

The absorptivity of SRSL absorber is related to the distance (H_2) between the substrate and the ground plane. Besides, the value of the loaded resistance will affect the absorptivity [19]. This article focuses on how to implement a broadband absorber at a lower profile. Therefore, the following parameters are unchanged: P=13.8mm, W=0.88mm, L_R=2mm, H_1=0.8mm, H_2=2.0mm. To obtain a better absorptivity, the absorption characteristics of different resistances loaded with different size square loops have been studied.

Five different sizes of the meta square loop of SRSL absorbers unit cell at the same height were analyzed. The simulated optimal absorption ratio of the different SRSL absorbers are shown in Fig. 4. It can be seen that five different SRSL units have five discretely absorption spectrums. Obviously, single resonant square loop structure has narrowband absorption spectral characteristics. It will get a continuous broadband absorption bandwidth if they work simultaneously in one plane.

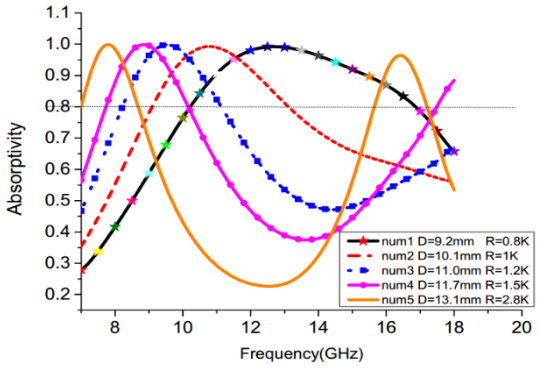

Fig. 4. The simulated absorptivity of the SRSL absorbers with different sizes meta square loops.

B. Simulation results of MRSL structure

The Broadband absorber is designed according to the ideas in the previous section. Generally speaking, multiple absorption spectra are discretely distributed unless the SRSL size was properly designed and the composite structure array was properly selected. Continuous multiple resonance absorption greatly expands the operating spectral range of a single layer structure.

The single resonant square loops in the previous section are selected to combine into different multi-resonant square loop structures. The metal square loops of different sizes have been numbered in Fig. 2, Fig. 7 and Fig. 8. The optimized parameters of the five SRSL are given in the Table 1. Other parameters remain unchanged.

Table 1: The optimized parameters of the five SSL absorber

SLL	D (mm)	R (ohm)	SLL	D (mm)	R (ohm)
#1	9.2	0.8K	#2	10.1	1K
#3	11.0	1.2K	#4	11.7	1.5K
#5	13.1	2.8K			

Four different multi-resonant structure unit cells are proposed in Fig. 5 to verify that different combinations of the MRSL can affect the absorption performance. The divergence is that different loops are placed in different positions, which will change the coupling capacitance between the square loops. In Fig. 5 (a), there is only one square loop No. 3 that placed in the middle of the cell, and the other square rings appear randomly in different positions twice. According to this rule, the intermediate unit cell is replaced in Figs. 5 (b), (c) and (d). These unit cells are used to simulate infinite periodic arrays in master-slave boundary conditions

The absorptivity of the different form MRSL absorbers are shown in Fig. 6. Simulation results show that the multi-form of arrangement and compositions have a great influence on the absorptivity performance, especially, the middle absorption spectrum decreased. In Fig. 6 (a), the absorptivity of b, c, and d is less than 0.8 in the middle spectrum. However, the absorption curve of a is above 0.8 from 12 GHz to 16 GHz, indicating an excellent absorption performance. Figure 6 (b) reveals the best absorptivity curve in Fig. 6 (a). It is clear that the efficient absorptivity of the best MRSL absorber in the four proposed absorbers is above 85% from 7.9 GHz to 18.9 GHz for the normal incident electromagnetic waves. Especially, the X-band and Ku-band are completely covered. Comparing the four MRSL unit cells with different arrangement, the structure shown in Fig. 8 (a) is the best combination.

The electric field distribution of the MRSL absorber unit cell is also studied, as it can help us analyze the information about the way and location of electromagnetic energy absorption. In Fig. 7, the surface electric field distributions are present at different frequencies, which correspond to the multiple absorption peaks. It can be seen that the electric field is mainly concentrated on the largest square loop when it is excited with a low frequency electromagnetic wave. As the frequency moves toward a high frequency, the electric field shift to other rings regularly. At the highest frequency, the electric field is mainly concentrated on the minimum square loops. Because of the coupling between the square loops,

the electric field may distribute over multiple square loops of similar size occasionally. Most of the resonant energy of square loops is absorbed by the resistor, indicating that the proposed MRSL Structure has broadband electromagnetic wave absorption capacity.

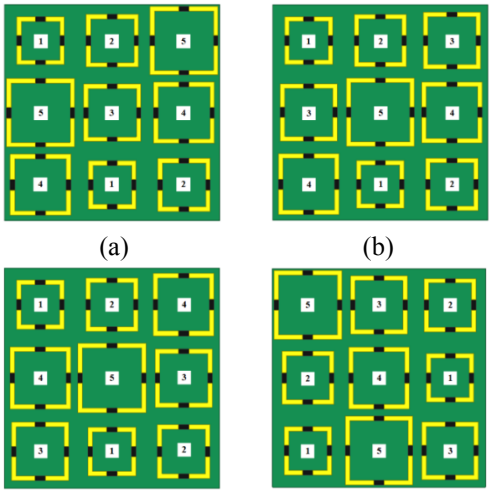

Fig. 5. The unit cell of four different MRSL absorbers.

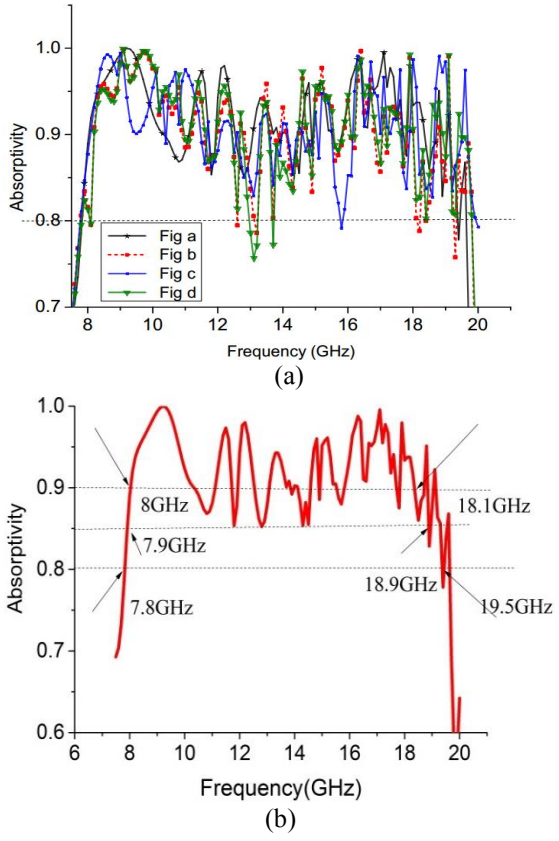

Fig. 6. (a)Simulation results of the proposed four MRSL absorbers, and (b) the best curve of Fig. (a).

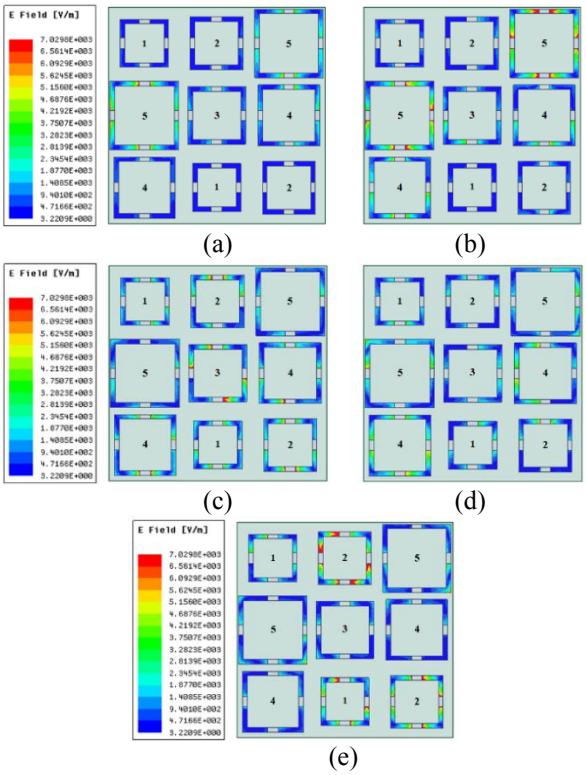

Fig. 7 The electric field distribution of the MRSL absorber unit cell: (a) at 8GHz, (b) at 9.5GHz, (c) at 10.5GHz, (d) at 11.5GHz, and (e) at 14GHz.

IV. EXPERIMENT RESULTS AND ANALYSIS

To validate the proposed design, a prototype has been fabricated on FR4 sheet using PCB technique. The overall size of the sample is 414 mm× 414 mm, where 10 × 10 unit cells are printed. Figure 8 (a) shows the photograph of the prototype and Fig. 8 (b) shows the prototype under test.

The characterization of the sample is achieved by a free space measure method to measure the reflectivity at normal incidence electromagnetic wave. In the experiment, one pair of horn antennas are connected to the vector network analyzer which works in the range of 1-40 GHz. The horn antenna used works in the range of 6-18 GHz.

The simulation and measurement results of the prototype are shown in Fig. 9. It can be seen that the absorption rate of both is above 80%. The difference between them is that the simulation result is smooth, but the test curve is a jittery curve. Overall, the trend of test results is consistent with the simulation result. The measurement method is shown in the Fig. 10. The receiving antenna receives electromagnetic wave scattered by the transmitting antenna and a bit of electromagnetic wave reflected by the absorber. In addition, machining errors and test system errors are not

considered in the simulation. These changes, which differ from the simulation, may cause small fluctuations in the absorption rate during testing.

(a) (b)

Fig. 8. (a) Photograph of the fabricated absorber, and (b) prototype under test.

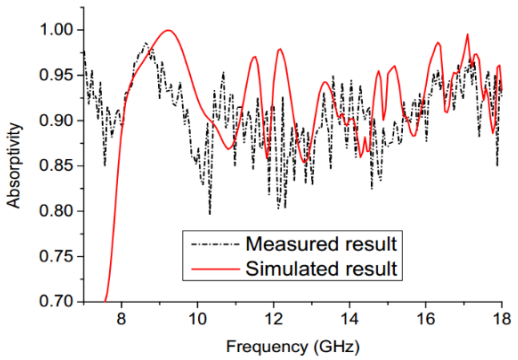

Fig. 9. Simulated and measured results for normal incidence.

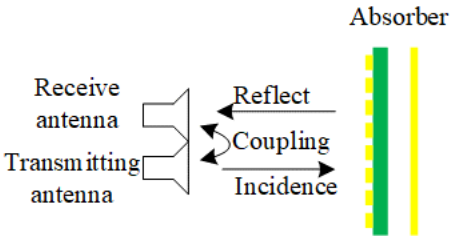

Fig. 10. Measurement method of the prototype.

V. CONCLUSION

Design of thin and broadband metamaterial absorber with Resistive Frequency Selective Surface (RFSS) has been presented. The structure has connected multiple isolate resonant frequency band to a continuous broadband due to the use of MRSL structure. However, the proposed absorber has a thin thickness of only 2.8 mm. Two prototypes have been fabricated using printed circuit board technology to highlight the simplicity of the fabrication for such kind of structures. The simulated and measured results exhibit a broadband absorption frequency band above 85% from 7.9GHz to 18.9GHz. Some future work may be interested in polarization insensitive performance and tunable frequency selective absorber.

REFERENCE

[1] K. N. Rozanov, "Ultimate thickness to bandwidth ratio of radar absorbers," *IEEE Transactions on Antennas and Propagation*, vol. 48, no. 8, pp. 1230-1234, Aug. 2000.

[2] T. Deng, Z. Li, and Z. N. Chen, "Ultrathin broadband absorber using frequency-selective surface and frequency-dispersive magnetic materials," *IEEE Transactions on Antennas and Propagation*, vol. 65, no. 11, Nov. 2017.

[3] N. I. Landy, S. Sajuyigbe, J. J. Mock, D. R. Smith, and W. J. Padilla, "Perfect metamaterial absorber," *Phys. Rev. Lett*., 100, 207402, 2008.

[4] O. Luukkonen, F. Costa, C. R. Simovski, et al., "A thin electromagnetic absorber for wide incidence angles and both polarizations," *IEEE Transactions on Antennas and Propagation*, vol. 57, pp. 3119-3125, 2009.

[5] C. Hu, Z. Zhao, X. Chen, et al., "Realizing near-perfect absorption at visible frequencies," *Optics Express*, vol. 17, no. 13, pp. 11039-11044, 2009.

[6] W. Li, X. Cao, J. Gao, et al., "A low RCS waveguide slot antenna array with metamaterial absorber," *IEEE Transactions on Antennas and Propagation*, pp. 1411-1781, 2018.

[7] J. Chen, H. Yang, S. Hu, and X. Huang, "Study on the absorption properties of a curved metamaterial absorber," *2016 11th International Symposium on Antennas, Propagation and EM Theory (ISAPE)*, Guilin, pp. 431-434, 2016.

[8] K. Yu, Y. Li, and X. Liu, "Mutual coupling reduction of a MIMO antenna array using 3-D novel meta-material structure," *ACES Journal*, vol. 33, no. 7, July 2018.

[9] G. Antonini, M. D. Astorino, F. Ferranti, F. Frezza and N. Tedeschi, "Efficient design of metamaterial absorbers using parametric macromodels," *ACES Journal*, vol. 33, no. 7, pp. 772-780, 2018.

[10] Q. Y. Wen, H. W. Zhang, Y. S. Xie, Q. H. Yang, and Y. L. Liu, "Dual band terahertz metamaterial absorber: Design, fabrication, and characterization," *Appl. Phys. Lett*., vol. 95, no. 24, p. 241111, 2009.

[11] X. Shen, T. J. Cui, J. Zhao, H. F. Ma, W. X. Jiang, and H. Li, "Polarization-independent wide-angle triple-band metamaterial absorber," *Opt. Express*, vol. 19, no. 10, pp. 9401-9407, May 2011.

[12] L. Li, Y. Yang, and C. Liang, "A wide-angle polarization-insensitive ultra-thin metamaterial absorber with three resonant modes," *Appl. Phys.*, vol. 110, no. 6, art. no. 063702, 2011.

[13] D. T. Viet, et al., "Perfect absorber metamaterials:

Peak, multi-peak and broadband absorption," *Opt. Commune*, vol. 322, pp. 209-213, 2014.
[14] J. Lee and S. Lim, "Bandwidth-enhanced and polarization-insensitive metamaterial absorber using double resonance," *Electron. Letter*., vol. 47, no. 1, pp. 8-9, Jan. 2011.
[15] H. Xiong, J. S. Hong, C. M. Luo, and L. L. Zhong, "An ultrathin and broadband metamaterial absorber using multi-layers structures," *J. Appl. Phys.*, vol. 114, no. 6, art. no. 064109, 2013.
[16] F. Ding, Y. Cui, X. Ge, F. Zhang, Y. Jin, and S. He, "Ultra-broadband microwave metamaterial absorber," *Appl. Phys. Letter*, vol. 100, art. no. 103506, 2012.
[17] S. Ghosh, S, Bhattacharyya, and K. V. Srivastava, "Design, characterization and fabrication of a broadband polarization-insensitive multi-layer circuit analogue absorber," *IET Microwaves Antennas & Propagation*, vol. 10, no. 8, pp. 850-855, 2016.
[18] Y. Z. Cheng, Y. Wang, Y. Nie, et al., "Design, fabrication and measurement of a broadband polarization-insensitive metamaterial absorber based on lumped elements," *Journal of Applied Physics*, vol. 111, no. 4, p. 44902, 2012.
[19] S. Ghosh and K. V. Srivastava, "An equivalent circuit model of FSS-based metamaterial absorber using coupled line theory," *IEEE Antennas & Wireless Propagation Letters*, vol. 14, pp. 511-514, 2015.

Peng Zhou was born in Henan, China, on 1990. He received the M.S. degree from Xidian University, Xi'an, Shaanxi, China, in 2017. He is currently working towards the Ph.D. degree in Electromagnetic Field and Microwave Technology at Xidian University, Xi'an, Shaanxi, China. His research interests on broadband absorber and tightly coupled array antenna.

Qiulin Huang (M'10) received the B.S. degree in Electronic Information Engineering and Ph.D. degree in Radio Physics from Xidian University, Xi'an, China, in 2001 and 2007, respectively. Since 2002, he has been with the National Key Laboratory of Antennas and Microwave Technology, Xidian University, as an Assistant Lecturer, Lecturer, and Associate Professor. From 2009 to 2010, he was a Postdoctoral Fellow with the University of Rouen, France. He has authored or coauthored over 20 international and regional refereed journal papers.

His recent research interests are mainly concentrated on smart antennas and antenna arraying technology.

Lei Ji received the M.S. degree from Xidian University, Xi'an, Shaanxi, China, in 2018. He is currently working towards the Ph.D. degree in Electromagnetic Field and Microwave Technology at Shanghai Jiao Tong University, Shanghai, China. His research interests on Spoof SPP and array antenna.

Xiaowei Shi received his B.S. and Ph.D. degrees from Xidian University, Xi'an, Shaanxi, China, in 1982 and 1995, respectively. In 1982, he joined the Xidian University, Xi'an, China, where he is currently a Professor in the School of Electronic Engineering. From June 1996 to July 1997, he went to the Korea Electronics and Telecommunications Research institute for collaborative research.

His research interests include smart antennas, antenna arraying technology, Radio Frequency Identification and Electromagnetic Compatibility.

RCS Reduction and Radiation Improvement of a Circularly Polarized Patch Antenna using AMC Structures

Wei Song*, Wen-Bo Zheng, Zi-Jian Han, and Xin-Qing Sheng

Center for Electromagnetic Simulation, School of Information and Electronics
Beijing Institute of Technology, Beijing, 100081, China
*wsong@bit.edu.cn

Abstract ─ Based on a polarization-dependent artificial magnetic conductor (AMC), a windmill-formed reflector is designed and applied to a circularly polarized patch antenna to reduce the radar cross section (RCS) and to improve the radiation properties of the antenna at the same time. Simulation and measurement results show that the proposed antenna bears an in-band RCS reduction for 10dB over a bandwidth of 30% for both polarizations. The 3dB axial ratio (AR) bandwidth is extended largely with gain improved compared with the reference antenna.

Index Terms ─ Artificial magnetic conductor (AMC), axial ratio (AR), circularly polarized (CP) antenna, radar cross section (RCS).

I. INTRODUCTION

Patch antennas have been widely used because of their advantages such as low profile, lightweight, low cost and easy fabrication [1]. With the development of aerospace technology and radar technology, the circularly polarized (CP) patch antenna is frequently applied in the field of electronic reconnaissance interference, wireless communication and GPS navigation [2-5].

Currently, many works can be found on CP patch antennas aiming at improving their radiation performances. Fabry-Perot (FP) cavity is often used for high-gain CP antenna designs [6-10]. Metasurface superstrates are incorporated on CP patch antennas [6, 8, 9], or CP patch antenna array [10]. In [6, 9], not only the FP cavity is formed between the superstrate and the ground of the antenna, but also the stopband property of the EBG superstrate prohibits the radiation of side lobes. As a result, the front gain is improved largely. In [8] and [10], with surface waves on the metasurface excited, extra resonances with minimum AR points are produced. Consequently, the impedance bandwidth, the AR bandwidths and the gain of the antennas are all improved. There is also effort in designing a wideband high-gain CP antenna by using a single dielectric superstrate [7]. The superstrate not only enhances the gain attributed to the FP cavity formed, but also generates extra CP radiation for the system, and consequently broadens the AR bandwidth significantly. In [11, 12], through polarization conversion metasurfaces, linearly polarized waves are converted into CP ones and thus CP antennas with wider impedance bandwidth and higher gain are developed.

However, for CP patch antennas, there are only a few studies devoted to reducing the RCS of the antennas. Circular [13] and quasi fractal [14] structures are etched on the ground of the CP patch antennas to reduce the RCSs of the CP antennas while maintaining their radiation performance. In an integrated structure, the antenna in [15] can possess the absorbing characteristic and the partially reflective characteristic simultaneously. The upper surface of the superstrate absorbs most of the incident wave by converting the electromagnetic (EM) wave into heat as Ohm loss to reduce the RCS of the antenna, while the bottom surface of the superstrate forms an FP resonance cavity to produce high directive gain. On the other hand, the artificial magnetic conductor made it feasible to design low RCS screen based on phase cancellation scheme [16]. Further, wideband property is enabled by adopting dual AMCs [17, 18]. Following such scheme, chessboard metasurfaces formed by dual polarization-dependent AMC (PD-AMC) is utilized to design low-RCS and high-gain CP antennas in [19, 20]. In both designs, the gain enhancement is obtained by using FP cavities, while the low-RCS feature is realized by phase cancellation from blocks of the chessboard metasurfaces. In [20] the AR is also improved by the metasurface. However, such CP antennas require certain thickness due to the requirement in forming a Fabry-Perot cavity.

In this paper, by incorporating a muti-functional metasurface, we propose a thin circularly polarized patch antenna with properties of low RCS, high gain and broader AR bandwidth. In this design, PD-AMCs arranged in windmill-form [21] is used to construct a low RCS reflector. By forming the windmill patterned reflector with triangular topology of the AMCs, the number of the interfaces is increased. Consequently, such configuration directs the EM scattering to a wider

Submitted On: March 7, 2019
Accepted On: June 1, 2019

angular range compared with the traditional chessboard reflector. The very windmill-form metasurface, instead of an FP cavity as in literatures [15, 19, 20], also works as parametric radiating parts for the CP antenna which provides gain improvement. Wider AR bandwidth can be obtained by rotating the key part of the AMC elements which are on the diagonal direction. The windmill-form pattern for the reflector shows a second benefit that minor destruction is resulted in the low RCS performance when the aforementioned elements rotation is introduced. The performance of the proposed antenna, including a low RCS, broader 3-dB AR bandwidths, and enhanced gain, have been demonstrated by simulation and by experiments. The ANSYS High-Frequency Structure Simulator (HFSS) is used throughout this work for simulations.

II. DESIGN OF ANTENNA WITH WINDMILL-FORMED REFLECTOR

A. Design of the unit cell and windmill-formed reflector

In this paper, a mushroom-like AMC is designed on a substrate with thickness of 2mm and dielectric constant of 2.2. As shown in Fig. 1, parameters of the unit cell are as follows: P = 10.6mm, L = 8.9mm, W = 6.4mm, h = 2mm, r = 0.5mm, $g1$ = 2.1mm, and $g2$ = 0.85mm. By rotating this AMC (AMC1) by 90 degrees, we obtain another AMC (AMC2) with different reflection phase property. The reflection phases of these two AMCs were obtained by HFSS software, with the master and slave boundary and the Floquet port shown in Fig. 2 (a). The phase difference of the two AMCs is plotted in Fig. 2 (b). According to [20], a low RCS reflector designed by phase cancelation scheme requires two kind of blocks with phase difference in the range of 180 ± 30º. With such a criterion, it can be checked in Fig. 2 (b) that the operating frequency band for these PD-AMCs is 8.8 GHz -10.8 GHz.

By assembling these PD-AMCs in triangular blocks based on an even-area strategy, a windmill-shaped reflector is formed, as shown in Fig. 3 (a). The monostatic RCS of this reflector for normal incidence of the x- and y-polarizations has been simulated. Referenced by that of a metallic board with the same size, the RCS reduction by this reflector is presented in Fig. 3 (b). From careful observation of Fig. 3 (a), it can be found that this windmill-formed structure is not rigorously x-y symmetrical. That is why this structure shows different RCS curves for different polarizations. Taking the RCS reduction of -10 dB as the criteria, the proposed windmill-formed reflector shows an RCS reduction band from 7.56 GHz to 11 GHz for x-polarization and 8.31 GHz to 11.13 GHz for y-polarization. The maximum RCS reduction around -25.7 dB is obtained at 8.05 GHz. The scattering pattern for x-polarization at this frequency is plotted in Fig. 4. It can be seen that the dominant EM energy is reflected from backward direction to (θ = 30º, φ = 28º) and (θ = 30º, φ = 208º), which is a typical signature for reflector designed by phase cancellation scheme. Similar scattering pattern can be observed for y-polarization.

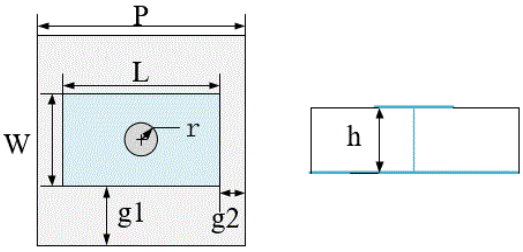

Fig. 1. The structure of AMC unit cell.

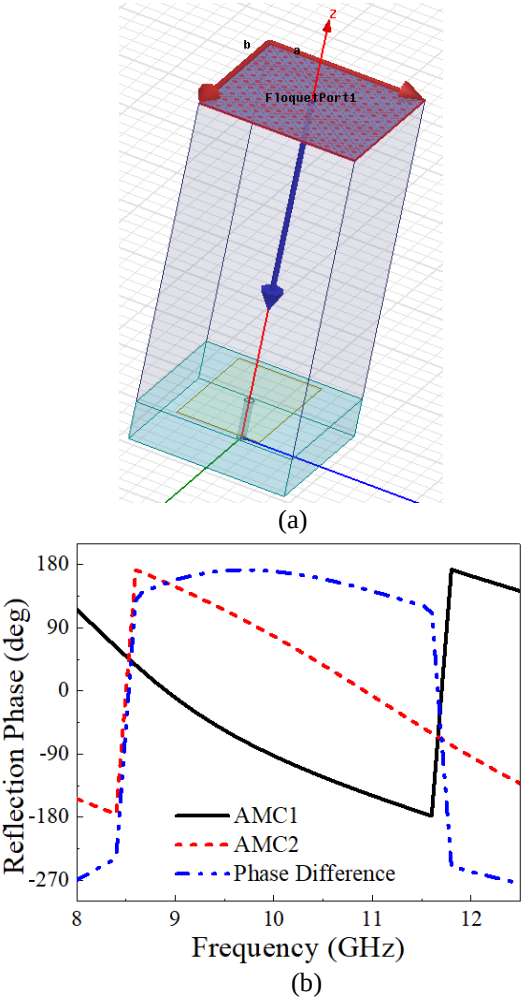

Fig. 2. (a) Simulation model of the AMC in HFSS, and (b) the reflection phase and phase difference of the two AMCs.

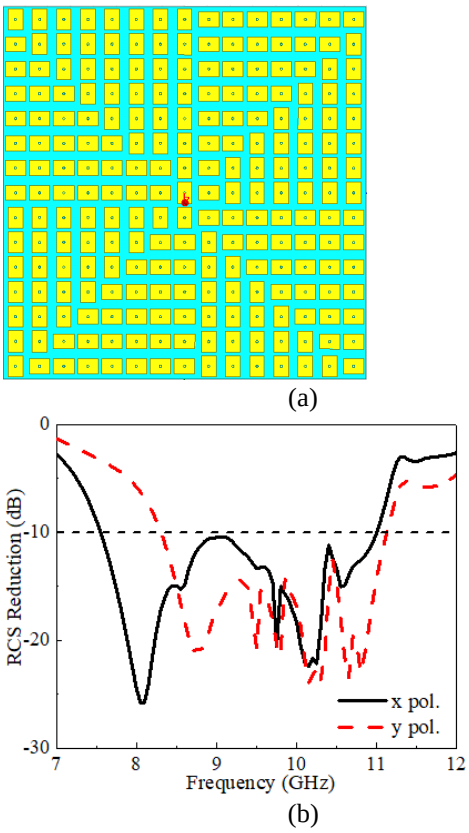

Fig. 3. (a) Illustration of the windmill-formed reflector, and (b) the simulated monostatic RCS of the windmill-formed reflector for normal incidences.

B. Design of the proposed antenna

In this section, the windmill-form reflector designed in section A is applied to a circularly polarized antenna. Based on a rectangular patch of 10*mm*×8.7*mm*, two isosceles right-angled triangles are cut from the central patch of the CP antenna [20], with details provided in Fig. 5 (a). The substrate is with dimension 159*mm*× 159*mm*×2*mm*. On top of the substrate, the windmill-formed reflector is applied surrounding the CP patch with a few modifications, as presented in Fig. 5 (b). Firstly, strong mutual coupling of the CP patch with its immediate neighboring AMCs will cause radiation degradation. Therefore, those AMC cells are removed to decrease this type of coupling. Secondly, the remaining central AMC elements dominantly work as parasitic radiating sources due to their coupling with the CP antennas [22], which enhances the gain of the patch. It is found by simulation that the axial ratio of the antenna is more sensitive to the currents on the diagonal direction of the substrate on which corners of the patch are cut. So a few centering AMC elements on this diagonal direction are rotated in order to adjust the induced x- and y-polarized currents. In this way, the AR bandwidth is obviously improved without violating the overall phase cancellation mechanism of the reflector when working in the scattering mode. After optimization, a rotation angle of 30º is obtained for this design to balance the multifunction of high gain, broad AR bandwidth, and low RCS of the antenna.

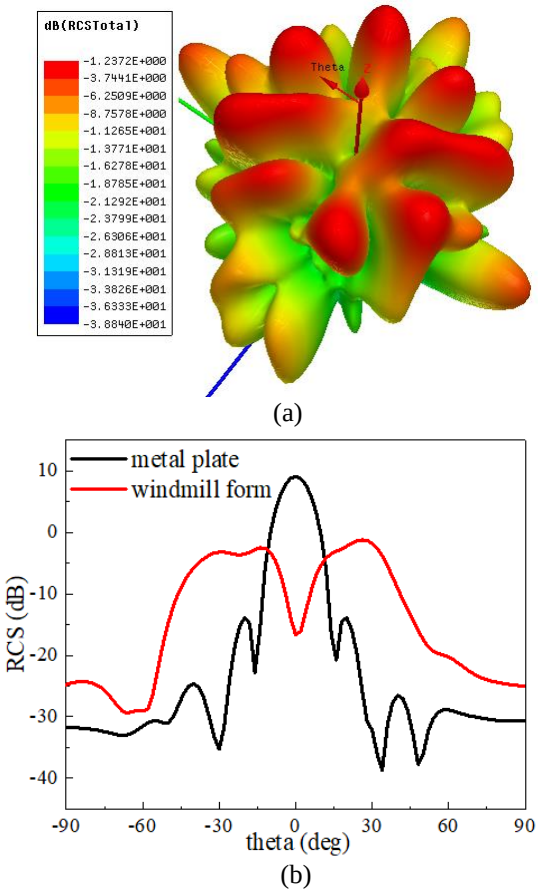

Fig. 4. The RCS pattern for the windmill-formed reflector at 8.05 GHz: (a) The 3-D pattern, and (b) the θ = 30º plane referenced by a metallic plate of the same size.

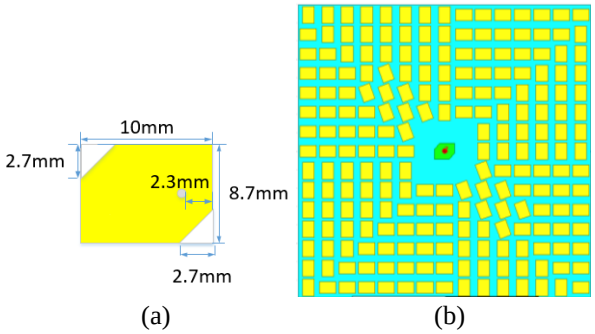

Fig. 5. Designs of: (a) the CP patch and (b) the proposed antennas.

Following the convention of [16, 17, 19, 20], the same CP antenna whose substrate is of the same size with the proposed antenna, is used as the reference antenna.

III. RESULTS AND DISCUSSION

A. Simulated radiation properties of the proposed antenna

Firstly, the radiation performance of the proposed antenna is examined by simulations. As shown in Fig. 6, the reference and the proposed CP antennas show almost the same impedance bandwidths (S_{11} < -10 dB) of 9.19 GHz - 11.3 GHz and 9.18 GHz - 11.34 GHz (21.1%). However, the bandwidth for 3dB AR of the main beam is extended from 9.91 GHz - 10.34 GHz (4.2%), to 9.86 GHz - 10.41 GHz (5.43%) by the proposed antenna, which means 29.3% increment in the AR bandwidth.

As shown in Fig. 7 (a), in the AR band, the gain of the reference antenna varies between 6.66 dB - 7.34 dB. In comparison, the proposed antenna yields a gain between 7.78 dB - 9.42 dB in its AR band. The gain enhancement is generally over 1 dB in the 3dB AR band, with a maximum of 2.44 dB at 10.1 GHz and minimum of 0.67 dB at 10.25 GHz.

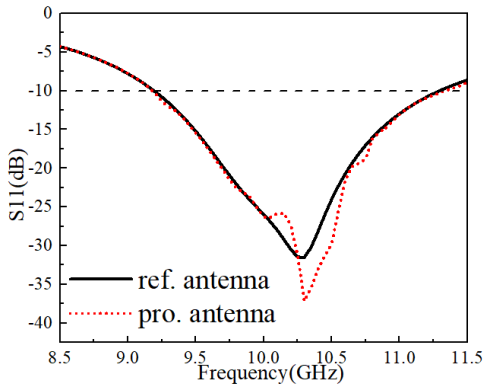

(a)

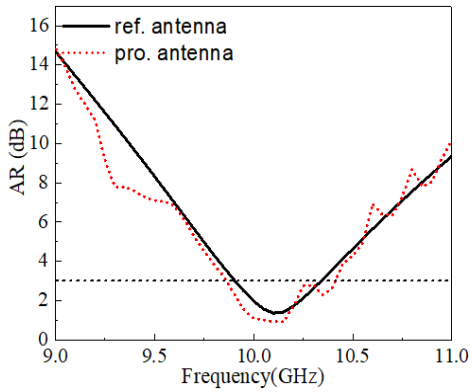

(b)

Fig. 6. (a) The impedance bandwidth, and (b) the AR bandwidth of the proposed and the reference antennas.

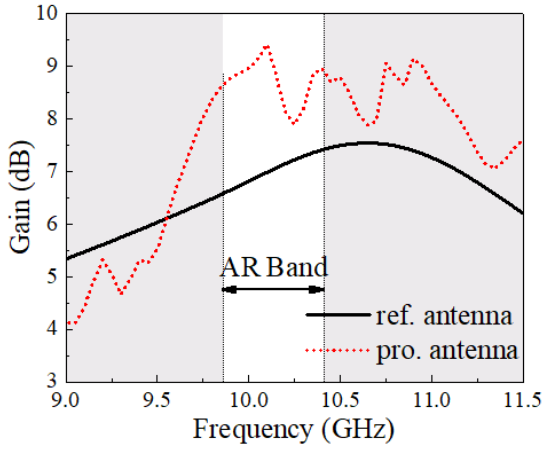

(a)

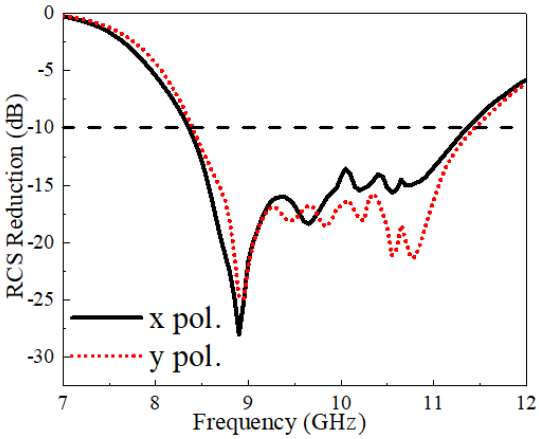

(b)

Fig. 7. (a) Gain of the proposed antenna and reference antenna, and (b) the RCS reduction of the proposed antenna for x- and y-polarized normal incidents.

B. RCS reduction of the proposed antenna

The monostatic RCS of the proposed and reference antennas for x-polarized and y-polarized normal incidents is also numerically investigated and the results are presented in Fig. 7 (b). It can be seen that, the proposed antenna with windmill-formed configuration shows an RCS reduction by more than 10 dB in a wideband frequency ranges from 8.35 GHz to 11.34 GHz (30.4% relative bandwidth) for x-x polarization. For y-y polarization, the 10dB RCS reduction frequency band is from 8.4 GHz to 11.4 GHz (30.3% relative bandwidth). Within the above bands, the maximum RCS reduction reaches 25.7 dB and 23 dB for x-x and y-y polarizations respectively. The operating band of the proposed antenna (9.91 GHz - 10.34 GHz) is covered by the RCS reduction band, which indicates an in-band RCS reduction is obtained. Compared with the similar work in [19, 20], the 3dB AR bandwidth is improved in this design, with detailed comparison listed in Table 1.

Table 1: Comparison of the AR bandwidth and RCS reduction

	AR 3dB-Bandwidth of CP Antenna	AR 3dB-Bandwidth of Improved CP Antenna	10dB-Bandwidth of RCS Reduction
Ref. [19]	5.87-6.07GHz (3.35%)	5.93-6.07GHz (2.3%)	13-15GHz (14.3%)
Ref. [20]	10.95-11.35GHz (3.6%)	10.45-11.85GHz (12.56%)	-
This paper	9.91-10.34GHz (4.2%)	9.86-10.41GHz (5.43%)	8.35-11.34GHz (30.4%)

C. Measurement results of the proposed antenna

The proposed antenna and the reference antenna were fabricated, with photos shown in Fig. 8. The setup in the anechoic chamber for measurement is shown in Fig. 9. The measurement results of S_{11} agree well with the simulation results, as shown in Fig. 10 (a). With regard to the axial ratio, as shown in Fig. 10 (b), the bandwidths are wider in measurement than in the simulation. The 3 dB AR band of the main beam is 9.9 GHz - 10.3 GHz for the reference antenna, with a bandwidth of 3.96%; while that for the proposed antenna is 9.8 GHz - 10.4 GHz, corresponding to a relative bandwidth of 5.94%. In other words, 50% expansion of the AR bandwidth is obtained in the measurement.

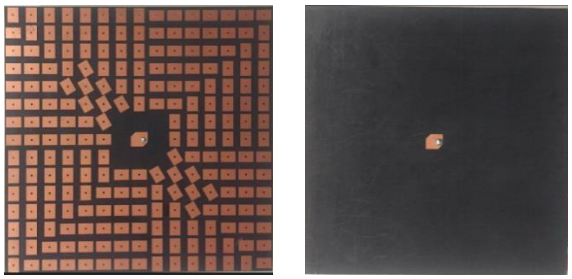

(a) (b)

Fig. 8. The photos of: (a) the proposed antenna and (b) the reference antenna.

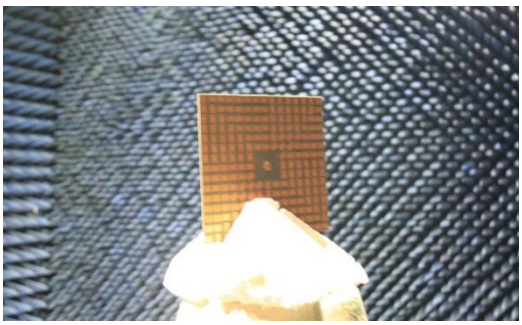

Fig. 9. Measurement setup in anechoic chamber.

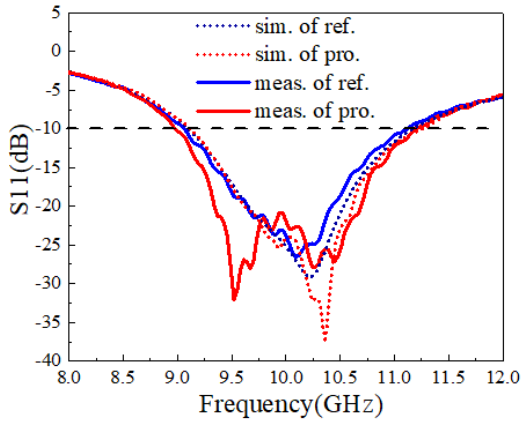

(a)

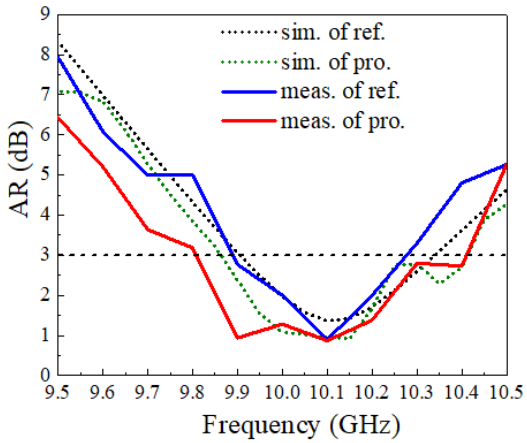

(b)

Fig. 10. (a) The S11 and (b) the AR of the proposed antenna and reference antenna.

The measured antenna gain is provided in Fig. 11 (a), in which improvement can be seen in the proposed antenna. The variation of the gain in the above AR band is below 3dB. As plotted in Fig. 11 (b), the measured radiation patterns agree well with those from the simulations. The fast changes in measured gain and the wider AR bandwidth could be attributed to the fabrication and measurement tolerance.

The monostatic RCSs of these antennas are measured from 8 GHz to 12 GHz and the results are provided in Fig. 12. An evident RCS reduction is seen for the vertical (corresponding to the x-x polarization in simulation due to the experimental set up) and the horizontal polarization (corresponding to y-y polarization in simulation). To be specific, 10 dB RCS reduction is obtained in frequency band of 8.6 GHz - 12.4 GHz, corresponding to a relative bandwidth of 32.6% for x-x polarization. The 10 dB RCS reduction band for y-y polarization is from 8.73 GHz to 11.95 GHz, with a relative bandwidth of 31.1%. The measured results of the RCS reduction generally agree with the simulations

except that the operating band for RCS reduction in measurement shifts upwards by nearly 1 GHz. This frequency shift may also be due to the fabrication tolerance. Despite of this frequency shift, the operating band of the proposed antenna is still covered by the RCS reduction band.

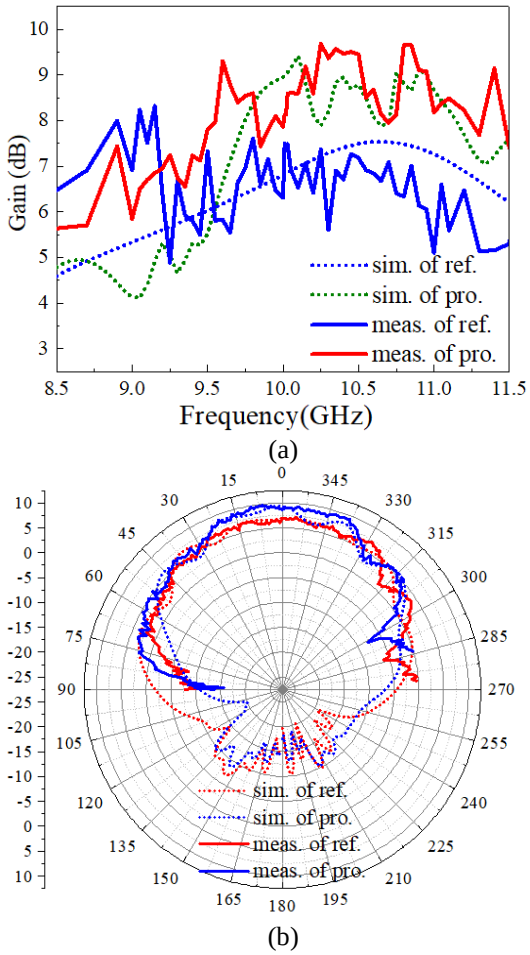

Fig. 11. (a) The gain and (b) the radiation patterns of the proposed and the reference antennas at 10GHz.

IV. CONCLUSION

In this paper, an in-band RCS reduction of the CP patch antenna is obtained by applying a modified windmill-formed configuration composed of PD-AMCs. By adopting windmill-formed reflector, backscatterings from different orientations of PD-AMCs cancel each other in the far field and lead to low RCS characteristics. It is verified by simulations and measurements that, 10 dB in-band RCS reduction is obtained with bandwidths of more than 30% for both x-x and y-y polarizations. By rotating some key AMC elements in the diagonal of the windmill-formed reflector, the axial ratio of the proposed antenna is improved. Referenced by the bare CP patch antenna, the experimental results show that the AR bandwidth of the proposed antenna is extended from 4.2% to 5.43% in simulation and from 3.96% to 5.94% in measurement. Gain improvement in the operating frequency band is also verified.

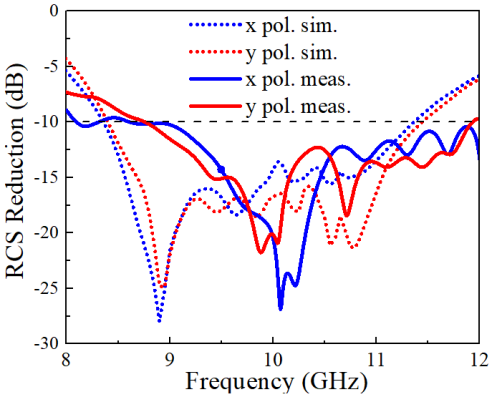

Fig. 12. Monostatic RCS of the proposed antenna and reference antenna.

ACKNOWLEDGMENT

This work is supported in part by the National Key R&D Program of China under Grant 2017YFB0202500, the NSFC under Grant Nos. 61601023 and U1730102.

REFERENCES

[1] K. F. Lee and K. F. Tong, "Microstrip patch antennas-basic characteristics and some recent advances," *Proc. IEEE*, vol. 100, no. 7, pp. 2169-2180, 2012.

[2] L. Sun, Y. H. Huang, and J. Y. Li, "A wideband circularly polarized candy-like patch antenna," *J. Electromagn. Waves Appl.*, vol. 25, no. 8, pp. 1113-1121, 2011.

[3] M. Ramírez and J. Parrón, "Dual-band circularly polarized microstrip antenna," *J. Electromagn. Waves Appl.*, vol. 26, no. 5, pp. 737-743, 2012.

[4] T. N. Chang and J. M. Lin, "Circularly polarized antenna having two linked slot-rings," *IEEE Trans. Antennas Propag.*, vol. 59, no. 8, pp. 3057-3060, 2011.

[5] A. A. Heidari, M. Heyrani, and M. Nakhkash, "A dual-band circularly polarized stub loaded microstrip patch antenna for GPS applications," *Progress in Electromagnetics Research.*, vol. 92, pp. 195-208, 2009.

[6] A. R. Vaidya, R. K. Gupta, and S. K. Mishra, "Right-hand/left-hand circularly polarized high-gain antennas using partially reflective surfaces," *IEEE Antennas Wireless Propag. Lett.*, vol. 13, pp. 431-434, 2014.

[7] S. X. Ta and T. K. Nguyen, "AR bandwidth and gain enhancements of patch antenna using single dielectric superstrate," *Electron. Lett.*, vol. 53, no.

15, pp. 1015-1017, 2017.

[8] K. L. Chung and S. Chaimool, "Diamagnetic metasurfaces for performance enhancement of microstrip patch antennas," *Proc. Eur. Conf. Antennas and Propagation (EUCAP)*, pp. 48-52, 2011.

[9] H. L. Dong, Y. J. Lee, J. Yeo, et al., "Directivity enhancement of circular polarized patch antenna using ring- shaped frequency selective surface superstrate," *Microwave Optical Techno Lett.*, vol. 49, no. 1, pp. 199-201, 2007.

[10] S. X. Ta and I. Park, "Compact wideband circularly polarized patch antenna array using metasurface," *IEEE Antennas Wireless Propag. Lett.*, vol. 16, pp. 1932-1936, 2017.

[11] H. L. Zhu, S. W. Cheung, and K. L. Chung, "Linear-to-circular polarization conversion using metasurface," *IEEE Trans. Antennas Propag.*, vol. 61, no. 9, pp. 4615-4623, 2013.

[12] Q. Zheng, C. Guo, and J. Ding, "Wideband and low RCS circularly polarized slot antenna based on polarization conversion of metasurface for satellite communication application," *Microwave Optical Techno Lett.*, vol. 60, no. 3, pp. 679-685, 2018.

[13] W. Jiang, Y. Zhang, and Z.-B. Deng, "Novel technique for RCS reduction of circularly polarized microstrip antennas," *J. Electromagn. Waves Appl.*, vol. 27, no. 9, pp. 1077-1088, 2013.

[14] W. Jiang, T. Hong, and S. X. Gong, "Research on the scattering characteristics and the RCS reduction of circularly polarized microstrip antenna," *International Journal of Antennas and Propaga.*, pp. 797-800, 2013.

[15] L. L. Cong, F. Qiang, X. Y. Cao, et al., "A novel circularly polarized patch antenna with low radar cross section and high-gain," *Acta Physica Sinica*, vol. 64, no. 22, 2015.

[16] M. Paquay, J. C. Iriarte, and I. Ederra, "Thin AMC structure for radar cross-section reduction," *IEEE Trans. Antennas Propag.*, vol. 55, no. 12, pp. 3630-3638, 2008.

[17] Y. J. Zheng, J. Gao, X. Y. Cao, et al., "A low radar cross-section artificial magnetic conductor reflection screen covering X and Ku band," *Acta Physica Sinica*, vol. 64, no. 2, pp. 24219-24219, 2015.

[18] J. C. I. Galarregui, A. T. Pereda, J. L. M. D. Falcón, I. Ederra, R. Gonzalo, and P. D. Maagt, "Broadband radar cross-section reduction using AMC technology," *IEEE Trans. Antennas Propag.*, vol. 61, no. 12, pp. 6136-6143, 2013.

[19] L. Zhang and T. Dong, "Low RCS and high-gain CP microstrip antenna using SA-MS," *Electron. Lett.*, vol. 53, no. 6, pp. 375-376, 2017.

[20] K. Li, Y. Liu, and Y. Jia, "A circularly polarized high-gain antenna with low RCS over a wideband using chessboard polarization conversion metasurface," *IEEE Trans. Antennas Propag.*, vol. 65, no. 8, 2017.

[21] Y. Zhang, R. Mittra, and B.-Z. Wang, "A novel design for low-RCS screens using a combination of dual-amc patches," *IEEE Antennas and Propagation Society International Symposium, Charleston, USA*, 2009.

[22] Z. J. Han, W. Song, and X. Q. Sheng, "Gain enhancement and RCS reduction for patch antenna by using polarization-dependent EBG surface," *IEEE Antennas & Wireless Propagation Letters*, vol. 16, pp. 1631-1634, 2017.

Wei Song obtained the Bachelor degree from the Northeastern University, China in 2002, and the M.Sc. and Ph.D. degrees in Queen Mary, University of London, U.K. in Electronic Engineering in 2003 and 2008 respectively. In 2008 she worked as a Postdoc Research Assistant in Antenna group, Queen Mary, University of London, and in the same year she joined the School of Information and Electronics at the Beijing Institute of Technology, where she is currently an Associate Professor.

Her research interests include computational electromagnetics, EM scattering analysis, antennas, and metamaterial analysis.

Wen-Bo Zheng was born in Shanxi, China in 1994. She received the Bachelor degree in Information and Electronic Engineering from Beijing Institute of Technology (BIT) in 2016. She is currently a graduate student in BIT.

Her main research interests are in the fields of antenna design, metasurface and Orbital Angular Momentum antenna.

Zijian Han was born in Liaoning, China in 1990. He graduated from Beijing Institute of Technology (BIT) in 2013. He started doing research as a Ph.D. student in BIT since 2013. He has already published SCI paper on IEEE AWPL and other EI papers.

His main research interests are in the fields of antenna design and metasurface.

Xin-Qing Sheng received his B.S., M.S., and Ph.D. degrees from the University of Science and Technology of China (USTC), Hefei, China, in 1991, 1994, and 1996, respectively. He is the Chang-Jiang Professor in the School of Information and Electronics, Beijing Institute of Technology, Beijing, China.

High Gain Circularly Polarized X-shaped Aperture Coupled Antenna for WLAN Applications

Mohammed A. Meriche [1,2], Abderraouf Messai [1], Tayeb A. Denidni [2], and Hussein Attia [3]

[1] Department of Electronics
Université des frères Mentouri, Constantine, Algeria

[2] EMT-INRS, Institut National de la Recherche Scientifique
800, rue De La Gauchetière O, Montréal (Qc) H5A 1K6 Canada

[3] King Fahd University of Petroleum and Minerals (KFUPM)
Dhahran 31261, Saudi Arabia

Abstract — This paper presents a new high gain compact aperture-coupled circularly polarized antenna for WLAN applications. The proposed antenna comprises an asymmetric X-shaped slot etched on a circular patch and fed through the coupling between an annular slot and a microstrip line. The circular polarization is mainly due to the asymmetrical crossed-slots, respecting the angle of 45^0 between its two arms. The antenna with overall size of $60 \times 60 \times 5.83$ mm^3 has a measured 10-dB impedance bandwidth of 36%, a 3-dB axial ratio bandwidth of 3.47% (5.67–5.87 GHz) and 1-dB gain bandwidth of 19.5% (4.85-5.90 GHz) with a peak gain of 8.65 dBi. To validate the simulated results, a prototype was fabricated, and good agreement between simulations and measurements has been accomplished.

Index Terms — Aperture-coupled, axial ratio, circularly polarized (CP), X-shaped slot.

I. INTRODUCTION

Recently, high gain antennas have been widely used for WLAN applications. To realize this type of antennas, different techniques are used in literature. These techniques include the integration of electromagnetic band gap (EBG) structures in ground plane acting as artificial magnetic conductor [1-2] or superstrates acting as partially reflective selective surface [3-5]. In this work, the aperture-coupled antenna method is used to enhance the antenna gain without using any EBG structures.

Circularly polarized (CP) patch antennas have attracted substantial attention in modern wireless communication systems due to its many advantages such as more flexibility in the orientation of transmitting and receiving antennas and polarization mismatch reduction compared to linear polarization [6-10].

The most popular types of single-fed CP patch antennas are the slotted and the notched patch [11-16]. Several methods have been proposed to design single-feed aperture-coupled antennas with CP [17-21]. The aperture-coupled antennas were designed and developed for broadband, high gain, CP and high efficiency applications. Therefore, single-fed aperture-coupled antennas with CP characteristics have received greater attention [17-20] over the past decade.

In this paper, a novel compact aperture-coupled CP antenna for WLAN applications is proposed. The new antenna consists of an asymmetric X-shaped slot with an angle $\theta = 45°$ between its two arms, the slotted antenna is etched on a circular patch fed through the coupling between an annular slot and a microstrip line. The CP is generated by cutting two unequal slots in the circular patch respecting the angle θ. This paper is organized as follows. In Section 2, the design of the proposed antenna is described. Section 3 presents fabrication and measured results. Finally, concluding remarks are given in the last Section.

II. ANTENNA DESIGN

The proposed configurations of the CP antenna fed through a microstrip-coupled annular slot is shown in Fig. 1. The X-shaped slot with unequal arms, width W_s, lengths L_1 and L_2 etched on a circular patch and the annular slot aperture feeding are depicted in the Figs. 1 (b) and 1 (c).

The annular slot with outer radius R_o and inner radius R_i with the microstrip feed line are etched on a Rogers RO4003C substrate of thickness h_1, relative permittivity of 3.38, and loss tangent $\tan\delta = 0.0027$. The 50-Ω microstrip feed line with length L_f and width W_f is printed at the center of the bottom side of the ground plane and is electromagnetically coupling the energy to the annular slot. Moreover, the aperture feed is employed to directly excite the X-shaped slot on the circular patch. An optimum air gap height of H_c between the X-shaped

Submitted On: January 14, 2018
Accepted On: August 17, 2019

slot antenna substrate and aperture-coupled substrate is employed. The aperture-coupled substrate of Rogers RO4003C is identical to the one employed for the X-shaped slot circular patch.

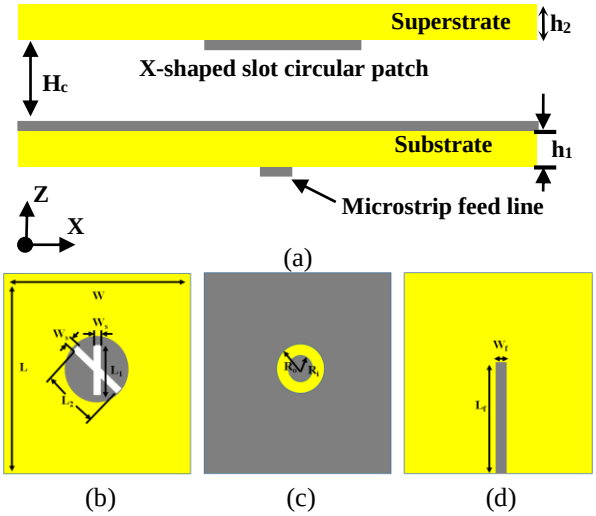

Fig. 1. Geometry of the proposed antenna: (a) side view, (b) bottom view of the X-shaped slot circular patch, (c) top view of the annular slot aperture coupling ground, and (d) the microstrip feed line.

The proposed antenna was simulated using the commercial software package CST Studio Suite. CST comprises three different solvers. These solvers are transient (i.e., time domain) solver based on finite integration technique (FIT), frequency domain solver based on finite element method (FEM), and integral equation solver based on method of moments (MoM). The transient solver has been adopted in this work due to its computational and memory-efficient performance. FIT is a finite difference method based on a small-scale interpretation of Maxwell's equations (as opposed to a large-scale integral equation approach). The formulation of the FIT utilizes voltage and current (i.e., integral of E and H fields), on a staggered grid.

Table 1: The detailed dimensions of the proposed antenna (all dimensions are in mm)

Parameter	Value	Parameter	Value
W	60	h_1	1.524
L	60	h_2	0.81
L_1	15	H_c	3.5
L_2	17	R_i	5
W_s	2	R_o	7
L_f	30	R (circular patch radius)	9.5
W_f	3.55		

Parametric sweep tool in CST is utilized to carefully choose the feed location, the annular slot and the X-shaped slot dimensions in order to obtain good impedance matching and CP. These dimensions have been swept within certain boundaries (about ± 25% of the selected value) to enable the calculation of far-fields or impedances based on the swept parameters. Table 1 presents the selected parametrized dimensions of the compact aperture-coupled CP antenna demonstrated in Fig. 1.

The performance of the proposed CP antenna is studied in order to gain a better insight into the effects of the X-shaped slot antenna over the whole structure and how the CP radiation is obtained. Figure 2 depicts the geometry of the X-shaped slot etched on the circular patch with different values of the angle θ between the asymmetrical crossed-slots of lengths L_1 and L_2. The variation of the angle θ may affect the impedance bandwidth and the CP behavior. Figures 3 and 4 show the parametric studies of the reflection coefficient (S_{11}) and the axial ratio (AR) versus the angle θ.

The angle θ is varied from 0° to 90° while L_1, L_2 are fixed (L_1 = 15 mm, L_2 = 17 mm). Only when θ = 45° the impedance matching gets better and covers the WLAN band as shown in Fig. 3.

Figure 4 shows the variation of AR at broadside. The AR improves when the angle θ = 45°, for θ = 0° and θ = 90° it can be seen that the minimum AR is about 40 dB, which implies that no circular polarisation has been achieved.

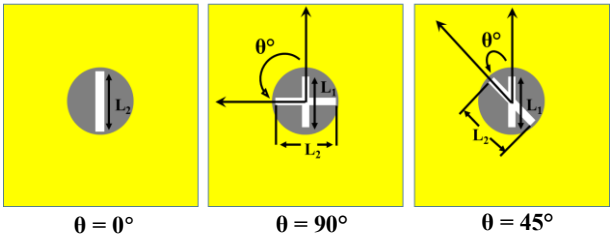

Fig. 2. Geometry of the asymmetrical crossed-slots etched on the circular patch with variation of theta.

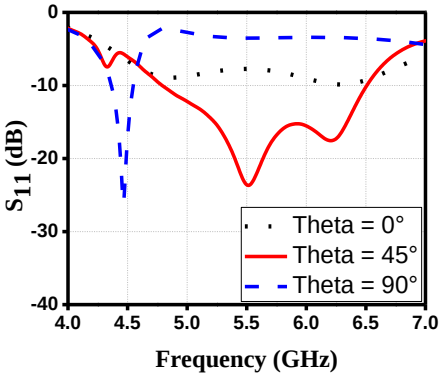

Fig. 3. Simulated reflection coefficient of the antenna with variation of the angle theta.

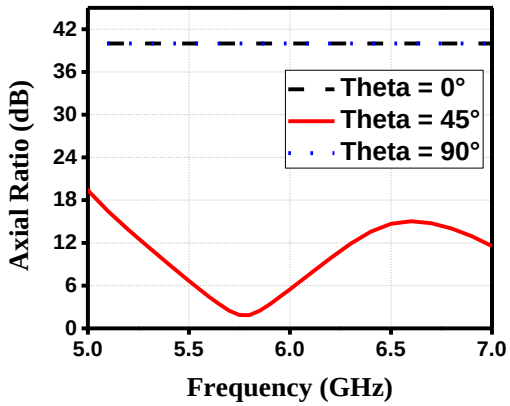

Fig. 4. Simulated axial ratio of the antenna with variation of the angle theta.

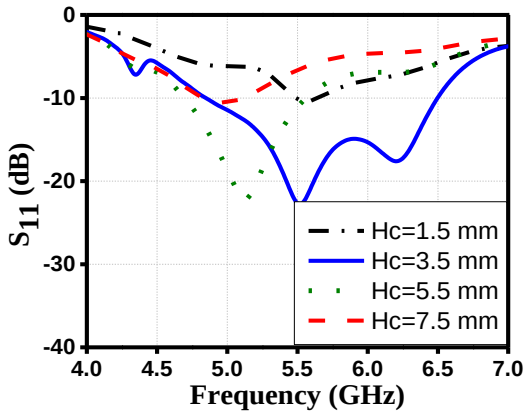

Fig. 5. Simulated reflection coefficient of the antenna with variation of H_c.

The distance between the feeding annular slot and the X-shaped slot is expected to affect the impedance bandwidth. Figure 5 shows the parametric studies of the reflection coefficient (S_{11}) versus the distance H_c. H_c is varied from 1.5 to 7.5 mm and L_1, L_2 are fixed (L_1 = 15 mm, L_2 = 17 mm). When H_c is increased from 1.5 to 3.5 mm, the impedance matching gets even better, then when the distance H_c is increased from 5.5 to 7.5 mm the impedance matching bandwidth shifts down.

Figures 6 and 7 show the parametric analysis of the reflection coefficient and the AR versus the lengths of asymmetrical crossed-slots L_1 and L_2. Within the operating frequency band and with an optimum gap height of H_c = 3.5 mm, only one geometrical parameter (L_2) is varied each time and the second parameter (L_1) is kept unchanged. Figure 6 presents the variation of reflection coefficient with $L_1>L_2$, $L_1=L_2$ and $L_1<L_2$. The S_{11} bandwidth improves as $L_1<L_2$ and the impedance matching also improves and gets even better, with an impedance bandwidth of 1.7 GHz (from 4.8 GHz to 6.5 GHz) which is about 30%. Figure 7 shows the variation of AR at broadside, with $L_1>L_2$, $L_1=L_2$ and $L_1<L_2$.

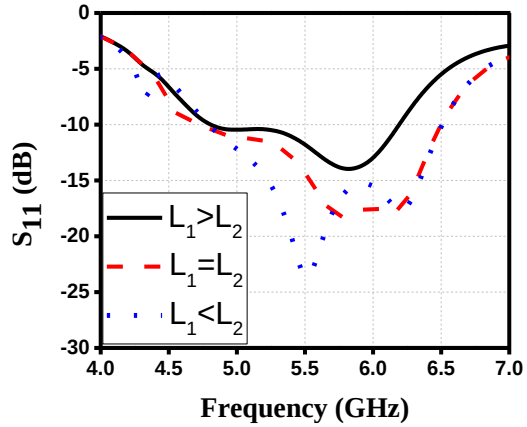

Fig. 6. Simulated reflection coefficient of the antenna with $L_1>L_2$, $L_1=L_2$ and $L_1<L_2$.

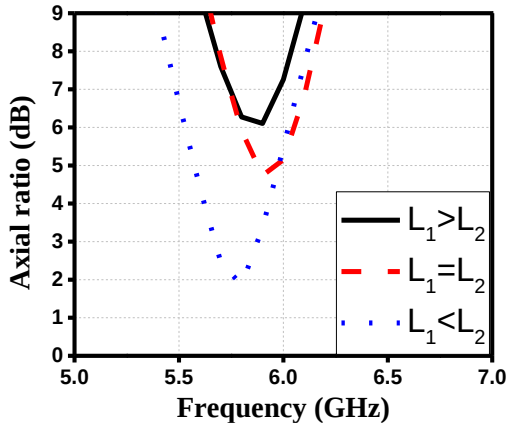

Fig. 7. Simulated axial ratio of the antenna when $L_1>L_2$, $L_1=L_2$ and $L_1<L_2$.

The minimum AR improves when $L_1<L_2$ with a 3-dB bandwidth of 3.47% (5.67–5.87 GHz) and a minimum AR value of about 2 dB at 5.75 GHz.

III. FABRICATION AND MEASUREMENT RESULTS

Using the annular slot and the X-shaped slotted circular patch etched on the bottom face of a superstrate, two superposed layers were assembled, and a prototype was fabricated as shown in Fig. 8. The antenna prototype was measured in a standard anechoic chamber. Foam is used for maintaining the air space between the two layers. An optimum gap height of H_c = 3.5 mm, which is $\lambda/15$ at 5.8 GHz, is verified experimentally. The reflection coefficient (S_{11}) is measured using an Agilent Vector Network Analyzer (VNA) 8722ES. Figure 9 shows the simulated and measured reflection coefficients of the proposed CP antenna. Simulated results show that the reflection coefficient is below -10 dB within the frequency range from 4.8 GHz to 6.5 GHz with an

impedance bandwidth of 1.7 GHz, which is about 30%. The impedance bandwidth of the fabricated CP antenna is 2 GHz from 4.5 GHz to 6.5 GHz, which is about 36%. It can be observed that a measured wideband reflection coefficient is achieved. The measured impedance bandwidth agrees with the simulated one. In addition, the trivial discrepancy between the simulation and measurement results is attributed to the unavoidable fabrication tolerance.

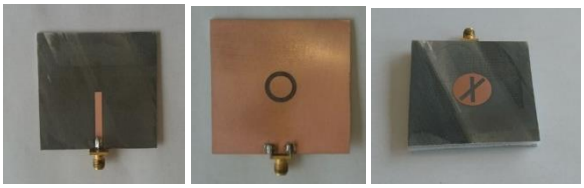

(a) (b) (c)

Fig. 8. Photograph of the fabricated prototype: (a) top view of the feeding annular slot, (b) microstrip feed line, and (c) bottom view of the X-shaped slot.

The simulated and measured AR are shown in Fig. 10. It can be seen that the measured AR has a lowest value of 1.6 dB at 5.8 GHz and 3-dB AR bandwidth of 3.47% form 5.67 GHz to 5.87 GHz. The lowest value of the simulated AR is about 1.83 dB at 5.8 GHz that supports WLAN bands. The 3-dB AR simulated bandwidth is still located within the impedance bandwidth of the proposed antenna and agrees well with the measured one.

Figure 11 shows the simulated and measured gain of the proposed CP antenna. It is illustrated that the simulated 3-dB gain bandwidth is about 46.62% (4.08-6.56 GHz), with a maximum gain of 8.85 dBi. The measured 1-dB gain bandwidth is about 19.5% from 4.85 GHz to 5.90 GHz. The maximum measured gain is about 8.65 dBi. The common bandwidth for measured 10-dB impedance and 1-dB gain is about 19.5% (4.85-5.90 GHz). It is worth mentioning that the measured gain is quite uniform with frequency over the operating bandwidth and agrees well with the simulated results.

Figure 12 shows the simulated and measured radiation patterns for both right-hand CP (RHCP) and left-hand CP (LHCP) at 5.8 GHz for phi=0° and phi=90° planes. It can be observed that the RHCP is radiated in the +Z direction, whilst LHCP in the -Z direction. In addition, the trivial discrepancy between the simulated and measured radiation patterns is attributed to the unavoidable fabrication tolerance and the presence of noise during the far-field measurement.

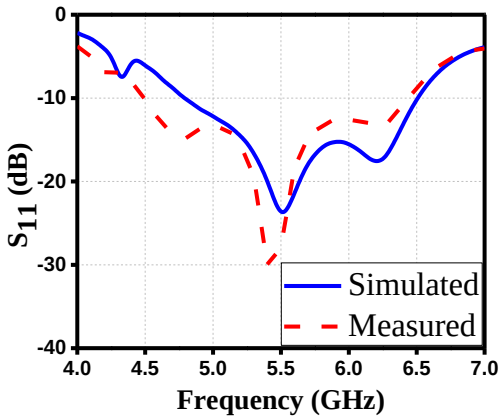

Fig. 9. Simulated and measured reflection coefficient of the proposed antenna.

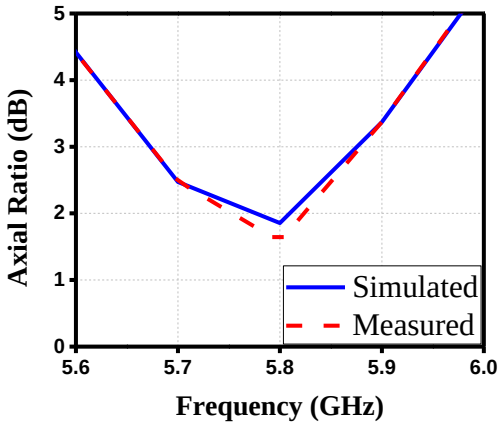

Fig. 10. Simulated and measured axial ratio of the proposed antenna.

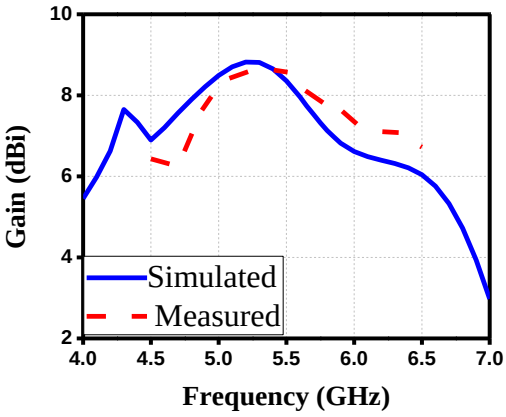

Fig. 11. Simulated and measured Gain of the proposed antenna.

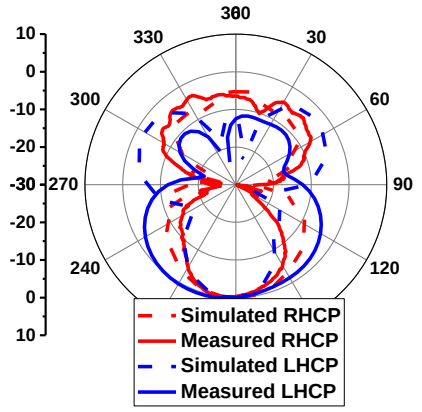

(a) Phi=0°

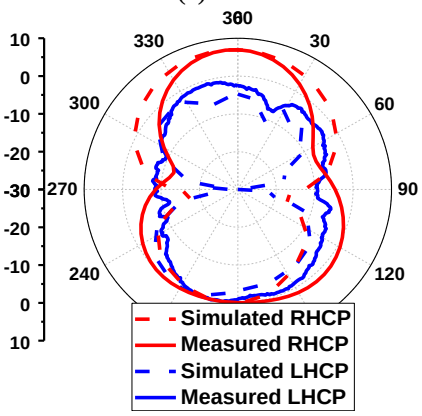

(b) Phi=90°

Fig. 12. Simulated and measured radiation patterns of the proposed antenna at 5.8 GHz at: (a) Phi= 0° and (b) Phi= 90°.

Table 2 presents a comparison of the proposed antenna with some previously published designs. As can be seen, the novel compact aperture-coupled CP antenna presented in this work has a better performance in terms of gain and 3-dB AR bandwidth compared with the published designs.

IV. CONCLUSION

A novel high gain compact aperture-coupled circularly polarized antenna for WLAN applications has been presented. The reported results have demonstrated that the circular polarization is obtained by employing the asymmetric X-shaped slot with an angle θ = 45° between the two arms etched on a circular patch antenna. Furthermore, the air gap between the X-shaped slot antenna substrate and the annular slot feeding substrate was used to maintain the gain of the proposed antenna. Consequently, the measured 1-dB gain bandwidth of 19.5% (4.85-5.90 GHz) and 3-dB AR bandwidth of 3.47% (5.67-5.87 GHz) are well overlapped by the measured 10-dB impedance bandwidth of 36% (4.5-6.5 GHz). The antenna has a maximum gain of 8.65 dBi. Measured results confirm that there is a good agreement between simulations and measurements.

ACKNOWLEDGMENT

This work was supported by King Fahd University of Petroleum and Minerals (KFUPM), Saudi Arabia, through DSR project No. GTEC1802 and by the Algerian Ministry of Higher Education and Scientific Research (MESRS). Authors would like to thank Mr. Arun Kesavan, EMT-INRS, for his help.

Table 2: Comparison of the proposed antenna with some previously published designs

Ref.	Size (mm^3)	Freq. (GHz)	S_{11} BW (%)	Gain Max	3-dB ARBW (GHz, %)
[16]	1.2 λ_0 × 1.2 λ_0 × 1.6	2.4/5.8	14.3/ 8.1	3.7/3.2 dBi	(≈5.7-5.93), 4.1
[22]	133.2 × 133.2 × 32.54	(2.37-2.75) (3.4–8)	14.84/80.70	5.95/6.92/6.37/6.07 dBic	5.7–5.87, 2.9
[23]	30 × 30 × 3.048	(2.43-2.52) (5.7-6.5)	3.63/13.11	6.6/6 dBi	(≈5.85-5.97), 2.03
Proposed antenna	60 × 60 × 5.83	(4.5-6.5)	36	7.8 dBi	5.67-5.87, 3.47

REFERENCES

[1] Y. Zhang, W. Yu, and W. Li, "Study on Fabry-Perot antennas using dipole exciters," *The Applied Computational Electromagnetics Society (ACES) Journal*, vol. 29, no. 12, pp. 1112-1115, Dec. 2014.

[2] M. A. Meriche, H. Attia, A. Messai, and T. A. Denidni, "Gain improvement of a wideband monopole antenna with novel artificial magnetic conductor," *17th International Symposium on Antenna Technology and Applied Electromagnetics (ANTEM)*, 2016.

[3] A. Chaabane, F. Djahli, H. Attia, L. M. Abdelghani, and T. A. Denidni, "Wideband and high-gain EBG resonator antenna based on dual layer PRS," *Microw. Opt. Technol. Lett*., vol. 59, no. 1, pp. 98-101, 2017.

[4] L. M. Abdelghani, H. Attia, and T. A. Denidni, "Dual and wideband Fabry–Perot resonator antenna for WLAN applications," *IEEE Antennas Wireless Propag. Lett.*, vol. 16, pp. 473-476, 2017.

[5] M. A. Meriche, A. Messai, H. Attia, B. Hammache, and T. A. Denidni, "High-gain wideband Fabry-Pérot slot antenna with partially reflective surface," *16th Mediterranean Microwave Symposium (MMS)*,

2016.

[6] Z. Jiang, H. Zhao, X. Zhao, J. Liu, M. Shui, T. Wan, and X. Qiao, "Gain-enhanced compact circularly polarized array microstrip antenna," *The Applied Computational Electromagnetics Society* (*ACES) Journal*, vol. 34, no. 3, pp. 397-402, Mar. 2019.

[7] M. A. El-Hassan, K. F. A. Hussein, A. E. Farahat, and K. H. Awadalla, "Shaped-beam circularly-polarized practical antenna array for land imaging SAR systems," *The Applied Computational Electromagnetics Society* (*ACES) Journal*, vol. 34, no. 5, pp. 642-653, May 2019.

[8] J. Su, Z. Li, Z. Li, Q. Guo, and Y. L. Yang, "Ku-band phase-gradient metasurface for broadband high-gain circularly polarized lens antenna," *The Applied Computational Electromagnetics Society* (*ACES) Journal*, vol. 34, no. 5, 2019.

[9] Nasimuddin, K. Esselle, and A. K. Verma, "High gain compact circularly polarized microstrip antenna," *TENCON 2005 - 2005 IEEE Region 10 Conference*, Melbourne, Qld., pp. 1-4, 2005.

[10] M. A. Choubar, S. Gupta, M. Farahani, A. R. Sebak, and T. A. Denidni, "Gain enhancement of circularly–polarized dielectric resonator antenna based on FSS superstrate for MMW applications," *IEEE Trans. Ant. Propag*., vol. 64, no. 12, pp. 5542-5546, 2016.

[11] K. Agarwal, Nasimuddin, and A. Alphones, "Triple-band compact circularly polarised stacked microstrip antenna over reactive impedance metasurface for GPS applications," *IET. Microw. Ant. Propag.*, vol. 8, pp. 1057-1065, 2014.

[12] L. B. K. Bernard, Nasimuddin, and A. Alphones, "An E-shaped slotted-circular patch antenna for circularly polarized radiation and radiofrequency energy harvesting," *Microw. Opt. Technol. Lett*., vol. 58, no. 4, pp. 868-875, 2016.

[13] H. L. Zhu, S. Cheung, K. L. Chung, and T. I. Yuk, "Linear-to-circular polarization conversion using metasurface," *IEEE Trans. Ant. Propag.*, vol. 61, no. 9, pp. 4615-4623, 2013.

[14] J. K. Pakkathillam and M. Kanagasabai, "Circularly polarized broadband antenna deploying fractal slot geometry," *IEEE Antennas Wireless Propag. Lett*., vol. 14, pp. 1286-1289, 2015.

[15] N. Herscovici, Z. Sipus, and D. Bonefacic, "Circularly polarized single-fed wide-band microstrip patch," *IEEE Trans. Ant. Propag*., vol. 51, no. 6, pp. 1277-1280, 2003.

[16] Y. Sung, "Dual-band circularly polarized pentagonal slot antenna," *IEEE Antennas Wireless Propag. Lett.*, vol. 10, pp. 259-261, 2011.

[17] Nasimuddin and Z. N. Chen. "Aperture-coupled asymmetrical C-shaped slot microstrip antenna for circular polarization," *IET. Microw. Ant. Propag.*, vol. 3, no. 3, pp. 372-378, 2009.

[18] J. S. Row, "Design of aperture-coupled annular-ring microstrip antennas for circular polarization," *IEEE Trans. Ant. Propag*., vol. 55, no. 5, pp. 1779-1794, 2005.

[19] T. F. Hung, J. Ch. Liu, Ch. Y. Wei, Ch. Ch. Chen, and Sh. Sh. Bor, "Dual-band circularly polarized aperture-coupled stack antenna with fractal patch for WLAN and WiMAX applications," *Int. J. RF. Microw. Compt. Aided. Eng*., vol. 24, no. 1, pp. 130-138, 2014.

[20] J. C. Liu, B. H. Zeng, L. Badjie, S. Drammeh, S. S. Bor, T. F. Hung, and D. Ch. Chang, "Single-feed circularly polarized aperture-coupled stack antenna with dual-mode square loop radiator," *IEEE Antennas Wireless Propag. Lett*., vol. 9, pp. 887-890, 2010.

[21] Y. T. Chen, S. W. Wu, and J. S. Row, "Broadband circularly-polarised slot antenna array," *Electron. Lett.*, vol. 43, no. 24, 2007.

[22] T. V. Hoang, T. T. Le, Q. Y. Li, and H. Ch. Park, "Quad-band circularly polarized antenna for 2.4/5.3/5.8-GHz WLAN and 3.5-GHz WiMAX applications," *IEEE Antennas Wireless Propag. Lett.*, vol. 15, pp. 1032-1035, 2016.

[23] S. Behera and D. Barad, "Circular polarized dual-band antenna for WLAN/Wi-MAX application," *Int. J. RF. Microw. Compt. Aided. Eng*., vol. 27, no. 1, pp. 1-7, 2017.

Broadband Circularly Polarized Antennas with Improved Gain

Meizhen Xiao, Hui Liu, and Yuehui Cui

The School of Electronic and Information Engineering
South China University of Technology, Guangzhou, 510641, China
eeyhcui@scut.edu.cn

Abstract ─ A broadband circularly polarized (CP) antenna with improved gain is proposed. The broadband CP antenna consists of two folded off-center-fed dipoles. Due to the two-dipole configuration, the antenna gain is improved by almost 2 dB. It is shown by simulation and experiment that the broadband CP antenna achieves an impedance bandwidth of 52% (1.71-2.89 GHz) for reflection coefficient<-15 dB and an axial ratio (AR) bandwidth of 45% (1.75-2.73 GHz) for AR<3 dB. The average antenna gain is about 10 dBi. A differentially-fed broadband CP antenna is also developed. Simulated and measured results show that the differentially-fed CP antenna fulfills an impedance bandwidth of 60% (1.53-2.83 GHz) for differential reflection coefficient <-15 dB and a 3-dB AR bandwidth of 44% (1.76-2.75 GHz). The average antenna gain is about 10 dBi. The gain-improved broadband CP antennas feature a simple planar configuration, which are suitable for applications in satellite/wireless communications.

Index Terms ─ Broadband antenna, circularly polarized antenna, differentially-fed antenna.

I. INTRODUCTION

Circularly polarized (CP) antennas have been widely used in satellite and wireless communications. Modern high-speed satellite and wireless communications usually require broadband CP antennas. For the long-distance wireless communication, an antenna with a high gain may show outstanding advantages in increasing the signal strength, improving the data rate and enhancing the communication quality. In recent years, a number of broadband CP antennas have been developed [1-11]. The performances of impedance bandwidths, bandwidths for axial ratio < 3dB, and the antenna gains of those CP antennas are listed in Table 1. The bandwidths of the antennas presented in [1-3] are not wide enough. Though the CP antennas in [4-11] have wide overlapped bandwidth for impedance matching and AR, these CP antennas have an average antenna gain of 6-8 dBi, which cannot meet the requirement for high-gain applications.

Differential circuits are important for communication systems due to their superior advantages of noise immunity, mode current elimination, and fundamental harmonic rejections [12]. Several differentially-fed CP antennas have been proposed in [13-21]. However, most of the antennas either have an overlapped bandwidth of less than 40% for impedance matching and AR or have an antenna gain no higher than 10 dBi. Some can neither meet the requirement of wide bandwidth nor high gain [13], [16]. Therefore, broadband CP antennas with high gain is desirable for long-distance wireless communication applications.

In this paper, we propose a broadband CP antenna with an average gain of 10 dBi and an overlapped bandwidth of 45% for reflection coefficient<-15 dB and AR<3 dB. A differentially-fed broadband CP antenna is also developed, which achieves an impedance bandwidth of 60% (1.53–2.83 GHz) for differential reflection coefficient<-15 dB and a 3-dB AR bandwidth of 44% (1.76–2.75 GHz) with an antenna gain of 10 dBi.

Table 1: The performances of the CP antennas

Ref.	Impedance BW	AR BW	Gain (dBi)
[1]	13.9%	8.3%	8
[2]	20.5%	11.5%	5.8
[3]	24%	24%	8
[4]	50.2%	27%	6.2
[5]	54.9%	53%	7
[6]	60%	55%	8
[7]	62.3%	61.7%	6
[8]	66.2%	41.3%	6
[9]	74.4%	70.8%	7.4
[10]	93.1%	90.9%	5
[11]	106.1%	89.7%	6
[13]	5.3%	5.3%	-
[14]	18%	17.9%	14
[15]	18%	16.7%	14.6
[16]	25.4%	22.8%	6.9
[17]	35.5%	24.69%	9.32
[18]	53.9%	35%	7.6
[19]	60.5%	31%	8
[20]	46.9%	49.5%	4.7
[21]	52%	32%	11.1

Submitted On: October 24, 2018
Accepted On: August 17, 2019

II. BROADBAND CP ANTENNA

A. Antenna configuration

The configuration of the broadband CP antenna is illustrated in Fig. 1. It consists of two folded off-centre-fed dipoles which are fed by a co-planar strip line. A T-shaped probe is used to feed the CP antenna through the co-planar strip line. The folded dipoles are printed on the back side of a dielectric substrate (Rogers 4350B, ε_r = 3.48 and thickness = 0.76 mm) while the T-shaped probe is etched on the front side of the substrate, featuring a planar configuration. A coaxial line is used to excite the antenna through the port. At the port, there is a non-metallic via through which the inner conductor of the coaxial cable is connected to the T-shaped probe. The outer conductor of the coaxial cable is soldered to the coplanar strip line.

The broadband CP antenna is placed above a metal reflector for unidirectional radiation pattern. The total height of the antenna is 33 mm, about 0.24λ_0 (λ_0 is the free-space wavelength at the center frequency 2.2 GHz).

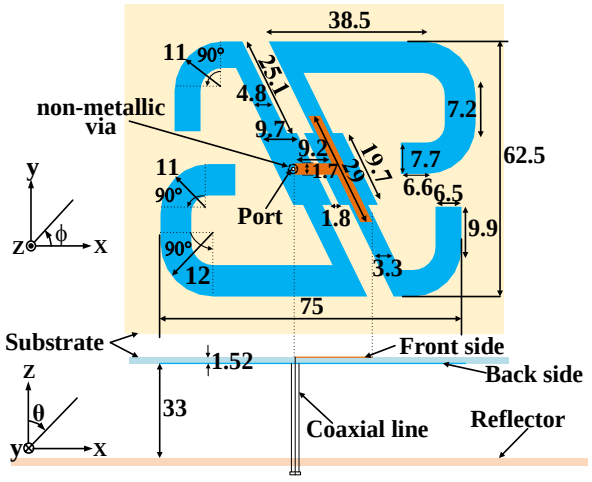

Fig. 1. Configuration of the broadband CP antenna (unit in mm).

B. Operating principle

To explain the operating principle of the broadband CP antenna, the current distributions on one of the two folded off-centre-fed dipoles at 1.8 and 2.6 GHz are plotted in Fig. 2. The magnitudes of the currents at 1.8 and 2.6 GHz have no significant difference. A 90° difference in phase is observed at both frequencies for the currents on two perpendicular sections (ABCD and DEF, AB⊥EF and CD⊥DE) of the folded dipole, which is required for circular polarization.

For dipole antennas, it is known that the distance between the antenna and the reflector plays an important role for the impedance matching and axial ratio due to effects from the image currents. For this broadband CP antenna, the antenna height also influences the antenna gain. As displayed in Fig. 3, with the increase of the antenna height, the antenna gain first gets improved then turns worse. The optimized value for the antenna height is 33 mm when a high gain of about 10.5 dBi is obtained.

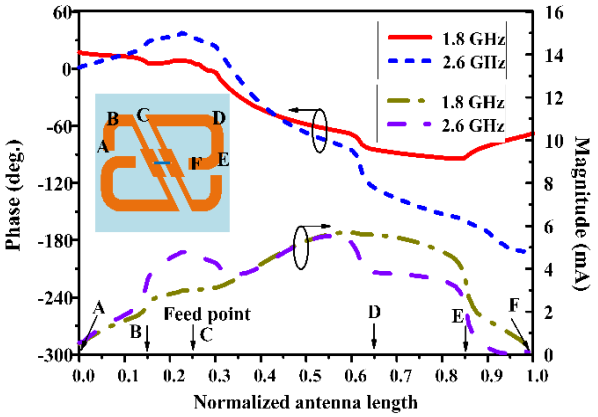

Fig. 2. Current distributions on one of the two folded off-center-fed dipoles of the broadband CP antenna.

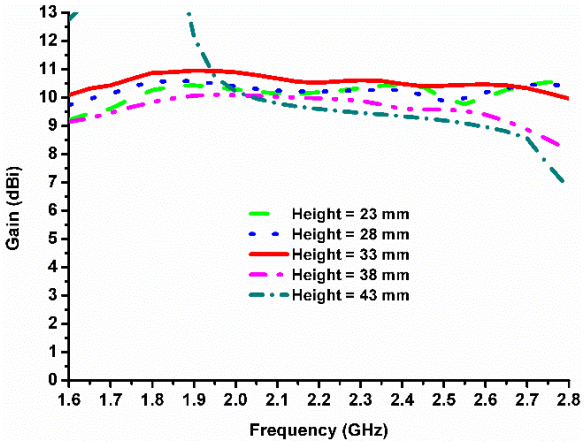

Fig. 3. Antenna gain of the CP antenna with different antenna height.

C. Results

The broadband CP antenna has been fabricated and measured. Figure 4 shows a prototype of the fabricated antenna. A semi-rigid coaxial cable is connected to the feeding port for measurement. The simulated and measured S-parameters are plotted in Fig. 5. The impedance bandwidth for refection coefficient (|S11|) <-15 dB is about 52% (1.71–2.89 GHz). The simulated and measured results for axial ratio (AR) and gain are demonstrated in Fig. 6. The bandwidth for AR<3 dB is about 45% (1.75–2.73 GHz). The averaged antenna gains are about 10 dBi. The improved gain is due to the

two-dipole configuration. The simulated and measured radiation patterns at 1.75, 2.2, and 2.7 GHz are depicted in Fig. 7. The radiation patterns are stable over the frequency range 1.75–2.7 GHz.

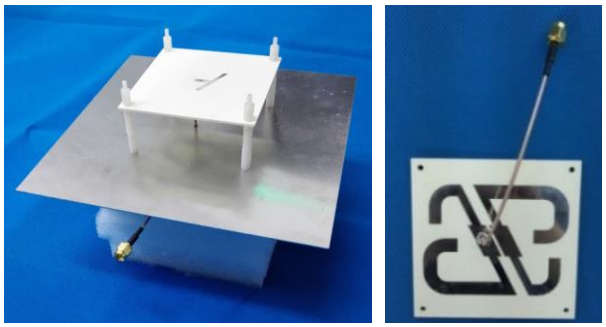

(a) (b)

Fig. 4. Prototype of the broadband CP antenna: (a) perspective view and (b) back view.

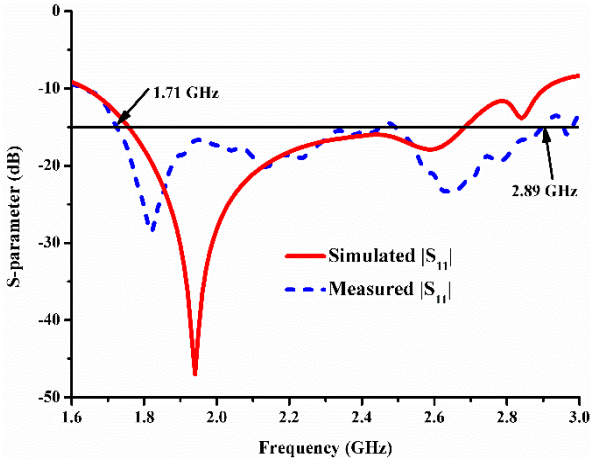

Fig. 5. S-parameters of the broadband CP antenna.

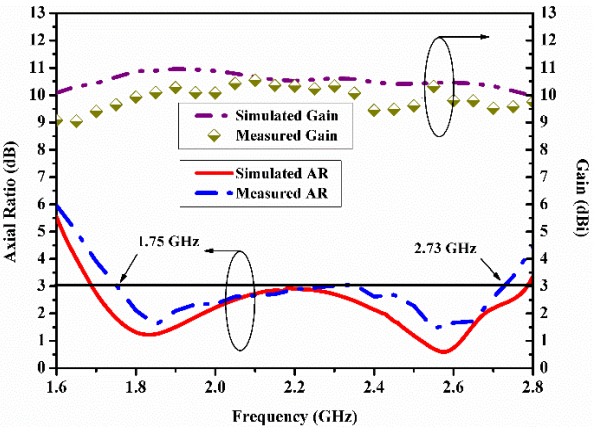

Fig. 6. Axial ratio and gain of the broadband CP antenna.

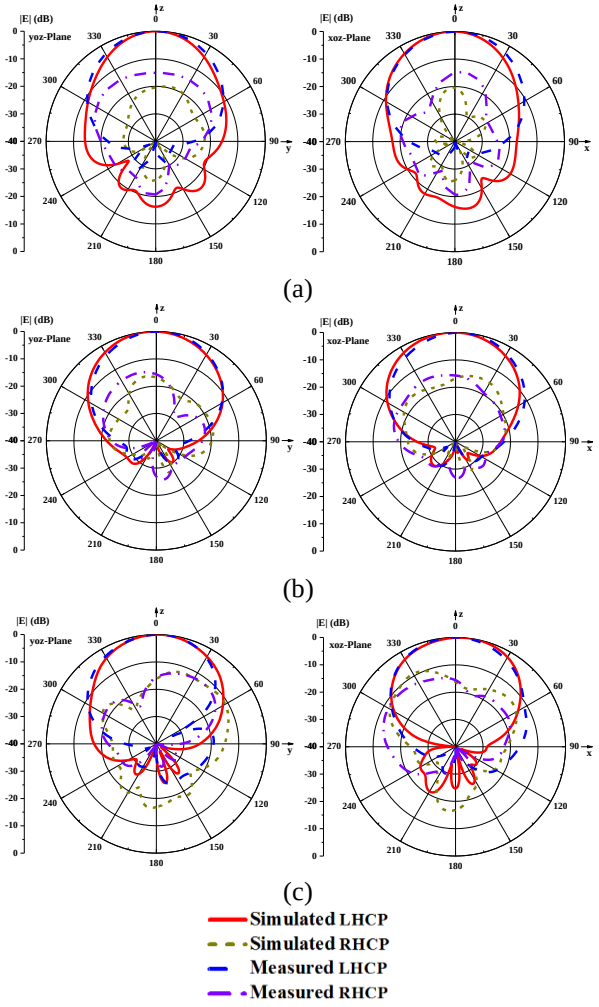

Fig. 7. Radiation patterns of the broadband CP antenna: (a) 1.75 GHz, (b). 2.2 GHz, and (c) .2.7 GHz.

III. DIFFERENTIALLY-FED CP ANTENNA

A. Antenna configuration

The configuration of the differentially-fed CP antenna is illustrated in Fig. 8. The CP antenna consists of two folded off-center-fed dipoles which are excited by a co-planar strip line. A short stub is used to bridge over the two strips of the coplanar strip line at the center of the two folded dipoles. The CP antenna is differentially fed through two coaxial cables at ports 1 and 2. The folded dipoles are printed on the back side of a dielectric substrate (Rogers 4350B, ε_r = 3.48 and thickness = 0.76 mm) while the short stub is etched on the front side of the substrate, featuring a planar configuration. The total size of the CP antenna is 74 mm × 56 mm ($0.54\lambda_0 \times 0.41\lambda_0$). The differentially fed CP antenna is placed above a flat square metal reflector with a size of 200 mm × 200 mm. The antenna height is H=33 mm ($0.24\lambda_0$). Four plastic

posts are employed to support the CP antenna.

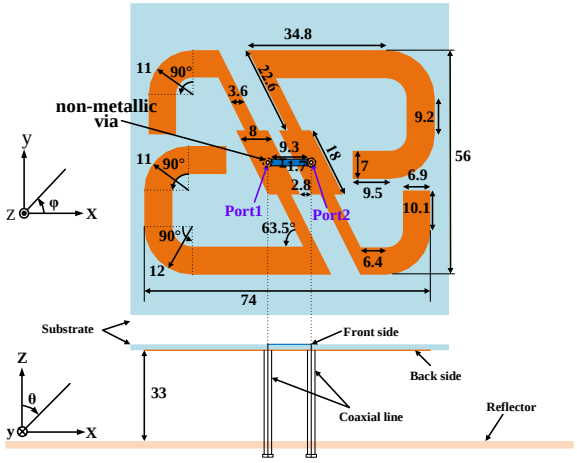

Fig. 8. Configuration of the differential-fed broadband CP antenna (unit in mm).

B. Operating principle

An equivalent circuit for impedance matching of the differentially-fed CP antenna is sketched in Fig. 9. The input impedance of each folded off-center-fed dipole is found to be Z~260 Ω. The input impedance required to match the differential feed is Z_{in}~100 Ω. Therefore, the coplanar strip line is composed of two sections: one with a characteristic impedance of Z_{01}~260 Ω matching to the folded dipole and the other with a characteristic impedance of Z_{02}~200 Ω matching to the differential feed.

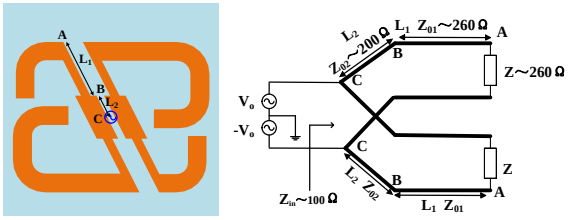

Fig. 9. Equivalent circuit for impedance matching of the differential-fed CP antenna.

The effects of the antenna height on the AR and gain is displayed in Fig. 10 and Fig. 11, respectively. The antenna height has significant influences on the AR. It can be observed that the antenna gain gets improved with the decrease of the antenna height. The optimized value is determined to be 33 mm for the trade-off between the optimized AR and antenna gain.

C. Results

The broadband differentially-fed CP antenna has been fabricated and measured. A prototype of the fabricated differentially-fed CP antenna is picture in Fig. 12. The simulated and measured differential coefficients |Sdd| are plotted in Fig. 13. The bandwidth for $|S_{dd}|$<-15 dB is about 60% (1.53–2.83 GHz). The simulated and measured for AR and gain are depicted in Fig. 14. The measured 3-dB AR bandwidth is about 44% (1.76–2.75 GHz). The averaged antenna gains are about 10 dBi. The measured radiation patterns at 1.7, 2.2, and 2.7 GHz are compared in Fig. 15; good agreement is observed.

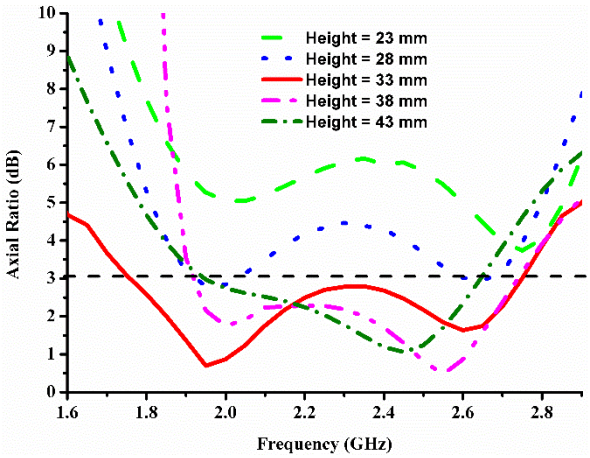

Fig. 10. Axial ratio of the differential-fed CP antenna with different antenna height.

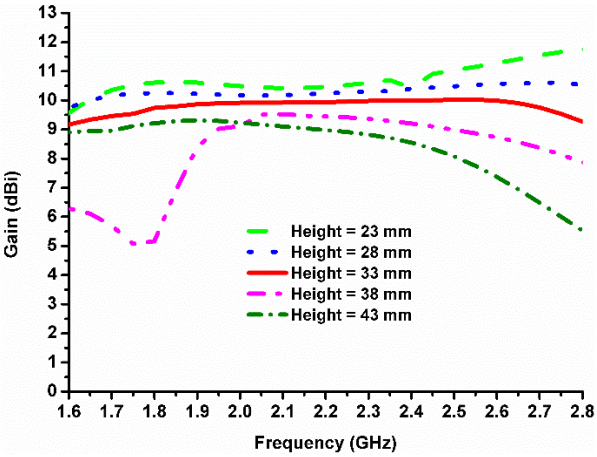

Fig. 11. Antenna gain of the differential-fed CP antenna with different antenna height.

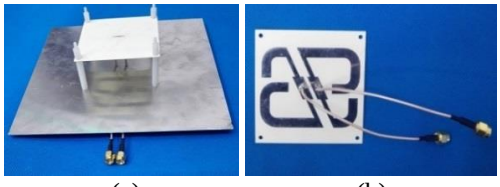

(a) (b)

Fig. 12. A prototype of the differential-fed broadband CP antenna: (a) perspective view and (b) back view.

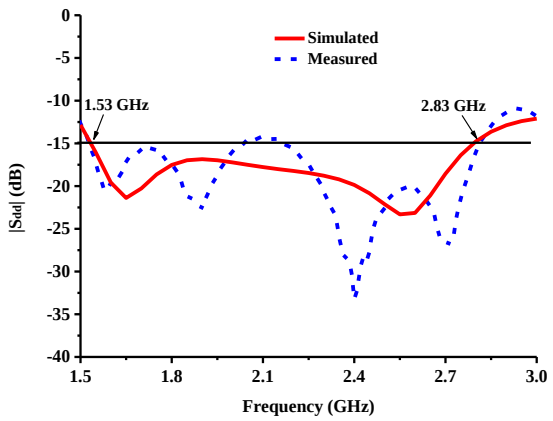

Fig. 13. Differential coefficient ($|S_{dd}|$) of the differential-fed broadband CP antenna.

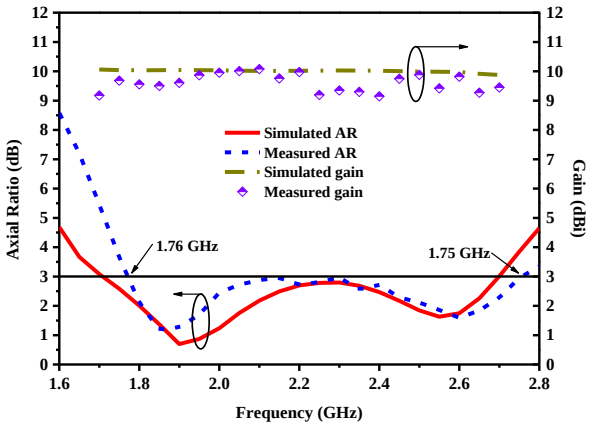

Fig. 14. Axial ratio and gain of the differentially-fed broadband CP antenna.

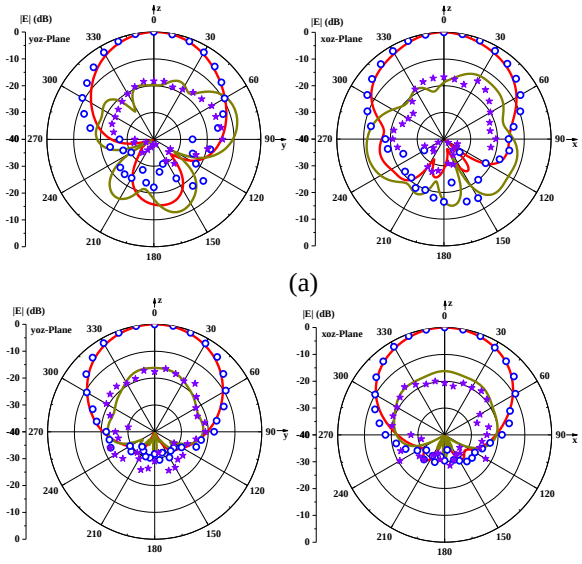

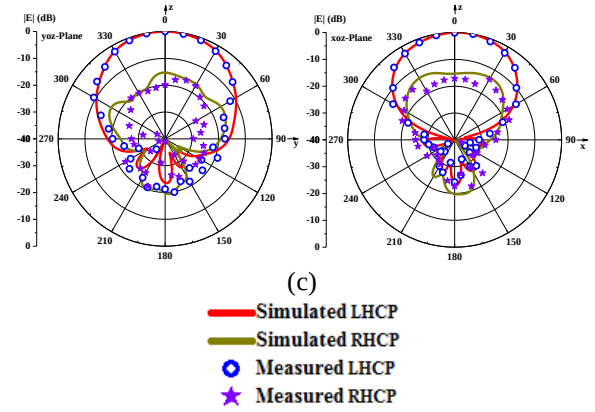

Fig. 15. Radiation patterns of the differential-fed broadband CP antenna: (a) 1.8 GHz, (b) 2.2 GHz, and (c) 2.7 GHz.

IV. CONCLUSION

A broadband CP antenna with improved gain is developed. The broadband CP antenna achieves an average antenna gain of about 10 dBi, ~2 dB higher than most existing CP antennas in literatures. The gain improved CP antenna also has better impedance matching than most CP antennas; the impedance bandwidth for reflection coefficient<-15 dB is about 52%. A differentially-fed broadband CP antenna is also developed. The impedance bandwidth achieved by the differentially-fed CP antenna is about 60% (1.53–2.83 GHz) for differential reflection coefficient<-15 dB and the 3-dB AR bandwidth obtained is 44% (1.76–2.75 GHz). The averaged antenna gain is about 10 dBi. The broadband CP antennas feature a simple planar configuration and thus may find applications in satellite/ wireless communications.

ACKNOWLEDGMENT

This work was supported in part by Guangzhou Science Technology and Innovation Commission under Grant 201804010404, the Fundamental Research Funds for the Central Universities under Grant 2018ZD08, the Chinese Scholarship Fund (201806155020), and the Guangxi Colleges and Universities Key Laboratory of Microwave and Optical Wave-applied Technology.

REFERENCES

[1] M. H. Rasekhmanesh, P. Mohammadi, and A. Piroutiniya, "A circularly polarized miniaturized patch array using combination of circle and rectangular lines in the sequential phase feed structure," *ACES Journal*, vol. 32, no. 4, pp. 339-344, Apr. 2017.

[2] V. Rafiei, H. Saygın, and S. Karamzadeh, "Circularly polarized aperture-coupled microstrip-line fed array antenna for WiMAX/C bands

applications, " *ACES Journal*, vol. 32, no. 12, pp. 1117-1120, Dec. 2017.

[3] J. Wu, Y. Yin, Z. Wang, and R. Lian, "Broadband circularly polarized patch antenna with parasitic strips," *IEEE Antennas Wirel. Propag. Lett.*, vol. 14, pp. 559-562, 2015.

[4] Y. He, W. He, and H. Wong, "A wideband circularly polarized cross-dipole antenna," *IEEE Antennas Wirel. Propag.*, vol. 13, pp. 67-70, 2014.

[5] J. M. Chen and J. S. Row, "Wideband circular polarized slotted patch antenna with a reflector," *IEEE Antennas Wirel. Propag. Lett.*, vol. 14, pp. 575-578, 2015.

[6] R. L. Li, L. J. Pan, and Y. H. Cui, "A novel broadband circularly polarized antenna based on off-center-fed dipoles," *IEEE Trans. Antennas Propag.*, vol. 63, no. 12, pp. 5296-5304, 2016.

[7] J. Zhuang, Y. Zhang, W. Hong, and Z. Hao, "A broadband circularly polarized patch antenna with improved axial ratio," *IEEE Antennas Wirel. Propag. Lett.*, vol. 14, pp. 1180-1183, 2015.

[8] R. Xu, J. Y. Li, and W. Kun, "A broadband circularly polarized crossed-dipole antenna," *IEEE Trans. Antennas Propag.*, vol. 64, no. 6, pp. 4509-4513, 2016.

[9] H. Liu, Y. Liu, and S. Gong, "Broadband microstrip-CPW fed circularly polarised slot antenna with inverted configuration for L-band applications," *IET Microw. Antennas Propag.*, vol. 11, no. 6, pp. 880-885, 2017.

[10] G. Feng, L. Chen, X. Wang, X. Xue, and X. Shi, "Broadband circularly polarized crossed bowtie dipole antenna loaded with parasitic elements," *IEEE Antennas Wirel. Propag. Lett.*, vol. 17, pp. 114-117, 2018.

[11] R. Xu, J. Y. Li, K. Wei, and G. W. Yang, "A broadband slot antenna with unidirectional circularly polarized radiation patterns," *IEEE Antennas Wirel. Propag. Lett.*, vol. 16, pp. 317-320, 2017.

[12] W. Eisenstadt, R. B. Stengel, and B. M. Thompson, *Microwave Differential Circuit Design Using Mixed-Mode S-Parameters*. Boston, MA, USA: Artech House, 2006.

[13] B. Li and X. Y. Liu, "A differentially fed implantable antenna with circularly polarization for biomedical telemetry," *IEEE International Conf. on Computational Electromagnetics (ICCEM)*, pp. 364-366, 2016.

[14] D. J. Bisharat, S. Liao, and Q. Xue, "Circularly polarized planar aperture antenna for millimeter-wave applications," *IEEE Trans. Antennas Propag.*, vol. 63, no. 1, pp. 5316-5324, 2015.

[15] D. J. Bisharat, S. Liao, and Q. Xue, "High gain and low cost differentially fed circularly polarized planar aperture antenna for broadband millimeter-wave applications," *IEEE Trans. Antennas Propag.*, vol. 64, no. 1, pp. 33-42, 2016.

[16] W. Sun, W. Yang, P. Chu, and J. Chen, "Design of a wideband circularly polarized stacked dielectric resonator antenna," *IEEE Trans. Antennas Propag.*, vol. 67, no. 1, pp. 591-595, Jan. 2019.

[17] K. Srivastava, A. Kumar, P. Chaudhary, et al., "Wideband and high-gain circularly polarised microstrip antenna design using sandwiched metasurfaces and partially reflecting surface," *IET Microw. Antennas Propag.*, vol. 13, no. 3, pp. 305-312, 2019.

[18] Q. Xue and S. Liao, "A wideband differentially driven circularly polarized antenna," *IEEE International Workshop on Electromagnetics (iWEM)*, Sapporo, Japan, pp. 269-270, 2014.

[19] Z. H. Tu, K. G. Jia, and Y. Y. Liu, "A differentially fed wideband circularly polarized antenna," *IEEE Antennas Wirel. Propag. Lett.*, vol. 17, pp. 861-864, 2018.

[20] M. Yang, Y. Pan, and W. Yang, "A singly fed wideband circularly polarized dielectric resonator antenna," *IEEE Antennas Wirel. Propag. Lett*., vol. 17, no. 8, pp. 1515-1518, Aug. 2018.

[21] W. Cao, Q. Wang, and Z. Qian, "Gain enhancement for wideband CP ME-dipole antenna by loading with spiral strip in Ku-band," *IEEE Trans. Antennas Propag.*, vol. 66, no. 2, pp. 962-966, Feb. 2018.

Effects of Array's Digital Beam Forming and Digital Polarization Synthesis Sequence on the Synthesis Results

Junrui Zhang [1], Lizhong Song [1], Qingfu Du [2], and Yao Chen [2]

[1] School of Electronics and Information Engineering
Harbin Institute of Technology, Harbin, 150001, China
ivyzhang@sdu.edu.cn, songlz@hit.edu.cn

[2] Institute of Space Sciences
Shandong University, Weihai, 264209, China
dqf@sdu.edu.cn, yaochen@sdu.edu.cn

Abstract ─ A polarized beamforming method of antenna array is addressed here. In this method, digital polarization synthesis (DPS) and digital beam forming (DBF) are processed separately in sequence. It synthesizes linearly-polarized antenna array into a circularly-polarized antenna whose main beam can scan in azimuth direction. The synthesis process and how the sequence affect the results are both expressed. It can be derived that with DPS-DBF (DPS first and DBF next), the beam is more smooth and has a better circular polarization in the main beam. This method can be used in solar radio observations and other systems that require wideband polarization measurements.

Index Terms ─ Antenna array, DBF, DPS.

I. INTRODUCTION

Polarization observation in the radio frequencies is critical to scientific studies in solar physics. Especially, circularly polarized signals are frequently used to infer the emission mechanism and the angle between the wave vector and the magnetic field. In order to meet the needs of the fine structure observation, the parabolic antenna or antenna arrays are always used to receive signals.

At meter or decameter wavelength, the parabolic is hard to construct, the antenna arrays are more commonly used. Then, due to the demand of circularly polarized observation, the polarization synthesis (PS) and beam forming (BF) are required. In some current solar radio observational systems, PS and BF are mostly implemented with analog devices (called APS and ABF), such as power combiner and phase shifter, they provide constant phase shift. Some systems uses hybrid digital and analog methods [6]. Some other systems use an identical coefficient matrix for both the PS and BF, such as the iterative least squares method [1,2,5], convex optimization [3,8], and other synthesizing methods [7,9,11]. However, according to the measuring methods [10], measurements indicate that the axial ratio of these antenna sets (the cross LPDA and the hybrid coupler) is greater than 3 dB and reaches as high as 6 dB at some frequencies. That will lead to a low accuracy of polarization measurement, especially when dealing with wideband antennas.

A DPS method has been proposed for the cross-LPDA [4]. Here the DPS method is used in an array, and is carried out with the DBF in sequence separately in FPGA. The sequence of the two processes may affect the results, so whether and how it affects will be discussed in this work.

II. THE PROPOSED METHOD

The DPS and DBF methods both starts with the radiation patterns of the antennas. In this work, a three elements dual-polarized antenna array is used, each element is a cross-LPDA, which is constructed by two LPDAs placed horizontally and vertically.

Normally, the radiation pattern of an antenna in spherical polar coordinates can be expressed as follows:

$$E\left(\theta,\varphi\right)=\begin{bmatrix}E_{\theta}e^{j\eta_{\theta}(\theta,\varphi)}\\ E_{\varphi}e^{j\eta_{\varphi}(\theta,\varphi)}\end{bmatrix}. \tag{1}$$

The upper and lower terms in the brackets represent the electric component in the θ and φ directions (vertical and horizontal). In a dual-polarized antenna system, two antennas placed horizontally and vertically are generally called E_H and E_V, respectively:

$$E_{H}\left(\theta,\varphi\right)=\begin{bmatrix}E_{HV}e^{j\eta_{HV}(\theta,\varphi)}\\ E_{HH}e^{j\eta_{HH}(\theta,\varphi)}\end{bmatrix}, \tag{2}$$

$$E_{V}\left(\theta,\varphi\right)=\begin{bmatrix}E_{VV}e^{j\eta_{VV}(\theta,\varphi)}\\ E_{VH}e^{j\eta_{VH}(\theta,\varphi)}\end{bmatrix}. \tag{3}$$

According to the direction of the antenna, the two items in the brackets indicate the co-polarization

Submitted On: December 23, 2018
Accepted On: May 5, 2019

component (subscript HH (horizontal radiation component of the horizontal antenna) and VV (vertical radiation component of the vertical antenna)) or the cross-polarization component (subscript HV (vertical radiation component of the horizontal antenna) and VH (horizontal radiation component of the vertical antenna)), respectively. The radiation pattern is mainly decided by the excitation current and the antenna itself, and can be derived through simulation or measurement.

The three element dual-polarized antenna array then can be expressed as E_{H1}, E_{V1}, E_{H2}, E_{V2}, E_{H3}, E_{V3}. The proposed method deals with the DPS and DBF separately. There will be two kinds of processes, one is carry out DPS first and DBF next (named DPS-DBF), the other one is carry out DBF first and followed by DPS (named DBF-DPS), the flowcharts are shown in Fig. 1. With DPS-DBF, the three cross-LPDA are synthesized into three circularly polarized antennas first, and then they are beam formed. With DBF-DPS, the three horizontal polarized antennas and the three vertical polarized antennas are beam formed first, and then the two linearly polarized antennas are polarization synthesized.

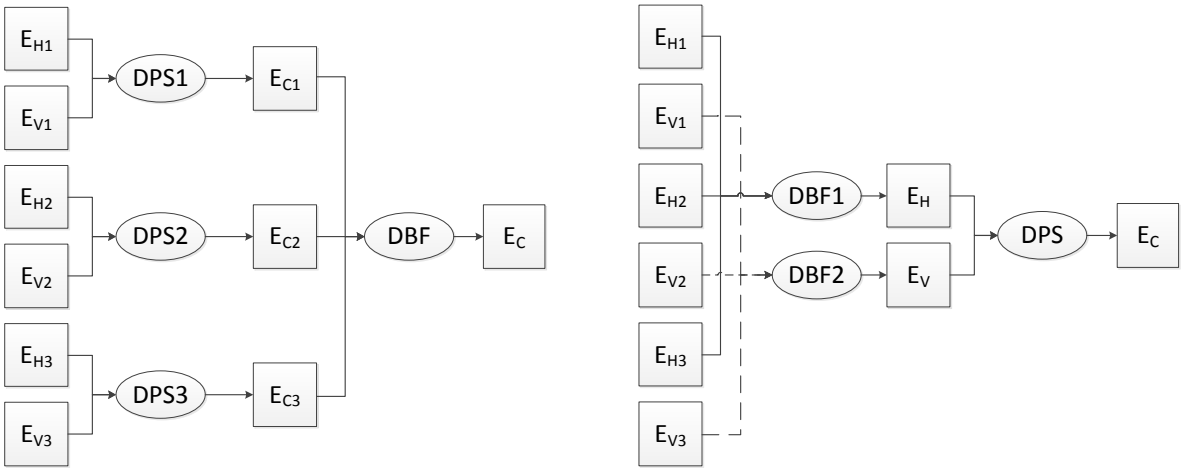

(a) DPS-DBF (b) DBF-DPS

Fig. 1. Flowcharts of the two processes.

In the DPS process, the synthesizing coefficients are deduced from the simulated or measured data, and then, the coefficients are used for synthesis.

The synthesis process aims to find a complex factor ($k = \alpha + j\beta$, where α and β are real numbers) as a weighting in the vertical channel (E_V). Instead of the constant phase shift in APS, the complex factor is deduced from simulated or measured data. Then, the two linearly polarized antenna patterns are converted into left-handed and right-handed polarized antenna patterns by the following equation, where the parameters related to circularly polarized antennas are indicated by the subscript C:

$$\begin{bmatrix} E_{HH}e^{j\eta_{HH}(\theta,\varphi)} \\ E_{HV}e^{j\eta_{HV}(\theta,\varphi)} \end{bmatrix} + (\alpha + j\beta)\begin{bmatrix} E_{VH}e^{j\eta_{VH}(\theta,\varphi)} \\ E_{VV}e^{j\eta_{VV}(\theta,\varphi)} \end{bmatrix} = \begin{bmatrix} E_{CH}e^{j\eta_{CH}} \\ E_{CV}e^{j\eta_{CV}} \end{bmatrix}. \quad (4)$$

For the left-handed circular polarization,

$$E_{CH} = E_{CV}, \quad \eta_{CV} - \eta_{CH} = \frac{\pi}{2}. \quad (5)$$

For the right-handed circular polarization,

$$E_{CH} = E_{CV}, \quad \eta_{CV} - \eta_{CH} = -\frac{\pi}{2}. \quad (6)$$

The antenna parameters (E_{HH}, η_{HH}, E_{HV}, η_{HV}, E_{VH}, η_{VH}, E_{VV} and η_{VV}) can be obtained from either simulation or measurements, and E_{CH}, E_{CV} can be derived according to the law of energy conservation, and then, α and β expressed with the antenna parameters can be calculated by equation 4.

The DBF uses typical pattern synthesis method combining to the Taylor line source synthesis method. It synthesizes antenna patterns of the same polarization. Take horizontal antenna DPS as an example, the method can be expressed by equation (7). c_1, c_2, c_3 are three complex factors. Set $c_2 = 1$, the relative phase shift and weighting coefficients are represented as c_1, c_3, which can be calculated by the frequency, the element spacing, beam pointing direction and so on:

$$E_H = c_1 \times E_{1H} + c_2 \times E_{2H} + c_3 \times E_{3H}. \quad (7)$$

III. SIMULATION OF THE ARRAY

A 30~150MHz dual-polarized cross-LPDA (log periodic antenna) array is simulated and fabricated, as shown in Fig. 2. It is consist of three 16-dipole cross-LPDA. The length of the dipole ranges from 0.54m to

4.96m, the height of LPDA is about 5.3m. The interval of the antennas is 5m, and the reflector is 15.5m long and 5.15m wide. The S-parameters are shown in Fig. 3. It can be seen that all the reflection coefficients are below -10 dB, and the isolations are all below -25 dB in the whole working band.

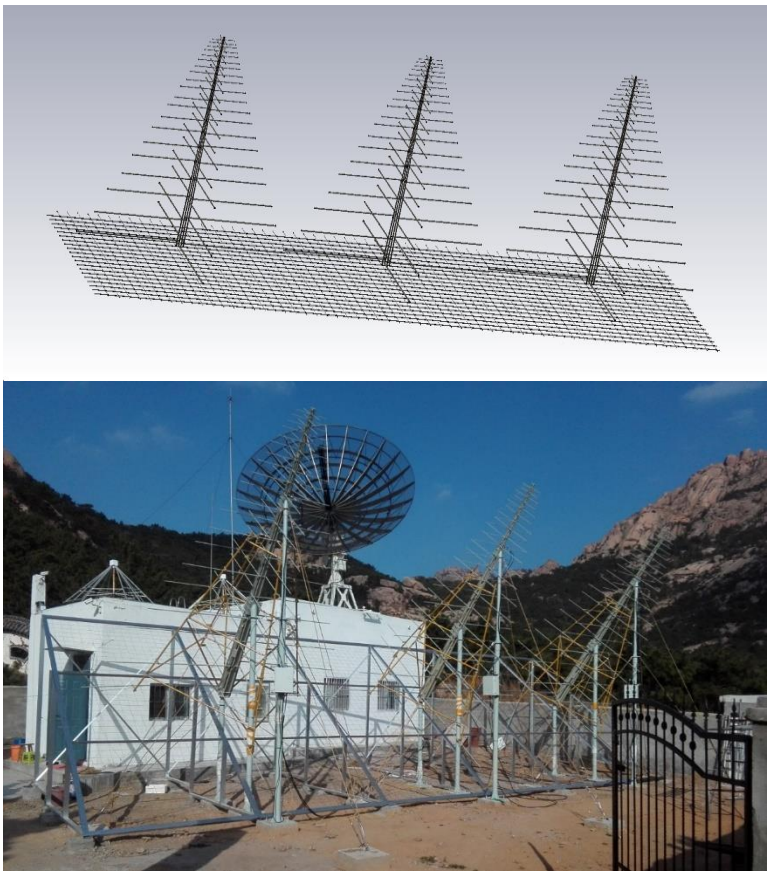

Fig. 2. The simulated model and the photo of the antenna array (three cross-LPDA with a flat reflector) installed at the Chashan solar radio station and operated by the Laboratory for Radio Technologies, Institute of Space Sciences at Shandong University.

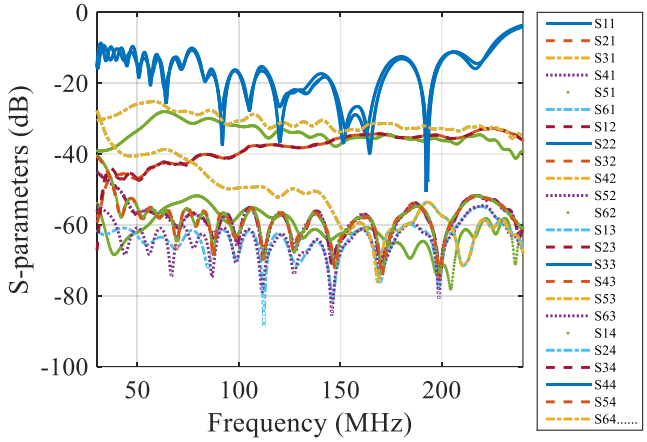

Fig. 3. S-parameters of the antenna array.

The 3dB beam width over the working frequency is shown in Fig. 4. It appears that the beam width is all above 90°. Hence, the array can scan in the range of -45°~45°. In a day, the sun passes about 15° per hour. When set 0°

points to the south (i.e., 12:00 noon), the array can be used to observe the sun from 9:00 to 15:00 every day.

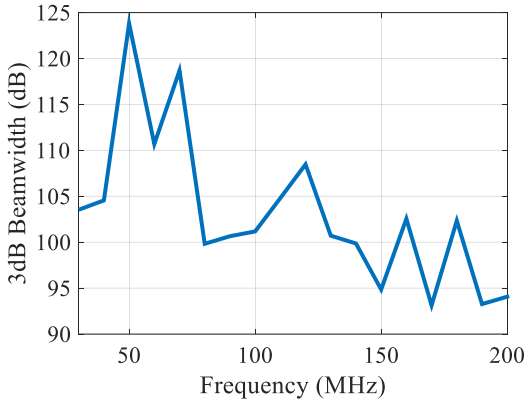

Fig. 4. 3dB beam width over frequency.

The simulated radiation patterns and the axial ratios of the three elements of the cross LPDA array are shown in Fig. 5. The results of the vertical ports are presented in Figs. 5 (a-b), and that of the horizontal ports are in (c-d). From Figs. 5 (a) and (c), it can be seen that the pattern of the three ports are almost the same, which shows good consistency. The maximum gains are both approximately 7.6 dB. From Figs. 5 (b) and (d), at the whole main beam (approximately -45°~45°), the axial ratios of the three ports are both greater than 35 dB, indicating good linear polarizations. The vertical ones have higher purity of linear polarization, the axial ratios of which are all higher than 40 dB.

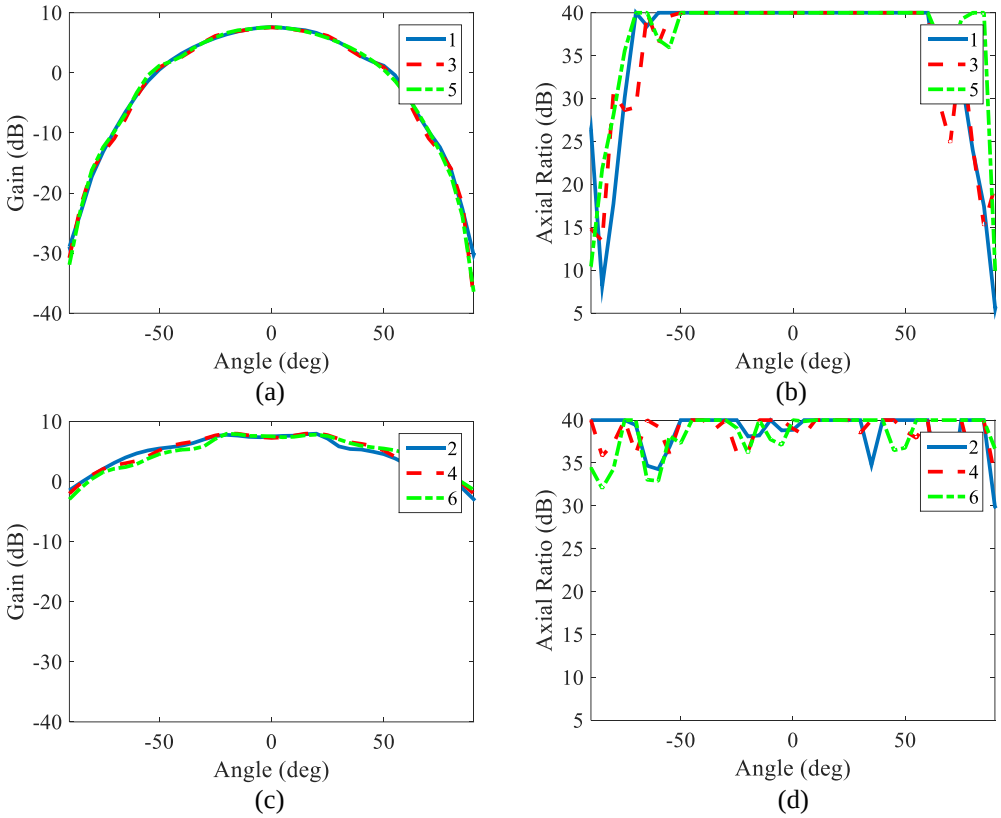

Fig. 5. The axial ratio and gain of the LPDA versus the angle (0° is the main radiation direction of the antenna) at a typical frequency of 90 MHz. Top panel: 3 vertical ports. Lower panel: 3 horizontal ports.

IV. ALGORITHM TEST AND COMPARISONS

Here we talk about the performance of the two kind of processes, DPS-DBF and DBF-DPS. The proposed method can be used in the main scan range, 0°, ±10°, ±20°, ±30°, ±40° are tested. The simulated results show accordant consequences. Here we present 0° and 10° as an example to compare the two kinds of processes.

A. Pointing to 0°

a) DPS-DBF

In this case, DPS is processed first, the three sets of cross-LPDAs are separately polarization-synthesized to circular polarization at 0°, as in Fig. 1 (a). The results are shown in Fig. 6. It shows that the axial ratio of the three sets are all 0 dB at 0°, and are lower than 3 dB in the main lobe. This indicates a good circular polarization performance. In addition, the maximum gain is 3 dB higher than the value before synthesis. This is due to the sum of energy of the two linearly polarized antennas.

Then, the three sets of synthesized circularly polarized antenna patterns are beam formed, the results are shown in Fig. 7. It can be seen that the axial ratio is still 0 dB at 0°, which shows pure circular polarization. Moreover, the axial ratio is relatively flat over the frequency. The maximum gain is about 20 dB, 3 dB bandwidth is about 10°, the gain of the first side beam is about 17 dB, which is 3 dB lower than the main beam.

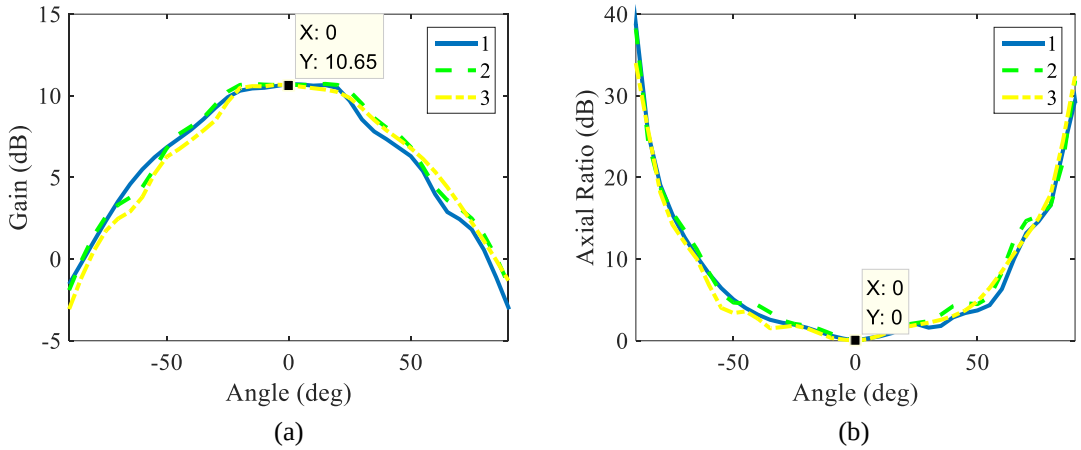

Fig. 6. The axial ratio and gain of the three sets of antenna elements after DPS at 0°.

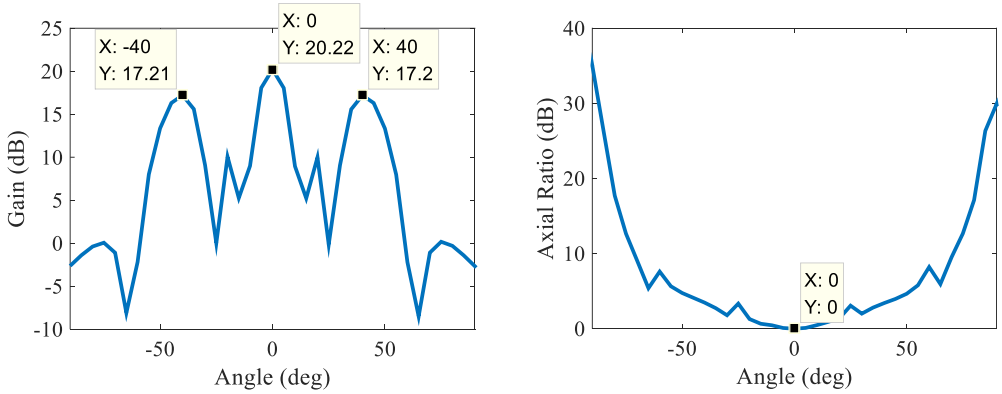

Fig. 7. The axial ratio and gain after DPS-DBF at 0°.

b) DBF-DPS

In this case, the three horizontal patterns and the three vertical patterns are first beam formed separately, as in Fig. 1 (b). The results are shown in Fig. 8. It shows that the maximum gain is still appears at 0°, but there is a sharp drop next to the main lobe, and the entire pattern is very uneven. The maximum gain of the side beams are only 1 dB lower than that of the main beam in the two cases.

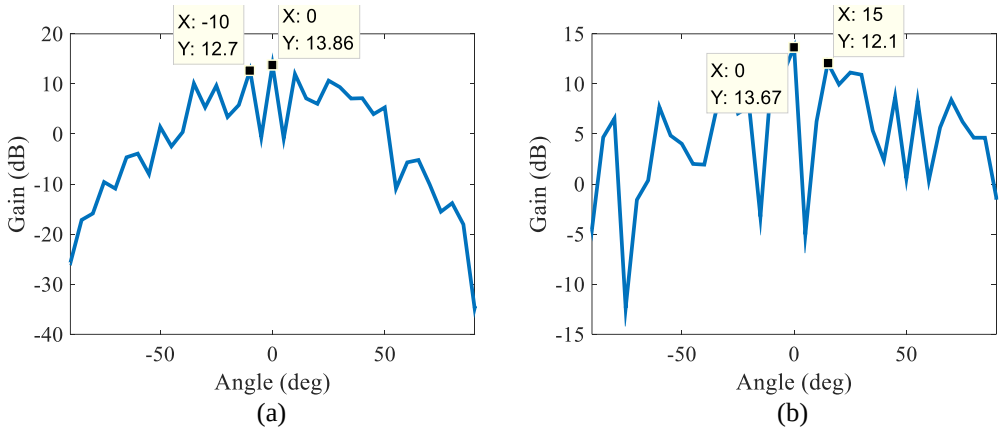

Fig. 8. Gain of the two patterns after DBF at 0°: (a) horizontal and (b) vertical.

On this basis, the two linearly polarized patterns are polarization synthesized to become a circularly polarized pattern. The axial ratio and gain are shown in Fig. 9. It can be seen that at 0°, the axial ratio is 0 dB, and the gain is 16.89 dB. The maximum gain of the side beam is 14.92, only 2 dB lower than the main beam, so further side-lobe suppression is required. In addition, the gain is not smooth and the main lobe is very narrow. Therefore, when the observation direction is slightly deviated, the observed results may have great errors.

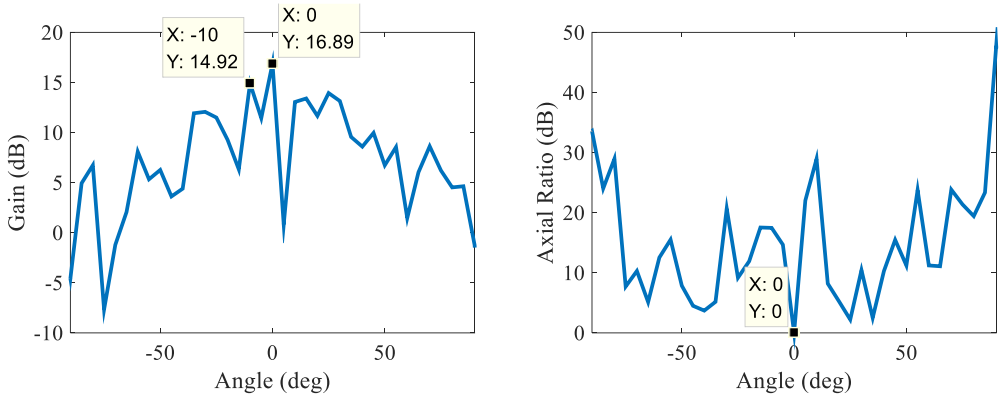

Fig. 9. The axial ratio and gain after DBF-DPS at 0°.

B. Pointing to 10°

This part talks about the scanning capability.

a) DPS-DBF

The three sets of cross-LPDA patterns are separately polarization-synthesized at 10°, as in Fig. 1 (a), and the results are shown in Fig. 10. It shows that maximum gain appears in 10°, the axial ratio of the three sets are all 0 dB at 10°, and it is lower than 3 dB in the main lobe. This indicates a good circular polarization performance.

Then, the three sets of patterns are beam formed, the results are shown in Fig. 11. It can be seen that the maximum gain is 19.87 dB, 3dB bandwidth is about 10°, the gain of the first side beam is 18.31 dB, which is 1.5 dB lower than the main beam. The axial ratio is still 0 dB at 10°, and is lower than 3 dB only in the main beam. That means the main beam is circularly polarized, and the side beam is not. Then, considering the axial ratio, when sun goes to 10°, the main beam is pointing to 10°, the side beam can receive few circularly polarized signals.

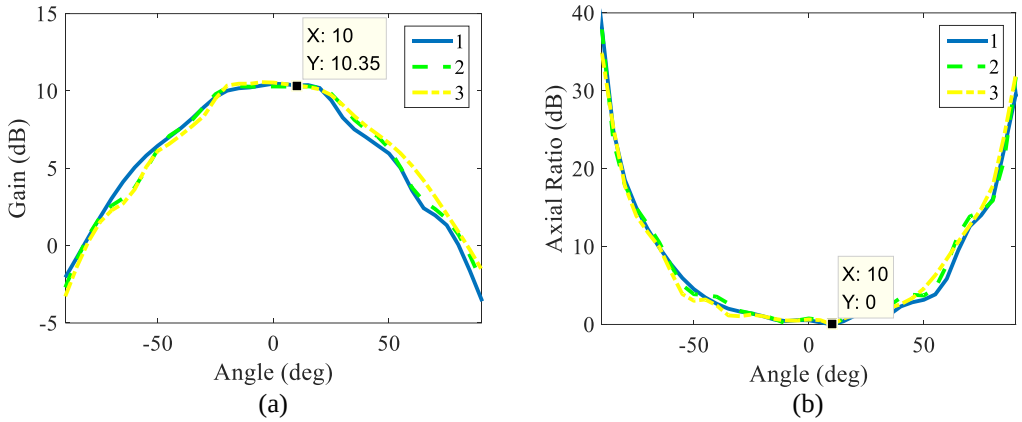

Fig. 10. The axial ratio and gain of the three synthesized antenna elements after DPS at 10°.

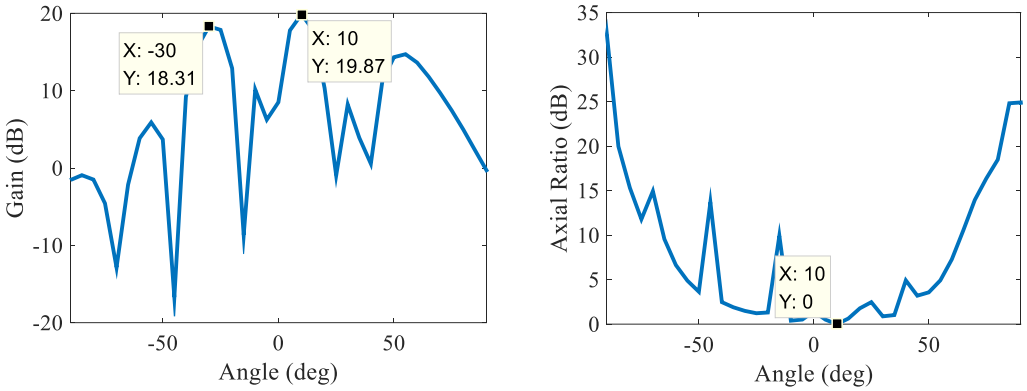

Fig. 11. The axial ratio and gain after DPS-DBF at 10°.

b) DBF-DPS

This time, the three horizontal patterns and the three vertical patterns are beam formed to 10° first, the results are shown in Fig. 12. It shows that the maximum gain is still appears at 10°, but the first side lobe is almost as high as the main lobe, and the entire pattern is very uneven.

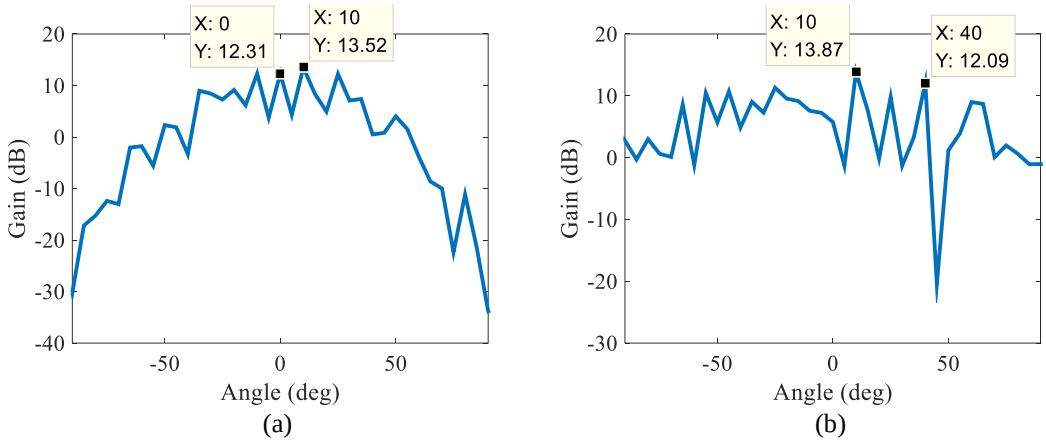

Fig. 12. Gain of the two patterns after DBF at 10°: (a) horizontal and (b) vertical.

Then, the two ports are polarization synthesized. The axial ratio and gain are shown in Fig. 13. It can be seen that at 10°, the axial ratio is 0 dB, and the gain is the largest, which is 16.6 dB. The maximum gain of the side beam is 14.14 dB, only 2 dB lower than the main beam.

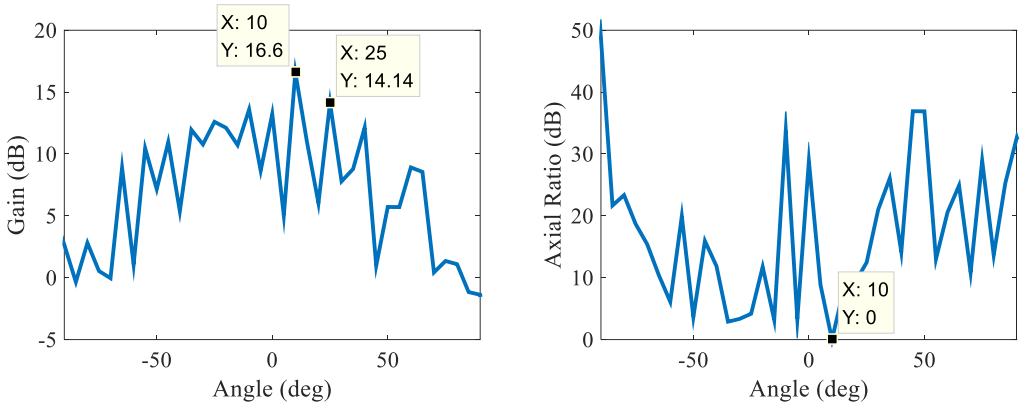

Fig. 13. The axial ratio and gain after DBF-DPS at 10°.

The results in 0° and 10° are compared in Table 1. With DPS-DBF, the total gain is larger, the axial ratio is smoother and circularly polarized in the main beam range. But with DBF-DPS, the axial ratio and gain both change greatly, so it can only be used in a very narrow range near the pointing point. In our work of solar observation, the DPS-DBF is more suitable.

Table 1: Comparison of the two processes

Pointing Direction	**0°**		**10°**	
Process	DPS-DBF	DBF-DPS	DPS-DBF	DBF-DPS
Maximum Gain (dB)	20.22	16.89	19.87	16.6
Maximum Gain of side beam (dB)	17.21	14.92	18.31	14.14

V. CONCLUSION

This paper discusses methods based on the demands of solar observation. They are used to synthesize linearly polarized antenna array into circularly polarized antenna. The results related to the sequences of DBF and DPS. It shows that with the DPS-DBF process, the synthesized antenna has a larger gain and better circular polarization at every directions.

These methods are also applicable to other fields which need polarized beam forming. When the measurement is carried out in real environments, the environmental interference and the inter-coupling between the antenna elements are also taken into account. It is easy to use when the measured errors can be neglected, and the axial ratio is reasonable. Even when the measurement is difficult to complete, we can first use the simulated data to deduce the synthesis parameters and then bring them into the system for observation and calibration.

In addition, as the DPS and DBF are working as two independent computational processes, this method can also be used to synthesize two-dimensional arrays.

ACKNOWLEDGMENT

This work is sponsored by the National Natural Science Foundation of China (Grant No. 61571154) and the Field Foundation of the Ministry of Equipment Development of the Central Military Commission of China (Grant No. 6140415010305). The study at Shandong University was supported by the National Natural Science Foundation of China (11790303 (11790300), 41774180, and U1831101), and Shandong Provincial Natural Science Foundation, China (ZR201702100072).

REFERENCES

[1] C. Dohmen, J. W. Odendaal, and J. Joubert, "Synthesis of conformal arrays with optimized polarization," *IEEE Transactions on Antennas & Propagation*, vol. 55, no. 10, pp. 2922-2925, 2007.

[2] L. I. Vaskelainen, "Iterative least-squares synthesis methods for conformal array antennas with optimized polarization and frequency properties," *IEEE Transactions on Antennas & Propagation*, vol. 45, no. 7, p. 1179, 1997.

[3] H. Lebret and S. Boyd, "Antenna array pattern synthesis via convex optimization," *IEEE Transactions on Signal Processing*, vol. 45, no. 3, p. 526, 1997.

[4] J. R. Zhang, L. Z. Song, Q. F. Du, et al., "A wideband digital polarization synthesis method," *International Journal of RF and Microwave Computer-Aided Engineering*, e21411-, 2018.

[5] B. M. Fabiani, et al., "Nonlinear constrained

beamforming algorithm for circularly-polarized phased arrays," *IEEE Antennas and Wireless Propagation Letters*, vol. 17, pp. 1692-1696, Sept. 2018.

[6] S. Foad and Y. Wei, "Hybrid digital and analog beamforming design for large-scale antenna arrays," *IEEE Journal of Selected Topics in Signal Processing*, vol. 10, no. 3, pp. 501-513, Apr. 2016.

[7] B. M. Fabiani and D. C. Nascimento, "Circularly-polarized antenna array for beam steering," *IEEE International Symposium on Antennas & Propagation IEEE*, 2016.

[8] B. Fuchs and J. J. Fuchs, "Optimal polarization synthesis of arbitrary arrays with focused power pattern," *IEEE Transactions on Antennas & Propagation*, vol. 59, no. 12, pp. 4512-4519, 2011.

[9] A. E. C. Tan and M. Y.W. Chia, "Beamforming and monopulse technique on sequentially-fed circularly-polarized ultra-wideband radar array," *International Microwave Symposium Digest, IEEE*, 2009.

[10] B. Y. Toh, R. Cahill, and V. F. Fusco, "Understanding and measuring circular polarization," *IEEE Trans. Educ.*, vol. 46, no. 3, pp. 313-318, Aug. 2003.

[11] S. Mubeen, A. M. Prasad, and A. J. Rani, "On the beam forming characteristics of linear array using nature inspired computing techniques," *ACES Journal*, vol. 33, no. 2, Feb. 2018.

Junrui Zhang was born in 1982. She received her master degree from Southeast University in 2007, and is working towards the Ph.D. degree at Harbin Institute of Technology. Her research interests include antenna design, wireless electromagnetic wave propagation, and radar signal processing.

Lizhong Song was born in 1975. He received master degree and Ph.D. degree from Harbin Institute of Technology in 2001 and 2005, respectively. He is a Professor and Doctoral Supervisor of Harbin Institute of Technology at Weihai. He focuses his academic interests on antenna design, wireless electromagnetic wave propagation, microwave technology and radar signal processing.

Qingfu Du received the master degree from Harbin Institute of Technology in 2007. He is an Assistant Professor of Shandong University (Weihai). His research interests mainly focus on sensors, high-precision instruments, industrial process automation and so on.

Yao Chen was born in 1975. He received his Ph.D. degree in Space Physics at USTC in 2004, and now is a Professor of Shandong University (Weihai). His primary research area is coronal dynamics, of particular interests are physical processes relevant to solar eruptions.

A Multiband Dual-Antenna System for MIMO Operation in Mobile Terminals

Zhirong An and Mang He

School of Information and Electronics
Beijing Institute of Technology, Beijing, 100081, China
aiyindien@163.com, hemang@bit.edu.cn

Abstract ─ A multiband dual-antenna design for multi-input-multi-output (MIMO) operation in mobile terminals is presented. The proposed dual-antenna system is composed of two symmetric antenna elements, and each of them consists of one driven branch and one parasitic branch. The dual-antenna system uses a simple decoupling structure to reduce the mutual coupling between two antenna elements. The impedance bandwidth with active $|S_{11}|\leq$-6dB covers two frequency bands of 700-960 and 1710-2690 MHz, and the isolation between the two antenna elements is better than 10dB within most of the operating bands. The envelop correlation coefficient, mean effective gain, diversity gain, and channel capacity are calculated exhaustively based on the three-dimensional radiation patterns. The results show that the antenna system has good diversity performance, which makes it suitable for MIMO operation in mobile terminals.

Index Terms ─ Decoupling structure, mobile terminal, multiband antenna, multiple-input-multiple-output operation.

I. INTRODUCTION

MIMO technology can exponentially increase the data transfer rate and spectrum efficiency without any need of increasing the transmission power and bandwidth. At present, MIMO technology has been widely used in base stations, but its application is rather limited in mobile terminals due to crowded space. For antennas in mobile terminals with long term evolution (LTE) functions, the operating bands should cover the LTE 700/2300/2500 (704-787/2300-2400/2500-2690 MHz), UMTS (1920-2170 MHz), GSM 850/900 (824-894/880-960 MHz), DCS (1710-1880 MHz), and PCS (1850-1990 MHz) bands. Meanwhile, in order to ensure that the system has good MIMO performance, high isolation is required between antenna elements. However, because of limited space in mobile terminals, it is difficult to obtain a wide operating band and high isolation simultaneously. Thus, multiband design and inter-elements decoupling are two major challenges for a good MIMO antenna system in mobile terminals.

Recently, several techniques have been proposed to design multiband dual-antenna system for mobile terminals [1]-[5]. In [1], a dual-antenna system consisting of two alphabetic-letter-shaped elements was presented for LTE wireless devices. In [2], a multiband dual-antenna system with high isolation using slotted and protruded ground was presented. A decoupled dual-antenna system with a neutralization line (NL) loaded between the antenna elements was proposed for smartphone applications in [3]. In [4], a dual-antenna system using the decoupling structure with embedded inductors and two crossed NLs was proposed for LTE/ WWAN applications. In [5], a multi-antenna system consisting of inverted-F and open-slot antennas was proposed for LTE MIMO operation. However, there are some deficiencies in previous designs, such as insufficient operating bands [1]-[3], overly complicated structures with folded branch and lumped components [3]-[5], and large sizes [5] etc. In addition, MIMO technology requires all antennas to work simultaneously, but in previous works only the performance of a single antenna was considered, i.e., only one antenna was excited while other antennas were terminated by matched loads. Thus, strictly speaking, this type of antenna system can only be used for the selection-diversity technique, because it allows one antenna to work normally at a time.

In this letter, a design of multiband dual-antenna for mobile terminals is presented. Compared with the previous work, the antenna presented in this paper has a simpler structure and is easy to fabricate under the premise of covering all the required frequency bands. The decoupling structure is theoretically analyzed and the results are in good agreement with simulation and measurement. The simulated and measured results indicate that the proposed antenna design has good MIMO performance.

II. ANTENNA DESIGN

The antenna is modeled by ANSYS HFSS, as shown in Fig. 1 (a). The antenna is placed in an air box with radiation boundary. The size of the box is 350×300×220 mm^3, and the distance between the box boundary and the antenna is quarter of the wavelengths at 700 MHz. The

Submitted On: March 4, 2019
Accepted On: April 6, 2019

antenna is printed on a FR4 substrate with ε_r=4.4 and tanδ=0.02. The size of the substrate is cut to 135×80×0.8 mm^3 to simulate actual mobile terminals of a 6.2-in screen. As in Fig. 1 (b), each antenna element is composed of a dual-line driven branch and a meander-line parasitic branch. The operating band of the longer folded-line in the driven branch covers part of the lower frequencies (800-960 MHz), and the shorter line operates at the higher frequency band (1710-2690 MHz). The parasitic meander-line provides an additional resonant frequency around 750 MHz. Each driven branch is connected to a 50-Ω coaxial line at the feeding point. Fig. 1 (d) shows the decoupling structure which is divided into two parts: the inverted L-shaped strip is designed to reduce the interference of the parasitic branch to the driven branch, and the fence-shaped strips in the middle are used to improve isolation between the two antennas elements. Compared with [4] under the same ground clearance (15mm), this layout makes full use of the limited space, which avoids folding antenna structure in the thickness direction and then reduces the profile of the antenna. Furthermore, the antenna structure is much simpler than those presented in [3]-[5] and is easy to fabricate since no additional lumped element is needed. Through detailed parametric studies, the optimum dimensions of the antenna are listed in Table 1.

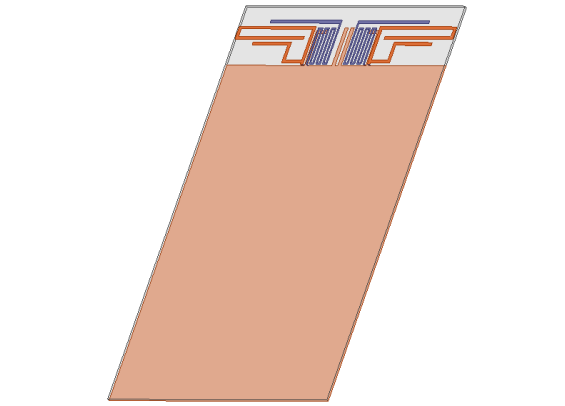

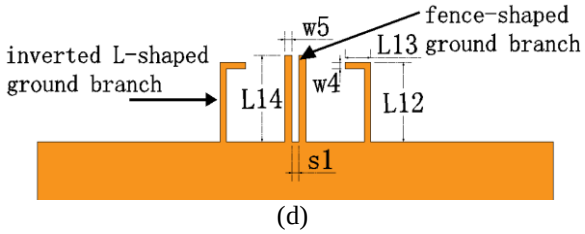

Fig. 1. The proposed dual-antenna system. (a) Simulation model, (b) two antenna elements, (c) sizes of the antenna elements, and (d) decoupling structure.

Table 1: Optimum dimensions of the antenna (Unit: mm)

Parameters	L1	L2	L3	L4	L5	L6
Values	12.9	28	4.4	24	7	6
Parameters	L7	L8	L9	L10	L11	L12
Values	13	12.5	1.7	15	26	12
Parameters	L13	L14	Ls	w1	w2	w3
Values	4	13	0.5	1	0.5	1
Parameters	w4	w5	s1			
Values	1	1.2	1			

A. Antenna structure analysis

MIMO technology requires that all antennas should work simultaneously. Therefore, active *S*-parameters of the proposed antenna are considered, and the active reflection coefficient S_{11a} of a single antenna is related to the passive *S*-parameters S_{11} and S_{12} as follows:

$$S_{11a} = \left(S_{11}a_1 + S_{12}a_2\right)/a_1 = S_{11} + S_{12}\left(a_2/a_1\right), \quad (1)$$

where, a_1 and a_2 are the normalized incident waves at the two ports if we consider the antenna system as a two-port network. The simulated $|S_{11a}|$ of the proposed antenna with and without the parasitic branch are given in Fig. 2. It is clear that the parasitic branch extends the operating bandwidth by adding a resonance at 750 MHz. The current distributions on the two branches are shown in Fig. 3, in which the currents concentrate mainly on the driven branch at 950 MHz and 2.5 GHz while the currents are strong along the parasitic branch at 750 MHz.

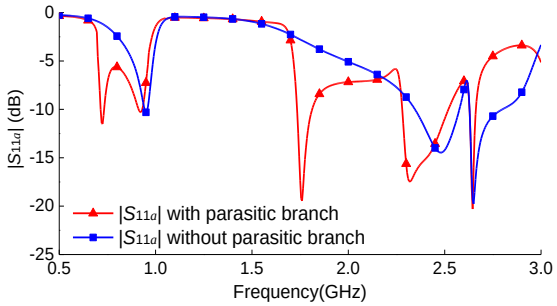

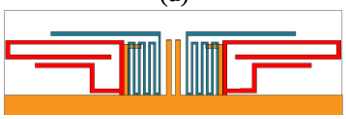

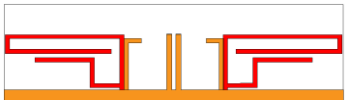

(c)

Fig. 2. The proposed antenna with/without the parasitic branch. (a) Simulated $|S_{11a}|$, (b) antenna with the parasitic meander-line branch, and (c) antenna without the parasitic branch.

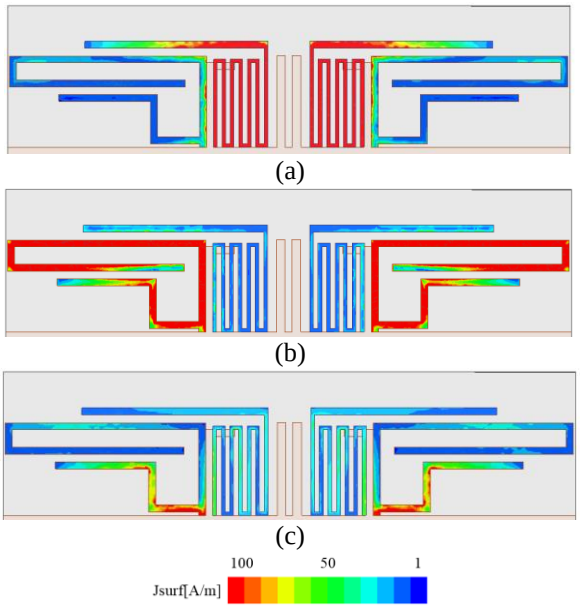

(a)

(b)

(c)

Fig. 3. Current distributions on the proposed dual-antenna system at different frequencies. (a) 750 MHz, (b) 950 MHz, and (c) 2.5 GHz.

B. Design of the decoupling structure

The inverted L-shaped strip in the decoupling structure can decrease the induced current on the parasitic branch at 2.5 GHz as shown in Fig. 4, which improves the impedance matching at higher frequency band as well.

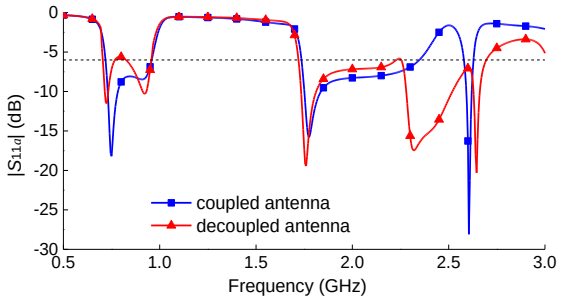

(a)

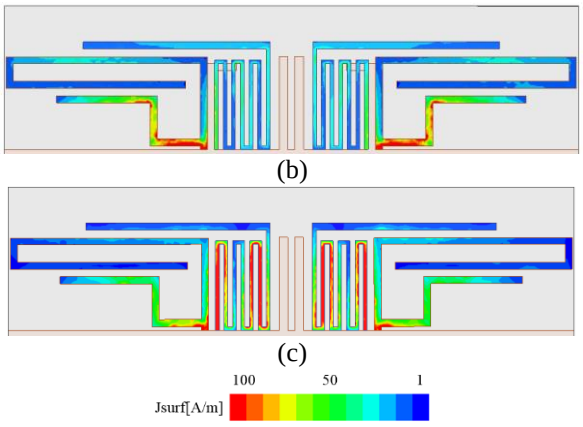

(b)

(c)

Fig. 4. $|S_{11a}|$ and current distributions of the proposed antenna. (a) Simulated $|S_{11a}|$, (b) current distributions on the antenna with the L-shaped strips, and (c) current distributions on the antenna without the L-shaped strips.

The fence-shaped strips in the middle consists of two protruded stubs which are equivalent to two grounded inductors L, and the gap between the two stubs and the gap between the stub and the parasitic branch can be seen as shunt capacitors C and C_0, respectively. Figure 5 presents the equivalent circuit of the structure between the two feeding ports of the antennas.

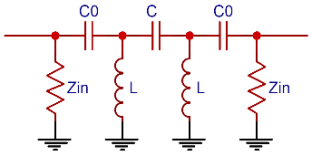

Fig. 5. Equivalent circuit of the fence-shaped strips between two antenna elements.

The corresponding T-matrix can be calculated by cascading the T-matrices of single components:

$$T = T_{Y_{in}} \cdot T_{C_0} \cdot T_L \cdot T_C \cdot T_L \cdot T_{C_0} \cdot T_{Y_{in}}, \tag{2}$$

where, Y_{in} is the admittance of a single antenna, and the involved T-matrices are:

$$\begin{aligned} T_{Y_{in}} &= \begin{bmatrix} 1+Y_{in}/2 & Y_{in}/2 \\ -Y_{in}/2 & 1-Y_{in}/2 \end{bmatrix}, \\ T_{C_0} &= \begin{bmatrix} 1+1/j2\omega C_0 & -1/j2\omega C_0 \\ 1/j2\omega C_0 & 1-1/j2\omega C_0 \end{bmatrix}, \\ T_L &= \begin{bmatrix} 1+1/j2\omega L & 1/j2\omega L \\ -1/j2\omega L & 1-1/j2\omega L \end{bmatrix}, \\ T_C &= \begin{bmatrix} 1+1/j2\omega C & -1/j2\omega C \\ 1/j2\omega C & 1-1/j2\omega C \end{bmatrix}, \end{aligned} \tag{3}$$

in which C_0, C, and L can be calculated by referring to [6]. Then, T_{11} is obtained as:

$$T_{11}=\frac{-\left(\omega C_0-jY_{in}+j\omega^2C_0L+j\omega^2C_0LY_{in}-j\right)\cdot A}{2\omega^5CC_0^2L^2}\ , \quad (4)$$

and

$$A=2\omega^2CL-j\omega C_0-Y_{in}+\omega^2C_0L+2j\omega^3C_0CL +2CL\omega^2Y_{in}+\omega^2C_0LY_{in}-1. \quad (5)$$

The mutual coupling between the two antennas' feeding ports is:

$$S_{21}=1/T_{11}\ . \quad (6)$$

In Fig. 6, it is seen that the fence-shaped strips can effectively reduce the mutual coupling between the antenna elements. In addition, the theoretical curve predicted by equations (2)-(6) is in good agreement with the simulated and measured $|S_{21}|$, which validates the correctness of the theoretical analysis. At the same time, the measured results show that the decoupling structure can achieve 10dB isolation between antennas, which meets the basic requirements of MIMO antenna decoupling. Compared with [2], the proposed decoupling structure is of compact size and is totally arranged within the antenna structure, so any extra space is not needed.

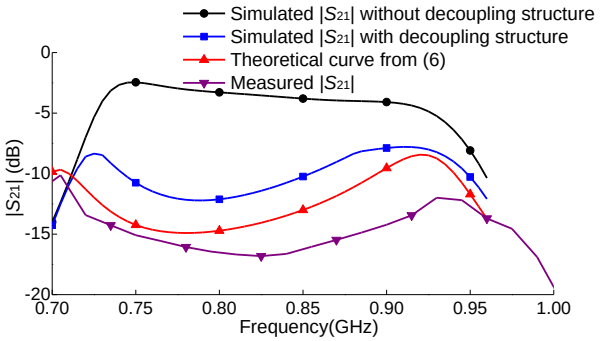

Fig. 6. Theoretical, simulated, and measured $|S_{21}|$ of the proposed antenna.

III. RESULTS AND DISCUSSION

The antenna is fabricated and measured, and the fabricated prototype is shown in Fig. 7. The simulated $|S_{11a}|$ using ANSYS HFSS is given in Fig. 8, which agrees well with the measured data. The measured impedance bandwidth with $|S_{11a}|\leqslant$-6dB is over 700-960 and 1710-2690 MHz, covering all the LTE700/2300/2500, UMTS, GSM850/900, DCS, and PCS bands. As well, the isolation between the two antenna elements is better than 10dB within most of the operating bands.

Figure 9 plots the simulated and measured radiation patterns in three principal planes at two typical operating frequencies in the LTE700/2500 bands. The measured peak gain of the proposed antenna is shown in Fig. 10, which ranges from -1.41 to 1.92 dBi at the lower frequency band and from -0.19 to 5.79 dBi at the higher frequency band. Figure 11 shows the simulation and measured results of radiation pattern null value. The total efficiency of the proposed antenna system is presented in Fig. 12. The total efficiency ranges from 50% to 74.2% at the lower band and from 43.4% to 78.5% at the higher band. Table 2 shows the performance comparison of the proposed antenna with those in existing literature. It is seen that the bandwidth of the proposed antenna covers all the LTE700/2300/2500, UMTS, GSM850/900, DCS, and PCS bands as compared with those in [1]-[3], and the thickness of the design is much smaller than that of the antennas presented in [3]-[5].

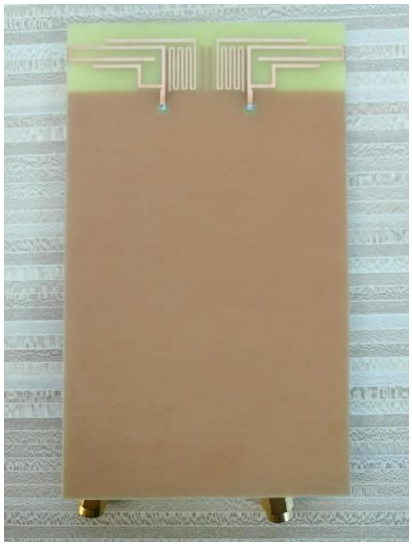

Fig. 7. Fabricated prototype sample.

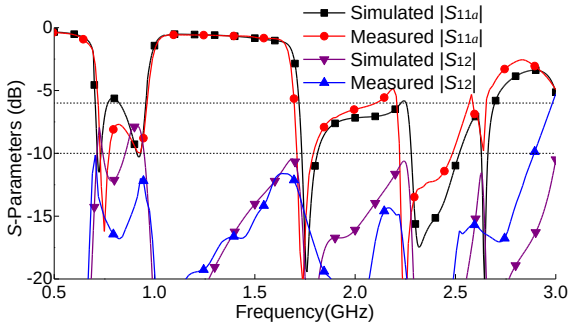

Fig. 8. Simulated and measured *S*-parameters of the proposed antenna.

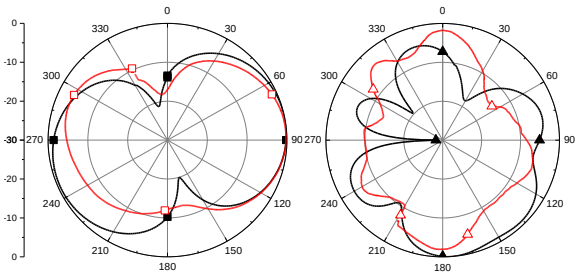

xoy-plane

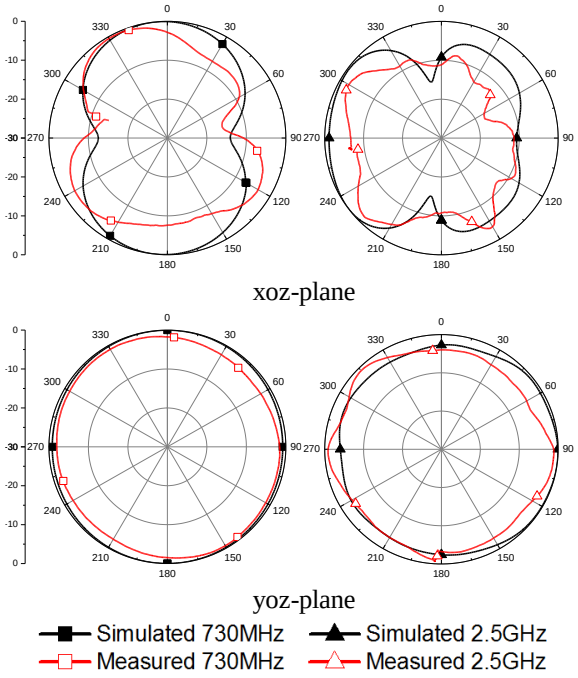

Fig. 9. Simulated and measured radiation patterns.

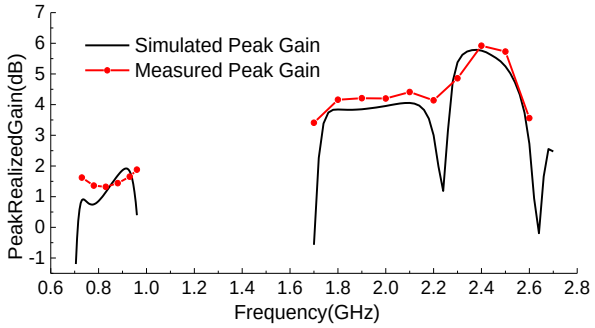

Fig. 10. Peak gain of the proposed antenna.

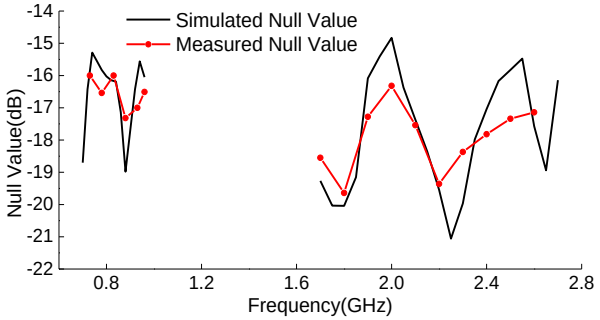

Fig. 11. Null value of the proposed dual-antenna system.

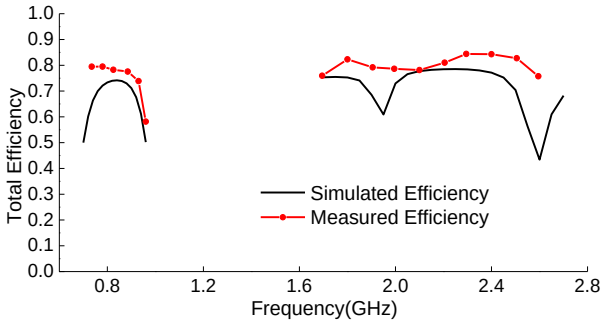

Fig. 12. Total efficiency of the proposed dual-antenna system.

Table 2: Comparison of the proposed antenna with previous works

	Operating Bands (MHz)	Dimension (mm)	Gain (dBi)	Isolation (dB)	Efficiency
Proposed	700-960, 1710-2690	15×80×0.8	-1.41-5.79	10	43.4-78.5
[1]	700-800, 1700-3800	24×70×0.8	1-5	5-15	-
[2]	740-965, 1380-2703	29×60×0.8[a]	0.764-4.505	10	40-67.2
[3]	823-968, 1697-2706	10×70×5	-0.5-3.7	10	40-60
[4]	702-968, 1698-2216, 2264-3000	15×80×5	-1.79-3.75	10	31.86-61.73
[5]	698-960, 1710-2690	8×78×7	-	10	45-83

[a]The area occupied by the slotted ground is calculated.

In order to investigate the diversity performance of the proposed antenna system, some critical parameters [7]-[10] are calculated:

$$\rho_e = \frac{\left|\iint_{4\pi}\left[\vec{F}_1(\theta,\phi)\bullet\vec{F}_2(\theta,\phi)\right]d\Omega\right|^2}{\iint_{4\pi}\left|\vec{F}_1(\theta,\phi)\right|^2 d\Omega \iint_{4\pi}\left|\vec{F}_2(\theta,\phi)\right|^2 d\Omega}, \tag{7}$$

$$\text{MEG}=\int_0^{2\pi}\int_0^{\pi}\left(\frac{\text{XPR}}{1+\text{XPR}}G_\theta(\theta,\phi)P_\theta(\theta,\phi) + \frac{1}{1+\text{XPR}}G_\phi(\theta,\phi)P_\phi(\theta,\phi)\right)\sin\theta d\theta d\phi, \tag{8}$$

$$\text{DG} = \left[\frac{\gamma_C}{\Gamma_C}-\frac{\gamma_1}{\Gamma_1}\right]_{P(\gamma_C<\gamma_S/\Gamma)}, \tag{9}$$

$$C = E\left\{\log_2\left[\det\left(I+\frac{SNR}{n_T}HH^H\right)\right]\right\}, \tag{10}$$

and the results are given in Fig. 13. It is observed that the envelope correlation coefficient (ECC) is less than

0.16 within the entire frequency bands, and comparable average received power (|MEG1/MEG2| <3dB) and high diversity gain (DG > 9.6 dB) at 1% of the cumulative distributed functions are obtained. Figure 14 provides the channel capacity of the proposed antenna design. It is seen that the channel capacity is more than 9.5 bps/Hz with 20dB SNR, which is much improved compared with the SISO antenna.

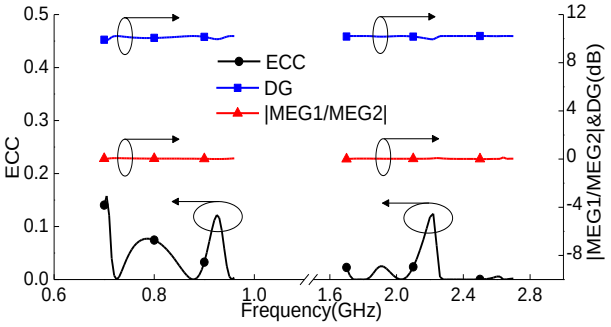

Fig. 13. Diversity performance of the proposed antenna.

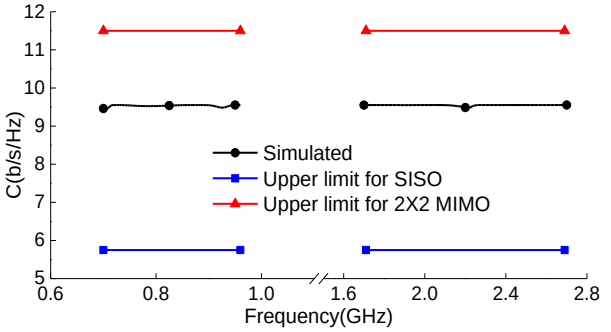

Fig. 14. Simulated channel capacity of the proposed antenna.

IV. CONCLUSION

In this letter, a multiband dual-antenna design for MIMO operation in mobile terminals is presented. The measured impedance bandwidth with $|S_{11a}|\leqslant$-6dB is over 700-960 and 1710-2690 MHz, covering all the LTE700/2300/2500, UMTS, GSM850/900, DCS, and PCS bands. The isolation between the two antenna elements is better than 10dB within most of the operating bands. The simulated and measured results show that the proposed antenna design has good diversity performance and high channel capacity, which makes it suitable for MIMO operation in mobile terminals.

REFERENCES

[1] F. Ahmed, M. H. M. Chowdhury, and A. M. A. Rahman, "A multiband MIMO antenna for future generation handset applications," *2017 International Conference on Electrical, Computer and Communication Engineering (ECCE)*, Cox's Bazar, pp. 91-94, 2017.

[2] J. Dong, X. Yu, and L. Deng, "A decoupled multiband dual-antenna system for WWAN/LTE smartphone applications," *IEEE Antennas and Wireless Propagation Letters*, vol. 16, pp. 1528-1532, 2017.

[3] Y. L. Ban, C. Li, C. Y. D. Sim, G. Wu, and K. L. Wong, "4G/5G multiple antennas for future multimode smartphone applications," in *IEEE Access*, vol. 4, pp. 2981-2988, 2016.

[4] S. Wang and Z. Du, "Decoupled dual-antenna system using crossed neutralization lines for LTE/WWAN smartphone applications," in *IEEE Antennas and Wireless Propagation Letters*, vol. 14, pp. 523-526, 2015.

[5] I. R. R. Barani and K. Wong, "Integrated inverted-F and open-slot antennas in the metal-framed smartphone for 2×2 LTE LB and 4×4 LTE M/HB MIMO operations," in *IEEE Transactions on Antennas and Propagation*, vol. 66, no. 10, pp. 5004-5012, Oct. 2018.

[6] K. Sarabandi and N. Behdad, "A frequency selective surface with miniaturized elements," in *IEEE Transactions on Antennas and Propagation*, vol. 55, no. 5, pp. 1239-1245, May 2007.

[7] S. Blanch, J. Romeu, and I. Corbella, "Exact representation of antenna system diversity performance from input parameter description," in *Electronics Letters*, vol. 39, no. 9, pp. 705-707, 1 May 2003.

[8] Y. Li, B. Yu, H. Shen, L. Zhu, and G. Yang, "An 8-port planar UWB MIMO antenna for future 5G micro wireless access point applications," *2017 International Applied Computational Electromagnetics Society Symposium (ACES)*, Suzhou, pp. 1-2, 2017.

[9] T. Taga, "Analysis for mean effective gain of mobile antennas in land mobile radio environments," in *IEEE Transactions on Vehicular Technology*, vol. 39, no. 2, pp. 117-131, May 1990.

[10] A. Diallo, C. Luxey, P. Le Thuc, R. Staraj, and G. Kossiavas, "Diversity performance of multi-antenna systems for UMTS cellular phones in different propagation environments," *International Journal of Antennas & Propagation*, vol. 2008 (1687-5869), pp. 264-276, 2008.

Design of Pin Loaded Reconfigurable Patch Antenna for Wireless Communications

Manavalan Saravanan [1] and Madihally J. S. Rangachar [2]

[1] Department of Electronics and Communication Engineering
Hindustan Institute of Technology and Science, Chennai, Tamil nadu 603103, India
msarawins@ieee.org

[2] Department of Electronics and Communication Engineering
Hindustan Institute of Technology and Science, Chennai, Tamil Nadu 603103, India
mjsranga@gmail.com

Abstract ─ The design and performance analysis of a single fed reconfigurable patch antenna for circular polarization is presented. The patch has a square shaped slot etched on it. Four ultra-miniature diode switches are placed at appropriate positions to bridge the gap in the slot regions and are used to switch the nature of polarization between left-hand circular polarization (LHCP) and right-hand circular polarization (RHCP). The antenna achieves an impedance bandwidth (S11 ≤ -10dB) between 2.34 GHz to 2.4 GHz (2.53%) with a center operating frequency of 2.37 GHz. The surface current distributions on the radiating patch along with its corresponding radiation patterns measured at the operating frequency are plotted. The antenna achieves an axial ratio beam width (AR ≤ 3dB) of -25° to 50° for left-hand circular polarization and -40° to 45° for right-hand circular polarization. Measured radiation pattern results show the antenna has a good cross-polarization isolation of -16.2 dB for RHCP configuration and -16.54 dB for LHCP configurations and hence the antenna is suitable for modern wireless applications.

Index Terms ─ Antenna feeds, antenna radiation patterns, circular polarization, microstrip antennas, slot antennas.

I. INTRODUCTION

Antennas capable of receiving at diverse polarizations are widely used in satellite communication, radars [1-2]. The requirement for multifunctional antennas has increased recently in wireless communication and hence reconfigurable antennas are gaining much attention due to their ability to configure their state of polarization without a change in physical dimension of the antenna [3]. To achieve polarization reconfiguration, RF PIN diodes, MEMS switches, reed switches, variable capacitors and also photoconductive switches are used. The selection of switches depends on circuit complexity including biasing network and power consumption. In general, reconfigurable antenna are designed by means of reconfigurable feed network or by reconfiguring radiating structure. Lin and Wong [4] presented reconfigurable antenna by biasing the pin diodes sequentially. Dual-Polarized Antenna Based on Metal Ring is presented by Lizhong Song and Sai Li [5]. Lin, Wei, and Hang Wong [6] demonstrated a reconfigurable antenna by exciting radiating element by means of cross aperture having controlled RF switches.

Most of the conventional reconfigurable antennas utilizes a slot etched on the radiating element and reconfiguring it by means of pin diodes [7], RF switches or varactor diodes. Bharathi, Lakshminarayana, and Somasekhar [8] presented a reconfigurable antenna which comprises of a square slot etched on radiating element embedded with pin diodes for reconfiguring the structure of the radiating element. A reconfigurable monopole antenna integrated with mushroom-like meta-surface to improve antenna performance is presented by Cao, Cheung, and Yuk [9]. Another common method of realizing circular polarization is by truncating the corners of square patch antenna. Bharathi, Lakshminarayana, and Somasekhar [10] uses four PIN diodes on reconfigurable truncated corners which are used to connect the truncated patch with its radiating element for polarization reconfiguration. Row and Shih [11] found the use of variable capacitors for tuning resonant frequencies and also utilizes several diodes along with DC bias network for changing polarization states which increases the complexity of the feed system. Polarization reconfiguration can also be achieved by reconfiguring feed network by means of pin diodes Lin, Wong, and Ziolkowski [12]. An annular slot microstrip antenna with reduced number of switching elements is analysed in Saravanan and Rangachar [13] where polarization reconfiguration is achieved by switching the diodes in the feed network. The effect of quadrature hybrid

Submitted On: February 20, 2019
Accepted On: April 6, 2019

network is used for achieving reconfigurable circular polarization Elhefnawy, Ismail, and Mandeep [14]. Varactor diodes are used recently to reconfigure the characteristics of the antenna Liang, Sanz-Izquierdo, Parker, and Batchelor [15]. By varying the bias voltage, the capacitance of the varactor diode is changed and thereby tuning the performance of the antenna. The polarization reconfiguration antenna by means of varactor diodes as presented in Babakhani and Sharma [16]. The model utilizes four varactor diodes to bridge the inner circular patch with outer concentric ring patch. The antenna is excited by means of two ports having 900 phase difference with each other which requires a separate feed network for feeding. Beno and Emmanuel [17] designed reconfigurable antenna by mechanical tuning of slot width along with rotation of strips on radiating patch. Lu, et al., [18] achieved polarization diversity by generating ±90 deg phase difference to signal going to patch element. Hucheng Sun and Sheng Sun [19] demonstrated reconfigurable antenna by inducing phase delay in the output ports by means of reconfigurable feed network. In recent times, fluid dielectrics are used for polarization reconfiguration due to its ability of linear control over polarization [20-21]. However, integration of these antenna model with other RF devices is difficult due to its requirement of separate fluid tank space.

The proposed antenna is a rectangular patch with a square shaped slot etched at its center operating at 2.37 GHz band. The antenna uses four ultra-miniature pin diodes for polarization diversity. Two bias lines are used to excite diodes for changing the shape of the radiating element and thereby achieving polarization diversity. A parametric analysis is carried out to study the effect of slot dimension over performance sensitivity of the antenna. The antenna is fabricated and its impedance and radiation characteristics are measured using antenna test systems and the obtained results are compared with simulation results. The simulation results agree with measured results and hence it is suited for modern wireless applications.

II. ANTENNA DESIGN

A. Antenna geometry

The antenna is designed on roger substrate (RO4350) having a size of 47 mm x 47 mm x 1.52 mm and having a relative permittivity ε_r of 3.66 and a loss tangent δ of 0.004. Figure 1 shows a rectangular patch having a dimension of 31.3 mm x 31.3 mm printed on roger substrate (RO4350) and a square shape slot is etched at its centre. The length and the width of the slot are obtained through parametric analysis of antenna performances over its dimensions. A 50Ω SMA coaxial connector is used to feed the antenna model whose characteristic impedance Z_0 is given below:

$$Z_0 = \frac{\eta_0}{2\pi\sqrt{\varepsilon_r}} ln\left(\frac{D}{d}\right) \Omega. \quad (1)$$

For an antenna to radiate effectively the antenna must be purely reactive and the reactive component in the impedance must be equal to zero at operating frequency. This is achieved by properly matching Z_0 and Z_{in}. A quarter wave transformer is used to match the impedance between radiating patch and the coaxial fed.

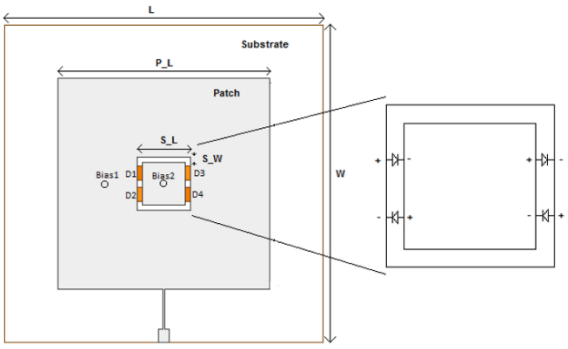

Fig. 1. Antenna geometry.

NXP BAP50-03, 50mA, 50V 2-pin diodes are used for polarization reconfiguration. The diodes operate at 0 to 12 GHz operating band with a minimum biasing voltage of 0.7V and hence best suited for reconfiguration. Four such ultra-miniature pin diodes are used for polarization diversity. The equivalent pin diode model is shown in Fig. 2. The diode has a minimum series resistance of 5Ω and inductance of 9nH under forward bias condition and maximum resistance of 50MΩ and capacitance of 0.35pf under reverse bias condition [22].

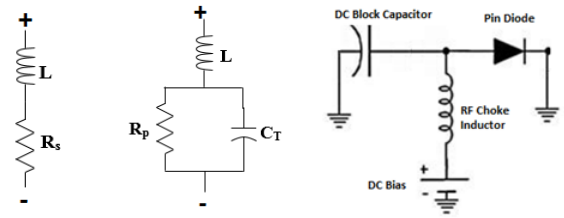

Forward Bias | Reverse Bias | DC Bias circuit

Fig. 2. Equivalent pin diode model and DC bias circuit.

The DC bias circuit comprises of RF choke inductor (TDK MLG0603Q Series Inductor, 22nH) to provide a DC bias path to the pin diode and also block the RF signal and a blocking Capacitor (AVX 0402 Series Ceramic Capacitors, 10pf) to avoid DC bias from reaching RF output.

B. Principle of operation

The antenna model comprises of square slot etched on the radiating patch. Four pin diodes are appropriately placed to bridge the gap in the slot region. The antenna generates either left hand polarization (LHCP) or right-hand polarization (RHCP) based on biasing potential given to excite the pin diodes. Table 1 gives the different operating states of the proposed antenna.

Table 1: Operating states

Bias 1	Bias 2	ON State	OFF State	Operating State
+3V	0 V	D1 and D4	D2 and D3	LHCP
0 V	+3V	D2 and D3	D1 and D4	RHCP

When a bias 1 terminal is excited with positive potential (+3 V), diodes D1 and D4 are forward biased (ON state) and diode D2 and D3 are reverse biased (OFF state). This reshapes the antenna structure as shown in Fig. 3 (a) and generates left hand circular polarization (LHCP). When a bias 2 terminal is excited with positive potential (+3 V), diodes D2 and D3 are forward biased (ON state) and diode D1 and D4 are reverse biased (OFF state). This reshapes the antenna structure as shown in Fig. 3 (b) and generates right hand circular polarization (RHCP).

(a) LHCP Configuration (b) RHCP Configuration

Fig. 3. Equivalent antenna structure.

III. PARAMETRIC ANALYSIS

Parametric analysis is carried to find the optimum dimension of the proposed antenna model. Ansoft high frequency structure simulator is used to tune the antenna dimensions and pin diode used in the antenna design is modelled based on the manufacture specification.

The performance of the antenna is greatly affected by slot dimension and hence it is taken as vital parameter to tune the antenna performance. The width of the slot is taken equivalent to the diode length given in manufacture data sheet. The length of the slot is tuned with respect to antenna operating frequency and axial ratio performances. From Fig. 4 it is observed that the resonating frequency of the proposed antenna model shifts from lower band to higher band with an increase in slot length due to increase in electrical length of the antenna and thereby making the antenna to resonate at the higher band with an increase in slot length.

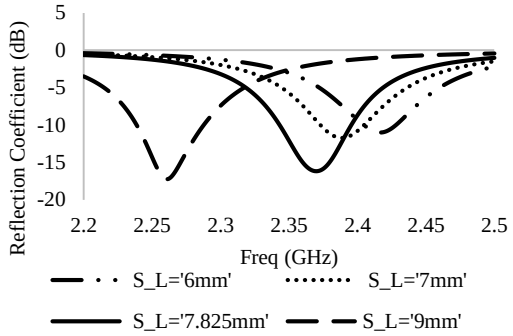

Fig. 4. Parametric analysis of Slot Length S_L on reflection coefficient.

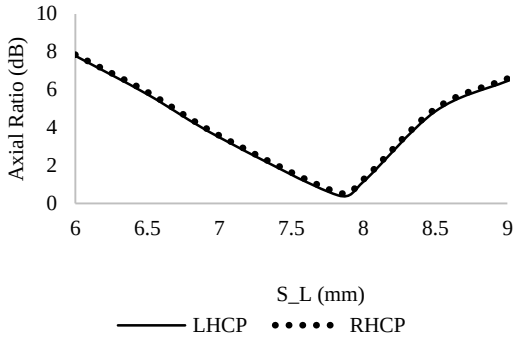

Fig. 5. Parametric analysis (Simulated) of slot length S_L on axial ratio.

Figure 5 shows the slot length effect on the purity of circular polarization. As shown in Fig. 5 the axial ratio is greatly affected by slot length. An optimum value of slot length is chosen to have a minimum axial ratio and to have good AR characteristics. Since the LHCP and RHCP configuration are symmetrical with each other, the effect of slot length on the axial ratio of both LHCP and RHCP configuration is similar and antenna exhibits a similar pattern as shown in Fig. 5. Based on the parametric analysis, the optimum dimension of the and slot width (S_W) is taken as 1.5 mm and slot length (S_L) is taken 7.825 mm and the corresponding surface current distribution at different instants of time is shown in Fig. 5.

The current distribution plot corresponding to LHCP and RHCP configuration is given in Fig. 6. It is observed that electric field vector traces clock wise direction for LHCP mode and anti-clock wise direction for RHCP mode. Figure 7 shows a front view and back view of the fabricated antenna model. The model is fabricated on roger substrate (RO4350) having a

thickness of 1.52 mm and having a length and width of 47 mm x 47 mm.

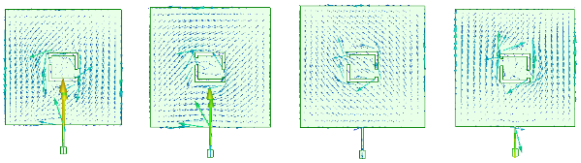

(a) t=0 (b) t=T/4 (c) t=T/2 (d) t=3T/4

(a) LHCP

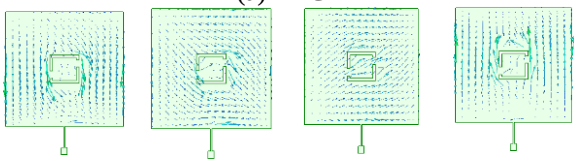

(a) t=0 (b) t=T/4 (c) t=T/2 (d) t=3T/4

(b) RHCP

Fig. 6. Current distribution in LHCP and RHCP.

(a) Front view (b) Back view

Fig. 7. Fabricated antenna model.

IV. RESULTS AND DISCUSSIONS

The performance of the antenna is validated by measuring its impedance and radiation characteristics using field fox network analyzer (N9925A) and antenna test systems. The impedance characteristics for the proposed model at LHCP and RHCP mode is shown in Fig. 8. LHCP mode is excited by biasing diode pair D1 and D4 and RHCP mode is excited by biasing diode pair D2 and D3 by means of DC bias line. The antenna gives -10 dB measured impedance bandwidth of 60 MHz in the range 2.34 GHz- 2.40 GHz for both modes with a center frequency of 2.365 GHz in WiMAX band. The axial ratio is calculated from horizontally and vertical polarized components (E_1 and E_2) based on equation given below,

$$A = \sqrt{\frac{1}{2}\left(E_1^2 + E_2^2 + \sqrt{E_1^4 + E_2^4 + 2E_1^2E_2^2\cos(2\delta)}\right)}, \quad (2)$$

$$B = \sqrt{\frac{1}{2}\left(E_1^2 + E_2^2 - \sqrt{E_1^4 + E_2^4 + 2E_1^2E_2^2\cos(2\delta)}\right)}, \quad (3)$$

$$\tau = \frac{1}{2}arctan\frac{2E_1E_2cos\,\delta}{E_1^2 - E_2^2}, \quad (4)$$

where δ is the phase difference between E_1 and E_2 and τ is the inclination of the polarization ellipse. The axial ratio (AR) is given by:

$$AR = \frac{2A}{2B} = \sqrt{\frac{E_1^2cos^2\tau + E_1E_2sin2\tau cos\,\delta + E_2^2sin^2\tau}{E_1^2sin^2\tau - E_1E_2sin2\tau cos\,\delta + E_2^2cos^2\tau}}. \quad (5)$$

The radiation characteristics of the antenna is measured using antenna test system and are shown in Fig. 9. It is observed that the antenna gives symmetrical radiation pattern and with better cross polarization isolation of ≥ 15 dB in the operating frequency.

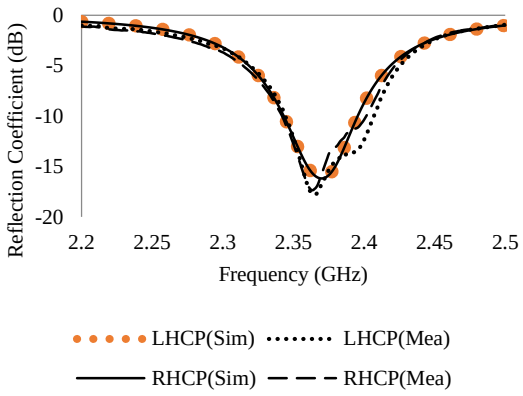

Fig. 8. Reflection coefficient (dB).

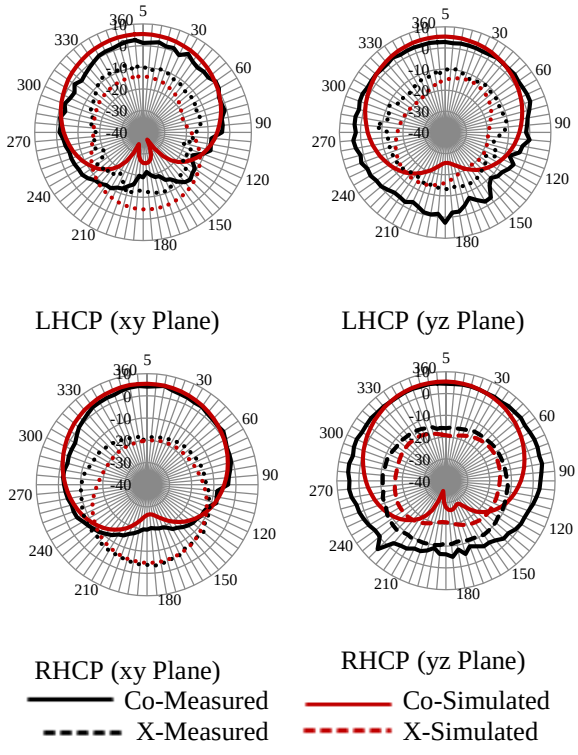

Fig. 9. Simulated and measured radiation pattern of LHCP/RHCP (dB).

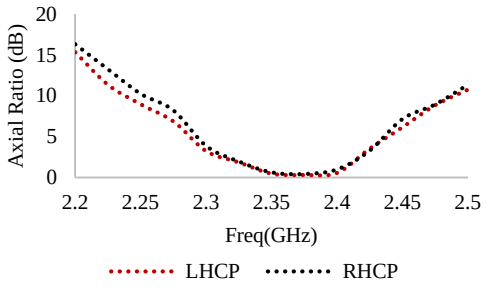

Fig. 10. Variation of the axial ratio (dB) against operating band (GHz).

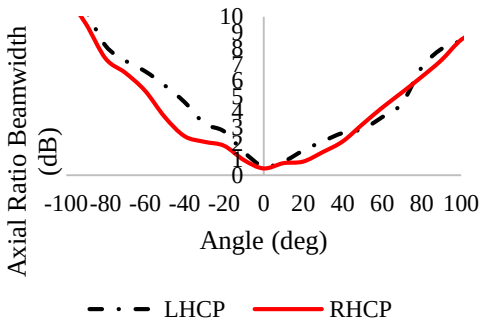

Fig. 11. Measured 3dB axial ratio beamwidth (dB).

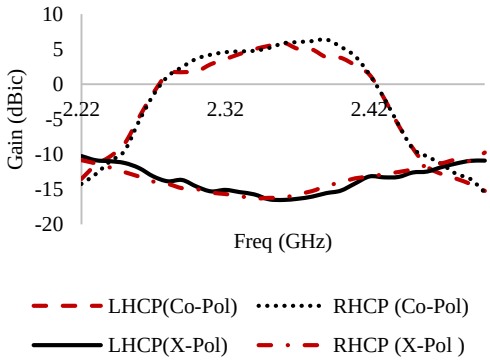

Fig. 12. Measured gain across the operating band for both modes.

Figure 10 shows that the antenna achieves a 3dB axial ratio bandwidth of 60 MHz (2.34 GHz - 2.4 GHz) for LHCP and RHCP configuration. The 3dB axial ratio beamwidth (ARBW) corresponding to both LHCP and RHCP mode is shown in Fig. 11. The antenna achieves a measured 3dB axial ratio beamwidth of -25°to 50°for LHCP and -40°to 45°for RHCP.

In order to validate the operating range of the proposed antenna, the gain characteristics of the proposed model with respect to operating band is measured using antenna test system and are shown in Fig. 12. The antenna archives a peak gain of 5.11 dBic in the LHCP mode and 5.52 dBic in the RHCP mode. The antenna gives stable gain response in the operating range as shown in Fig. 12.

Table 2 gives a performance comparison of the proposed antenna with some of the conventional antenna.

Table 2: Performance comparison of proposed antenna

Para.	Size (λ)	Switch	3dB AR Beam Width	3dB AR Band Width	X Pol Isolation
[6]	2.8λ x 2.8λ x 0.027λ	4 pin diodes	NA	NA	≥14 dB (±45° LP)
[8]	0.55λ x 0.55λ x 0.042λ	8 pin diodes	60° (LHCP, RHCP)	0.78% (5.09-5.12) GHz and 0.70% (5.68-5.72) GHz	17 dB (LHCP, RHCP)
[9]	0.46λ x 0.36λ x 0.107λ	9 DPDT	64° (LHCP) 46° (RHCP)	27.9% (1.42-1.88) GHz	13 dB (LHCP, RHCP)
[10]	1.15λ x 1.15λ x 0.12λ	12 pin diodes	60° (LHCP, RHCP)	0.05% (5.17-5.22) GHz and 0.12% (5.76-5.88) GHz	≥15 dB
[18]	2.98λ x 2.98λ x 0.37λ	4 pin diodes	58° (LHCP, RHCP)	10.5% from 2.35 to 2.61 GHz	≥20 dB
[19]	0.57λ x 0.57λ x 0.095λ	8 pin diodes	Not Reported	1.6% (923-943) MHz	≥20 dB
Proposed	0.37λ x 0.37λ x 0.012λ	4 pin diodes	75° (LHCP) 85° (RHCP)	2.54% (2.34-2.4 GHz)	16.2 dB (LHCP) 16.54 dB (RHCP)

Compared to other traditional antenna models, the proposed model achieves greater miniaturization along with the use of a reduced number of switching element for polarization reconfiguration. It is also observed that the proposed antenna achieves good AR beam width characteristics and also achieves better cross-polarization isolation in the operating band. Hence, the proposed model best suits for modern wireless communication systems.

V. CONCLUSION

A polarization reconfigurable rectangular patch antenna is presented. Four pin diodes are used for switching polarization states. The antenna achieves -10dB measured impedance bandwidth of 60 MHz in the range 2.34 GHz- 2.40 GHz for both LHCP and RHCP mode with a centre frequency of 2.365 GHz. The antenna gives two different polarization states (LHCP/RHCP) based on

excitation of appropriate pair of diodes with a peak gain of 5.11 dBic gain in the LHCP mode and 5.52 dBic in the RHCP mode and also it gives good cross polarization isolation of ≥15 dB and a wider 3-dB axial ratio beam width of 75° (-25° ≤AR ≤50°) for LHCP and 85° (-40° ≤AR ≤45°) for RHCP configurations.

REFERENCES

[1] H. Khan, B. Aslam, J. Khan, et al., "A novel asterisk-shaped circularly polarized RFID tag for on-metal applications," *Applied Computational Electromagnetics Society Journal*, vol. 31, no. 9, pp. 1035-1042, 2016.

[2] S. Heydari, J. Payam, and A. S. Arezoomand, "Circular polarization fractal slot by jerusalem cross slot for wireless applications," *Progress in Electromagnetics Research*, vol. 63, pp. 79-84, 2016.

[3] X.-Y. Wang and G.-M. Yang, "Dual frequency and dual circular polarization slot antenna for BeiDou navigation satellite system applications," *Microwave and Optical Technology Letters*, vol. 56, no. 10, pp. 2222-2225, 2014.

[4] W. Lin and H. Wong, "Wideband circular polarization reconfigurable antenna," *IEEE Trans. Antennas Propag.*, vol. 63, no. 12, pp. 5938-5944, 2015.

[5] L. Song and S. Li, "Dual-polarized antenna based on metal ring and microstrip patch," *Applied Computational Electromagnetics Society Journal*, vol. 33, no. 11, pp.1201-1208, 2018.

[6] W. Lin and H. Wong, "Polarization reconfigurable aperture-fed patch antenna and array," *IEEE Access*, vol. 4, pp. 1510-1517, 2016.

[7] V. Zarei, H. Boudaghi, M. Nouri, et al., "Reconfigurable circular polarization antenna with utilizing active devices for communication systems," *Applied Computational Electromagnetics Society Journal*, vol. 30, no. 9, pp. 990-995, 2015.

[8] A. Bharathi, M. Lakshminarayana, and P. V. D. Somasekhar Rao, "A novel single feed frequency and polarization reconfigurable microstrip patch antenna," *AEU - Int. J. Electron. Commun.*, vol. 72, pp. 8-16, 2017.

[9] Y. F. Cao, S. W. Cheung, and T. I. Yuk, "Dual-cap mushroom-like metasurface used in CP reconfigurable monopole antenna for performance enhancement," *IEEE Trans. Antennas Propag.*, vol. 63, no. 12, pp. 5949-5955, 2015.

[10] A. Bharathi, M. Lakshminarayana, and P. V. D. Somasekhar Rao, "A quad-polarization and frequency reconfigurable square ring slot loaded microstrip patch antenna for WLAN applications," *AEU - Int. J. Electron. Commun.*, vol. 78, pp. 15-23, 2017.

[11] J. Row and C.-J. Shih, "Polarization-diversity ring slot antenna with frequency agility," *IEEE Trans. Antennas Propag.*, vol. 60, no. 8, pp. 3953-3957, 2012.

[12] W. Lin, H. Wong, and R. W. Ziolkowski, "Circularly polarized antenna with reconfigurable broadside and conical beams facilitated by a mode switchable feed network," *IEEE Trans. Antennas Propag.*, vol. 66, no. 2, pp. 996-1001, 2018.

[13] M. Saravanan and M. J. S. Rangachar, "Circular ring shaped polarization reconfigurable antenna for wireless communications," *Progress in Electromagnetic Research M*, vol. 74, pp. 105-113, 2018.

[14] M. Elhefnawy, W. Ismail, and J. S. Mandeep, "Circular polarisation diversity with small size microstrip antenna," *International Journal of Electronics*, vol. 96, no. 11, pp. 1197-1205, 2009.

[15] B. Liang, B. Sanz-Izquierdo, E. A. Parker, and J. C. Batchelor, "A frequency and polarization reconfigurable circularly polarized antenna using active ebg structure," *IEEE Transactions on Antennas and Propagation*, vo. 63, no. 1, Jan. 2015.

[16] B. Babakhani and S. Sharma, "Wideband frequency tunable concentric circular microstrip patch antenna with simultaneous polarization reconfiguration," *IEEE Antennas Propag. Mag.*, vol. 57, no. 2, pp. 203-216, 2015.

[17] A. Beno, and D. S. Emmanuel, "Miniaturised reconfigurable window slot antenna using mechanical tuning," *International Journal of Electronics*, vol. 102, no. 11, pp. 1902-1918, 2015.

[18] Y. Lu, Y. Wang, S. Gao, C. Hua, and T. Liu, "Circularly polarised integrated filtering antenna with polarisation reconfigurability," *IET Microwaves, Antennas Propag.*, vol. 11, no. 15, pp. 2247-2252, 2017.

[19] H. Sun and S. Sun, "A novel reconfigurable feeding network for quad-polarization-agile antenna design," *IEEE Trans. Antennas Propag.*, vol. 64, no. 1, pp. 311-316, 2016.

[20] G. Li, Y. Huang, G. Gao, et al., "A broadband helical saline water liquid antenna for wearable systems," *International Journal of Electronics*, vol. 105, no. 4, pp. 645-658, 2017.

[21] Y. Qian and Q. Chu, "A polarization-reconfigurable water-loaded microstrip antenna," *IEEE Antennas Wirel. Propag. Lett.*, vol. 16, pp. 2179-2182, 2017.

[22] NXP Semiconductors (https://sg.rs-online.com/web/p/pin-diodes/3801092/).

M. Saravanan received M.E. Communication Systems from Anna University in the year 2012 and currently he is pursuing Ph.D. in Hindustan Institute of Technology and Science, India. His research interest includes antenna design, wireless communications and micro-wave circuit design.

M. J. S. Rangachar received M.Sc. during the year 1963 and Ph.D. during the year 1971. He is with Hindustan Institute of Technology and Science, India as Senior Professor and had more than 47 years of teaching experience. His research interests include antenna design and microwave propagations systems.

Frequency Reconfigurable Fractal CPW-Fed Antennas Designed for Telecommunication Applications

Sondos Mehri [1], Ines Rouissi [1], Hatem Rmili [1], Bandar Hakim [1], and Raj Mittra [1,2]

[1] Electrical and Computer Engineering Department, Faculty of Engineering
King Abdulaziz University, P.O. Box 80204, Jeddah 21589, Saudi Arabia
hmrmili@kau.edu.sa

[2] Electrical and Computer Engineering Department
University of Central Florida, EMC Lab, Orlando, FL 32816, USA
rajmittra@ieee.org

Abstract ─ A frequency reconfigurable fractal antenna for wireless communication application is presented in this paper. Three RF switches are incorporated into the antenna design to achieve frequency reconfigurability. The proposed antenna is designed and simulated using the HFSS code and then fabricated. The experimental results confirm the numerical simulation and demonstrate that integrating the RF switches improves the antenna flexibility and enables us to switch the antenna from single-band to dual-band as well as to a multi-band state with minimal design complexity and high degree of miniaturization.

Index Terms ─ Frequency reconfigurability, notched band, ultrawide band, varactor diode.

I. INTRODUCTION

Recent rapid growth in wireless and communication technologies has prompted us to create new and more advanced antennas capable of operating in multiple bands. Wireless standards such as GSM 800/900 and GSM 1800/1900 govern the operation in the lower UHF band, while WIFI and WIMAX do the same in the upper UHF band. Recently, frequency reconfigurable antennas have been proposed to achieve multipleband operation [1-5], as opposed to fixed antennas which can only operate in a frequency band. Reconfigurable antennas are capable of dynamically altering their performance in order to adapt to environmental conditions and to meet system requirements that can be complex, and for this purpose various reconfiguration techniques have been investigated [6, 7]. Approaches based on electrical switching circuits, such as RF-switches and varactors [8-11] represent the most commonly used tuning techniques owning the simplicity of their integration into the antenna system and their capability of rapid switching. These switching elements are often used at specific locations in an antenna to modify its current distribution and, thereby modify its RF properties. Despite providing multiband operation, the antenna maintains its compactness and light weight feature to facilitate its integration with other microwave components in a device. Toward this goal, the fractal technique is adopted in this work to improve the size of the antenna in comparison to non-fractal design [12-14]. Such a design has the salutary features at low profile, multi-frequency operation, impedance compatibility and ease of integration for different wireless application system.

In this paper we propose a frequency reconfigurable Hilbert curve CPW-fed antenna which is, designed and fabricated. This work is inspired by the antenna designs presented in our previous work [15], but with enhanced performance achieved by incorporating RF switches to realize frequency reconfigurable characteristics. Three RF switches are placed across, the arms of the antenna and enable the antenna to operate in multiple bands by altering the switches states. To validate the simulation results, the Hilbert curve reconfigurable antenna is fabricated, and tested. The measurement results confirm that the proposed antenna is capable of operating in three different states, namely single-band, dual-band and multi-band for a small area of dimensions of 17 × 23 mm^2. So, the main merit of the proposed design lies in achieving, multiband switching operations, acceptable gain with minimal complexity and high degree of miniaturization.

The reminder of the paper is organized as follows. The next section describes the antenna structure and fractal design. Simulation and experimental results are presented and discussed in Section 3. Finally, the last section presents the conclusions of this study.

Submitted On: February 13, 2019
Accepted On: May 7, 2019

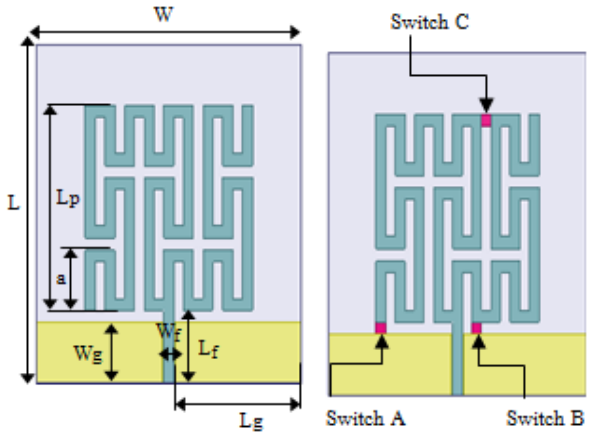

(a) (b)

Fig. 1. Geometry of the planar fractal CPW-fed antenna: (a) reference structure, and (b) incorporation of three switches: A, B, and C.

Table 1: Geometric parameters of the proposed design

Parameters	Dimensions (mm)
Substrate width	27
Substrate length	28
Antenna length	17
Metal width	1
Hilbert curve length at the second iteration	5
Substrate width	1
Microstrip feed width	6
Microstrip feed length	5
Ground width	12.89
Ground length	1
Ground and Microstrip feed spacing	1

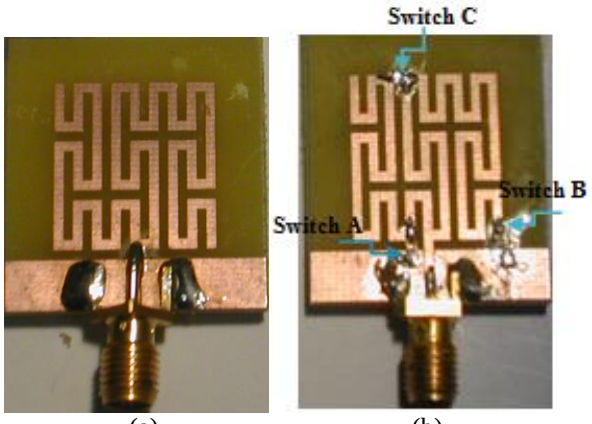

(a) (b)

Fig. 2. Prototypes of the fabricated antennas: (a) reference structure, and (b) antenna prototype with the integration of A, B, and C switches.

Table 2: Switch configuration of the antenna design

States	Switches		
	A	B	C
1	OFF	OFF	OFF
2	OFF	OFF	ON
3	OFF	ON	OFF
4	OFF	ON	ON
5	ON	OFF	OFF
6	ON	OFF	ON
7	ON	ON	OFF
8	ON	ON	ON

II. ANTENNA DESIGN

The geometry of the reference antenna design is presented in Fig. 1 (a). This figure shows the compact fractal antenna presented in our previous work [15]. The design uses the second iteration of the Hilbert curve, whose geometrical parameters are provided in Table 1. To reconfigure the reference structure in specific bands, we propose a new design which uses RF switches, inserted in specific locations as shown in Fig. 1 (b). The inserted switches are denoted A, B, and C where, A and B are placed between the ground and the antenna while C is located on the upper arms of the antenna. The proposed structures are printed on FR4 substrate of thickness 0.8 mm, relative dielectric constant ε_r = 4.4 and loss tangent δ = 0.02. Figure 2 shows the prototypes of the fabricated antennas in which three RF switches have been integrated. The switch itself has two states these are: State 1, when the switch is OFF and State 2, when the switch is ON. As indicated in Table 2, eight possible switching states are provided by the three incorporated switches.

III. RESULTS AND DISCUSSIONS

A. Reflection coefficient S_{11}

The variation of the input reflection coefficient vs. the frequency is shown in Fig. 3 for each state. In this figure simulated S_{11} curves corresponding to the eight operating states are compared to the measured S_{11}. Inspection of these figures shows that there is good agreement between the measured and simulated results. The measured results show that, the proposed antenna can be made to resonate at eight different frequencies by using various combinations of the switches A, B, and C. The experimental results for different states are summarized in Table 3, which shows that the proposed antenna generates fifteen frequencies in the frequency range of 0.8 GHz to 4.7 GHz. As shown in this table, State 1 resonates at four frequencies, State 2 at three frequencies, while State 5 and state 7 resonate at two other frequencies. For all other states, one resonance is realized per state. Experimental results show also that the proposed antenna is able to cover various bands. As and (h) State 8. An example, the antenna covers 4 bands

when operating in state 1 and three bands for State 2; hence a dual-band operation is obtained for both states 5 and 7. However, a single band per state is obtained for the remaining states. These results demonstrate the fact that the ability of the proposed antenna to achieve frequency agility which, in turn, makes it suitable for use in wireless communication systems. It is worth to note that an acceptable agreement between numerical and experimental results is obtained expect for some specific states (notably when switches A and B are activated). This small disagreement reported for states 3 and 5 is due to the fact that switches A and B are connected to the antenna ground plane which influences the antenna behavior. In fact, the surface currents flowing on the ground plane may affect the switches, and then the input reflection coefficient of the antenna. In addition, the coaxial connector effect was not taken into consideration in our simulated model, which may explain also the difference between simulation and measurements [8].

Table 3: Performances summary of the proposed antenna for different states

States	Number of Resonated Frequency		Operating Bands (GHz)	
	Simulation	Measurement	Simulation	Measurement
1	4	4	0.8-10; 1.2-1.4; 2.2-3.8	0.9-1.0; 1.4-1.5; 2.7-3.2; 3.5-3.8
2	3	3	0.8-1.1; 1.9-3.2; 3.7-4.2	2.5-3.14; 3.7-3.9; 4.7
3	2	1	1.2-1.3; 4.4-4.7	4.45-4.71
4	1	1	4.1-4.4	3.8-4.3
5	1	2	3.6-3.8	0.95-1; 4.5-4.6
6	1	1	3.7-4.0	4.5-4.7
7	2	2	2.6; 4.5	2.6; 4.5
8	1	1	2.4-2.6	2.4-2.6

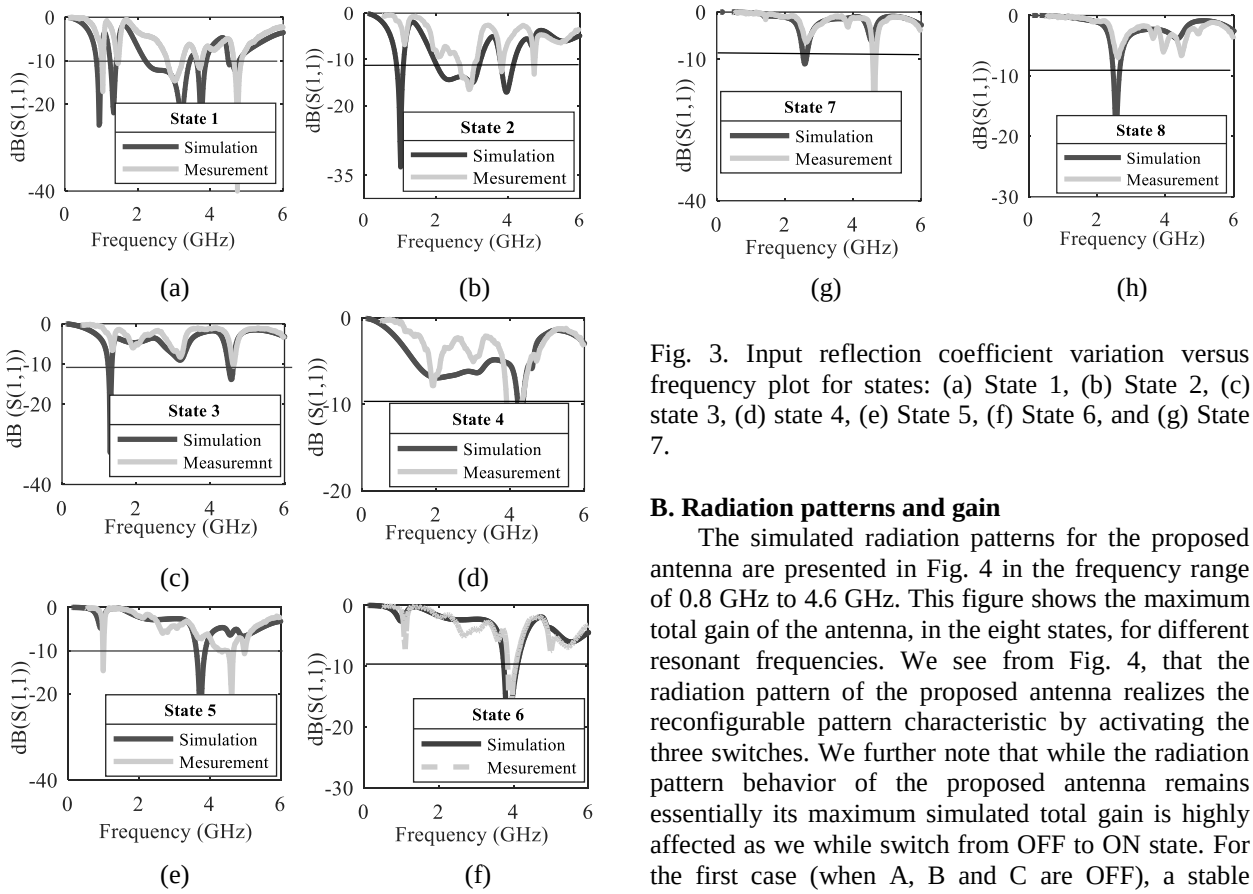

Fig. 3. Input reflection coefficient variation versus frequency plot for states: (a) State 1, (b) State 2, (c) state 3, (d) state 4, (e) State 5, (f) State 6, and (g) State 7.

B. Radiation patterns and gain

The simulated radiation patterns for the proposed antenna are presented in Fig. 4 in the frequency range of 0.8 GHz to 4.6 GHz. This figure shows the maximum total gain of the antenna, in the eight states, for different resonant frequencies. We see from Fig. 4, that the radiation pattern of the proposed antenna realizes the reconfigurable pattern characteristic by activating the three switches. We further note that while the radiation pattern behavior of the proposed antenna remains essentially its maximum simulated total gain is highly affected as we while switch from OFF to ON state. For the first case (when A, B and C are OFF), a stable

radiation pattern is observed. An omni-directional radiation pattern in the (yoz) plane is shown with a maximum total gain of -2.2 dB at f = 3.74 GHz. For the second case per state (State 2, State 3, and State 5), the radiation pattern retains the same omni-directional behavior when one switch is activated, and its maximum total gain is 0.4 dB at 3.84 GHz. For the third case, when two switches are activated per state (State 6 and State 7), the radiation pattern is still omni-directional, and has a maximum total gain of -3.8 dB for f = 3.84 dB. Similar characteristics are also obtained for the last case, when all the switches are activated (State 8). Measured radiation pattern obtained by activating the A, B, and C switches states are presented in Fig. 5 to validate the simulation results. This figure shows that the measured gain varies from -11.54 dB to -2 dB in the lower band (0.9-2.11 GHz), and from -2.4 dB to 5 dB in the upper band (3-4.7 GHz). The results of maximum measured gain the different states are summarized in Table 4. The table, which compares the gain performances of the proposed antenna for different switches states, shows that the gain of the antennas is highly affected when the switch B is activated. Table 4 also measurements shows that, the lower measured gain is adversely affected when the switches A and B are activated (corresponding states are: 3, 4, 5, 6, 7, and 8). As explained earlier, this degradation is caused by the coupling between the ground plane and the switches.

Table 4: Maximum measured gain for different states

States	Frequency (GHz)	Maximum Measured Gain (dB)
1	4.7	3.02
2	3.8	5
3	4.6	0.3
4	4.63	0.31
5	4.6	1.9
6	3.9	4.7
7	4.6	0.31
8	2.6	-0.13

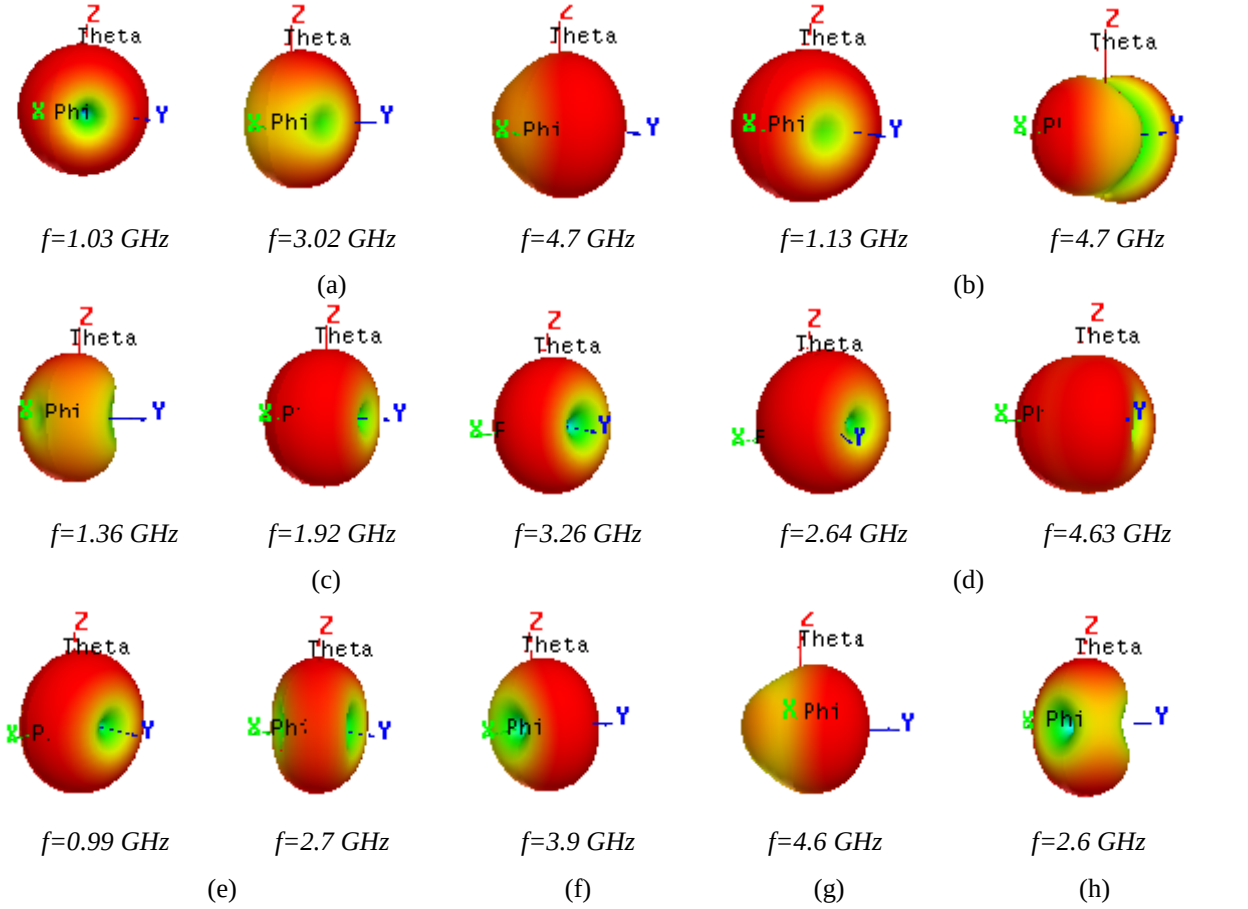

Fig. 4. 3D simulated radiation patterns for states: (a) State 1, (b) State 2, (c) State 3, (d) State 4, (e) State 5, (f) State 6, (g) State 7, and (h) State 8.

C. Comparative study

To mark the advantages of the proposed design compared to those reported in literature, a comparative study was performed, and results are summarized in Table 5. We can note from Table 5 that better performances in terms of size, design complexity are achieved with the proposed design. For example, the design proposed in [16] giving higher gain and more operating bands is achieved at the expense of the antenna size and the design complexity. In fact, by referring to Table 5, the antenna size is 4 times larger than our proposed design, and the number of PIN diodes is 8 instead of 3. So, our structure successes in achieving high degree of miniaturization, multiband switching capabilities with acceptable gain and minimum number of PIN diodes.

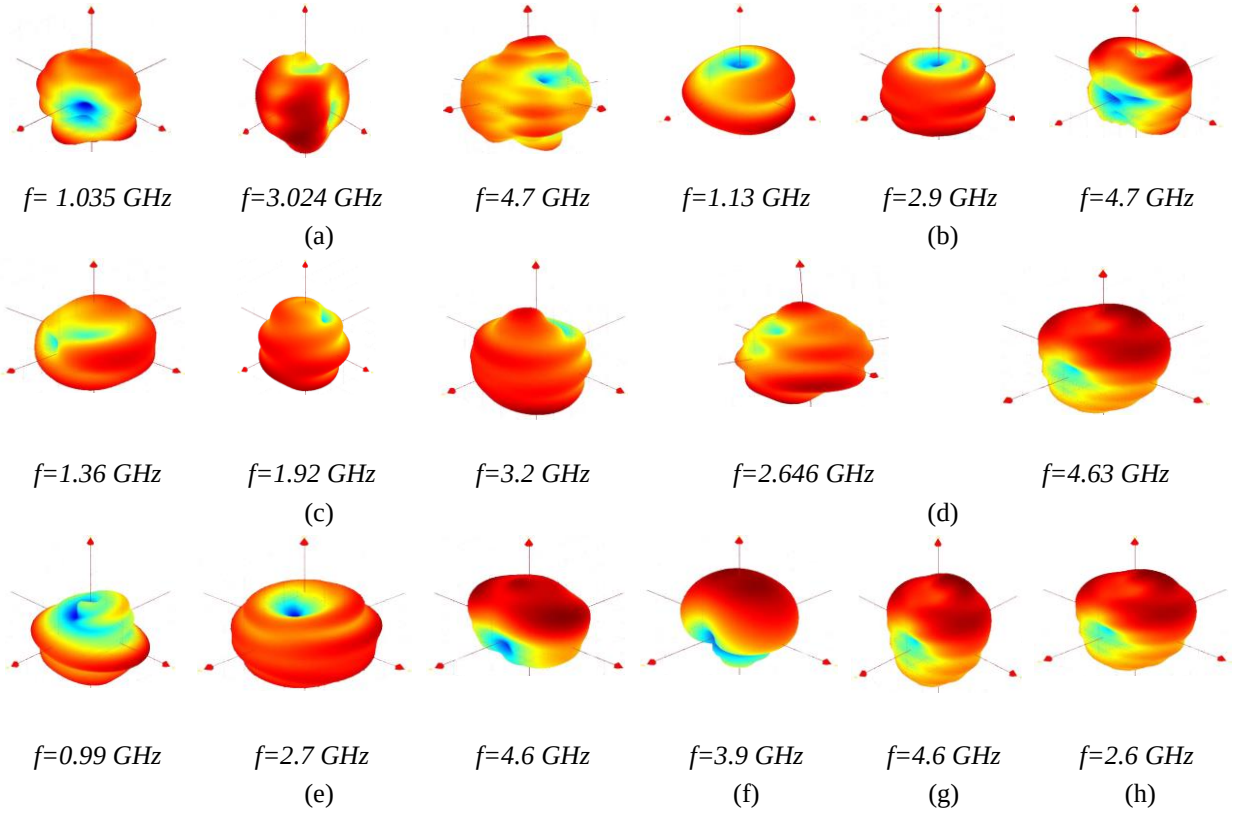

Fig.5. 3D measured radiation patterns for states: (a) State 1, (b) State 2, (c) State 3, (d) State 4, (e) State 5, (f) State 6, (g) State 7, and (h) State 8.

Table 5: Comparison of the proposed fractal multiband antenna (e) with those present in the state-of-art literature

Ref.	Antenna Design Geometry	Number of PIN Diodes	Max. Gain (dB)	Total Area (mm^2)	Number of Operating Bands
[17]	No Fractal	4	2.5	58.8 × 40	3
[18]	No Fractal	5	3.2	25 × 45	5
[19]	Fractal	6	-11.37	30 × 30	13
[16]	Fractal	8	6.8	80 × 80	18
[20]	Fractal	1	5.36	35 × 30	5
[21]	Fractal	2	4	35 × 30	6
Prop.	Fractal	3	4.7	17 × 23	14

IV. CONCLUSION

A frequency reconfigurable antenna has been designed, analyzed and fabricated in this paper. To achieve reconfigurability characteristics, three switches were incorporated in the designed antennas which were fabricated and experimentally evaluated to validate the simulated results. The designed reconfigurable antenna, which can operate in one, two, three and four bands,

has a total area of 17×23 mm^2. So, the proposed design success in achieving, multiband switching operations, acceptable gain with minimal complexity and high degree of miniaturization. Such features provided by the proposed antenna makes it suitable for use in telecommunication devices that operate in multiple frequency bands.

ACKNOWLEDGMENT

This project was funded by the Deanship of Scientific Research (DSR), King Abdulaziz University, under Grant No. KEP-Msc-3-135-39. The authors, therefore, acknowledge technical and financial support of KAU.

The authors are grateful to the help of Dr Jean-Marie Floch from the IETR institute, INSA Rennes, France, for his helps during experiments.

REFERENCES

[1] Z. Hao and J. Hu, "Design of a frequency and polarization reconfigurable patch antenna with a stable gain," *IEEE Access*, vol. 6, pp. 68169-68175, 2018.

[2] M. A. Alam and A. Abbosh, "Reconfigurable band-rejection antenna for ultra-wideband applications," *IET Microwaves, Antennas & Propagation*, vol. 12, no. 2, pp. 195-202, 2018.

[3] S. K. Beheraa and Y. K. Choukiker, "Wideband frequency reconfigurable Koch snowflake fractal antenna," *IET Microwaves, Antennas & Propagation*, vol. 11, no. 2, pp. 203-208, 2017.

[4] I. Rouissi, J. M. Floc'h, H. Rmili, and H. Trabelsi, "Design of a frequency reconfigurable patch antenna using capacitive loading and varactor diode," *European Conference on Antennas and Propagation*, 2015.

[5] I. B. Trad, J. M. Floch, H. Rmili, L. Laadhar, and M. Drissi, "Planar elliptic broadband antenna with wide range reconfigurable narrow notched bands for multi-standard wireless communication devices," *Progress in Electromagnetic Research*, vol. 146, pp. 69-80, 2014.

[6] V. Arun, L. R. Karlmarx, K. J. J. Kumar, and C. Vimlitha, "N-shaped frequency reconfigurable antenna with auto switching unit," *ACES Journal*, vol. 33, no. 6, pp. 710-713, 2018.

[7] S. Chilukuri, K. Dahal, A. Lokam, and W. Chen, "A CPW fed T-shaped frequency reconfigurable antenna for multi radio applications," *ACES Journal*, vol. 33, no. 11, pp. 1276-1285, 2018.

[8] B. Babakhani, S. K. Sharma, and N. R. Labadie, "A frequency agile microstrip patch phased array antenna with polarization reconfiguration," *IEEE Transactions on Antennas and Propagation*, vol. 64, no. 10, pp. 4316-4327, 2016.

[9] R. Herzi, M. Bouslama, L. Osman, and A. Gharsallah, "Frequency agile Vivaldi antenna with enhanced gain for wireless applications," *IEEE MTT-S International Microwave Workshop Series on Advanced Materials and Processes for RF and THz Applications*, 2017.

[10] I. B. Trad, H. Rmili, J. M. Floch, and H. Zangar, "Design of planar mono-band rejected UWB CPW-Fed antennas for wireless communications," *Mediterranean Microwave Symposium*, 2011.

[11] S. Dakhli, H. Rmili, J. M. Floch, M. Sheikh, K. Mahdjoubi, F. Choubani, and R. Ziolkowski, "Capacitively loaded loop-based antennas with reconfigurable radiation patterns," *International Journal on Antennas and Propagation*, pp. 1-10, 2015.

[12] J. Zhou, X. Wu, B. You, Y. P. Shang, J. Huang, and T. Huang, "A band-notched UWB antenna loaded with tree-shaped fractal," *Progress in Electromagnetics Research Symposium*, 2018.

[13] R. M. H. Bilal, A. A. Rahim, H. Maab, and M. M. Ali, "Modified wang shaped ultra-wideband (UWB) fractal patch antenna for millimetre-wave applications," *Progress in Electromagnetics Research Symposium*, 2018.

[14] S. Srivastava, P. Mishra, and R. K. Singh, "Design of a reconfigurable antenna with fractal geometry," *IEEE UP Section Conference on Electrical Computer and Electronics*, 2015.

[15] I. Rouissi, I. B. Trad, J. M. Floch, M. Sheikh, and H. Rmili, "Design of miniature multiband fractal CPW-fed antenna for telecommunication applications," *Progress in Electromagnetics Research Symposium*, 2013.

[16] H. Altun, E. Korkmaz, and B. Türetken, "Reconfigurable fractal tree antenna for multiband applications," *URSI General Assembly and Scientific Symposium*, 2011.

[17] S. Sharma and C. C. Tripathi, "Frequency reconfigurable U-slot antenna for SDR application," *Progress In Electromagnetics Research Letters*, vol. 55, pp. 129-136, 2015.

[18] L. Pazin and Y. Leviatan, "Reconfigurable slot antenna for switchable multiband operation in a wide frequency range," *IEEE Antennas and Wireless Propagation Letters*, vol. 12, pp. 329-332, 2013.

[19] Y. B. Chaouche, F. Bouttout, I. Messaoudene, L. Pichon, M. Belazzoug, and F. Chetouah, "Design of reconfigurable fractal antenna using pin diode switch for wireless applications," *Mediterranean Microwave Symposium*, 2016.

[20] T. Alia, N. Fatimab, and R. C. Biradar, "A miniaturized multiband reconfigurable fractal slot antenna for GPS/GNSS/Bluetooth/WiMAX/X-band

applications," *International Journal of Electronics and Communications*, vol. 94, pp. 234-243, 2018.

[21] P. Pokkunuri, B. T. P. Madhav, G. K. Sai, M. Venkateswararao, B. Ganesh, N. Tarakaram, and D. P. Teja, "Metamaterial inspired reconfigurable fractal monopole antenna for multiband applications," *International Journal of Intelligent Engineering and Systems*, vol. 12, no. 2, pp. 53-61, 2019.

Sondos Mehri has received the Ph.D. degree in 2017 in Electrical Engineering, from the National School of Engineering in Tunis (ENIT), Tunisia and is currently working as a Postdoctoral Researcher under the supervision of Prof. Raj Mittra. Her research interests are focused on the design of a substrate integrated waveguide slot array for millimeter waves frequencies.

Mehri has been awarded the 2nd Prize of Students Paper Poster Competition of the IEEE Melecon in 2016.

Hatem Rmili received the B.S. degree in General Physics from the Science Faculty of Monastir, Tunisia in 1995, and the DEA diploma from the Science Faculty of Tunis, Tunisia, in Quantum Mechanics, in 1999. He received the Ph.D. degree in Physics (Electronics) from both the University of Tunis, Tunisia, and the University of Bordeaux 1, France, in 2004. From December 2004 to March 2005, he was a Research Assistant in the PIOM Laboratory at the University of Bordeaux 1. During March 2005 to March 2007, he was a Postdoctoral Fellow at the Rennes Institute of Electronics and Telecommunications, France. From March to September 2007, he was a Postdoctoral Fellow at the ESEO Engineering School, Angers, France. From September 2007 to August 2012, he was an Associate Professor with the Mahdia Institute of Applied Science and Technology (ISSAT), Department of Electronics and Telecommunications, Tunisia. Actually, he is Associate Professor with the Electrical and Computer Engineering Department, Faculty of Engineering, King Abdulaziz University, Jeddah, Saudi Arabia. His main research activities concern antennas, metamaterials and metasurfaces.

Bandar Hakim is an Assistant Professor of Electrophysics at KAU. He received his Ph.D. degree in Electrophysics from the University of Maryland. He worked with the Medical Robotics group at the ÉcolePolytechnique Fédérale de Lausanne in Switzerland, the Center for Devices and Radiological Health at the Food and Drug Administration in Washington DC and the Neurology Department at Mount Sinai School of Medicine in the New York NY. He served as an Industrial Consultant in the US, Switzerland and Germany.

Raj Mittra is a Professor in the Department of Electrical & Computer Science of the University of Central Florida in Orlando, FL., where he is the Director of the Electromagnetic Communication Laboratory. Prior to joining the University of Central Florida, he worked at Penn State as a Professor in the Electrical and Computer Engineering from 1996 through June 2015. He also worked as a Professor in the Electrical and Computer Engineering at the University of Illinois in Urbana Champaign from 1957 through 1996, when he moved to the Penn State University. Currently, he also holds the position of Hi-Ci Professor at King Abdulaziz University in Saudi Arabia,

He is a Life Fellow of the IEEE, a Past-President of AP-S, and he has served as the Editor of the Transactions of the Antennas and Propagation Society. He won the Guggenheim Fellowship Award in 1965, the IEEE Centennial Medal in 1984, and the IEEE Millennium medal in 2000. Other honors include the IEEE/AP-S Distinguished Achievement Award in 2002, the Chen-To Tai Education Award in 2004 and the IEEE Electromagnetics Award in 2006, and the IEEE James H. Mulligan Award in 2011.

Mittra is a Principal Scientist and President of RM Associates, a consulting company founded in 1980, which provides services to industrial and governmental organizations, both in the U.S. and abroad.

An Experimental Performance Investigation of an Ultra-Wideband Directional Antenna in the Microwave Imaging of Breast Cancer Tumor

Ali R. Celik [1], Muhammed B. Kurt [1], and Selcuk Helhel [2]

[1] Department of Electrical and Electronics Engineering
Dicle University, Diyarbakir, 21280, Turkey
ali.celik@dicle.edu.tr, bkurt@dicle.edu.tr

[2] Department of Electrical and Electronics Engineering
Akdeniz University, Antalya, 07058, Turkey
selcukhelhel@akdeniz.edu.tr

Abstract ─ The purpose of this study is testing the performance and success of a compact-sized, ultra-wideband and directional printed circular monopole antenna proposed in a previous study for detection of the small breast cancer tumors. For this aim, simple but basic experimental studies of the radar-based ultra-wideband microwave measurement system are presented. In the measurements, different breast phantoms that have low dielectric constant materials representing the fat tissue and high dielectric constant object representing the tumor are formed and used. The object is located at different positions and the reflected signals are observed. The mono-static system which uses the same antenna to perform both the transmitting and receiving task of the signals is preferred in the study. According to the measured frequency domain signals, the reflected energy increases when the tumor is present. According to the amplitude and phase of the time domain signals, the presence, position and size of the tumor are inferenced. In order to provide more clear information about the tumor, a sample image is also created by implementing delay-and-sum algorithm. Furthermore, specific absorption rate of the breast is discussed. In summary, the performance of the antenna is valid for using in the radar-based ultra-wideband microwave imaging with respect to its features of the size, bandwidth, directivity, and beamwidth.

Index Terms ─ Breast cancer, microwave measurement, radar imaging, scattering parameters, ultra-wideband antenna.

I. INTRODUCTION

The World Health Organization reported about the cancer types in females that the most prevalent one is the breast cancer throughout the world [1]. Breast cancer stages are usually expressed as a number on a scale of 0 through IV, success rate in the treatment according to the stage decreases as the stages progress from 0 to IV. Hence, diagnosis at the early stages (when the tumor size is not larger than 20 mm) is very crucial in the breast cancer treatment [2].

Breast cancer detection is primarily made by X-Ray Mammography, Magnetic Resonance Imaging (MRI), and Ultrasound techniques. Also, radar-based ultra-wideband (UWB) microwave imaging (MI) method has lately become applicable for this aim [3-8]. In the microwave frequencies (in the range of 0.3 and 300 GHz), the breast tissue can pass more signals than other tissues such as brain and muscle. In addition, the breast can be illuminated with microwave sources and multiple measurements can be made thanks to its position in the body. Due to these characteristics, one of the most suitable organs to test the success of microwaves in imaging is the breast [9].

The radar-based UWB MI method differs from X-ray Mammography method by using nonionizing radiation and illuminating power even less than a mobile phone. Therefore, it is much safer and even easier as there is no need for compression in the imaging [10]. This method has a comfortable system in contrast to MRI method having some negative features such as long process and uncomfortable measurement environment. Radar-based UWB MI method is also intended to overcome the main disadvantage of the Ultrasound method which needs experienced physicians to interpret the results in order to prevent obtaining false-negative/ positive results [11].

When an electromagnetic wave passes from one medium to another, one part of the wave passes to the second medium and the rest is reflected back from the surface. In order to find the reflected wave, the reflection coefficient (Γ) is calculated. If the wave impinges normally, the Γ value is calculated using (1). To find the impedance (η) values, (2) is used:

$$\Gamma = \frac{\eta_2 - \eta_1}{\eta_2 + \eta_1}, \tag{1}$$

Submitted On: March 17, 2019
Accepted On: May 23, 2019

$$\eta = \sqrt{\frac{\mu}{\varepsilon - j\frac{\sigma}{\omega}}}, \quad (2)$$

where **μ** is the magnetic permeability of the medium, **ε** is the electrical permittivity, **σ** is the conductivity, and ***ω*** is the angular frequency [12].

When the values of η are put into place in the related equation with Γ, it will be seen that higher ε or σ increases the reflection. Since the ε and σ values of the tumor have much greater values compared to the healthy breast in the microwave frequencies, the presence of the tumor leads to an increase in the amount of the reflections that allows detection of the tumor. So, the main principle of the radar-based UWB MI method is based on the significant difference in the electrical properties of the malignant tumors and normal breast tissue in the microwave frequencies [13].

In the measurement system, an UWB pulse which includes low to high frequencies is used. The lower band ensures adequate depth of penetration while the higher band ensures the enough resolution of the images. Hence, both the deeply buried and small-sized tumor can be detected based on the broad frequency bands [14,15].

In the system, the breast is illuminated by UWB pulses. The presence, position and size of any tumor can be seen on the images which are obtained by collecting and processing the reflected signals.

The used antenna is very critical to radiate and receive the pulses in the radar-based UWB MI systems. These systems require compact-sized, UWB, stable and directive antennas as their sensors [16]. A printed circular disc monopole antenna (PCDMA) having these properties was developed in [17] for early detection of the breast cancer. Although the features of the antenna were demonstrated to be suitable for using in the MI systems, the required test measurements were not being performed to investigate the success of the antenna.

In this paper, the main purpose is to investigate how the antenna of [17] would perform when used in the radar-based UWB MI system. For this aim, the frequency and time domain signals are examined. Also, an image is created to show the size and position of the tumor.

In the measurements, the proposed antenna is expected to work as previously stated and is intended to show better performance than some similar studies.

II. MATERIAL AND METHODS

In the radar-based UWB MI systems, generally three different methods can be used. These are: mono-static, bi-static, and multi-static radar methods [18,19]. In this study, the mono-static system which uses the same antenna to perform both the transmitting and receiving task of the signals is preferred. Hence, S_{11} scattering parameters which enable the determination of the reflections are measured.

In this study, experimental measurements are made to observe the performance of the PCDMA in sensing the small tumors. In the measurements, two different breast phantoms are used to mimic the electrical properties of the healthy breast fat tissue. A 6 mm sized plastic object filled with sea water is used to mimic malignant tumor. One of the formed phantoms is planar and the other is hemi-spherical. In the measurement configurations, the planar phantom is scanned by the antenna manually. However, in order to measure the hemi-spherical phantom, the antenna must be turned around the phantom 360 degrees to save the S_{11} data from different positions by using the turn table device.

The properties of the antenna, the structures of the phantoms and the information about the measurements are given in sub-headings.

A. Characteristics of the developed antenna

In the study of [17], a compact-sized PCDMA including circular patch and L-shaped ground plane was designed and printed on a FR4 substrate. In the design process, a parasitic element was added to the patch side and a number of slots were etched on the ground plane in order to improve the bandwidth and directivity of the antenna as proposed in [20].

Simulated and measured S_{11} parameters showed good agreement between 3 and 10 GHz. But the return loss (RL) shifted above the -10 dB in a small number of frequencies. It was reported that these disagreements were due to the uncertainties in the dielectric material, fabrication constrains, effects of soldering of SMA connector, measurement loss and accuracy rate of full-wave simulation program not to be 100%. In order to overcome these drawbacks, in this study we have reconstructed the antenna and soldered the connector more carefully. The measurements have been taken in an anechoic chamber this time. As a result of these operations, it is observed that the RL curve is drawn below the -10 dB line over the entire frequency range of 3-10 GHz. The simulated and measured S_{11} results of reconstructed antenna are given in Fig. 1.

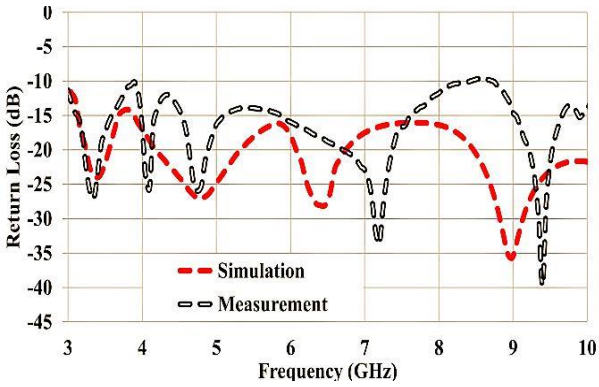

Fig. 1. The RL results of the antenna proposed previously in the study of [17] (after reconstruction).

When carefully examined, it is seen that the measured results shift systematically to higher frequencies according to the simulation. For this reason, a resonance that actually occurred before 3 GHz shifts to the 3-10 GHz frequency region. Therefore, a more resonance mode appears in the measurement results.

The RL results show that the proposed antenna is suitable for using in an MI system of the breast cancer with respect to the working frequency range. But, as mentioned before, the antenna does not only need to have broad bandwidth but also should have narrow half power beamwidth (HPBW) and stable directional radiation pattern to be used in a radar-based MI.

The directivity of the antenna changes between 6 dB and 9.4 dB in the 3-10 GHz; the radiation efficiency is higher than 90% over the entire band. Moreover, the antenna has both narrow HPBW and stable directional radiation pattern as seen in Fig. 2. These results show that the antenna is also suitable with respect to the radiation features for using in an MI system.

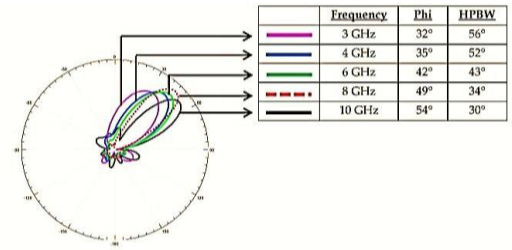

Fig. 2. Beam variation of the antenna proposed in [17].

In brief, the UWB directional antenna which was proposed in [17] is reconstructed and analyzed more carefully in this study. Here, we will present some experimental systems to investigate the capabilities of the antenna for the aim of using in the radar-based UWB MI of the breast cancer, which was not performed in [17].

B. Breast phantoms

As mentioned before, two different breast phantoms are formed and used in the experiments. One of these phantoms has rectangular shape, and the other has hemi-spherical. The dimension of the rectangular phantom is 15x5x7 cm^3, and the radius of the hemi-spherical phantom is 6 cm.

Since the working frequency range is 3-10 GHz in this study, the electrical properties of the fat and tumor structures are based on according to approximately mean value of the range, 7 GHz. At this frequency, the relative permittivities (ε_r) of the fatty breast tissue and tumor are 4.2 and 64, respectively. Also, the σ of the breast tissue and tumor are 0.5 and 10 S/m, respectively [21,22]. Since the study is intended to determine the presence of the tumor, it is not necessary to add skin to the phantoms. A borosilicate glass with 2 mm thickness is used as skin tissue in the planar phantom, whereas the hemi-spherical phantom contains only the tumor and fatty tissue.

There are some materials that possess close dielectric properties to the breast such as vegetable oils, pure glycerine, dry cornflour, beeswax, etc. Similarly, there are some materials having close dielectric properties to the tumor tissue such as agar, gelatine, sea-water, etc. In the rectangular phantom, we use canola oil having $\boldsymbol{\varepsilon_r}$ of 4 and $\boldsymbol{\sigma}$ of 0.3 S/m at 7 GHz [23,24] as a fat-mimicking material. However, in the hemi-spherical phantom, the beeswax having $\boldsymbol{\varepsilon_r}$ of 3 and $\boldsymbol{\sigma}$ of 0.1 S/m at 7 GHz [25-27] is preferred. The tumor-mimicking object is in the form of a plastic cylinder filled with sea-water having $\boldsymbol{\varepsilon_r}$ of 69 and $\boldsymbol{\sigma}$ of 9 S/m at 7 GHz [27] and is placed inside the phantoms similar to the studies of [27-29]. Since the dielectric properties of the plastic are similar to the properties of the oil, using the plastic material to keep sea-water does not affect the measurement results considerably [30].

C. Configurations of the measurements systems

This section explains the measurements on the phantoms by using the PCDMA. Throughout the measurements of the rectangular phantom, the antenna is placed 20 mm above the phantom. Throughout the measurements of the hemi-spherical phantom, the PCDMA is positioned at a height of 30 mm on the z-axis while the center coordinate of the sphere and tumor are (x=0, y=0, z=0 mm) and (x=0, y=0, z=30 mm), respectively. The distance between the phantom and the upper right corner of the antenna is set to 20 mm. The measurement systems are shown in Fig. 3 and Fig. 4.

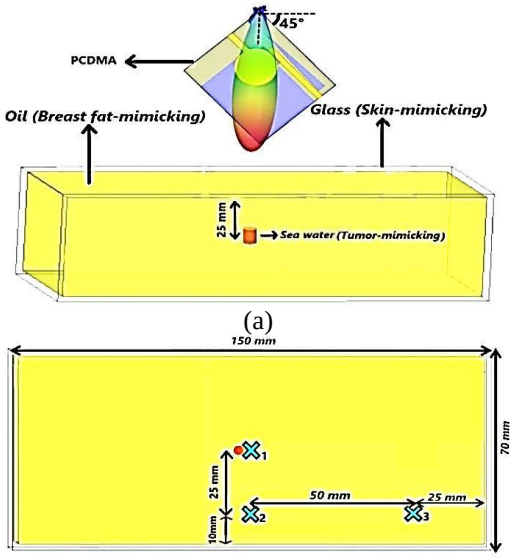

Fig. 3. Measurement configuration of the planar phantom: (a) front view with tumor, and (b) top view with tumor and measurement points.

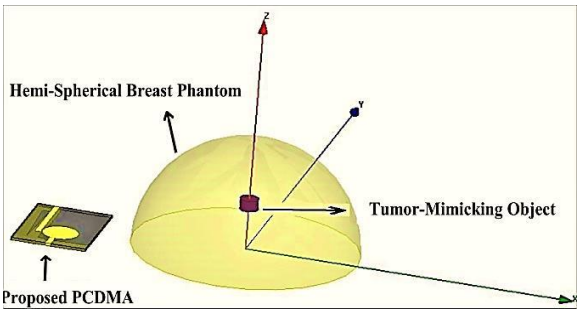

Fig. 4. Measurement configuration of the hemi-spherical phantom.

Firstly, the measurements are made when there wasn't a tumor in the phantoms. Then, the tumor-mimicking object is placed in the phantoms and the measurements are repeated as seen from Figs. 3 and 4. Since the direction of the main beam moves from φ=32 to φ=54 degrees as given from the Fig. 2, the antenna is positioned so that the direction of the main beam is as perpendicular as possible to the phantoms. In the measurements of the rectangular phantom, the measurement values recorded for different locations (X_1, X_2, X_3) as shown in Fig. 3 (b). In the measurements of the hemi-spherical phantom, the antenna is turned around the phantom 360 degrees by using the turn table, and the results are recorded one every 45 degrees.

III. MEASUREMENTS, RESULTS AND DISCUSSIONS

A. Experimental measurements

In the experiments, Anritsu MS2028C 10 kHz-20 GHz Vector Network Analyzer (VNA) and test port extension cable are used to send the microwave signals to the breast phantoms and to measure the signals reflected from them. Prior to the measurements, the VNA is calibrated over UWB (3-10 GHz in the present case) using a one-port calibration procedure [31]. The measurement systems using the rectangular and hemi-spherical phantoms are shown in Fig. 5 and Fig. 6, respectively.

The measurement of the planar phantom has been made in the laboratory. In order to minimize the reflections from the walls, desks and other equipments, two square absorbers (60x60 cm^2) and an isolation material is used during the measurement.

In the measurement of the hemi-spherical phantom, scanning the phantom 360 degrees is necessary to obtain successful results. For this aim, a turn table with an isolation material (foamed sealant) which is put to reduce the coupling effect and to align the phantom with the antenna is used in a fully anechoic chamber.

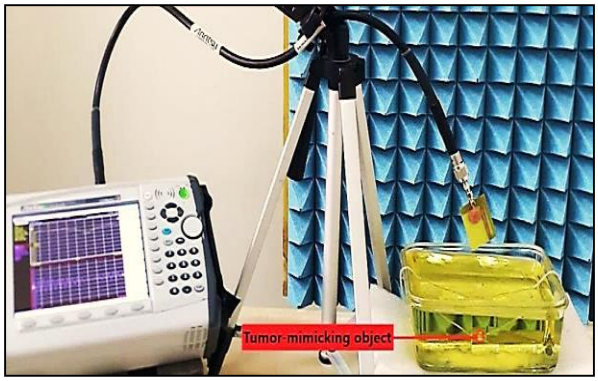

Fig. 5. The measurements for the planar phantom.

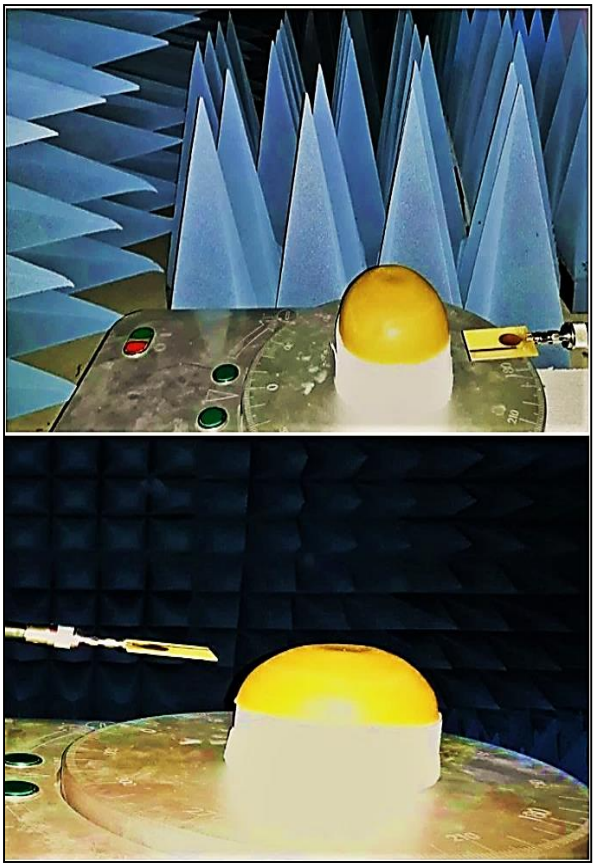

Fig. 6. The measurements for hemi-spherical phantom.

B. Results in the frequency domain

The measurement results for the planar phantom are given in the frequency domain. The measured S_{11} vs. frequency values for the cases of with and without tumor for the point of X_1 are shown in Fig. 7.

Also, the recorded S_{11} values for three locations (X_1, X_2, and X_3) are plotted in Fig. 8.

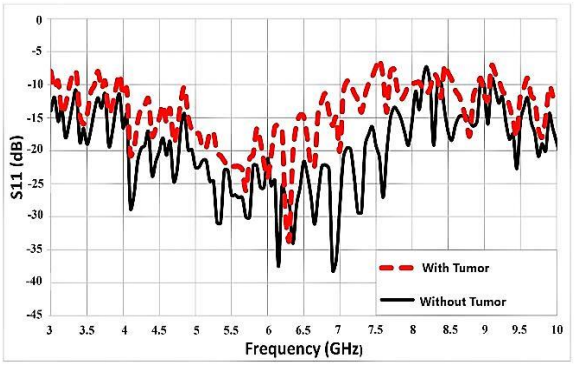

Fig. 7. S_{11} results in the frequency domain (at X_1 point).

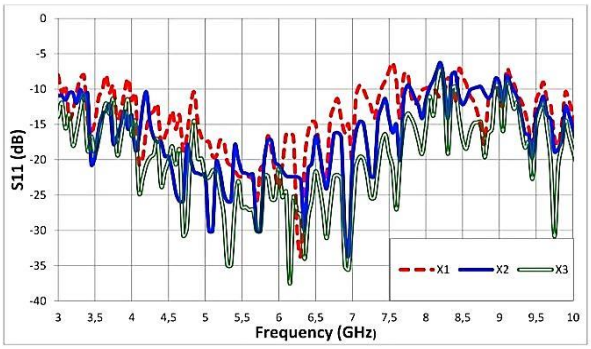

Fig. 8. S_{11} results for different locations (with tumor).

S_{11} and Γ values are related to each other according to the Equation (3) which means that the smaller the magnitude of S_{11}, the larger the reflection becomes [32]:

$$S_{11}(dB) = 20\log_{10}|\Gamma|. \quad (3)$$

As given before, there are significant differences in the electrical properties of the tumor and normal breast tissue in the microwave frequencies. So, the transmission of the microwaves is less (means that the reflection is high) when the tumor is present. Hence, the magnitude of S_{11} decreases over the working frequency in the tumorous case as it is seen from the Fig. 7. Furthermore, it is understood from the Fig. 8 that the reflected energy decreases when the antenna moves away from the tumor and vice versa.

The RL differences between the tumorous and non-tumorous cases can be seen more clearly in the range of 6 to 8 GHz. Hence, another important deduction from the Figs. 7 and 8 is that the best frequencies for tumor detection are these frequencies. However, in the detection process, not only 6-8 GHz range is used, but also all frequencies of 3-10 GHz range are used.

In another experiment, the object which was previously placed at a depth of 25 mm is placed at a depth of 45 mm. Then the measurements are performed again. S_{11} results for the point of X_1 when the tumor is buried at a deeper position are shown in Fig. 9.

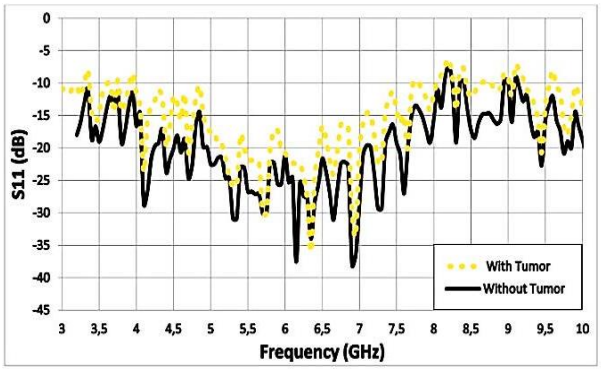

Fig. 9. S_{11} results for deeply buried tumor (at X_1 point).

C. Results in the time domain

The results for the hemi-spherical phantom are given in the time domain. In these measurements, a Gaussian pulse is emitted from the antenna. The pulse signal becomes narrower as the bandwidth of the antenna increases. Since the used antenna has the bandwidth of 7 GHz, it can send a narrow pulse signals. Thus, one of the processes required to obtain high resolution images is provided.

As mentioned before, the values of the reflected signals for tumorous and non-tumorous states are recorded in 8 positions where the antenna and tumor-mimicking object are at the height of 30 mm on the z axis. Since the object is at (x=0, y=0), the distance between the antenna and object remains same while the phantom is being scanned. So, the reflections from the 8 positions will be similar and showing one of the signals would be sufficient for observing the cases.

The emitted Gaussian signal and the reflected signal received by the antenna are shown in Fig. 10. Since a delay time would occur during the return of the transmitted signal, and the amplitude decreases due to the losses, it is seen from the Figs. 10 (a) and (b) that there are differences in the phase and amplitude of the sent and reflected signals. In the Fig. 10 (b), for the 1.5 to 2 ns interval, it is seen that the signal amplitude is higher in the tumorous case than amplitude of the non-tumorous case.

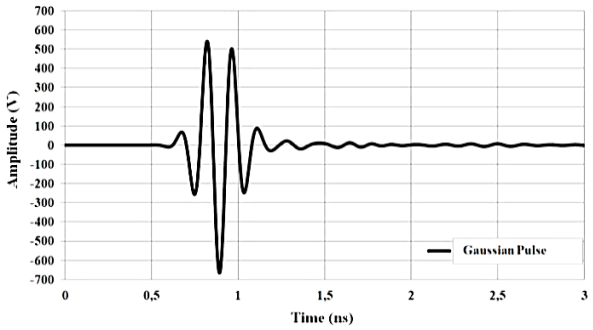

(a)

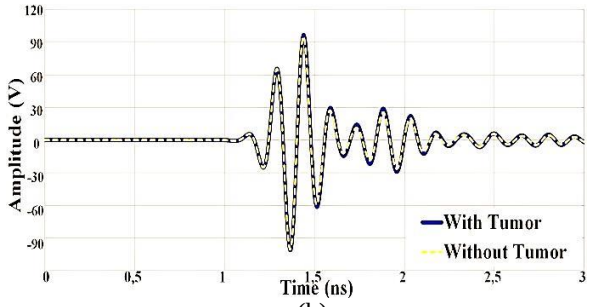

(b)

Fig. 10. (a) Gaussian pulse emitted from the antenna, and (b) reflected signals from the hemi-spherical phantom.

In another measurement, the tumor-mimicking object is placed at the point of (x=0, y=40, z=30) mm. Therefore, the distance between the antenna and object changes when the phantom is scanned. Hence, the signal values taken from 8 different points are at the different levels. The values when the antenna is at the closest and farthest to the tumor are given in Fig. 11.

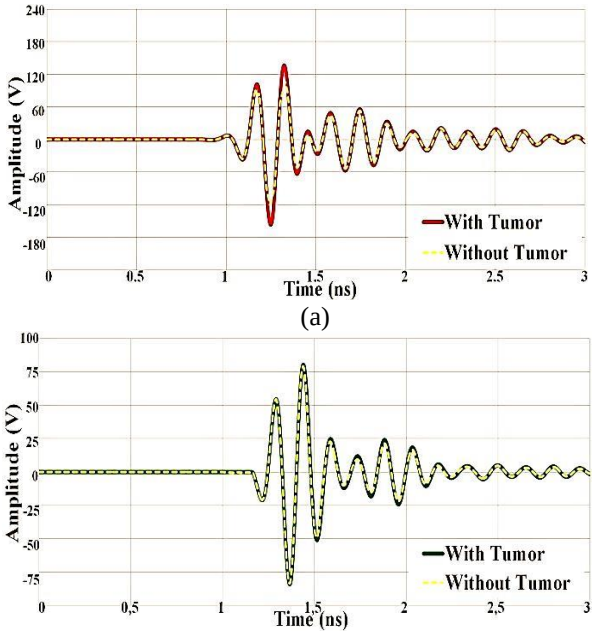

(a)

(b)

Fig. 11. Reflected time domain signals: (a) antenna is at the closest, and (b) antenna is at the farthest to the tumor.

As expected, it is seen from the Fig. 11 (a) that the amplitude of the reflected signal is higher in the tumorous case than amplitude obtained in the non-tumorous case. Further, since the tumor is closer to the surface and provides more reflections, this time the difference is greater than that of obtained in the Fig. 10 (b). Also, it is seen again that there is a phase difference between the Gaussian pulse and the reflected signal. However, this time it is not as much as in Fig. 10 (b) since the signal reaches to the tumor and reflects back from it in a less time.

When Fig. 11 (b) is examined, it is seen that the amplitude of the reflected signal is higher in the tumorous case. But, since the tumor is at a point far away from the surface and provides less reflections, this time the difference is less than that of obtained in the Fig. 10 (b). Also, it is seen again that there is a phase difference between the Gaussian pulse and the reflected signal. Since the signal reaches to the tumor and reflects back from it in a longer time, this time it is more than that of seen in Fig. 10 (b).

For a better understanding of the graphs, the amplitude differences of the tumorous and non-tumorous cases between 1.5 and 2 seconds for the different positions of the tumor are given in Table 1. The maximum amplitudes and phase differences of the reflected signals are also given in Table 2.

Table 1: Amplitude differences between the reflected signals of tumorous and non-tumorous situations (V)

Time (ns) / Tumor Position	**1,6**	**1,75**	**1,9**
Tumor is closest to the antenna	60–54=**6**	70–58=**12**	35–30=**5**
Tumor is at the center	30–27=**3**	19–15=**4**	31–27=**4**
Tumor is farthest to the antenna	29–27=**2**	18–16=**2**	30–28=**2**

Table 2: The maximum amplitudes and phase differences of the reflected signals

	Maximum Amplitude	**Starting Time**
Tumor is closest	130 V	0.9 ns
Tumor is at the center	95 V	1.1 ns
Tumor is farthest	80 V	1.25 ns

D. Imaging result

The measurements made up to this stage have been performed in the frequency and time domains. However, in order to make a more successful diagnosis, the obtained data must be converted into images.

The signals must be subjected to various processes such as pre-processing, filtering, calibration, energy calculation to create image. For this purpose, the calibration phase is carried out by taking the difference between the signal reflected from the tumor tissue and the signal reflected from the healthy tissue as suggested in the study of [33]. After obtaining the tumor response by the calibration process, the stage of obtaining the energy profile of the breast is started. For this aim, the

points in the breast are considered as pixels and the individual energies of these pixels are calculated. Then time delays are calculated and collected in order to determine the positions of the pixels. Finally, the image is created. In order to calculate the energy values, the delay-and-sum algorithm which has been used in many other studies like [34-36] is preferred.

As shown before, the time domain data from different positions have been obtained for the hemi-spherical phantom which has tumor-mimicking object at the (0, 0, 30 mm) position. The image that is created by using these data is given in Fig. 12. In the image, the object is seen as the black colour. It is known that the cylindrical object has a diameter of 6 mm and a height of 4 mm. So, it is expected to be seen as the size of 6 mm in the x-axis direction and the size of 4 mm in the z-axis direction. It is displayed as 6.6 mm and 3.6 mm in the created image. Hence, the size is determined with an accuracy rate of 90%. The center position of the object is displayed at the points of (x=-1 and z=31 mm) which is actually at the points of (x=0 and z=30 mm). Therefore, it can be said that the position is also determined with very high accuracy.

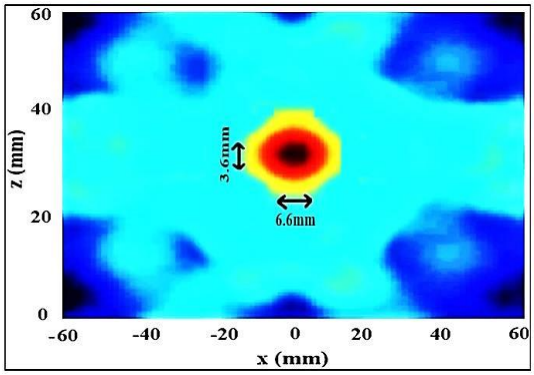

Fig. 12. A sample image showing the size and position of the tumor placed at the point of (x=0, y=0, z=30) mm.

E. Specific absorption rate considerations

Specific Absorption Rate (SAR) means a measure of the rate at which energy is absorbed by the human body when exposed to the electromagnetic field [37,38]. It is defined as the power absorbed per mass of tissue as expressed in (4):

$$SAR = \frac{\sigma |E|^2}{\rho}, \quad (4)$$

where σ is the conductivity (S/m) of the tissue, E is the internal electric field (V/m), and ρ is the mass density (kg/m^3).

It is necessary to observe whether the power levels for the operation of microwave breast cancer detection systems are lower than the acceptable SAR levels. International Commission on Non-Ionizing Radiation Protection (ICNIRP) accepts the SAR value to be 0.4 w/kg for those who are exposed to electromagnetic fields as a matter of professions (in controlled environment), and 0.08 w/kg for the public population (in uncontrolled environment). In addition to the limit values of whole body (WB), the limits of local SAR over 1g and 10g of the tissues are also determined [39]. These values are displayed in Table 3.

Table 3: SAR exposure limits in different environments

	SAR_{WB}	SAR_{1G}	SAR_{10G}
Controlled Environment	0.4	8	20
Uncontrolled Environment	0.08	1.6	4

Since the aim of this study is to make a measurement for breast tumor detection which is intended to be used in the hospitals, the standards for the controlled environment should be considered. Also, the tumor detection measurements involve the exposure of the breast to the electromagnetic fields locally. So, it is crucial to ensure that peak SAR values conform to the standards set for the maximal peak averaged over a small amount of mass as opposed to WB average [40].

In this study, the SAR distributions are obtained for 1.0g volume of tissue with the aid of HFSS program. According to the simulation results obtained at 7 GHz, the maximum average SAR1g value of fatty tissue without tumor is 1.2292 W/kg. When the 6 mm sized tumor is located to the (0,0,30 mm) point, the maximum average SAR1g values of the fatty tissue and tumor are 3.6091 W/kg and 6.8817 W/kg, respectively. The results show that, the SAR values of the breast tissue for the tumorous and non-tumorous cases are below the determined limit values.

It is seen from the SAR values that a large amount of power is absorbed on the tumor concealed area due to the high dielectric property of the tumor tissue. Similarly, the SAR values over the breast fat are lower for non-tumorous case compared to the tumorous case. So, it is understood that measuring the SAR values is helpful to determine the presence and position of the tumor. The maximum SAR coordinate in the breast with 6 mm tumor is obtained as (-1.8, 2.1, 28.8 mm) where the actual center position of tumor is (0, 0, 30 mm). Hence, the coordinates of the corresponding maximum value of SAR can be identified for detecting the locations of tumor inside the breast.

F. Comparison with the similar studies

Several compact-sized UWB antenna designs have been proposed for the radar systems, see-through-wall imaging, wireless communications applications, cognitive radio applications, C and X bands operations, and medical imaging [41-60]. Each has its own advantages

and drawbacks. Some of these antennas exhibit omnidirectional radiations whereas some others have directional radiation patterns. For the performance analysis of the used PCDMA, a comparison with the antennas of [41-60] is given in Table 4. According to this table, the bandwidth is increased, the HPBW values are reduced and the directivity is improved with compared to the some works reported in the literature.

In the studies of [53-60], not only antenna designs were made, but also measurements were performed for the breast cancer detection. Thus, the performances of the antennas in the MI systems were investigated. But, many conditions such as measurement environments, designed antennas, constructed phantoms, used VNA devices and the methods preferred for the image generation are different in these studies. Hence, it is not possible to compare the results of our study clearly with the results given in other studies. However, we have tried to make a comparison with the studies [53-60] that have the systems which are similar to our study with respect to the measurement environment and phantom structures. These comparisons are given in Table 5.

Table 4: Comparison of the performance of the used antenna with the antennas reported in some previous work

Reference Antenna	Size (mm)	Frequency Band (GHz)	Bandwidth (%)	Radiation Type	HPBW Moves (°)	Gain (dB)
[41]	32 x 30	3.1 - 14.0	127.5	Omnidirectional	--- [1]	2.2 - 6.0
[42]	32 x 24	3.9 - 11.0	114	Omnidirectional	--- [1]	1.7 - 5.3
[43]	32 x 24	2.7 - 12.0	126.5	Omnidirectional	--- [1]	0.5 - 5.5
[44]	18 x 12	3.02 - 15.21	133	Omnidirectional	--- [1]	--- [1]
[45]	50 x 46	3.1 - 12.6	120	Directional	75 - 25	4.0 - 8.0
[46]	50 x 50	6.0 - 8.0	28	Directional	47 - 37	--- [1]
[47]	32 x 30	4.2 - 8.5	68	Directional	78 - 43	5.2 - 9.3
[48]	50 x 50	4.0 - 9.0	77	Directional	56 - 25	7.0 - 10.0
[49]	40 x 26	1.0 - 8.0	155	Directional	--- [1]	--- [1]
[50]	50 x 50	4.1 - 11.5	95	Directional	49 - 22	2.5 - 8.4
[51]	50 x 50	3.1 - 11.0	112	Directional	--- [1]	4.3 - 10.8
[52]	50 x 40	3.0 - 8.0	91	Directional	60 - 40	5.0 - 6.8
[53]	62.5 x 62.5	2.0 - 4.0	66	Directional	--- [1]	--- [1]
[54]	50 x 50	2.75 - 11.0	126	Directional	--- [1]	--- [1]
[55]	36 x 36	2.5 - 10.4	122	Directional	--- [1]	1.0 - 9.0
[56]	40 x 40	3.6 - 8.0	76	Directional	--- [1]	3.8 - 7.0
[57]	73.5 x 42	3.0 - 10.0	108	Directional	--- [1]	2.5 - 10.0
[58]	27.3 x 14	4.5 - 10.5	80	Directional	--- [1]	--- [1]
[59]	63 x 51	2.5 - 8.5	109	Directional	--- [1]	2.0 - 7.5
[60]	80 x 44	2.4 - 18.0	153	Directional	--- [1]	--- [1]
Used Antenna	**55 x 40**	**3.0 - 10.0**	**108**	Directional	**56 - 30**	**6.0 - 8.4**

Table 5: Comparison of the performance of this study with the measurements reported in some previous work

Reference	Antenna Type	Phantom Type	Shape and Size of the Tumor
[53]	Bow-tie	With Skin (2 mm)	Ellipsoid - (L=15mm & W=5mm)
[54]	Probe	With Skin (Thin)	Spherical - 5 mm
[55]	Tapered-Slot	Without Skin	Cylindrical Pipe (H=20mm & R=5mm)
[56]	Planar Plate	With Skin (4 mm)	Cylindrical - 4.5 mm
[57]	Slotted Vivaldi	With Skin (1 mm)	Spherical - 10 mm
[58]	Vivaldi	With Skin (2 mm)	Spherical - 10 mm
[59]	Vivaldi	With Skin (Thin)	Cylindrical Pipe (H = 20mm & R = 2.5mm)
[60]	Antipodal Vivaldi	With Skin (Thin)	Cylindrical - 16 mm
This Study	**PCDMA**	**With Skin in Planar & Without Skin in Hemi-Spherical**	**Cylindrical - 6 mm**

IV. CONCLUSION

In this study, firstly it was mentioned that the success rate of the breast cancer treatment is very high if it is detected at an early stage. Then, early detection methods of the breast cancer were introduced. The radar-based UWB MI system which is one of the emerging methods was explained in detail. After that, it was emphasized that the used antenna is very critical to radiate and receive the pulses in this system.

In the study, the compact-sized UWB directional antenna was used in the experimental measurements and the performance of it was investigated which was the main purpose of this study. For the experiments, the breast phantoms with different shapes and materials were formed. A 6 mm object having similar electrical properties to the malignant tumor was placed in the phantoms, and the measurements have been made in the different domains. According to the both frequency and time domain results, it was concluded that the presence of the tumor could be clearly determined. In addition, inferences about the position and size could be made. But, in order to make more clear observation, the reflected signals were converted into image. Thus, the location and size of the tumor was detected successfully. Hence, the other aim of the study was achieved. Furthermore, SAR consideration for the breast was made. As a conclusion, in this study it was demonstrated that the UWB and directive PCDMA is capable of detecting small tumors in a radar-based UWB microwave breast cancer detection system which is a new method having some features supporting existing detection methods.

ACKNOWLEDGMENT

This research is related to the Ph.D study of A. R. Celik and supported by the Researching Projects Committee of the University of Dicle (DUBAPK) with the project number MUHENDISLIK.17.011. We are grateful to DUBAPK for financial assistance.

REFERENCES

[1] World Health Organization: WHO, Breast cancer awareness, Available: http:// www.who.int/cancer/ breast_cancer_awareness/en, 2017.

[2] M. Weiss, "Your guide to the breast cancer pathology report," http://www.breastcancer.org, 2017.

[3] E. C. Fear and M. A. Stuchly, "Microwave detection of breast cancer," *IEEE Transactions on Microwave Theory and Techniques*, vol. 48, pp. 1854-1863, 2000.

[4] X. Li and S. C. Hagness, "A confocal microwave imaging algorithm for breast," *IEEE Microwave and Wireless Components Letters*, vol. 11, pp. 130-132, 2001.

[5] E. J. Bond, X. Li, S. C. Hagness, and B. D. Van Veen, "Microwave imaging via space-time beamforming for early detection of breast cancer," *IEEE Transactions on Antennas and Prop.*, vol. 51, pp. 1690-1705, 2002.

[6] M. Klemm, I. Craddock, J. Leendertz, A. Preece, and R. Benjamin, "Radar-based breast cancer detection using a hemispherical antenna array-experimental results," *IEEE Transactions on Antennas and Propagation*, vol. 57, pp. 1692-1704, 2009.

[7] A. K. Alqallaf, R. K. Dib, and S. F. Mahmoud, "Microwave imaging using synthetic radar scheme processing for the detection of breast tumors," *Applied Computational Electromagnetics Society (ACES) Journal*, vol. 31, no. 2, pp. 98-105, 2016.

[8] S. Sadeghi and R. Faraji-Dana, "A practical UWB microwave imaging system using time-domain DORT for tumor detection," *ACES Journal*, vol. 31, no. 6, pp. 692-699, 2016.

[9] O. Güren, "Surface impedance based microwave imaging method for breast cancer screening," *Istanbul Technical University*, Turkey, *PhD*, 2014.

[10] E. C. Fear, X. Li, S. C. Hagness, and M. A. Stuchly, "Confocal microwave imaging for breast cancer detection: Localization of tumors in three dimensions," *IEEE Transactions on Biomedical Engineering*, vol. 49, pp. 812-822, 2002.

[11] A. R. Celik, "Detection of the breast tumors by ultra-wideband radar based microwave method," *Dicle University*, Diyarbakir, Turkey, *PhD*, 2018.

[12] F. Ulaby, *Fundamentals of Applied Electromagnetics*. Prentice Hall, Washington DC, 2006.

[13] M. Islam, M. T. Islam, M. R. I. Faruque, M. Samsuzzaman, N. Misran, and H. Arshad, "Microwave imaging sensor using compact metamaterial UWB antenna with a high correlation factor," *Materials*, vol. 8, pp. 4631-4651, 2015.

[14] X. Xiao and T. Kikkawa, "Influence of the organism interface on the breast cancer detection by UWB," *Applied Surface Science*, vol. 255, pp. 597-599, 2008.

[15] H. Zhang, T. Arslan, and B. Flynn, "A single antenna based microwave system for breast cancer detection: experimental results," *Loughborough Antennas & Propagation Conference*, UK, 2013.

[16] J. J. Golezani, "Directional wide band printed monopole antenna for use in microwave breast cancer imaging," *Istanbul Technical University*, *MS*, 2012.

[17] A. R. Celik and M. B. Kurt, "Development of a novel ultra-wideband, stable and high directive monopole disc antenna for radar-based microwave imaging of breast cancer," *Journal of Microwave Power and Electromagnetic Energy*, vol. 52, no. 2, pp. 75-93, 2018.

[18] J. M. Sill and E. C. Fear, "Tissue sensing adaptive

radar for breast cancer detection - experimental investigation of simple tumor models," *IEEE Trans. on Microwave Theory and Techniques*, vol. 53, pp. 3312-3319, 2005.

[19] Y. Xie, B. Guo, L. Xu, J. Li, and P. Stoica, "Multi-static adaptive microwave imaging for early breast cancer detection," *39th Asilomar Conference on Signals, Systems, and Computers*, CA, USA, 2005.

[20] Y. Li, W. Li, Q. Ye, and R. Mittra, "A survey of planar ultra-wideband antenna designs and their applications," in *Forum for Electromagnetic Research Methods and application Technologies (FERMAT)*, ID: Li-ART-2014-01-002, pp. 1-6, 2014.

[21] P. M. Meaney, K. D. Paulsen, A. Hartov, and R. K. Crane, "An active microwave imaging system for reconstruction of 2-D electrical property distributions," *IEEE Transactions on Biomedical Engineering*, vol. 42, pp. 1017-1026, 1995.

[22] I. Craddock, R. Nilavalan, J. Leendertz, A. Preece, and R. Benjamin, "Experimental investigation of real aperture synthetically organised radar for breast cancer detection," *IEEE on Antennas and Propagation Society International Symposium*, Washington, DC, USA, 2005.

[23] S. Adnan, R. A. Abd-Alhameed, M. Usman, C. H. See, J. M. Noras, and M. B. Child, "Simulation and experimental measurements for near field imaging," *Progress In Electromagnetics Research Symposium*, Malaysia, 2012.

[24] J. D. Garrett and E. C. Fear, "Average dielectric property anlaysis of complex breast tissue with microwave transmission measurements," *Sensors*, vol. 15, pp. 1199-1216, 2015.

[25] S. Vedantham, A. Karellas, G. R. Vijayaraghavan, and D. B. Kopans, "Digital breast tomosynthesis: State of the art," *Radiology*, vol. 277, no. 3, pp. 663-684, 2015.

[26] N. Kiarashi, A. C. Nolte, G. M. Sturgeon, W. P. Segars, S. V. Ghate, L. W. Nolte, E. Samei, and J. Y. Lo, "Development of realistic physical breast phantoms matched to virtual breast phantoms based on human subject data," *Medical Physics*, vol. 42, no. 7, pp. 4116-4126, 2016.

[27] B. J. Mohammed, "Design and implementation of microwave imaging systems for medical applications," *The University of Queensland School of Information Technology and Electrical Engineering*, Australia, *PhD*, 2014.

[28] M. E. Bialkowski, "Ultra wideband microwave system with novel image reconstruction strategies for breast cancer detection," *40th European Microwave Conference*, France, 2010.

[29] W. C. Khor and M. E. Bialkowski, "Investigations into cylindrical and planar configurations of a microwave imaging system for breast cancer detection," *IEEE Antennas and Propagation Society International Symposium*, Albuquerque, 2006.

[30] B. Riddle, J. B. Jarvis, and J. Krupka, "Complex permittivity measurements of common plastics over variable temperatures," *IEEE Transactions on Microwave Theory and Techniques*, vol. 51, no. 3, 2003.

[31] Anritsu Measurement Guide, "Vector network analyzer for Anritsu RF and microwave handheld instruments," *Anritsu Company*, USA, 2016.

[32] C. A. Balanis, *Antenna Theory: Analysis and Design*. Wiley, New Jersey, USA, 2015.

[33] E. C. Fear, S. C. Hagness, P. M. Okoniewski, and M. Stuchly, "Enhancing breast tumor detection with near-field imaging," *IEEE Microwave Magazine*, vol. 3, no. 1, pp. 48-56, 2002.

[34] Y. Zhao, W. Shao, and G. Wang, "UWB microwave imaging for early breast cancer detection: Effect of two synthetic antenna array configurations," *IEEE International Conference on Systems, Man., & Cybernetics*, The Hague, Netherlands, 2004.

[35] M. Klemm, I. J. Craddock, J. A. Leendertz, A. Preece, and R. Benjamin, "Improved delay-and-sum beamforming algorithm for breast cancer detection," *International Journal of Antennas and Propagation*, pp. 1-9, 2008.

[36] G. Matrona, A. S. Savoia, G. Caliano, and G. Maganes, "The delay multiply and sum beam-forming algorithm in ultrasound B-mode medical imaging," *IEEE Transactions on Medical Imaging*, vol. 34, no. 4, pp. 940-949, 2014.

[37] S. I. Al-Mously and M. M. Abousetta, "A study of the hand on the EM interaction of a cellular handset and a human," *World Academy of Science, Engineering and Technology International Journal of Electronics and Communication Engineering*, vol. 2, no. 2, 2008.

[38] D. Yin, M. L. Li, and J. L. Li, "Non-invasive breast cancer thermotherapy studies using conformal microstrip antennas," in *Proc. ISAPE2012*, pp. 159-162, 2012.

[39] "International commission on non-Ionizing protection (ICNIRP) 1998 - Guidelines for limited exposure to time varying electric, magnetic and electromagnetic fields (up to 300 GHz)," *Health Physics*, vol. 74, no. 4, pp. 494-522, Apr. 1998.

[40] P. Bernardi, M. Cavagnaro, S. Pisa, and E. Piuzzi, "Specific absorption rate and temperature elevation in a subject exposed in the far-field of radio-frequency sources operating in the 10-900-mhz range," *IEEE Trans. Biomed. Eng.*, vol. 50, pp. 295-304, 2003.

[41] Y. Li, W. Li, and Q. Ye, "A reconfigurable triple notch band antenna integrated with defected

microstrip structure band-stop filter for ultra-wideband cognitive radio applications," *International Journal of Antennas and Propagation*, vol. 2013, Article ID:472645, pp. 1-13, 2013.

[42] Y. Li, W. Li, and W. Yu, "A switchable UWB slot antenna using SIS-HSIR and SIS-SIR for multi-mode wireless communications applications," *Applied Computational Electromagnetics Society (ACES) Journal*, vol. 27, no. 4, pp. 340-351, 2012.

[43] Y. Li, W. Li, and Q. Ye, "A compact circular slot UWB antenna with multimode reconfigurable band-notched characteristics using resonator and switch techniques," *Microwave and Optical Technology Letters*, vol. 56, no. 3, pp. 570-574, 2014.

[44] N. Ojaroudi, M. Ojaroudi, N. Ghadimi, and M. Mehranpour, "UWB square monopole antenna with omni-directional radiation patterns for use in circular cylindrical microwave imaging systems," *ACES Journal*, vol. 28, no. 2, pp. 123-129, 2013.

[45] M. Mokhtaari and J. Bornemann, "Directional ultrawideband antennas in planar technologies," in *Proc. 38th European Microwave Conference*, Amsterdam, Netherlands, 2008.

[46] A. Locatelli, D. Modotto, F. M. Pigozzo, S. Boscolo, E. Autizi, C. D. Angelis, A. D. Copabianco, and M. Midrio, "Highly directional planar ultrawide band antenna for radar applications," *European Microwave Conference*, Munich, Germany, 2007.

[47] F. Zhu, S. Gao, A. T. S. Ho, T. W. C. Brown, J. Z. Li and J. D. Xu, "Low-profile directional ultra-wideband antenna for see-through-wall imaging applications," *Progress In Electromagnetics Research*, vol. 121, pp. 121-139, 2011.

[48] J. J. Golezani, M. Abbak, and I. Akduman, "Modified directional wide band printed monopole antenna for use in radar and microwave ımaging applications," *Progress In Electromagnetics Research Letters*, vol. 33, pp. 119-129, 2012.

[49] I. Unal, B. Turetken, and C. Canbay, "Spherical conformal bowtie antenna for ultrawide band microwave imaging of breast cancer tumor," *Applied Computational Electromagnetics Society (ACES) Journal*, vol. 29, no. 2, pp. 124-133, 2014.

[50] M. L. Meena, M. Kumar, G. Parmar, and R. S. Meena, "Design analysis and modeling of directional UWB antenna with elliptical slotted ground structure for applications in C- & X-bands," *Progress In Electromagnetics Research-C*, vol. 63, pp. 193-207, 2016.

[51] A. M. Abbosh, "Directive antenna for ultra-wideband medical imaging systems," *International Journal of Antennas and Propagation*, pp. 1-6, 2008.

[52] A. R. Celik, "Simulation measurement for detection of the breast tumors by using ultra-wideband radar-based microwave technique," *International Research Journal of Engineering and Technology*, vol. 5, no. 11, pp. 1521-1525, 2008.

[53] X. Yun, E. C. Fear, and R. H. Johnston, "Compact antenna for radar-based breast cancer detection," *IEEE Transactions on Antennas and Propagation*, vol. 53, no. 8, pp. 2374-2380, 2005.

[54] W. C. Khor, M. E. Bialkowski, A. Abbosh, N. Seman, and S. Crozier, "An ultra wideband microwave imaging system for breast cancer detection," *IEICE Transactions on Communications*, vol. E90B, no. 9, pp. 2376-2381, 2007.

[55] M. Bialkowski and Y. Wang, "UWB cylindrical microwave imaging system employing virtual array antenna concept for background effect removal," *Microwave and Optical Technology Letters*, vol. 53, no. 5, pp. 1100-1104, 2011.

[56] S. Adnan, "Ultra-wideband antenna design for microwave imaging applications," *School of Eng., Design, and Tech. University of Bradford*, *PhD*, 2012.

[57] Y. Zhang, "Microwave imaging for ultra-wideband antenna based cancer detection," *The University of Edinburgh*, Scotland, *PhD*, 2014.

[58] I. Unal, "A new ultrawide-band (UWB) microwave imagıng system with minimized mutual coupling effects for breast tumor detection," *Yeditepe University*, Istanbul, Turkey, *PhD*, 2013.

[59] M. Abbak, "Antenna and measurement system for microwave imaging of breast tumors," *Istanbul Technical University*, *PhD*, 2015.

[60] M. A. Elahi, B. R. Lavoie, E. Porter, M. Glavin, E. Jones, E. C. Fear, and M. O'Halloran, "Comparison of radar-based microwave imaging algorithms applied to experimental breast phantoms," *32nd International Union of Radio Science General Assembly & Scientific Symposium*, Montreal, 2017.

Ali Recai Celik received his B.Sc. from the Gaziantep University, M.Sc. from the Sutcu Imam University and Ph.D. from the Dicle University, all in Rlectrical and Electronics Engineering. Since 2013, he has worked as a Research Assistant at Dicle University. His research interests are mainly antenna design and nondestructive testing of materials.

Muhammed Bahaddin Kurt received the B.Sc. and M.Sc. degrees from the Hacettepe University, Ankara in 1992 and 1996, respectively and Ph.D. degree from the Sakarya University, Turkey in 2002, all in Electrical and Electronics Engineering. He has been a member of Dicle University as an Assistant Professor since 2005 and as an Associate Professor since 2018. His research interests are mainly computational electromagnetics, microstrip patch antennas, and nondestructive testing of material.

Selcuk Helhel received his B.S. E.E. from Hacettepe University (1993), M.S. E.E. from Gebze Institute of Technology (1997) and Ph.D. E.E. from Sakarya University (2005). He has been a member of Akdeniz University as an Assistant Professor since 2006 and as a Full Professor since 2012. His research interests are microwave propagation, radar systems, EMC, EMI, WiMAX and WiMAX based video transmission, and capacity planning for telecommunication systems.

Design and Implementation of Frequency Selective Radome for X-Band Applications

Cumhur Topcuoglu [1], Cihan Dogusgen Erbas [2], and Nurhan Turker Tokan [1]

[1] Department of Electronics and Communication Engineering
Yildiz Technical University, Istanbul, 34220, Turkey
f0518053@std.yildiz.edu.tr, nturker@yildiz.edu.tr

[2] Department of Electrical and Electronics Engineering
Istanbul Yeni Yuzyil University, Istanbul, 34010, Turkey
cihan.dogusgen@yeniyuzyil.edu.tr

Abstract ─ A triple layer X-band FSS is designed and its reflection and transmission characteristics are explored for normal/oblique incidence. The proposed planar FSS is confirmed by simulation and measurement results. Then, by using the X-band FSS, a novel X-band radome is designed. Its reflection and transmission characteristics are investigated for in-band and out-of band frequencies by integrating an ultra-wide band antenna. A comparison of radiation patterns at selected frequencies for cases with and without radome is examined. Adaptation of radome to the antenna is achieved without significant reduction in radiation performance at the design frequency of FSS.

Index Terms ─ Endfire radiation, frequency selective radome, unit cell, Vivaldi antenna.

I. INTRODUCTION

Frequency selective surfaces (FSSs) are planar periodic structures composed of either slot or patch elements that interact with electromagnetic waves within certain frequency band(s). They act as analogue spatial filters such that these spatial filters transmit or block waves in a specific frequency band of interest. Design process of the FSSs involves a proper choice of topology characteristics such as unit cell type and geometry, spacing between unit cells, substrate permittivity and thickness as well as presence or absence of superstrates in order to obtain the desired spectral selectivity. FSSs have a wide range of applications in electromagnetic spectrum, including radar cross section (RCS) reduction, electromagnetic interference reduction, millimeter and terahertz wave operations, antenna reflectors, quasi-optical filters, polarizers and switches [1-5].

A substantial amount of research has been conducted on the FSSs as they have unique properties and a large number of practical uses. Various FSS elements such as center connected structures (e.g., dipoles, tripoles, square spirals, Jerusalem crosses), circular, square and hexagonal loops along with numerous shapes have been intensively analyzed [6-8]. Varactor, Schottky and PIN diodes have also been embedded in active FSS design for the reconfiguration of these FSSs, while inductors are utilized as control lines [9-11]. Recently, FSSs with different unit cell geometries have been used as ground planes of microstrip patch antennas as well [12-14]. Several studies have addressed different aspects of FSSs such as mutual coupling reduction of antenna arrays, and shielding applications [15, 16]. Optimization-based design of the FSSs is also possible [17].

Another specific application of FSSs is radomes. A radome protects an antenna from outer environment with smallest effect on the radiation properties of the antenna within a frequency band of interest. Performance of a radome depends on matching its configuration and materials composition to a particular application and RF frequency range. A radome produced by curved FSSs acts as a bandpass filter that allows transmission in an operating frequency band, and reflection out of the band. It is usually difficult or impossible to control the RCS of antennas over a wide frequency range. Instead of shielding the antenna to protect it from a threat radar, which blocks the antenna operation, it is a wiser approach to cover the antenna with an FSS radome that is transparent at the operating frequency band, yet opaque at the threat radar frequency.

Although the usage of FSSs as a protective radome leads to a considerable reduction in the RCS of the enclosed antenna outside the operating band, it might affect the electrical performance of the antenna in terms of polarization purity reduction, sidelobe level increase, transmission losses, degradation in impedance matching properties, tilting of the main beam, and strong undesired electromagnetic interference. Hence, accurate radome design and production using FSSs are important.

Several studies have been reported on FSS radome design: Liu et al. [18] investigated the effect of incidence

Submitted On: March 7, 2019
Accepted On: May 23, 2019

angle and polarization on bandwidth stability for a proposed FSS structure for radomes. Angular instability was observed in the presented results. Qu et al. [19] designed a cylindrical radome based on a graphene FSS that has a tunable bandpass filtering characteristic. Sensitivity analysis for different incidence angles was not carried out in that study. Lin et al. [20, 21] developed an axi-symmetric conical FSS radome in S-band and another miniature conical thick-screen FSS in C-band, then explored the impact of these radomes on monopole antennas. Impact of the designed radomes on gain performance was unkown. Combination of different materials with FSS structures have also been of interest. In one study [22], a modified silica ceramic was developed and used in Jerusalem FSS. It was concluded that the modified substance could be used as a dielectric material for FSS radomes. Choi et al. [23] formed an X-band hybrid composite low-observable radome that consisted of a composite sandwich construction including E-glass/aramid/epoxy hybrid composite faces, a polymethacrylimide foam core and an FSS.

In this article, firstly, a triple layer X-band FSS is designed. Its reflection and transmission characteristics planar FSS is confirmed by simulation and measurement results. In the experimental verification, a waveguide measurement setup is used. Next, a novel X-band radome is designed by using a triple layer X-band FSS. Its reflection and transmission characteristics are investigated for in-band and out-of band frequencies by integrating an UWB Vivaldi as the antenna inside the radome. Design steps of the FSS radome are explained. Radiation pattern simulations at 8, 10, 12 GHz are presented. It is found that radiation properties of the antenna are not significantly affected by the coverage of the FSS radome for in-band frequencies of the FSS structure. Moreover, a flat top transmission feature is obtained. All simulations are performed with CST Microwave Studio, a commercial Finite Integration Technique (FIT) based software package. FIT is a spatial discretization technique to numerically solve electromagnetic problems in both time and frequency domain. In the process, basic topological properties of the continuous equations are preserved. The basic idea of this approach is to apply the Maxwell equations in integral form to a set of staggered grids. Thus, the accuracy and performance of a simulation in CST are heavily dependent on the quality of the mesh that describes the structure. Achieving very high mesh quality leads to more qualitative definition of the problem space. In this work, analysis process is performed in CST by using the adaptive mesh refinement to obtain better accuracy with less unknowns, especially in simulations with radome.

II. GEOMETRY OF UNIT CELL

Designed planar FSS consists of 3-layer periodic unit cells. Each unit cell has a circular metallic structure at the top and bottom layers, and a square metal part with a cross-shaped slot as the middle layer. A dielectric material fills the inter-layer volume. After a series of optimizations for the unit cell parameters and the dielectric profile, dimensions of the unit cell are obtained for X-band characteristics. Also, the dielectric material, which affects the unit cell capacitance as well as reflectance at the air-dielectric interface, is determined. Diameter of the metallic circle is denoted by D, while the arm length and width of the cross-shaped slot are expressed by L_p and W_p, respectively. Edge of the metal square in the middle layer is denoted by W. The FSS is implemented on a commercially available Rogers RO4003C high-frequency laminate with a 0.51 mm dielectric thickness and 17.5 um copper. The laminates are bonded to each other by using spray glue, which has negligible effect on electromagnetic performance [24]. The dielectric material has a relative dielectric constant of $\varepsilon_r = 3.38 \pm 0.05$, and a loss tangent of 0.0035 at 10GHz. Low dielectric loss of this laminate facilitates its use in many applications where higher operating frequencies limit the use of conventional circuit board laminates. Figure 1 shows the unit cell geometry, and Table 1 illustrates the dimensions of the unit cell. Since the array is considered as infinite in size, *y*- and *x*-boundaries are set to unit cell of the array. Floquet ports are defined at the *z*-boundaries.

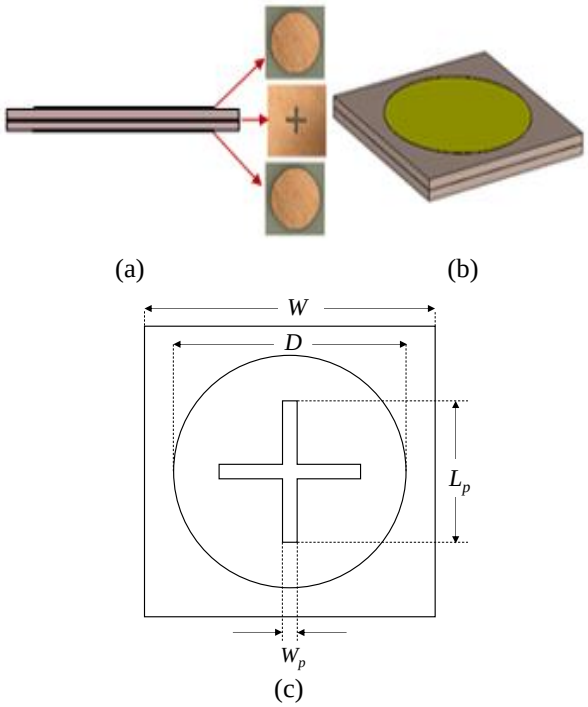

Fig. 1. Unit cell of the designed FSS: (a) side view, (b) perspective view, and (c) top view with design parameters.

Table 1: Dimensions of the unit cell for the proposed FSS

Parameter	Dimension (mm)
W	10
L_p	3.5
W_p	0.4
D	8.19

A parametric analysis is carried out to realize the identified design requirements. Our investigations (not shown here for brevity) demonstrate that top of the transmission curve occurs at smaller frequencies as W becomes larger and smaller resonant frequencies occur as L becomes larger. This is due to the increase of equivalent inductance with increasing L.

Resonant frequency of the unit cell is calculated as:

$$f = \frac{1}{2\pi\sqrt{L_U C_U}}, \quad (1)$$

where L_U and C_U are the equivalent inductance and equivalent capacitance of the unit cell, respectively. As the slot length L_p increases, the resonant frequency decreases because path length of the current increases. Lower resonant frequencies are observed as the parameter D increases. Furthermore, a flat top transmission is obtained for all D values. An increase in the dielectric constant of the dielectric material results in an increase in capacitance, which results in a decrease in the resonant frequency.

It is useful to explore the effect of incidence angle on the reflection and transmission coefficients as well. Figure 2 illustrates the incident wave that impinges on the unit cell with an angle of θ. A set of incidence angles between θ=0^O and θ=50^O with an increment of $\Delta\theta$=10^O is applied. Although resonant frequency remains unchanged with varying incidence angles, as verified by Fig. 3, the reflection coefficient becomes larger at the resonant frequency as the incidence angle increases. In order to cover a larger range of incidence angles, reflection and transmission coefficients simulated between θ=0^O and θ=90^O are depicted in Fig. 4.

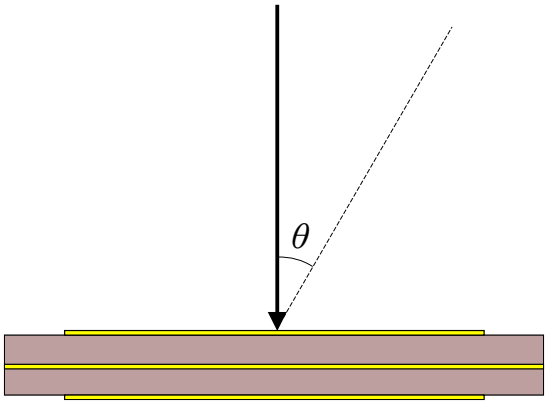

Fig. 2. Incident wave on unit cell.

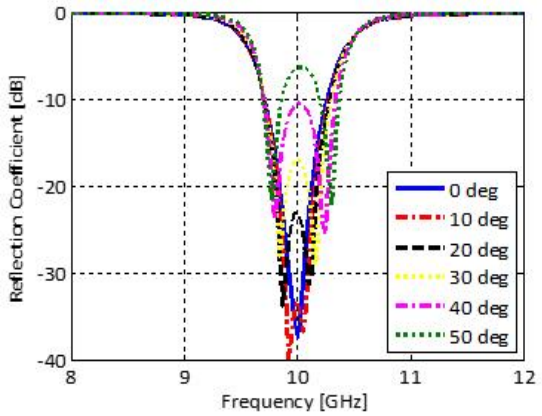

Fig. 3. Sensitivity analysis of the EM wave: reflection coefficient.

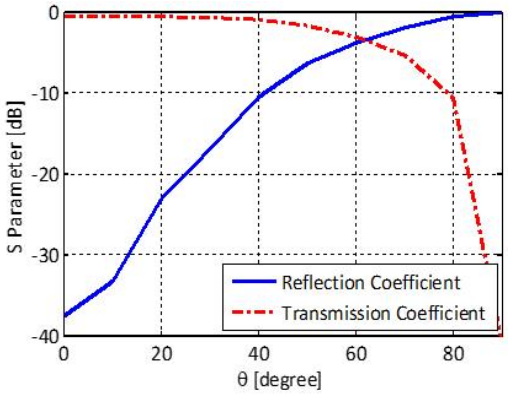

Fig. 4. Sensitivity analysis of the EM wave: comparison of reflection and transmission coefficients.

III. PLANAR FSS MEASUREMENT RESULTS

The planar FSS is theoretically infinite in extent and lies in x-y plane. Taking the two-dimensional periodicity into account, the analysis of the FSS is simplified by use of the Floquet's theorem. Practically, size of the FSS has to be limited, which is 80x80 mm (in x-y plane) consisting of 8 by 8 unit cells. Incident wave propagates in z-direction. Oblique plane waves can also impinge on the structure.

In order to verify the simulation results, the proposed FSS structure is fabricated and tested. In the fabrication process of the FSS, chemical etching technique with photolithography is employed. For the periodic structures such as FSSs, the waveguide transmission lines can be used for the measurement [25-26]. Thus, a waveguide measurement setup is used. The measurement system is illustrated in Fig. 5 (a) and Fig. 5 (b) shows the prototype of the three-layer FSS with the top array visible. The sample FSS was fitted properly within the waveguide

flanges. Part of the fabricated FSS structure and WR-90 waveguide used in the measurement are shown in Fig. 5 (b). Anritsu MS4644A 2-port vector network is used in measurements. Waveguide to coaxial adapter is used at both sides for transition. With this measurement setup, the transmission and the reflection coefficients of the FSS are measured for the dominant mode (TE_{10}). Note that due to planar behavior of the structure, the resonant frequency does not depend on the size of the FSS [27].

Figure 6 and Fig. 7 depict the measured as well as simulated results of the reflection and transmission coefficients, respectively, versus frequency. As seen from the figures, measurements and simulations are in good agreement for reflection and transmission coefficients.

The planar FSS structure might be considered as a second-order bandpass filter consisting of LC circuits [28] that yield a double resonance in the reflection coefficient curve in Fig. 6. The double resonance is observed in both the simulation and measurement results. A fast roll-off is obtained in the simulated and measured transmission coefficient curve in Fig. 7. The split at the top of the measured transmission coefficient curve could be due to measurement errors.

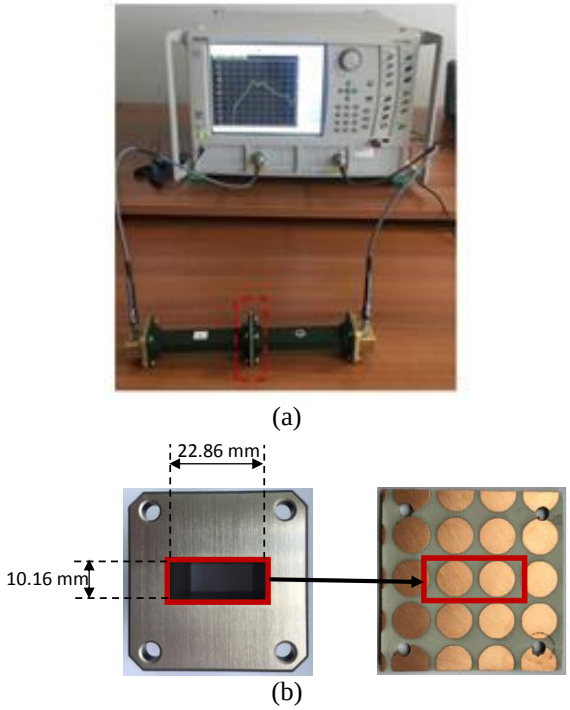

Fig. 5. Planar FSS Measurements: (a) measurement set up and (b) part of the fabricated FSS and waveguide. WR90 waveguide with 6.5 GHz cutoff frequency for dominant mode (TE_{10}) is used in the measurements. The following mode (TE_{20}) starts at 13.1 GHz.

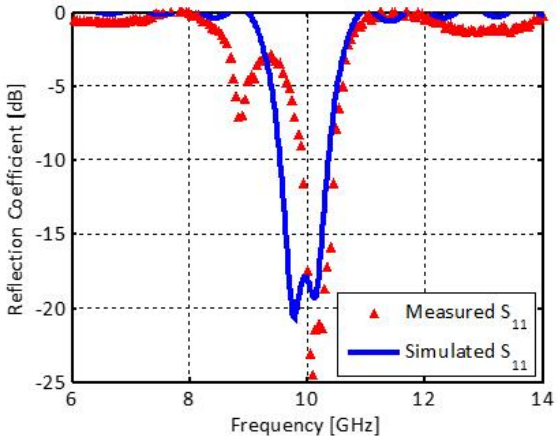

Fig. 6. Measured and simulated reflection coefficient versus frequency for the planar FSS structure.

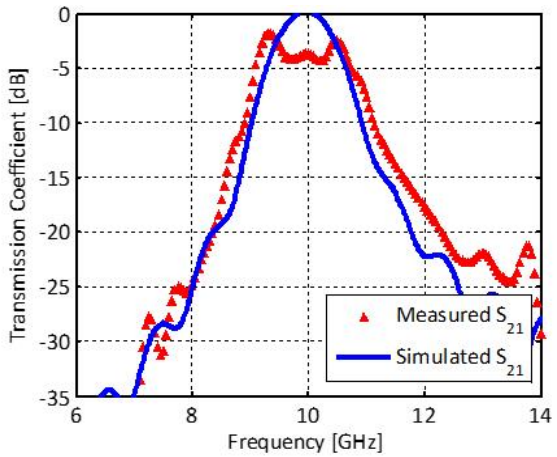

Fig. 7. Measured and simulated transmission coefficient versus frequency for the planar FSS structure.

IV. FSS RADOME DESIGN FOR ENDFIRE RADIATION

When the FSS is used in curved structures, the fundamental properties of planar FSS, namely the periodicity and the infinite extent of the surface, are lost. This makes it impossible to reduce the analysis to that of a single unit cell [29]. Therefore, electrically large curved array of FSSs have to be analyzed. The geometrical optics (GO) is commonly used for the analysis. However, multiple internal reflections are not accounted by GO.

A novel X-band radome in the shape of an extended hemispherical lens is designed by using triple layer X-band FSS. Its reflection and transmission characteristics are investigated for in-band and out-of band frequencies through simulations by integrating an available UWB Vivaldi antenna as the antenna inside the radome. Vivaldi

antenna with endfire radiation operates efficiently as a transmitter and receiver in the band of 3 GHz–15 GHz. The slot curve for the Vivaldi antenna is an exponential function expressed as:

$$S(z) = (W_{slot}/2)\, exp(az), \quad (2)$$

where a=0.165 and W_{slot}=0.25 mm. A $\lambda/4$ open circuit stub is used for wide band matching. Rogers RT/Duroid 5870 (ε_r=2.33) with a 0.51 mm dielectric thickness, and 17.5 um copper is chosen for the design. The prototype is shown in Fig. 8. The reflection behavior is measured in terms of S_{11} characteristics in Fig. 9.

The shape of the radome is synthesized as the union of a hemisphere of radius r = 60 mm (corresponds to 2λ in free space), and a cylindrical dielectric slab base with a height of h = 30mm (corresponds to 1λ in free space). These dimensions are chosen to ensure main beam inclusion of the antenna within the FSS radome for end-fire radiation. Figure 10 illustrates the designed radome, and the integrated antenna.

(a) (b)

Fig. 8. Fabricated Vivaldi antenna: (a) top view and (b) back view.

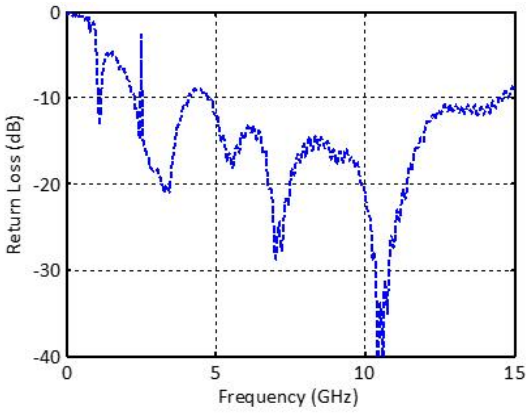

Fig. 9. Measured return loss of Vivaldi antenna.

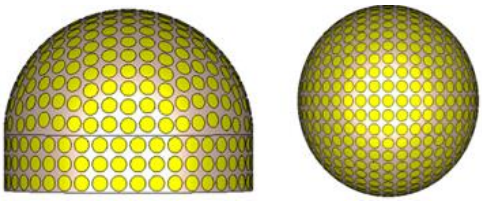

(a) (b)

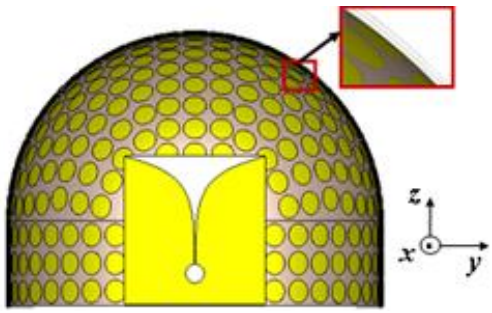

(c)

Fig. 10. FSS radome: (a) Side view, (b) top view, and (c) cut view with Vivaldi antenna.

The structure that consists of the FSS radome, located to the reactive near field region of the antenna, and Vivaldi antenna is simulated. Simulations are performed in X-band (a frequency band of 8 GHz-12 GHz), which covers the operation frequency range of the antenna. Simulated gain patterns of the antenna with and without the radome at 8 GHz, 10 GHz, and 12 GHz are given in Fig. 11. It is observed that the minimal degradation in the gain pattern occurs at 10 GHz and the direction of the main beam remains unchanged. While the gain of Vivaldi antenna at 10 GHz is 7.4 dBi, which is almost equal in E and H planes, the Vivaldi antenna with the radome has a gain of 6.7 dBi in H-plane, and 7.2 dBi in E-plane. Although E-plane results excellently match each other with/without FSS radome, H-plane patterns are degraded to some extent by the integration of FSS radome.

The gain patterns obtained with radome at 8 GHz and 12 GHz has opposite main beam direction compared to the Vivaldi antenna. This proves the no transmission and high reflection characteristics of radome for out-of-band operations.

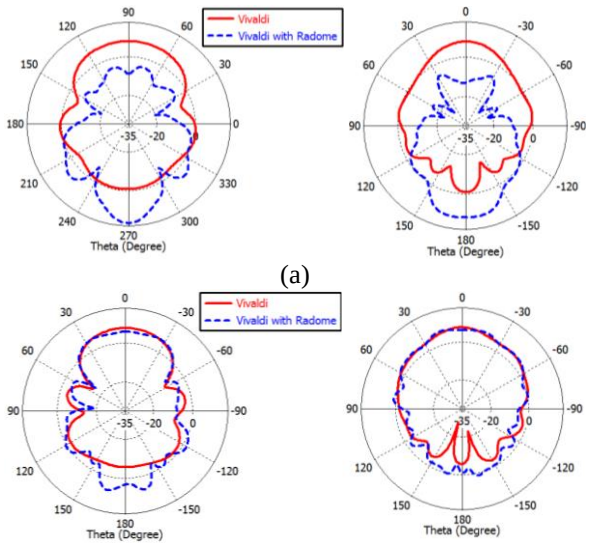

(a)

(b)

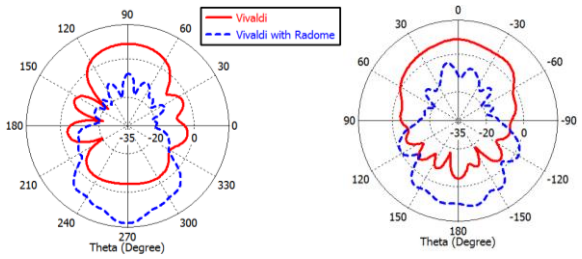

(c)

Fig. 11. Simulated gain pattern of Vivaldi antenna with FSS radome: (a) H-plane at f=8 GHz (left), E-plane at f=8 GHz (right), (b) H-plane at f=10 GHz (left), E-plane at f=10 GHz (right), and (c) H-plane at f=12 GHz (left), E-plane at f=12 GHz (right).

V. CONCLUSION

A curved radome designed through an FSS structure is presented. Unit cell geometry of the planar FSS is described in detail. The triple layer planar FSS is fabricated, assembled, and measured. Measurement and simulation results for the reflection along with transmission coefficient of the planar FSS are given. Measurement results show sufficiently good performance. FSS radome design integrated with an UWB Vivaldi antenna with endfire radiation is illustrated. Gain patterns of the Vivaldi antenna at 8 GHz, 10 GHz, and 12 GHz for the cases with and without the radome are explored. It is revealed that the gain pattern at 10 GHz yields the optimum result compared to the gain patterns at 8 GHz, and 12 GHz. Intended design of the radome is consistent with the obtained results. Compared with other previously developed radomes, current design has some advantages such as angular stability for different incidence angles, and insignificant change in gain at an optimal design frequency. A flat-top transmission feature is also achieved. It is concluded that the designed radome could be used in X-band applications. In the future, impact of the change in the radome radius on the reflection and transmission characteristics could be analyzed as the hemispherical radome approaches to a planar structure with increasing radius.

REFERENCES

[1] R. Mittra, C. H. Chan, and T. Cwik, "Techniques for analysing frequency selective surfaces – A review," *Proc. IEEE*, vol. 76, pp. 1593-1615, 1988.

[2] X. Q. Lin., T. J. Cui, Y. Fan, et al., "Frequency selective surface designed using electric resonant structures in terahertz frequency bands," *J. of Electromagnetic Waves Appl*., vol. 23, pp. 21-29, 2009.

[3] P. S. Taylor, A. C. M. Austin, E. A. Parker, et al., "Angular independent frequency selective surfaces for interference control in indoor wireless environments," *Electronics Letters*, vol. 48, pp. 61-62, 2012.

[4] G. I. Kiani, L. G. Olsson, A. Karlsson, et al., "Transmission of infrared and visible wavelengths through energy-saving glass due to etching of frequency-selective surfaces," *IET Microw. Antennas Propag*., vol. 7, pp. 955-961, 2010.

[5] R. Panwar and J. R. Lee, "Progress in frequency selective surface-based smart electromagnetic structures: A critical review," *Aerospace Science and Technology*, vol. 66, pp. 216-234, 2017.

[6] B. A. Munk, *Frequency Selective Surfaces: Theory and Design*. Wiley-Interscience, New York, 2000.

[7] M. Wang, L. Zhao, J. Wang, et al., "A low-profile miniaturized frequency selective surface with insensitive polarization," *Applied Computational Electromagnetics Society Journal*, vol. 33, no. 9, pp. 1003-1008, 2018.

[8] Y. Lin, X. Xu, Z. Dou, et al., "A novel multi-band polarization insensitive frequency selective surface based on centrosymmetric L-shaped metal strips," *Applied Computational Electromagnetics Society Journal*, vol. 30, no. 3, 2015.

[9] H. Wang, P. Kong, W. Cheng, et al., "Broadband tenability of polarization-insensitive absorber based on frequency selective surface," *Scientific Reports*, vol. 6, pp. 1-8, 2016.

[10] F. Deng, X. Xi, J. Li, et al., "A method of designing a field-controlled active frequency selective surface," *IEEE Antennas and Wireless Propagation Letters*, vol. 14, pp. 630-633, 2015.

[11] S. H. Mahmood and T. A. Denidni, "Pattern-reconfigurable antenna using a switchable frequency selective surface with improved bandwidth," *IEEE Antennas and Wireless Propagation Letters*, vol. 15, pp. 1148-1151, 2016.

[12] M. Z. Joozdani, M. K. Amirhosseini, and A. Abdolali, "Wideband radar cross-section reduction of patch array antenna with miniaturised hexagonal loop frequency selective surface," *Electronics Letters*, vol. 52, pp. 767-768, 2016.

[13] Y. Liu, Y. Hao, H. Wang, et al., "Low RCS microstrip patch antenna using frequency-selective surface and microstrip resonator," *IEEE Antennas and Wireless Propagation Letters*, vol. 14, pp. 1290-1293, 2015.

[14] Y. Jia, Y. Liu, H. Wang, et al., "Low RCS microstrip antenna using polarisation-dependent frequency selective surface," *Electronics Letters*, vol. 50, pp. 978-979, 2014.

[15] K. Yu, Y. Li, and X. Liu, "Mutual coupling reduction of a MIMO antenna array using 3-D novel meta-material structures," *Applied Computational Electromagnetics Society Journal*, vol. 33, no. 7, pp. 758-763, 2018.

[16] M. Idrees, S. Buzdar, and S. Khalid, "A miniaturized polarization independent frequency selective surface with stepped profile for shielding applications," *Applied Computational Electromagnetics Society Journal*, vol. 31, no. 5, 2016.

[17] N. F. Amini, M. Karimipour, K. Paran, et al., "Optimization of frequency selective surface with simple configuration based on comprehensive formation method," *Applied Computational Electromagnetics Society Journal*, vol. 30, no. 4, 2015.

[18] N. Liu, X. Sheng, C. Zhang, et al., "Design of frequency selective surface structure with high angular stability for radome application," *IEEE Antennas and Wireless Propagation Letters*, vol. 17, pp. 138-141, 2018.

[19] M. Qu, M. Rao, S. Li, et al., "Tunable antenna radome based on graphene frequency selective surface," *AIP Advances*, vol. 7, pp. 1-7, 2017.

[20] B. Lin, S. Du, H. Zhang, et al., "Design and simulation of frequency-selective radome together with a monopole antenna," *ACES Journal*, vol. 7, pp. 620-625, 2010.

[21] B. Lin, F. Li, Q. R. Zheng, et al., "Design and simulation of a miniature thick-screen frequency selective surface radome," *IEEE Antennas and Wireless Propagation Letters*, vol. 8, pp. 1065-1068, 2009.

[22] L. L. Zhang, J. H. Zhang, X. L. Chen, et al., "Modified silica ceramic for frequency selective surface radome," *Journal of the Ceramic Society of Japan*, vol. 123, pp. 937-941, 2015.

[23] I. Choi, D. Lee, and D. G. Lee, "Hybrid composite low-observable radome composed of E-glass/ aramid/epoxy composite sandwich construction and frequency selective surface," *Composite Structures*, vol. 117, pp. 98-104, 2014.

[24] R. Orr, V. Fusco, D. Zelenchuk, G. Goussetis, et al., "Circular polarization frequency selective surface operating in ku and ka band," *IEEE Trans. Antennas Propag*., vol. 63, pp. 5194-5197, 2015.

[25] S. Cimen, "Novel closely spaced planar dual-band frequency-selective surface," *IET Microw. Antennas Propag.*, vol. 7, pp. 894-899, 2013.

[26] F. Bayatpur and K. Sarabandi, "Tuning performance of metamaterialbased frequency selective surfaces," *IEEE Trans. Antennas Propag.*, vol. 57, pp. 590-592, 2009.

[27] Z. Sipus, M. Bosiljevac, and S. Skokic, "Analysis of curved frequency selective surfaces," *Report*, p. 48, 2007.

[28] M. N. Jazi, M. R. Chaharmir, J. Shaker, and A. R. Sebak, "Broadband transmitarray antenna design using polarization-insensitive frequency selective surfaces," *IEEE Trans. Antennas Propag*., 64, vol. 1, pp. 99-108, 2016.

[29] Z. Sipus, M. Bosiljevac, and S. Skokic, "Analysis of curved frequency selective surfaces," *The Second European Conference on Antennas and Propagation (EuCAP 2007)*, Edinburgh, UK, pp. 1-5, 2007.

Development of a High Gain, Dual-Band and Two-Layer Miniaturized Microstrip Antenna for 5.8 GHz ISM and 10 GHz X-Band Applications

İsa Ataş [1], Teymuraz Abbasov [2], and Muhammed B. Kurt [3]

[1] Vocational School of Technical Sciences
Dicle University, Diyarbakır, 21280, Turkey
isa_atas@dicle.edu.tr

[2] Department of Electrical and Electronics Engineering
İnönü University, Malatya, 44280, Turkey
teymuraz.abbasov@inonu.edu.tr

[3] Department of Electrical and Electronics Engineering
Dicle University, Diyarbakır, 21280, Turkey
bkurt@dicle.edu.tr

Abstract ─ In this study, it is explained how to increase the gain of a two-layer stacked miniaturized microstrip patch antenna (MPA) operating at 5.8 GHz and 10 GHz step by step by combining several different methods used in the literature for performance improvement of MPAs. A commonly used FR4 substrate material was preferred to design and produce the antenna. For electromagnetic modeling of the prototype structure, numerical analysis, and optimization, ANSYS HFSS was used. The performance of the proposed antenna was evaluated in terms of return loss (RL), surface current distribution, radiation patterns and gain/directivity. To confirm the study, the simulation results were compared with the measurements taken over the antenna prototype and good agreement has been achieved. The peak gain values of the proposed antenna at 5.8 GHz and 10 GHz are obtained as 4.11 dBi and 7.15 dBi, respectively.

Index Terms ─ Dual-band, gain, impedance matching, microstrip antenna.

I. INTRODUCTION

Due to the rapid increase in communication technologies and the demand for different frequency applications in wireless devices, compact structured and multi-band MPAs offer the best solution. These antennas can be integrated with various portable devices for efficient data transmission and reception [1].

MPA has many advantages, but it has two main disadvantages as low gain and narrow bandwidth. Various methods are used to overcome these disadvantages. These methods are:

a. Etched slots on the patch [2],
b. Appropriate feeding [3],
c. Defected Ground Structure (DGS) [4],
d. Adding different shaped parasitic patches to the patch at appropriate positions [5],
e. Multi-layer structure [6].

Although these methods were used to increase the gain and bandwidth of the antenna in the literature, in our study we focused on increasing the number of working band and the gain of an antenna by using these methods. As far as we can see in the literature, DGS method was used to increase the bandwidth of an antenna. In our study, we used it to increase the gain of our antenna.

There have been numerous designs of double-band MPAs over the past decades, especially for wireless communications, 3.5 GHz WiMAX (3.3-3.7 GHz), 5.5 GHz (5.150-5.825 GHz) and/or 2.4 GHz (2.4-2.483 GHz) WLAN and 10 GHz (8-12 GHz) radar applications. Some of those were planar multiple shaped strips with binomial curved conductor support [7], meander line and a patch in the form of a reverse toothbrush [8], microstrip line feeder split ring metamaterial structure [9], DGS with multi-strip monopole antenna [10], inverted-F antenna (IFA) structure [11], H-shaped antenna for GPS and Wi-Fi applications [12], microstrip antenna with improvement in performance using DGS [13], extended L-shaped multiband antenna for wireless applications [14], multi-layer stacked patch antenna [15]. However, most of these antennas are large in size. As far as literature studies are concerned, most of the techniques used for compact size and multi-band antennas are complicated due to the necessity of additional structures or due to their large size. In order to design a small and compact wireless device, it is necessary to miniaturize the antenna size accordingly.

The ITU (International Telecommunication Union)

Submitted On: December 25, 2018
Accepted On: March 27, 2019

had originally reserved a portion of the RF spectrum globally for industrial, scientific and medical (ISM) applications [16]. One of the ISM bands, which has center frequency of 5.8 GHz is between 5.725 GHz and 5.875 GHz. The frequency band of 5.8 GHz is especially important for high speed Wi-Fi routers, FPV (First Person View) applications where antennas with smaller dimensions and profile are desirable. This allows users to access the microwave spectrum without the need for regulations and restrictions that can be applied elsewhere [17, 18].

In radar engineering, X-band (8.0 to 12.0 GHz) is used extensively for detection and identification of reflective objects such as aircraft, ship, space vehicle, vehicle, human and natural environment [19].

The higher the frequency, the smaller the antenna dimensions. Since the our antenna was designed initially according to 10 GHz and then a second operating frequency was added at a frequency of 5.8 GHz, the designed antenna dimensions were smaller than the antenna designed at the 5.8 GHz band. Thus, an antenna operating in the 5.8 GHz band was designed with the small dimensions of 10 GHz. In addition, in the literature search as far as we have seen, we did not find any antenna that works in both 10 GHz and 5.8 GHz as dual band.

This study proposes a new design approach for gain improvement of two-layer stacked MPA with dual band operating at 5.8 GHz ISM and 10 GHz X-Band Radar applications.

This article is organized as follows. Section II covers the antenna configuration and design procedure. Simulation and measurement results are discussed in Section III and comparison tables are given in this section. Section IV contains the result of this study.

II. DESIGN SPECIFICATIONS OF PROPOSED ANTENNA

This section presents a description of the geometric configuration and basic steps involved in the design of the proposed antenna.

A. Antenna configuration

The geometrical configuration of the proposed antenna is shown in Fig. 1. This antenna is designed to operate in dual band as 5.8 GHz ISM band (from 5.725 to 5.875 GHz) and 10 GHz X band (from 9.623 to 10.427 GHz). The proposed antenna is implemented on a FR4 substrate with thickness of 1.575 mm, relative permittivity 4.4 and loss tangent of 0.019, while copper patch having a thickness of 0.035 mm is used as the radiating element. MPA was fed using a microstrip feed line which was terminated with a 50Ω SMA connector for signal transmission and antenna simulation.

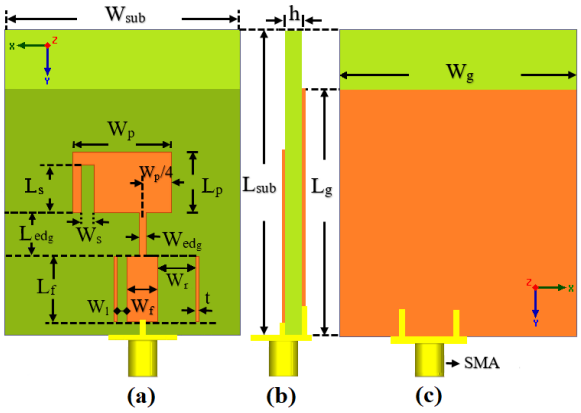

Fig. 1. Configuration of the dual band proposed antenna structure: (a) front view, (b) side view, and (c) back view.

B. Design procedure

In our study, we used the parametric analysis of HFSS at each step and ultimately improved the antenna design parameters. The values given in our paper are in fact the result of many parametric analyzes. Since more details would make the paper too long, we showed only the best results of each parametric analysis in our paper. Also, we give our design methodology as a flowchart shown in Fig. 2.

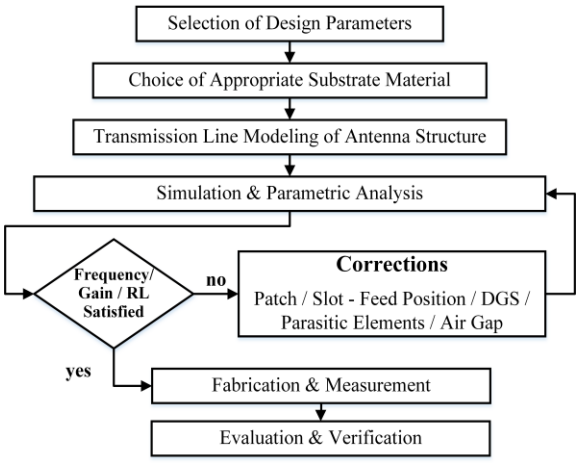

Fig. 2. Flow chart of design methodology.

The antenna development procedure is shown systematically in Fig. 3 within four step.

Initially, even though its loss tangent is relatively high, we preferred the FR4 substrate in our design because of the advantages of being cheap and easy to obtain. The FR4 substrate consists of an epoxy matrix reinforced with woven glass. This composition of epoxy resin and fiber glass varies in thickness and depends on direction [14, 20].

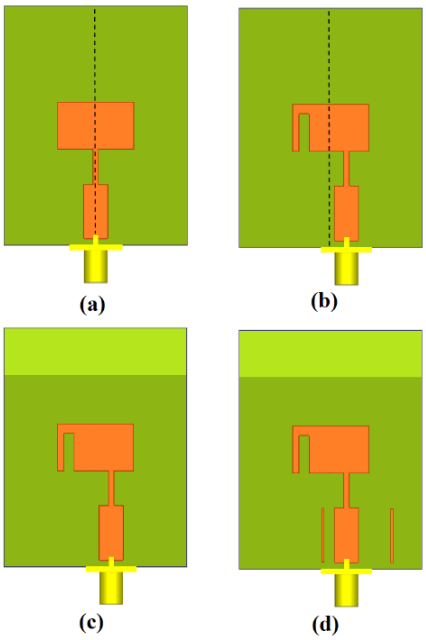

Fig. 3. Antenna design steps: adjusting of (a) initial antenna (Step #1), (b) slot-feed position (Step #2), (c) DGS (Step #3), and (d) parasitic element (Step #4).

In step 1, we obtained the initial dimensions of MPA with the rectangle patch with edge feed by using Transmission Line Model (TLM) for 10 GHz resonance frequency. To operate in the fundamental mode, the length of the patch should be slightly less than $\lambda g/2$, where λg is the wavelength in the dielectric medium and is equal to $\lambda o/\sqrt{\varepsilon_{eff}}$, where λo is the free-space wavelength and ε_{eff} is the effective relative permittivity which can be obtained by the following equation (1) [21]:

$$\varepsilon_{eff} = \frac{\varepsilon_r + 1}{2} + \frac{\varepsilon_r - 1}{2}\left(1 + 12h/W\right)^{-1/2}, \quad (1)$$

where h, W, and ε_r are the thickness of substrate, the width of microstrip patch and relative permittivity, respectively.

The initial antenna was fed from the side by a quarter-wave microstrip line to provide impedance matching. The relationship between resonance length L_{edg} and directed wavelength λg is given equation (2) below [22]:

$$L_{edg} = \lambda_g / 4 = \frac{c}{4 f_r \sqrt{\varepsilon_{eff}}}, \quad (2)$$

where c refers to speed of light and fr is the resonance frequency.

Since the accuracy of the TLM approach is not very good, the results obtained from the simulation with these TLM values do not provide desired characteristics as much. At this point, adjusting of the patch size is necessary for desired characteristics of antenna. This is done by trial and error method and some simulation programs. In our case, parametric analysis tool of HFSS [23] program was used to obtain right size of the patch which is to be used in the next steps shown in Fig. 3 (a). In all the other steps we used the same HFSS tool for optimum performance as well. Some of the different RL curves obtained for different values during these analyzes are shown in each step. By looking at the curves in these figures, the values that yields the best value of RL and gain in the working frequencies were selected.

In step 2, slot opening method was used to obtain dual-band characteristic on a standard rectangular antenna. Firstly, we fixed the feed position at the center and opened a slot on the patch and changed the position of it while observing the return loss variation [24]. As a result, a second frequency (changing from 5 to 7 GHz) with 10 GHz appeared.

Then, the feeding position has been changed for further improvement of the RL [25]. After then, for the intended dual band of 5.8 GHz and 10 GHz frequencies, good results have been obtained with the use and optimization of these two methods together. The resulting antenna is shown in Fig. 3 (b). The return loss change for some different slot lengths and widths values is shown in the Fig. 4.

In step 3, DGS method was used for gain improvement. When we use MPA, the problems which will occurs are surface waves and high loss in the substrate layer. The losses that are due to the surface waves excitation will cause decrease in the antenna gain, efficiency and the bandwidth. When we use DGS on MPA, it reduces the surface waves on the ground plane that reflect from the edge of the ground plane which will influence the current flow and the input impedance of the antenna and therefore changes return loss and increases the gain [26-29].

In this step, in order to increase the gain while maintaining the resonances at the frequencies 5.8 and 10 GHz, the ground surface is optimally removed without overlapping the patch and feed region as shown in Fig. 3 (c). The return loss change for some different ground lengths is shown in the Fig. 5.

In step 4, for further return loss and gain improvement, parasitic element (PE)s were optimally placed parallel to the right and left of the feed line as shown in Fig. 3 (d) [30]. The return loss change for some different locations of parasitic element is shown in the Fig. 6.

The effects of the evolutionary steps on the S_{11} of the antennas designed with the methods explained in steps #1 to #4 used is shown in Fig. 7. Here, since the return loss graphs overlap one another, the return loss change for each step is shown in the Table 1 for a better view of the results. Design stages play an important role on the operating frequency of the antenna. In our design, DGS and parasitic element addition outside the slot opening region as in the Fig. 3, does not change the upper

working band (10 GHz) and the lower working band (5.8 GHz) as seen from Fig. 7.

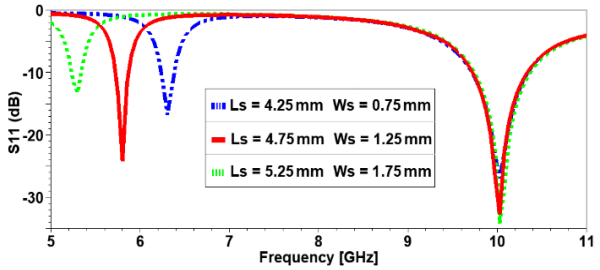

Fig. 4. RL results of the different slot lengths and widths.

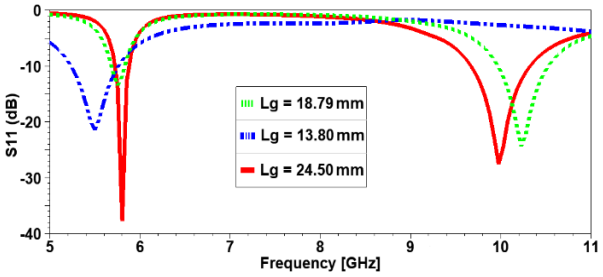

Fig. 5. RL results of different ground (DGS) lengths.

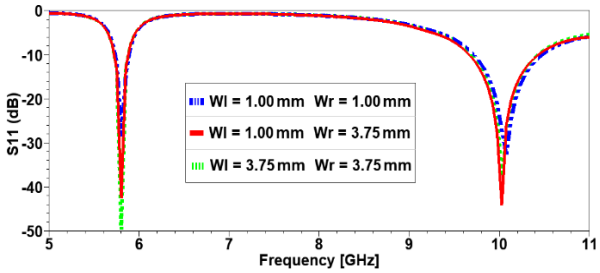

Fig. 6. RL results of different locations of parasitic element.

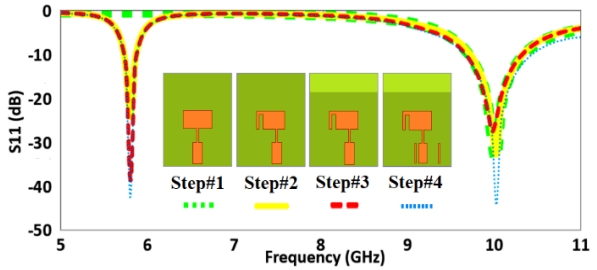

Fig. 7. S_{11} for the steps #1 to #4.

As a final step (Step #5), in order to further increase the gain, under the MPA used in step #4, after an air gap we used a one-sided second layer with the same properties and dimensions as shown in Fig. 8.

The purpose of using a second FR4 layer underneath the antenna is to add an air gap to the structure. Aim of the air gap between the radiating element and the lower ground plane is to reduce high substrate loss of the material used and so increase the gain.

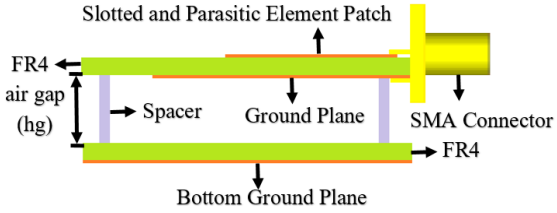

Fig. 8. Step #5: Side view of proposed antenna structure.

Table 1: Comparison of steps in terms of RL

Steps of Design	RL (dB)	
	5.8 GHz	10 GHz
Step #1	-	33.41
Step #2	24.20	32.75
Step #3	38.67	27.57
Step #4	42.52	44.25

For the second layer used, possible situations such as whether the second layer will be over or under MPA, double sided or single sided, top or bottom ground and with or without DGS were analyzed separately. For best results, it was concluded that the ground should be under the second layer without DGS. Next to these, the effect of the air gap on the gain was investigated parametrically with the HFSS.

As a result, optimum value of the air gap thickness, hg was found as 7.5 mm. Since it was observed that insertion of the air gap did not change the return loss much, only the gain versus the air gap thickness has given in Table 2. In this table, the gain describes the peak gain in the boresight direction.

Table 2: Simulated antenna gain versus the air gap thickness

Air Gap, hg (mm)	Gain (dBi)	
	5.8 GHz	10 GHz
3.5	3.56	6,68
5.5	3.72	6,79
7.5	**4.11**	**7,15**
9.5	4.03	6,74

The created air gap reduces both the effective dielectric constant of the radiating plane and the electric field concentration on the lossy epoxy. In the work done, the effective dielectric constant ε_{eff} was reduced by using the air gap to reduce the high insulation loss of the FR4

material [31]. Equation (3) was used to obtain this value which yields ε_{ort} = 1.59 which is smaller than ε_{eff} = 3.57,

$$\varepsilon_{ort} = \frac{\varepsilon_{r1}h + \varepsilon_{r2}h_g}{h + h_g}. \quad (3)$$

Finally, the optimum performance of the antenna was achieved by the parametric studies carried out with the HFSS and the final parameters of the antenna are shown in Table 3.

Table 3: Dimensions of proposed antenna

Parameter	Size (mm)	Parameter	Size (mm)
Lsub	30	*Ledg*	4.3
Wsub	23	*Wedg*	0.7
Lp	6	*Lf*	6.5
Wp	9.6	*Wf*	3
Lg	24.5	*Wr*	3.75
Wg	23	*Wl*	1
Ls	4.75	*t*	0.25
Ws	1.25	*h*	1.575
hg	7.5		

III. RESULTS AND DISCUSSIONS

The main performance parameters of an antenna are RL, surface current distribution, radiation patterns and gain/directivity. For the proposed antenna, these parameters were simulated and obtained using the HFSS. On the other hand, RL measurement were performed using a portable vector network analyzer (ANRITSU MS2028C) covering 10 kHz-20 GHz.

A. Return loss

The return loss (negative of the S_{11}) graphics of the proposed antenna at frequencies of 5.8 GHz and 10 GHz are shown in Fig. 9.

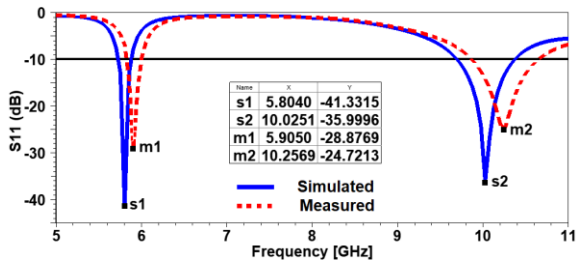

Fig. 9. S_{11} values of the proposed antenna.

The measured result is shifted systematically to higher frequencies. This can be attributed to the incorrectness of the catalog information of the dielectric constant of the epoxy material used or errors in manufacturing and measurement processes.

According to Fig. 9, S_{11} = -10 dB bandwidth of the simulated and measured of the proposed antenna are 160 MHz at 5.8 GHz and 680 MHz at 10 GHz, 176 MHz at 5.8 GHz and 785 MHz at 10 GHz, respectively.

B. Surface current distribution

Looking at the surface current distributions shown in Fig. 10, the current flow at 10 GHz is stronger and more continuous than 5.8 GHz, and is also concentrated at patch edges and quarter wave zones. The figure shows that the slot radiates at 5.8 GHz and the patch at 10 GHz.

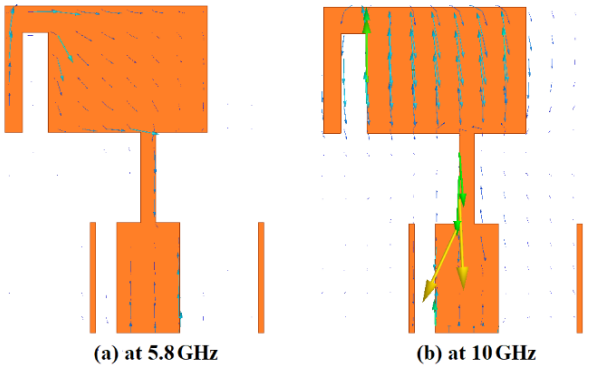

Fig. 10. Surface current distributions on the proposed antenna.

C. Radiation patterns and gain/directivity

The simulated far-field radiation patterns of the proposed antenna at both resonance frequencies are plotted in Fig. 11.

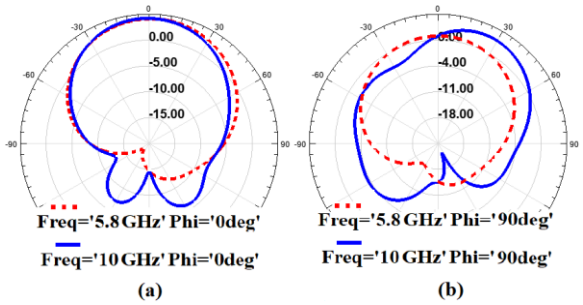

Fig. 11. Simulated far-field radiation patterns: (a) E-plane (x-z) and (b) H-plane (y-z).

The proposed antenna is optimized for the best radiation efficiency, ηre. Radiation efficiency can be defined as the ratio of the output power of the antenna (P_{out}) to the input power (P_{in}) of the antenna and is defined in equation (4) as:

$$\eta_{re} = P_{out} / P_{in}. \quad (4)$$

The directivity and gain of the antenna are related to efficiency as given equation (5) below:

$$G(dB) = \eta_{re} D(dB). \quad (5)$$

The gains of the proposed antenna are 4.11 dBi at 5.8 GHz and 7.15 dBi at 10 GHz, respectively. Figure 12 shows the gain and directivity of the proposed antenna

for frequencies 5.8 GHz and 10 GHz. Here, only a few frequencies have been chosen so that the gain and directivity values are displayed locally.

Table 4: Comparison of design steps in terms of the gain

Steps of Design	Gain (dBi)	
	5.8 GHz	10 GHz
Step#1	–	5.46
Step#2	1.78	5.46
Step#3	2.40	6.26
Step#4	2.28	6.55
Step#5	**4.11**	**7.15**

The proposed antenna is compared with some recently published studies. In terms of several parameters, the comparison is presented in Table 5.

The directivity of the antenna at 5.8 GHz is 6.85 dBi and the gain is 4.11 dBi and the directivity at 10 GHz is 8.65 dBi and the gain is 7.15 dBi. Because FR-4 material is lossy, the efficiency is low. Therefore, the directivity value is much higher than the gain value.

The effects of the evolutionary stages on the gain of the antenna are given in Table 4. In this table, the gain describes the peak gain in the boresight direction.

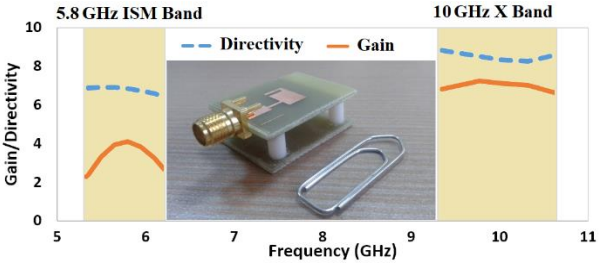

Fig. 12. Gain and directivity for the 5.8 GHz and 10 GHz band.

Table 5: Comparison among other most similar available antennas encountered in the literature

Reference	[13]		[14]			[20]		[32]		[33]		Proposed	
Area (mm^2)	100		1520			1140		484		3600		690	
Height (mm)	1		1.6			1.57		1.6		1		1.57	
Substrate	FR4		FR4			Rogers		FR4		Rogers		FR4	
Resonance Frequencies (GHz)	9.2	11.7	1.5	2.4	4.5	8.2	9.9	3.4	5.5	5.3	6.1	5.8	10
Bandwidth (MHz)	266	450	86	109	284	1028	1030	700	680	230	360	160	680
VSWR	1.04	1.09	1.06	1.24	1.50	1.15	1.16	Not mentioned		Not mentioned		**1.01**	**1.03**
Gain (dB)	4.34	4.59	1.03	1.33	1.84	2.96	4.24	2.04	3.44	7.00	5.00	4.11	**7.15**

IV. CONCLUSION

In this study, it is explained how to increase the gain of a miniaturized dual-band MPA operating at 5.8 GHz and 10 GHz step by step by combining several different methods used in the literature for performance improvement of patch antennas. Design approach consisting of five systematic steps was introduced. Parametric analysis was performed to verify the proposed design and optimize the antenna structure. The results were compared in terms of return loss, standing wave ratio and gain. This antenna can be used in dual-band communication systems for Wi-Fi (5.8 GHz) and Radar (10 GHz) applications. The compatibility of the simulation and measurement results, the compact size of the designed antenna (23 mm × 30 mm), the simple structure and the low cost make the proposed antenna suitable for practical applications.

ACKNOWLEDGMENT

This research was financially supported by the Researching Projects Committee of the University of Dicle (DUBAPK) with project number 14-MF-71. We are grateful to DUBAPK for financial assistance.

REFERENCES

[1] H. Wang and M. Zheng, "An internal triple-band WLAN antenna," *IEEE Antennas and Wireless Propagation Letters*, vol. 10, pp. 569-572, Feb. 2013.

[2] A. Srilakshmi1, N. V. Koteswararao, and D. Srinivasarao, "X band printed microstrip compact antenna with slots in ground plane and patch," *Recent Advances in Intelligent Computational Systems, IEEE*, pp. 851-855, Sept. 2011.

[3] C. U. Ndujiuba and A. O. Oloyede, "Selecting best feeding technique of a rectangular patch antenna for an application," *International Journal of Electromagnetics and Applications*, vol. 5, no. 3, pp. 99-107, May 2015.

[4] L. H. Weng, Y. C. Guo, X. W. Shi, and X. Q. Chen, "An overview on defected ground structure," *Progress in Electromagnetic Research B*, vol. 7,

pp. 173-189, July 2008.

[5] Z. H. Tu, Q. X. Chu, and Q. Y. Zhang, "High-gain slot antenna with parasitic patch and windowed metallic superstrate," *Progress in Electromagnetics Research Letters*, vol. 15, pp. 27-36, Jan. 2010.

[6] R. N. Tiwari, P. Singh, and B. K. Kanaujia, "Dual U-slot loaded patch antenna with a modified L-probe feeding," *Journal Microwaves, Optoelectronics and Electromagnetic Applications (JMOE)*, vol. 16, no. 3, Sept. 2017.

[7] S. Verma and P. Kumar, "Compact arc-shaped antenna with binomial curved conductor-backed plane for multiband wireless applications," *IET Microwaves Antennas and Propagation*, vol. 9, no. 4, pp. 351-359, Mar. 2015.

[8] Y. Li and W. Yu, "A miniaturized triple band monopole antenna for WLAN and WiMAX applications," *International Journal Antennas Propagation*, pp. 1-5, Oct. 2015.

[9] R. Kumar and S. Raghavan, "A compact metamaterial inspired triple band antenna for reconfigurable WLAN/WiMAX applications," *AEU-International Journal of Electronics and Communications*, vol. 69, no. 1, pp 274-280, Jan. 2015.

[10] J. Kaur, R. Khanna, and M. Kartikeyan, "Novel dual-band multistrip monopole antenna with defected ground structure for WLAN/BLUETOOTH/WIMAX applications," *International Journal Microwave Wireless Technologies*, vol. 6, no. 1, pp. 1-8, Sept. 2013.

[11] T. Hirano and J. Takada, "Dual-band printed inverted-F antenna with a nested structure," *Progress in Electromagnetic Research Letter*, vol. 61, pp. 1-6, Jan. 2016.

[12] T. H. Chang and J. F. Kiang, "Compact multi-band H-shaped slot antenna," *IEEE Transactions on Antennas and Propagation*, vol. 61, no. 8, pp. 4345-4349, May 2013.

[13] A. S. Bhadouria and M. Kumar, "Microstrip X-band antenna with improvement in performance using DGS," *Electrical and Electronic Engineering*, vol. 4, no. 2, pp. 31-35, Feb. 2014.

[14] A. Ahmad, F. Syeda, I. Naqvi, Y. Amin, and H. Tenhunen, "Design, fabrication, and measurements of extended L-shaped multiband antenna for wireless applications," *Applied Computational Electromagnetics Society Journal (ACES)*, vol. 33, no. 4, Apr. 2018.

[15] W. Jin, X. Yang, X. Ren, and K. Huang, "A novel two-layer stacked microstrip antenna array using cross snowflake fractal patches," *Progress in Electromagnetics Research C*, vol. 42, pp. 95-108, Jan. 2013.

[16] [Online]. Available: https://www.everythingrf.com/community/ism-frequency-bands.

[17] M. S. Sharawi, M. U. Khan, A. B. Numan, and D. N. Aloi, "A CSRR loaded MIMO antenna system for ISM band operation," *IEEE Transactions on Antennas and Propagation*, vol. 61, no. 8, pp. 4265-4274, Aug. 2013.

[18] M. R. Sobhani, N. Majidi, and Ş. T. Imeci, "Design and implementation of a quad element patch antenna at 5.8 GHz," *Applied Computational Electromagnetics Society Journal (ACES)*, vol. 33, no. 10, Oct. 2018.

[19] B. Datta, A. Das, A. Kundu, S. Chatterjee, M. Mukherjee, and S. K. Chowdhury, "Twice-band irregular rectangular cut-in microstrip patch antenna for microwave communication," *International Conference on Information Communication and Embedded System*, Feb. 2013.

[20] M. T. Islam and M. Samsuzzaman, "Miniaturized dual band multi slotted patch antenna on Poly-tetrafluoroethylene glass microfiber reinforced for C/X band applications," *Hindawi Publishing Corporation the Scientific World Journal*, June 2014.

[21] C. A. Balanis, *Antenna Theory: Analysis and Design*. John Wiley & Sons - Interscience, USA, 2005.

[22] D. M. Pozar and D. H. Schaubert, *Microstrip Antennas, the Analysis and Design of Microstrip Antennas and Arrays*. New York/ABD: IEEE Press, 1995.

[23] Ansoft High Frequency Structure Simulation (HFSS), ver. 15.2, Ansoft Corporation, Pittsburgh, PA, 2015.

[24] A. Elboushi and A. R. Sebak, "High gain hybrid DRA/horn antenna for MMW applications," *IEEE Antennas and Propagation Society International Symposium (APSURSI)*, July 2014.

[25] H. Zhang, U. Zhou, Z. Wu, H. Xin, and R. W. Ziolkowski, "Designs of ultra wideband (UWB) printed elliptical monopole," *Microwave and Optical Technology Letters*, vol. 52, pp. 466-471, Feb. 2010.

[26] A. Desai, T. Upadhyaya, R. Patel, S. Bhatt, and P. Mankodi, "Wideband high gain fractal antenna for wireless applications," *Progress in Electromagnetics Research Letters*, vol. 74, pp. 125-130, Apr. 2018.

[27] A. K. Arya, M. V. Kartikeyan, and A. Patnaik, "Defected ground structure in the perspective of microstrip antenna," *Frequenz*, vol. 64, no. 5-6, pp.79-84, Oct. 2010.

[28] F. Y. Zulkifli, E. T. Rahardjo, and D. Hartanto, "Radiation properties enhancement of triangular patch microstrip antenna array using hexagonal defected ground structure," *Progress in Electromagnetics Research*, no. 5, pp. 101-109, 2008.

[29] D. Marotkar, P. Zade, and V. Kapur, "To study the effect of DGS on antenna parameters,"

International Journal of Industrial Electronics and Electrical Engineering, vol. 3, no. 7, July 2015.

[30] M. R. Zaman, M. T. Islam, N. Misran, and J. S. Mandeep, "Analysis of resonance response performance of C-band antenna using parasitic element," *Hindawi Publishing Corporation the Scientific World Journal*, May 2014.

[31] M. Özenç, M. E. Aydemir, and A. Öncü, "1, 26 GHz rezonans frekansında çalışan çift tabakalı yüksek kazançlı mikroşerit dikdörtgen yama anten tasarımı," *Journal of the Faculty of Engineering and Architecture of Gazi University*, pp. 743, Jan. 2013.

[32] D. K. Naji, "Compact design of dual-band fractal ring antenna for WiMAX and WLAN applications," *International Journal of Electromagnetics and Applications*, vol. 6, vol. 2, pp. 42-50, Sept. 2016.

[33] F. R. Rostami, G. Moradi, and R. S. Shirazi, "Dual-band wide-angle circularly-polarized microstrip antenna by ferrite ring inserted in its cavity domain," *Applied Computational Electromagnetics Society Journal (ACES)*, vol. 32, no. 1, Jan. 2017.

İsa Ataş was born in Diyarbakır, Turkey, in 1975. He received the B.Sc. and M.Sc. degrees Electrical and Electronics Engineering from the Dicle University, Diyarbakır in 2000 and 2011. He is currently a Ph.D. student at Electrical and Electronics Engineering Department of Inonu University. Since 2007, he has been a lecturer at the Diyarbakır Vocational School of Technical Sciences of Dicle University.

His research is focused on linear, planar and miniaturized, high gain, wide band antenna design, microstrip antenna arrays for next generation wireless communication systems. His Ph.D. thesis is related to the design and implementation of high gain microstrip patch antennas.

Teymuraz Abbasov received the B.Sc. and M.Sc. degrees in Electrical Engineering from Moscow Technical University (MAMI), Moscow in 1981 and his Ph.D. degree in Electrical Engineering and Electromagnetic Technology from National Academy Science of Azerbaijan, Baku, Azerbaijan in 1991. His main research interests are mathematical modelling and measurement of electromagnetic field and waves, magnetic separation and filtration processes, numerical modelling of magneto-hydrodynamics and nonlinear electrical circuits, bio-electromagnetic sensors and actuators, MEMS, magnetic fluids theory and applications.

Since 1996, he has been working as a Professor at Inonu University, Malatya, Turkey. His main interests are electromagnetic fields and its applications.

Muhammed Bahaddin Kurt was born in Diyarbakır, Turkey, in 1970. He received the B.Sc. and M.Sc. degrees from the Hacettepe University, Ankara in 1992 and 1996, respectively and Ph.D. degree from the Sakarya University, Sakarya, Turkey in 2002, all in Electrical and Electronics Engineering. Between 1996 and 2005, he worked as a Teaching and Research Assistant in the Department of Electrical and Electronics Engineering at Dicle University, Diyarbakır, Turkey.

Since 2005, he has been working as an Assistant Professor in the same department. His research interests are mainly computational electromagnetics, artificial intelligence, microstrip patch antennas, and non-destructive testing of materials.

Electrical Characterization of Concrete Using the Parallel Plate Capacitor Method

Marcelo B. Perotoni [1], Marcos S. Vieira [2], Kenedy M. dos Santos [3], and Danilo B. Almeida [3]

[1] UFABC
Santo Andre, SP,09210-580, Brazil
Marcelo.perotoni@ufabc.edu.br

[2] Mackenzie Presbyterian University
Sao Paulo, SP, 01302-907, Brazil
marcos.vieira@mackenzie.br

[3] IFBA
Vitoria da Conquista, BA, 45078-900, Brazil
kenedymarconi@gmail.com

Abstract — This article describes the measurement of the complex dielectric constant of pure concrete and a brick wall, in the frequency range up to 2 MHz, with a view towards more accurate material description in electromagnetic simulations. The measurement system is based on the use of the materials under test as the dielectric material placed inside a parallel plate capacitor, in series with an external known fixed resistor. The theory behind the measurement is covered, and the results of both real and imaginary relative dielectric constants for both materials are presented. Finally, an electromagnetic simulation showing the shielding effectiveness of a hollow box made of a brick wall is presented, using the measured data in comparison with data from a commercial simulator database.

Index Terms — Electromagnetic compatibility, materials testing, numerical simulation, shielding.

I. INTRODUCTION

The importance of correctly addressing the lightning effect on buildings and structures increases with the number of sensitive electronic systems inside [1-3]. Real world tests of lightning strikes on buildings and structures are complicated, therefore computer simulations are attractive, and permit evaluation of a first order effect of the induced fields inside. Lightning simulators that generate equivalent currents and resultant electromagnetic field waveforms are still large and complex. Existing regulations and literature present some analytical waveforms that represent typical lightning strikes. Correct material characterization ensures more reliable computer simulations. Not only lightning studies benefit from the correct material description, also applications where the electromagnetic shielding of a room or closed area is important, such as when dealing with secure communications, resistant against Tempest (NATO and NSA - National Security Agency given name for spying activities based on unintended electromagnetic emissions) or other similar eavesdrop methods [4, 5]. Walls made of reinforced concrete with an internal metallic frame could help isolate and contain the major part of the fields outside the volume, preventing undesired field configuration inside the structure based on unintended emissions.

Several papers cover the measurement of the electrical permittivity of concrete. However, most of these studies aim to electrically characterize the concrete in the range of the microwave and RF frequencies, from a few hundred to a few thousand Megahertz.

The reflection and transmission of a CW (Continuous Wave) signal incident on a concrete block are used to compute the material complex dielectric constant [6]. A cylindrical coaxial transmission line was built using concrete poles as the dielectric core, whose water content was varied and used to measure the complex dielectric constant from 50 MHz to 1.6 GHz using two different methods [7]. Other technique measured several materials used in construction by fitting measured time domain reflection and transmission signals to the Kirkwood-Fuoss equation, the measured data obtained from two antennas connected to a vector network analyzer (frequency range from 1 GHz to 6 GHz), with the sample material as an obstacle [8]. GPR (Ground Penetration Radar) has been used to address material parameters measurements, such as asphalt, for frequencies between 900 MHz and 1.5 GHz [9] and also concrete, for frequencies on the range of 500 MHz and 5 GHz [10]. Time-Domain Reflectometry (TDR) was also employed

Submitted On: April 10, 2019
Accepted On: May 7, 2019

to determine the electrical parameter of concrete, in the range of 100 MHz to 1 GHz [11]. Measurements of complex dielectric constants at lower frequencies employ the step voltage [12, 13] with variants of Wheatstone bridges in capacitors built with guard electrodes, as to diminish fringing fields.

Since most of the studies focus on the VHF and UHF range, to address losses associated with indoor wireless communication, this work presents a simple and low-cost method based in a material-filled parallel plate capacitor, focusing on frequencies that are present in lightning strikes and other emission and susceptibility analyses, up to 2 MHz. The instrumentation is based on a signal generator, oscilloscope and the test capacitor is built considering the characteristics and size of the concrete material.

II. MEASUREMENT THEORY

In the electrical model presented in Fig. 1 the external reference resistor *R* is placed in series with the capacitor, symbolized by the lumped element *C* and its loss resistor R_L, also known as the capacitor Equivalent Series Resistance, or ESR. The loss resistor is considered to be in series in cases where the leakage current is low, other than that it is presented as a shunt element [12]. It is worth mentioning that the ESR value typically varies with frequency [14]. From the capacitor *C* it is possible to extract the real value of the permittivity (ε') whereas the loss resistor will relate to the imaginary part (ε''). V_1 and V_2 are the nodes whose voltages are measured, using two channels of the oscilloscope. Since the two elements that represent the capacitor cannot be accessed individually, the two physical quantities need to be indirectly found.

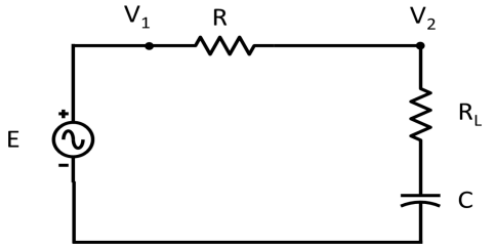

Fig. 1. Electric model representing the measurement system.

Figure 2 shows the quantities effectively measured with the oscilloscope, with a bold trace: the voltages V_1 and V_2 and their respective phase. Since the real and imaginary parts that model the capacitor cannot be physically separated, indirect manipulations will eventually provide their results.

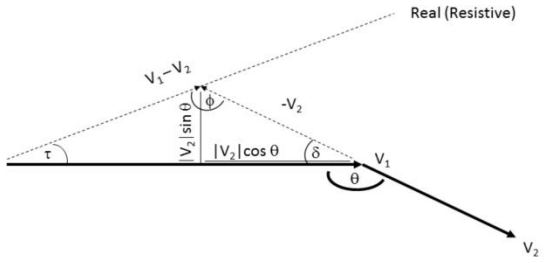

Fig. 2. Phasor representation of the measured quantities.

From Fig. 2 the vector subtraction between both measured voltages is the voltage drop on the external resistor *R* - therefore it is purely real. The current in the series circuit is found to be:

$$I = \frac{\sqrt{V_1^2+V_2^2-2V_1V_2\cos\theta}}{R}. \quad (1)$$

The numerator expresses the voltage drop on the external resistor (using the law of cosines). The complex impedance of the capacitor is given by:

$$Z_C = R_L + \frac{1}{j\omega C} = \frac{V_2 R}{\sqrt{V_1^2+V_2^2-2V_1V_2\cos\theta}}. \quad (2)$$

The angle ϕ, once found, will permit describe both real (the R_L voltage drop) and imaginary (due to *C*) voltages in terms of the three measured quantities. The following relation is valid for the internal angles of the triangle:

$$\phi + \delta + \tau = \pi, \quad (3)$$

δ, however, is equal to $(\pi - \theta)$. Therefore, the angle ϕ can be written as:

$$\phi = \theta - \tau. \quad (4)$$

The angle τ can be written as:

$$\tau = \operatorname{atan}\left(\frac{|V_2|\sin\theta}{|V_1|-|V_2|\cos\theta}\right), \quad (5)$$

so that it provides:

$$\phi = \theta - \operatorname{atan}\left(\frac{|V_2|\sin\theta}{|V_1|-|V_2|\cos\theta}\right). \quad (6)$$

Figure 3 shows again the real and imaginary phasors of V_2. It is possible then to isolate both real and imaginary parts of the capacitor voltage.

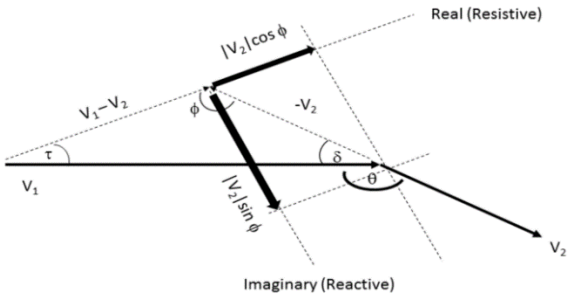

Fig. 3. Decomposition to extract the V2 components.

Using (2) and (6), the complete capacitor model can be written as:

$$Z_C = R_L + \frac{1}{j\omega C} = Z_C(\cos\phi - j.\sin\phi). \quad (7)$$

Neglecting the fringing fields of the parallel plate capacitor, the real part of the permittivity can be found using (8), where d is the distance between both plates; A indicates their respective area and ε_o the absolute (vacuum) permittivity:

$$\varepsilon_r' = \frac{Cd}{A\varepsilon_o}. \quad (8)$$

Considering the loss tangent (*tan D*) definition as in (9):

$$\tan D = \frac{\varepsilon''}{\varepsilon'} = \frac{R_L}{|X_C|}. \quad (9)$$

The imaginary part of the permittivity is then found after the relation from (10), with ω representing the angular frequency (recalling that R_L physically represents the ESR):

$$\varepsilon'' = R_L \omega C \varepsilon'. \quad (10)$$

The measurement setup needs a signal generator and oscilloscope, with at least two channels. The generator sets the signal frequency of a sinusoidal wave with adequate amplitude, and both oscilloscope channels inform the voltage amplitudes and their phase difference, in degrees.

III. MEASUREMENT RESULTS: SOLID CONCRETE

A parallel plate capacitor, square (length of 30 cm) is filled with concrete (3 cm thick) according to Fig. 4. For this specific case, the mixture is pure concrete (water, cement, and sand as aggregate, in equal proportions), i.e., there are no further elements such as rocks or steel.

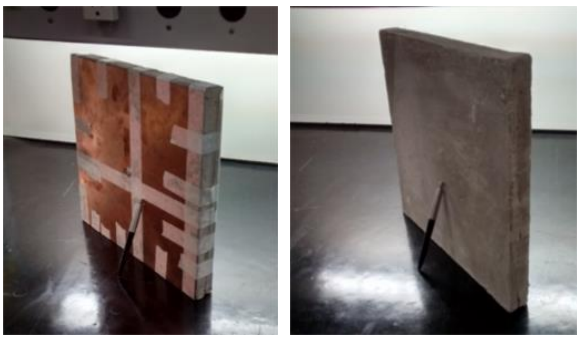

Fig. 4. (Left) Capacitor with its metallic plates and (right) its dielectric inner part.

Two sets of measurements were performed: one with a fresh concrete (3 days old) and other one cured or dried (3 months old). Results are presented in Fig. 5 and also in Table 1.

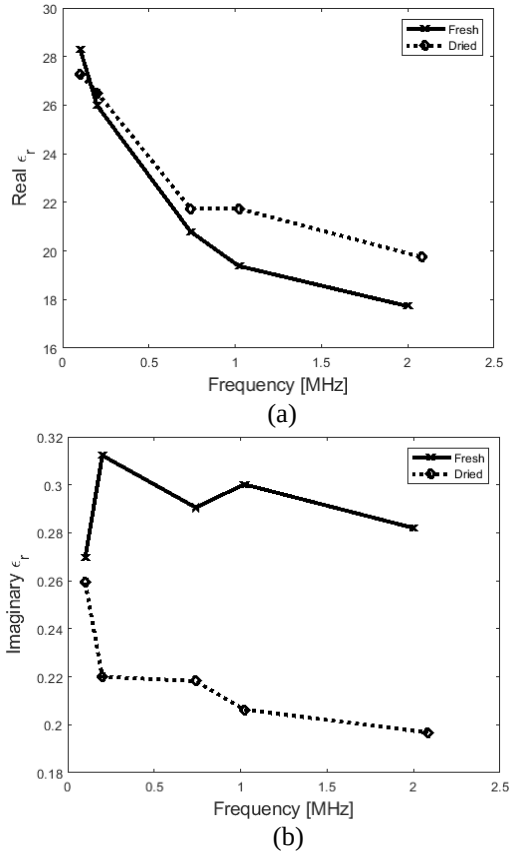

Fig. 5. Measured: (a) εr' and (b) εr'' for pure concrete.

Table 1: Measured relative dielectric constant

	Fresh		Dry	
Frequency [MHz]	**ε_r'**	**ε_r''**	**ε_r'**	**ε_r''**
0.10	28.31	0.26	27.27	0.26
0.20	25.97	0.31	26.50	0.22
0.74	20.79	0.29	21.74	0.21
1.02	19.38	0.30	21.74	0.20
2.00	17.72	0.28	19.74	0.20

During the measurements, as the frequency was swept, the external resistor R was set (using a potentiometer) so that the voltage drops on V_1 and V_2 were kept constant (for this case, with a ratio $V_1/V_2 \approx 1.67$). The results showed that the dry concrete has a slightly higher ε_r' in comparison to the fresh – where the water content is still high. As for the losses, the fresh concrete showed that ε_r'' was higher than the dried material, indicating the water again as the likely responsible for the observed higher dielectric losses. A similar study, for the frequencies 500 MHz and covering the 1 GHz to 2 GHz also showed a substantial variation on the complex permittivity due to the moisture content [15].

IV MEASUREMENT RESULTS: SOLID CONCRETE

A real masonry wall was built, with dimensions of 1.4 x 1.6 x 0.16 meters. It employed concrete bricks (shown in Fig. 6) and was covered with a cement mixture layer, as to emulate real walls. It was covered with a thin aluminum metallic sheet- to work as the contact plates. The measurement workflow followed suit the presented in the former section, but for safety reasons, the concrete cure time was duly observed, so only the dry condition was evaluated.

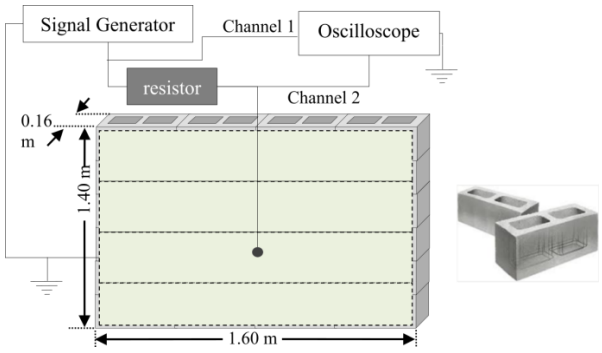

Fig. 6. (Left) real masonry wall used for concrete permittivity characterization and (right) concrete block used.

Table 2 provides the permittivity (real and imaginary) results and Fig. 7 shows the respective plots.

Table 2: Measured relative dielectric constant

Frequency [MHz]	ε_r'	ε_r''
0.05	32.89	0.29
0.10	27.67	0.25
0.15	19.19	0.25
0.20	19.07	0.37
0.25	17.25	0.44
0.30	16.22	0.45
0.35	15.59	0.43
0.40	14.45	0.51
0.50	12.95	0.58
0.75	10.48	0.48
1.00	9.16	0.51
1.21	8.96	0.50
1.50	8.24	0.46
1.70	8.15	0.48
2.00	7.95	0.48
2.30	7.60	0.45

It can be seen that the wall has smaller values for εr' in comparison to the pure concrete, given to the fact there is a larger air content on bricks not totally solid.

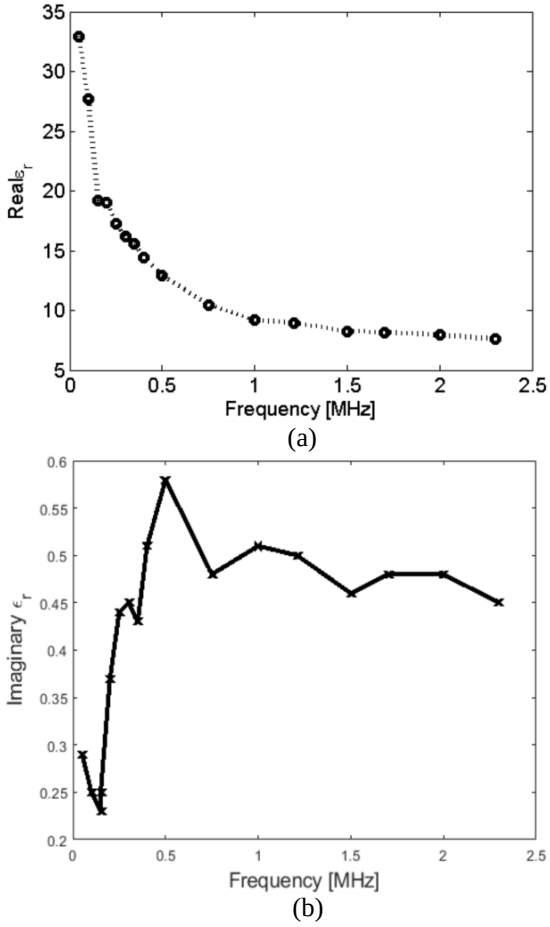

Fig. 7. Measured: (a) εr' and (b) εr'' for the wall.

V. APPLICATION: SHIELDING SIMULATION

With the proper material data, one is able to more accurately address electromagnetic effects in simulation tools. To exemplify it, the electromagnetic shielding provided by a brick box (according to Table 2) is simulated, against an incident plane wave (Fig. 8). The simulation was performed within FEKO, based on the Method of Moments (MoM) [16]. The MoM discretizes the structure in a tetrahedral mesh so that the integral equation is solved in an iterative way. The matrix is usually ill-conditioned, and to speed up the solution an MLFMM (Multi-Level Fast Multipole Method) can be employed, where the coupling among distant elements is considered zero [17]. For this specific problem, the pure MoM method was used since it is not electrically large. The plane wave has a broadband spectrum, covering DC to 2.3 MHz, amplitude of 1 V/m. The simulation model has a simple box with 4m length and wall thicknesses of 16 cm.

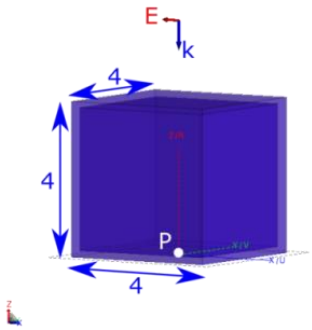

Fig. 8. Model used for the simulation. The plane wave is shown at top.

The electric field is measured by a probe (marked *P* in Fig. 8) placed on the bottom of the box volume. Figure 9 shows the comparison between the electric field attenuation (i.e., comparing the electric field amplitude on the point P for the free space and concrete box scenarios) inside the box with its material description given by the measurements (Table 2) and the available material data for "Construction Brick", inside FEKO database. The material data corresponds to the higher frequencies, starting from 1 GHz, and the lower range of frequencies is obtained after interpolation. It can be seen that the attenuation using the electrical material characteristics from the measurements resulted in a much larger attenuation across a large part of the frequency range.

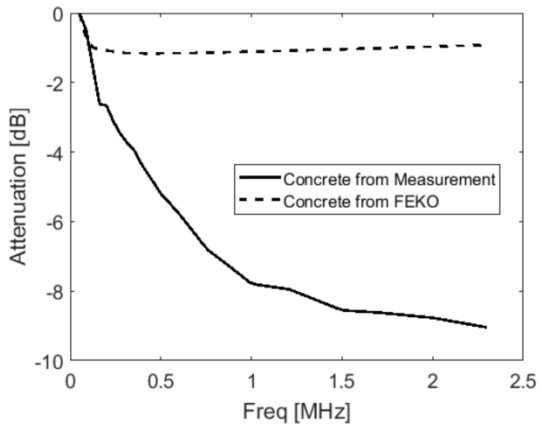

Fig. 9. Computed attenuation of the Electric Field inside the box, for two types of concrete.

VI. CONCLUSION

The article covered a simple and low-cost method to measure the electrical characteristics of concrete, which was applied to either a small block and also to a large wall. The results provided the material characterization in a frequency range where available similar results were not found by the authors, and whose importance is vital for applications in lower frequencies (down to few MHz), like lightning strikes and electromagnetic shielding. Comparison to existing data inside the material database of commercial numerical field codes also shown that the attenuation considering the measured material is larger, across the almost entire band up to 2.5 MHz.

REFERENCES

[1] J. Kato, H. Kawano, T. Tominaga, and S. Kuramoto, "Investigation of lightning surge current induced in reinforced concrete buildings by direct strikes," *2001 IEEE International Symposium on Electromagnetic Compatibility*, pp. 1009-1014, 2001.

[2] J. Chen, B. Zhou, F. Zhao, and S. Qiu, "Finite-difference time-domain analysis of the electro-magnetic environment in a reinforced concrete structure when struck by lightning," *IEEE Transactions on Electromagnetic Compatibility*, vol. 52, no. 4, pp. 914-920, Nov. 2010.

[3] IEEE 299-2006 - *IEEE Standard Method for Measuring the Effectiveness of Electromagnetic Shielding Enclosure*, 2006.

[4] S. Pennesi and S. Sebastiani, "Information security and emissions control," *2005 IEEE International Symposium on Electromagnetic Compatibility*, pp. 777-781, 2005.

[5] H. Seikiguchi and S. Seto, "Study on maximum receivable distance for radiated emission of information technology equipment causing information leakage," *IEEE Transactions on Electromagnetic Compatibility*, vol. 55, no. 3, pp. 547-554, June 2003.

[6] X. Hui, L. Bangyu, X. Shaobo, and F. Hongzhuan, "The measurement of dielectric constant of the concrete using single-frequency CW radar," *First International Conference on Intelligent Networks and Intelligent Systems*, pp. 588-591, 2008.

[7] G. Villain, A. Ihamouten, and X. Dérobert, "Use of frequency power law to link the results of two testing methods for the characterization of humid concretes," *2011 6th International Workshop on Advanced Ground Penetration Radar (IWAGPR)*, pp. 1-5, 2011.

[8] C. A. Grosvenor, R. T. Johnk, J. Barker-Jarvis, M. D. Janezic, and B. Riddle, "Time-domain free-field measurements of the relative permittivity of building materials," *IEEE Transactions on Instrumentation and Measurements*, vol. 58, no. 7, pp. 2275-2282, July 2009.

[9] S. Ji-tong, G. Xiu-jun, Z. Xiao-wei, "Research on dielectric properties of asphalt concrete with GPR," *2012 14th International Conference on Ground Penetration Radar (GPR*), pp. 542-545, 2012.

[10] Z. Yanhui, Z. Bei, S. Wenbo, and W. Tao, "Experimental research on relationships between dielectric constant of cement concrete materials

and measuring frequency," *2012 14th International Conference on Ground Penetrating Radar (GPR)*, pp. 403-406, 2012.

[11] S. Lihua, X. Qiwei, C. Bin, and G. Cheng, "Measurement of the frequency-dependent dielectric constant of concrete materials by TDR and wavelet modeling method," *CEEM 2003 Asia-Pacific Conference on Environmental Electromagnetics*, pp. 626-629, 2003.

[12] J. G. Webster, *The Measurement, Instrumentation and Sensors Handbook (Electrical Engineering Handbook)*. CRC Press, pp. 1402-1413, 1998.

[13] A. V. Hippel, *Dielectric Materials and Applications*. MIT Technology Press and John Wiley & Sons, pp. 47-63, 1954.

[14] S. Pfeifer, S. H. Park, and P. R. Bandary, "Modeling the relative dielectric permittivity and impedance of carbon nanotube constituted polymer composites in the sub-GHz regime," *ECS Solid State Letters*, vol. 2, no. 1, pp. M5-M7, Oct. 2012.

[15] X. Jin and M. Ali, "Simple empirical formulas to estimate the dielectric constant and conductivity of concrete," *Microwave and Optical Technology Letters*, vol. 61, no. 2, pp. 386-390, Feb. 2019.

[16] M. N. O. Sadiku, *Numerical Techniques in Electromagnetics*. CRC Press, pp. 274-336, 2001.

[17] J. J. von Tonder and U. Jakobs, "Fast multipole solution of metallic and dielectric scattering problems in FEKO," *IEEE/ACES International Conference on Wireless Communications and Applied Computational Electromagnetics, 2005.*

Marcelo B. Perotoni Electrical Engineer (UFRGS, Porto Alegre, Brazil), M.Sc. and Ph.D. in Electrical Engineering from USP (Sao Paulo, Brazil). He has been involved with electromagnetic simulation since 2002 and is interested in RF and EMC. He is currently a professor at UFABC.

Marcos S. Vieira B.Sc. in Electrical Engineering (1996) - UMC, M.Sc. in Electrical Engineering (2004) - Mackenzie Presbyterian University, Ph.D. in Electrical Engineering (2015) - USP (Sao Paulo, Brazil). Currently is a Professor at the Mackenzie Presbyterian University. He has experience in Electrical Engineering with emphasis on Numerical Methods, Microwave and Antennas.

Kenedy M. G. Santos is B.Sc. in Electrical Engineering (2006) - PUC MG, M.Sc. in Electrical Engineering (2011)-UFMG, Ph.D. in Electrical Engineering (2018) - UFBA. Currently is Professor at the IFBA. He has experience in Electrical Engineering with emphasis on EMC, Microwave and Antennas.

Danilo B. Almeida is B.Sc. in Electrical Engineering (2005) - UNIP - SP. He is a specialist in Occupational Safety and Energy Efficiency. Currently is Professor at the IFBA and FAINOR.

Six-Channel Diplexer using Stub-Loaded Stepped Impedance Resonators

Jinlin Liu, Tao Su*, Huanhuan Lv, Lei Lin, and Bian Wu

National Laboratory of Science and Technology on Antennas and Microwaves
Xidian University, Xi'an, 710071, China
xdjinlinliu@126.com, *taosu@mail.xidian.edu.cn, lvhuanhuan4213@126.com,
linleimail@126.com, bwu@mail.xidian.edu.cn

Abstract ─ In this paper, a compact six-channel diplexer with low insertion loss and high isolation level is presented. The diplexer consists of two tri-band bandpass filters (BPFs), two meander transmission lines and hook-shaped feeding lines. The BPFs are designed based on stub-loaded stepped impedance resonators (SLSIRs). Based on even- and odd-mode (EOM) analysis of the resonator, there are two resonant modes that operate at the same frequency. For splitting the two modes, stub-stub coupling is employed here. The combination of the two BPFs is implemented by utilizing two meander transmission lines as the impedance matching network. Finally the proposed diplexer operating at 1.46/1.74/2.96 GHz (for Load 1) and 0.89/1.15/2.40 GHz (for Load 2) is fabricated and measured. A good agreement between simulated and measured results evidently validates the proposed diplexer.

Index Terms ─ Bandpass filters, six-channel diplexer, stub-loaded stepped impedance resonators, stub-stub coupling.

I. INTRODUCTION

Multiplexers with multiple passbands, low insertion loss, high isolation level and compact size attract much interest in multi-band wireless communication systems. There is an increasing demand of improving the performance of the multiplexers. To achieve this aim, many of literatures have been published to introduce research and development of the multiplexers. Stepped impedance resonator (SIR) is widely used in the design of multiplexers [1-5]. In [1], new three-way resonators using connected- and edge-coupling mechanisms are designed for diplexers. In [3], a triplexer using multiple-mode resonators is presented and the triplexer features high isolation level. In order to improve the isolation level, branch-line coupler is employed to design the diplexer in [6]. Open-loop ring resonators are studied in [7-9], which can provide good performance in designing multiplexers. A distributed coupling technique, which needs no extra matching networks, is presented for designing a quadruplexer in [9]. In [10-13], several effective methods and novel structures are presented to design multiplexers.

The goal of this work is to design a six-channel diplexer with low insertion loss and high isolation level while maintaining a compact size. Even- and odd-mode (EOM) analysis method is adopted to analysis the tri-band bandpass filters (BPFs) which is the main part of the diplexer. The BPFs are designed by stub-loaded stepped impedance resonators (SLSIRs). Utilization of SLSIRs makes the diplexer feature compact size and the high harmonics can be controlled by tuning the impedance ratio and the electrical length ratio of the resonators. The impedance matching network between the two BPFs is properly designed and hook-shaped transmission lines are employed as feeding lines to provide appropriate external coupling for the passbands of the diplexer. The proposed diplexer features low insertion loss and high isolation level with a compact size. The design process is demonstrated as follows.

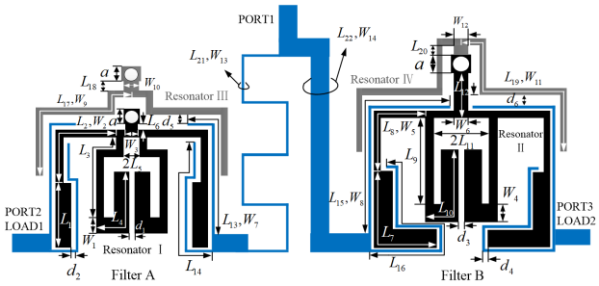

Fig. 1. Geometry of the proposed diplexer.

II. DESIGN METHODOLOGY

The geometry of the proposed diplexer consisting of two tri-band BPFs is shown in Fig. 1. Filter A is designed for Load 1 operating at 1.46/1.74/2.96 GHz and Filter B is designed for Load 2 at 0.89/1.15/2.40 GHz. The structures of two BPFs are both based on a quad-mode SLSIR (Resonator I, Resonator II) and a dual-mode SLSIR (Resonator III, Resonator IV). In this

Submitted On: January 6, 2019
Accepted On: April 3, 2019

paper, High Frequency Structure Simulation (HFSS) software with Finite Element Method (FEM) is used to analyse and optimize the performance of the proposed structure. The numerical analysis and optimization procedure is demonstrated as follows.

The equivalent structure of the SLSIR with four resonant modes (Resonator I, Resonator II) is shown in Fig. 2 (a). Because of the symmetry of the structure, EOM analysis method is used to analysis its resonant characteristics [14]. Figure 2 (b) shows the even-mode (EM) equivalent circuit of the SLSIR. Figure 2 (c) shows the odd-mode (OM) equivalent circuit of the SLSIR. As the EM and OM equivalent circuits in Fig. 2 (b) and Fig. 2 (c) are still symmetrical (L_1=L_4, L_2=L_3), EOM analysis method is used to analysis the structure again. The EOM equivalent circuits of Fig. 2 (b) are shown in Fig. 2 (d), and the EOM equivalent circuits of Fig. 2 (c) is shown in Fig. 2 (e).

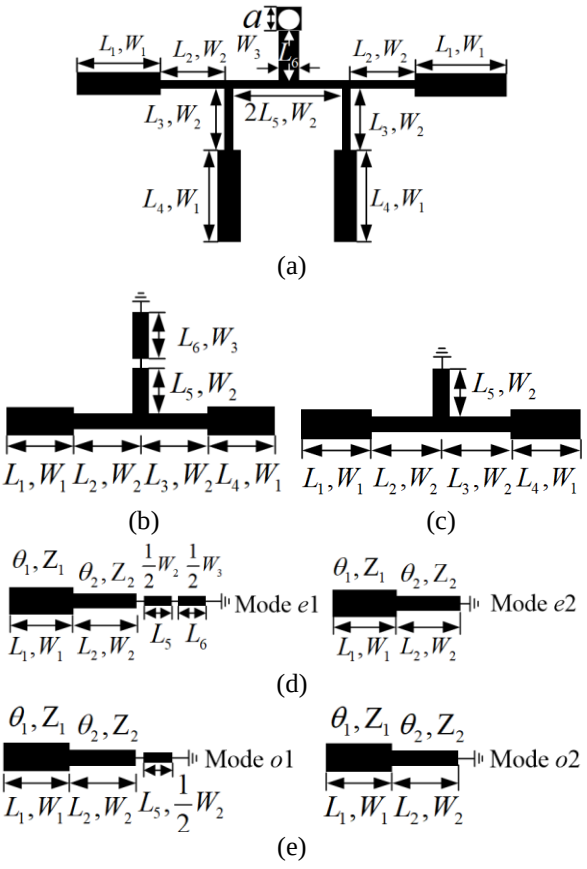

Fig. 2. (a) Schematic of the SLSIR; (b) EM equivalent circuit of the SLSIR; (c) OM equivalent circuit of the SLSIR; (d) EOM equivalent circuits of Fig. 2 (b); (e) EOM equivalent circuits of Fig. 2 (c).

It can be seen from Fig. 2 (d) and Fig. 2 (e) that there are four resonant modes in total, which are named as *e*1, *e*2, *o*1, and *o*2 respectively. It is obviously that the equivalent circuits of the four resonant modes are quarter wavelength SIRs [15]. The basic frequencies are defined as f_{e1}, f_{e2}, f_{o1} and f_{o2}. Figure 3 (a) and Fig. 3 (b) show the fundamental frequencies of four modes under different L_5 and L_6. It can be observed from Fig. 3 (a) that the variation of L_5 has an influence on f_{e1} and f_{o1}, while f_{e2} and f_{o2} remain constant. From Fig. 3 (b), it can be seen that only f_{e1} changes with the variation of L_6, while f_{e2}, f_{o1} and f_{o2} keep constant. The equivalent circuits of mode *e*2 and mode *o*2 can be considered as the basic structures of $\lambda/4$ SIR. The resonance condition can be deduced as:

$$\tan(\alpha\theta_T)\tan[(1-\alpha)\theta_T] = R_z, \quad (1)$$

$$\theta_T = \theta_1 + \theta_2, \quad (2)$$

where R_z is the impedance ratio and α is the electrical length ratio. R_z and α are defined as $R_z = Z_1 / Z_2$ and $\alpha = \theta_1 / \theta_T$ [16].

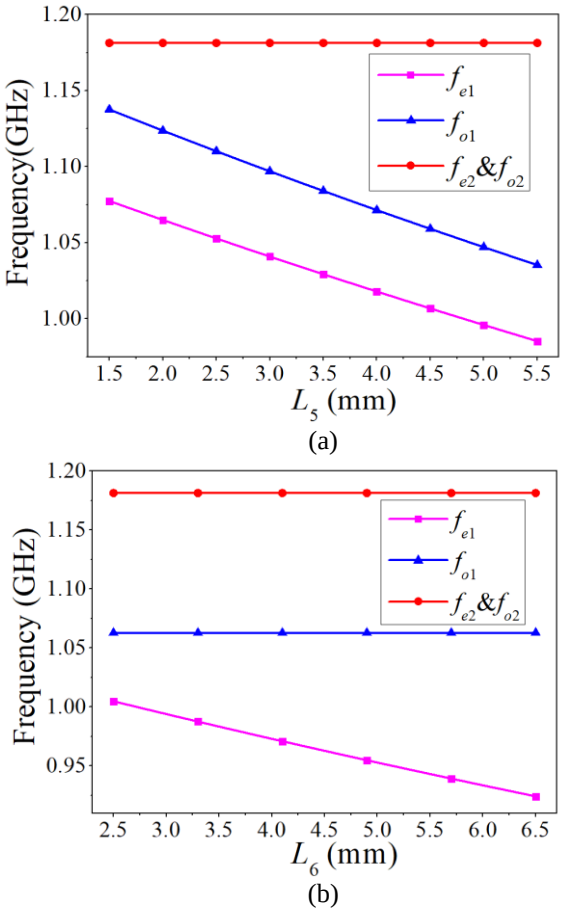

Fig. 3. Effect of (a) L_5 and (b) L_6 on fundamental frequencies of the resonant modes.

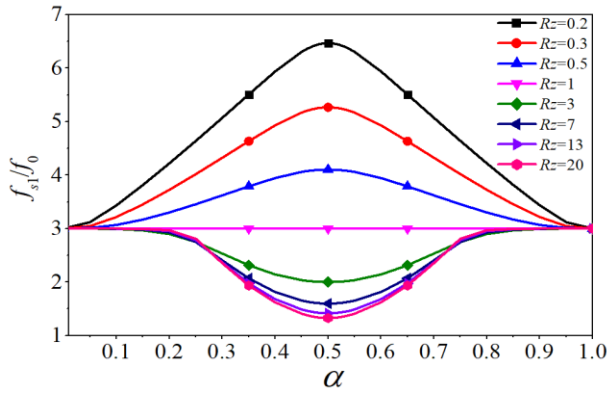

Fig. 4. Ratios of f_{s1}/f_0 with varied α and R_z.

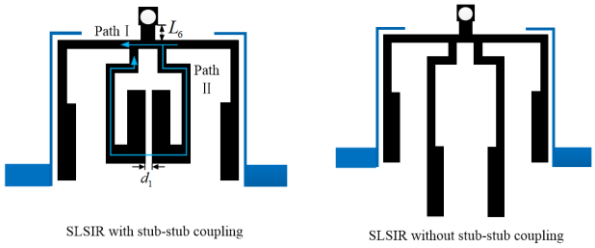

Fig. 5. SLSIR with and without stub-stub coupling.

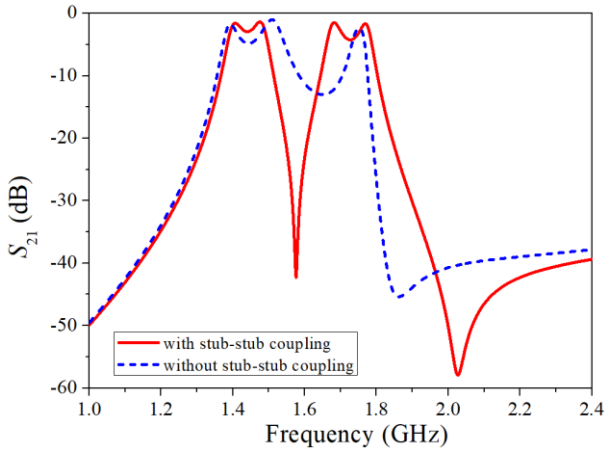

Fig. 6. Simulated results of the SLSIR with and without stub-stub coupling.

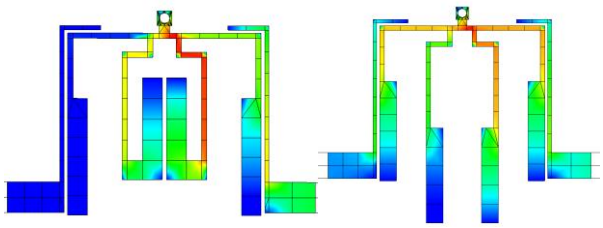

Fig. 7. Current distributions of the SLSIR at 1.58 GHz with and without stub-stub coupling.

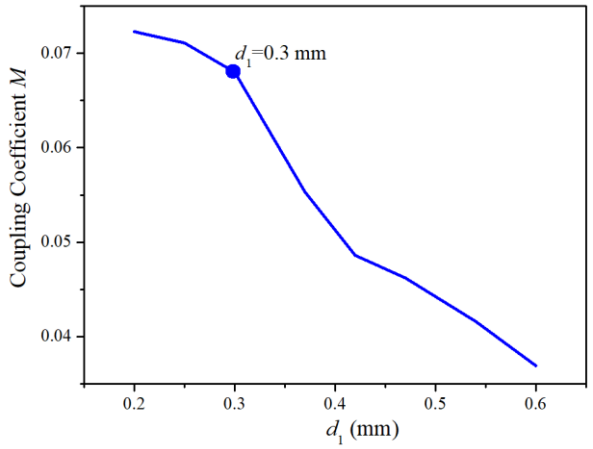

(a)

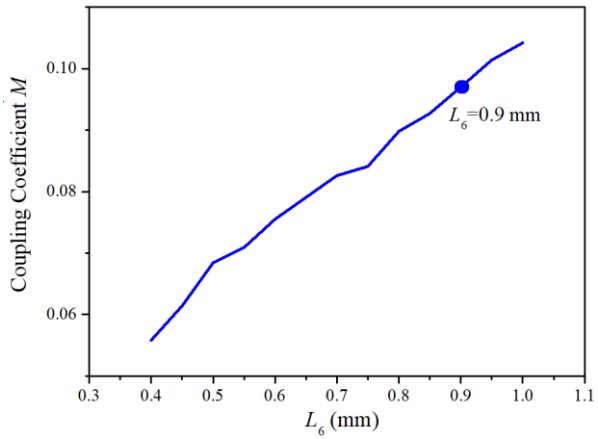

(b)

Fig. 8. (a) Simulated coupling coefficient M (for 1.74 GHz) under different d_1. (b) Simulated coupling coefficient M (for 1.46 GHz) under different L_6.

It can be seen that resonance condition of $\lambda/4$ type SIR is related to the electrical length ratio and the impedance ratio. Thus, the spurious generation can be controlled. The first harmonic frequency is defined as f_{s1} and Fig. 4 shows the relation between f_{s1}/f_0 and α with different R_z. It is obviously that frequency ratio can be configured in a wide range.

It can be seen from Fig. 2 that the equivalent circuits of Mode $e2$ and Mode $o2$ are identical. To spilt two resonant modes, we employ stub-stub coupling to introduce capacitive coupling between two stubs in the proposed SLSIR. Figure 5 shows the structure of Resonator I with and without stub-stub coupling. The resonator is folded inwards to form coupling effect, which provides additional signal deliver path. Figure 6 shows the simulated S_{21} parameter of the resonator without stub-stub coupling. By the stub-stub coupling, a transmission zero at 1.58 GHz is created. Current distributions of the resonator at the transmission zero, which are shown in Fig. 7, can be adopted here to

demonstrate the effect of stub-stub coupling. The electric current passes through the Path II due to stub-stub coupling and cancels the electric current which passes through the Path I, and this effect stimulates the transmission zero.

The coupling between the two resonant modes, which form one passband, needs to be optimized. The passband ripple is set as 0.1 dB and element values of the lowpass prototype filter are g_0=1, g_1=0.8431, g_2=0.6220 and g_3=1.3554, respectively. For the structure of Resonator I in Fig. 5, the central frequencies of the passbands are set as 1.46 GHz and 1.74 GHz. The 3 dB fractional bandwidths (FBW) is 7% and 5%, respectively. The required coupling coefficients are M=0.097 (for 1.46 GHz) and M=0.069 (for 1.74 GHz), which can be calculated theoretically from the equation:

$$M = \frac{\mathrm{FBW}}{\sqrt{g_1 g_2}}. \tag{3}$$

It is worth noting that equation (3) is used in theoretical synthesis. During the simulation and optimization, the coupling coefficients can be computed as:

$$M = \frac{f_H^2 - f_L^2}{f_H^2 + f_L^2}, \tag{4}$$

where f_H and f_L represent the higher resonant frequency and lower resonant frequency [17]. The simulated coupling coefficient at 1.46 GHz is mainly influenced by L_6 and the simulated coupling coefficient at 1.74 GHz is mainly influenced by d_1. As the length of L_6 does not influence the simulated coupling coefficient at 1.74 GHz, the value of d_1 is first decided based on the required coupling coefficient of 1.74 GHz band. Then, the value of L_6 is optimized based on the required coupling coefficient of 1.46 GHz band. Thus, the coupling coefficients of two bands can be tuned independently. Figure 8 shows the simulated coupling coefficient M under different lengths d_1 of and L_6. It can be observed that the coupling coefficient of 1.46 GHz increases with the increasing of the length of L_6, while the coupling coefficient of 1.74 GHz decreases with the increasing of the length of d_1. The optimized lengths are set as d_1=0.3 mm and L_6=0.9 mm for the required coupling coefficients. To obtain a tri-band response, we employ a dual-mode SLSIR (Resonator III), which is placed on the upper side of Resonator I as shown in Fig. 1 and operates at 2.96 GHz. Similarly, EOM method can be adopted here to make an analysis of Resonator III. The corresponding dimensions of Resonator III are optimized and a tri-band BPF Filter A can be obtained. Meanwhile, hook-shaped lines are used as feeding lines of the BPF. According to the above discussion, Filter B consisting of Resonator II and Resonator IV as shown in Fig. 1 can be designed by using the same method. The proposed diplexer is formed by the combination of Filter A and Filter B, which is implemented by utilizing two meander transmission lines as the impedance matching network.

To summarize the design procedure, design specifications are given as follows:

a) Decide the original dimensions of Resonator I and Resonator II based on the required frequencies using EOM method.

b) Calculate the required coupling coefficients, design stub-stub coupling structure and optimize the dimensions of Resonator I and Resonator II.

c) Design Resonator III and Resonator IV using EOM method.

d) Combine two BPFs by meander transmission lines and carry out final optimization of the diplexer.

III. TEST OF DIPLEXER

The thickness of the dielectric is h = 1 mm and relative permittivity of the substrate is ε_r = 2.65. The specification of the proposed diplexer is set as the center frequencies f_1=0.89 GHz, f_2=1.15 GHz, f_3=1.46 GHz, f_4=1.74 GHz, f_5=2.40 GHz, and f_6=2.96 GHz with 3 dB FBW of FBW1=11%, FBW2=9%, FBW3=7%, FBW4=5%, FBW5=4% and FBW6=3%, respectively. The required coupling coefficients are M=0.152 (for 0.89 GHz), M=0.124 (for 1.15 GHz), M=0.097 (for 1.46 GHz), M=0.069 (for 1.74 GHz), M=0.055 (for 2.40 GHz) and M=0.041 (for 2.96 GHz), respectively. The optimized dimensions are given in Table 1 (all in mm).

Table 1: Design parameters of the six-channel diplexer

PARM	Value	PARM	Value	PARM	Value
L_1	10.1	L_2	13.3	L_3	13.3
L_4	10.1	L_5	1.1	L_6	0.9
L_7	18.6	L_8	17.07	L_9	17.07
L_{10}	18.6	L_{11}	3.85	L_{12}	2.26
L_{13}	18.35	L_{14}	20.3	L_{15}	31.8
L_{16}	30.4	L_{17}	19.14	L_{18}	0.2
L_{19}	23.12	L_{20}	0.48	L_{21}	69.07
L_{22}	39.3	W_1	1.9	W_2	0.5
W_3	1	W_4	1.85	W_5	0.5
W_6	1	W_7	0.4	W_8	0.4
W_9	0.5	W_{10}	1.4	W_{11}	0.15
W_{12}	1	W_{13}	0.7	W_{14}	2.7
d_1	0.3	d_2	0.35	d_3	0.3
d_4	0.2	d_5	0.4	d_6	0.52
a	1.4				

Figure 9 shows the photograph of the fabricated diplexer. The circuit size is around $0.37\lambda_g \times 0.18\lambda_g$, where λ_g is the guide wavelength on the used substrate at 0.89 GHz.

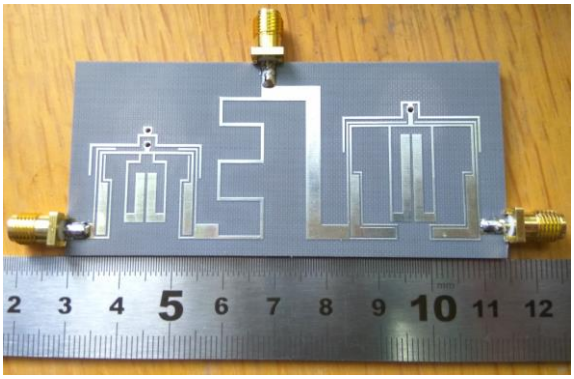

Fig. 9. Photograph of the fabricated diplexer.

Simulated and measured *S*-parameters of the proposed diplexer are shown in Fig. 10. Agilent 8719ES network analyzer is adopted here to measure the performance of the diplexer. The measured central frequencies of six channels of the diplexer locate at 0.89 GHz, 1.16 GHz, 1.46 GHz, 1.75 GHz, 2.4 GHz and 2.96 GHz with 3dB FBW of 10%, 9%, 6%, 6%, 4% and 3%, respectively. The measured minimum insertion losses of six channels are 0.95 dB, 0.84 dB, 1.3 dB, 1.17 dB, 1.57 dB and 1.8 dB, whereas the simulated minimum insertion losses are 0.72 dB, 0.77 dB, 0.95 dB, 0.81 dB, 1.21 dB and 1.58 dB, respectively. The small deviation may be caused by the fabrication machining error. The S_{11} parameters are lower than -15.6 dB and the measured S_{32} is lower than -37 dB as shown in Fig. 10.

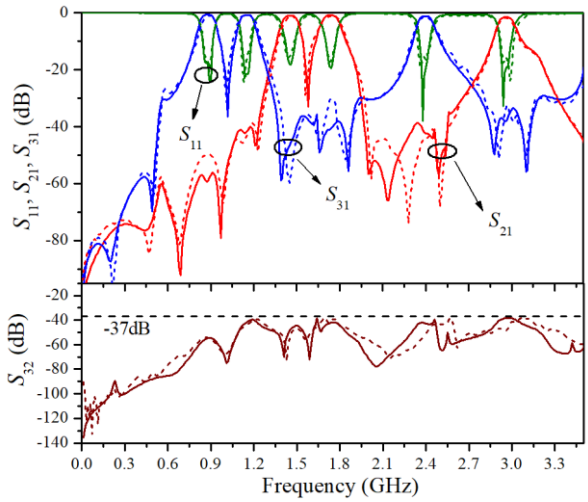

Fig. 10. Simulated and measured *S*-parameters of the proposed diplexer.

Table 2 shows comparisons between this work and previous research. It can be seen that the proposed diplexer features lower insertion loss and higher isolation with a compact size.

Table 2: Comparisons between this work and previous research

Ref.	Passbands (GHz)	Insertion Loss (dB)	Isolation (dB)	Size (λ_g^2)
6	0.9/1.5/ 2.4/3.5	2.02/1.56/ 2.08/2.52	>29	0.041
16	1.8/2.4/3.0/ 3.8/4.7/5.8	1.8/1.9/1.0/ 1.5/2.1/2.6	>30	0.057
This work	0.89/1.16/ 1.46/1.75/ 2.4/2.96	0.95/0.84/ 1.3/1.17/ 1.57/1.8	>37	0.067

IV. CONCLUSION

In this letter, a six-channel diplexer using novel SLSIRs is presented. The proposed diplexer is formed by two tri-band BPFs, which can be designed using the EOM analysis method. Two meander transmission lines are utilized to combine two BPFs and achieve impedance matching. A good agreement between simulated and measured results evidently validates the proposed diplexer.

ACKNOWLEDGMENT

This work was supported in part by the National Natural Science Foundation of China under Project 61771360 and Project 61601360, and in part by the Shaanxi Youth Science and Technology Star Project

REFERENCES

[1] S. C. Lin and T. L. Jong, "Microstrip bandpass filters with various resonators using connected- and edge-coupling mechanisms and their applications to dual-band filters and diplexers," *IEEE Trans. Microw. Theory Tech.*, vol. 60, no. 4, pp. 975-988, Apr. 2012.

[2] H. W. Liu, W. Y. Xu, Z. C. Zhang, and X. H. Guan, "Compact diplexer using slotline stepped impedance resonator," *IEEE Microw. Wireless Compon. Lett.*, vol. 23, no. 2, pp. 75-77, Feb. 2013.

[3] J. Y. Wu, K. W. Hsu, Y. H. Tseng, and W. H. Tu, "High-isolation microstrip triplexer using multiple-mode resonators," *IEEE Microw. Wireless Compon. Lett.*, vol. 22, no. 4, pp. 173-175, Apr. 2012.

[4] J. F. Chen and F. C. Chen, "Design of microstrip lowpass-bandpass quintuplexer," *Journal of Electromagnetic Waves and Applications*, vol. 30, no. 11, pp. 1474-1480, 2016.

[5] K. W. Hsu, W. C. Hung, and W. H. Tu, "Design of four-channel diplexer using distributed coupling technique," *Microwave and Optical Technology Letters*, vol. 58, no. 1, pp. 166-170, Jan. 2016.

[6] H. Sajadinia, M. Dahmardeh, and M. Khalaj-Amirhosseini, "Novel planar diplexer using branch-line coupler," *Microwave and Optical Technology Letters*, vol. 60, no. 11, pp. 2773-2777, Mar. 2018.

[7] C. M. Chen, S. J. Chang, J. C. Zheng, J. C. Liou,

and C. F. Yang, "Using folded open-loop ring resonator to design a common-mode suppression and frequency adjustable balun-bandpass filter," *Applied Computational Electromagnetics Society Journal*, vol. 31, no. 1, pp. 45-51, Jan. 2016.

[8] C. M. Chen, S. J. Chang, and C. F. Yang, "Fabrication of a novel diplexer using folded open-loop ring resonators and microstrip lines," *Applied Computational Electromagnetics Society Journal*, vol. 29, no. 11, pp. 864-869, Nov. 2014.

[9] S. J. Zeng, J. Y. Wu, and W. H. Tu, "Compact and high-isolation quadruplexer using distributed coupling technique," *IEEE Microw. Wireless Compon. Lett.*, vol. 21, no. 4, pp. 197-199, Apr. 2011.

[10] H. Chu, R. Mao, and J. X. Chen, "Development of diplexers based on dual-mode substrate integrated waveguide cavities," *Applied Computational Electromagnetics Society Journal*, vol. 32, no. 2, pp. 171-177, Feb. 2015.

[11] X. H. Guan, F. Q. Yang, H. W. Liu, and L. Zhu, "Compact and high-isolation diplexer using dual-mode stub-loaded resonators," *IEEE Microw. Wireless Compon. Lett.*, vol. 24, no. 6, pp. 385-387, June 2014.

[12] Y. X. Ji and J. Xu, "Compact BPF and diplexer using capacitively loaded λ/4 shorted meander line resonator," *Journal of Electromagnetic Waves and Applications*, vol. 28, no. 1, pp. 112-118, 2014.

[13] C. X. Zhou, Y. X. Guo, and W. Wu, "Design of lowpass filter and lowpass-highpass diplexer with LTCC technology," *Applied Computational Electromagnetics Society Journal*, vol. 31, no. 7, pp. 817-822, July 2016.

[14] T. Yang, P. L. Chi, and T. Itoh, "Compact quarter-wave resonator and its applications to miniaturized diplexer and triplexer," *IEEE Trans. Microw. Theory Tech.*, vol. 59, no. 2, pp. 260-269, Feb. 2011.

[15] F. C. Chen and Q. X. Chu, "Novel multistub loaded resonator and its application to high-order dual-band filters," *IEEE Trans. Microw. Theory Tech.*, vol. 58, no. 6, pp. 1551-1556, June 2010.

[16] Q. Li and Y. H. Zhang, "Six-channel diplexer with compact size and high isolation," *Electron. Lett.*, vol. 53, no. 17, pp. 1205-1207, Aug. 2017.

[17] Q. Li, Y. H. Zhang, and C. M. Wu, "Compact and high-isolation microstrip diplexer using distributed coupling feeding line," *Microwave and Optical Technology Letters*, vol. 60, no. 1, pp. 192-196, June 2017.

A Diplexer based on Hybrid Cavity and Microstrip Structure

Jiao Shu and Yerong Zhang

College of Electronic and Optical Engineering
Nanjing University of Posts and Telecommunications, Nanjing, 210003, China
sjsj6668@outlook.com, zhangyr@njupt.edu.cn

Abstract ─ This paper presents a high selective diplexer with hybrid filters, which is composed by dual-mode microstrip resonators with metallic coaxial shielding cases of RF module. By utilizing vertical space above microstrip circuits which greatly saves space, an additional pair of transmission pole and zero are hereby added in the passband and stopband, respectively. The proposed structure provides high quality-factors to enhance frequency selectivity. For demonstration, a diplexer prototype is designed and fabricated at the center frequencies (CF) of 2.40 and 3.45 GHz with a 3-dB passband bandwidth of 200 MHz. The measured insertion losses (IL) are 1.45 dB and 1.61 dB in the lower and upper passbands respectively. The output isolation between two channels is measured greater than 32 dB.

Index Terms ─ Cavity, diplexer, hybrid structure, microstrip.

I. INTRODUCTION

Diplexers are the key components in modern multi-services and multi-band communication systems, especially in the radio frequency (RF) front-ends. They are used to separate one input signal from two different frequencies into two individual signals at the output ports, or to combine two separate input signals into one. In order to decrease the number of antennas, the full-duplex wireless communication systems utilize diplexers for transmitting and receiving signals. In order to meet the demands of modern systems with stringent requirements, high-performance diplexers are necessary. Numerous literatures on designing diplexers have been reported in recent years. Compact composite right/left-handed (CRLH) microstrip resonators were used in diplexer [1]. Dual-mode resonators were employed to achieve a compact and wide-stopband diplexer [2]. High quality-factor (Q-factor) dielectric resonators were utilized to design diplexer in base station applications [3]. Substrate integrated waveguide (SIW) loaded with complementary split ring resonators (CSRRs) were applied to develop a compact diplexer [4]. SIW dual-mode filters with circular and elliptic cavities were implemented on a high performance diplexer [5].

In this paper, the diplexer with two triple-mode high-selectivity bandpass filters is designed. The proposed hybrid filter structure is realized by a metallic coaxial resonator formed by shielding cavity with a copper rod in space and a dual-mode planar microstrip resonator on the surface. In the case of maximizing the vertical space above the planar circuit, the third resonant mode has been generated without size enlargement. These hybrid structures not only introduce pairs of transmission zeros and poles which improved the out-of-band suppression but also greatly enhance the unloaded Q-factors. A high selective diplexer at frequencies of 2.4/3.45 GHz is designed and fabricated to demonstrate the proposed structure with good in-band performance. The measured results exhibit good agreements with the simulated ones by careful comparisons.

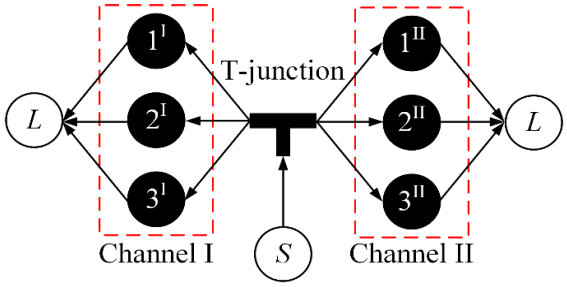

Fig. 1. Coupling and routing topology of the proposed diplexer.

II. DESIGN OF DIPLEXER AND FILTERS

The coupling and routing topology of the hybrid diplexer with triple-mode responses is illustrated in Fig. 1. Figure 2 shows the 3D configurations of the proposed hybrid diplexer which consists of two triple-mode filters. Meanwhile, the structures of the planar circuit parts are described in Fig. 3.

The proposed diplexer is comprising of two individuation channels connected with 50Ohm common input/output ports through a T-junction. Figure 1 shows the routing topology of triple mode resonator. The black node in each channel represents a resonant mode. For each proposed hybrid filter, the even and odd modes

Submitted On: December 27, 2018
Accepted On: May 12, 2019

(mode 1 and 3) are generated by planar microstrip structures, while the shielding cavity forms the high-Q resonant mode (mode 2) with a copper rod. Symbol S and symbol L are utilized to represent the input and output port. The band-pass filters of each channel are designed by using the hybrid cavity-microstrip structure with different specifications.

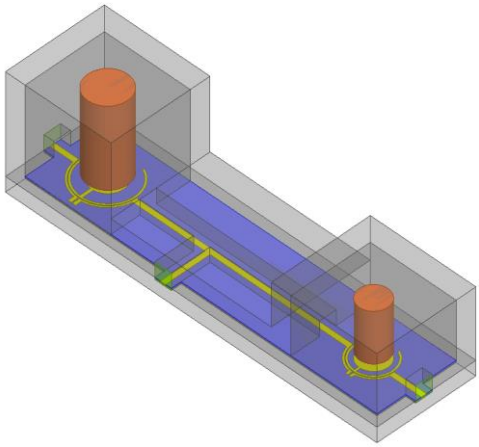

Fig. 2. 3D Configuration of the proposed diplexer.

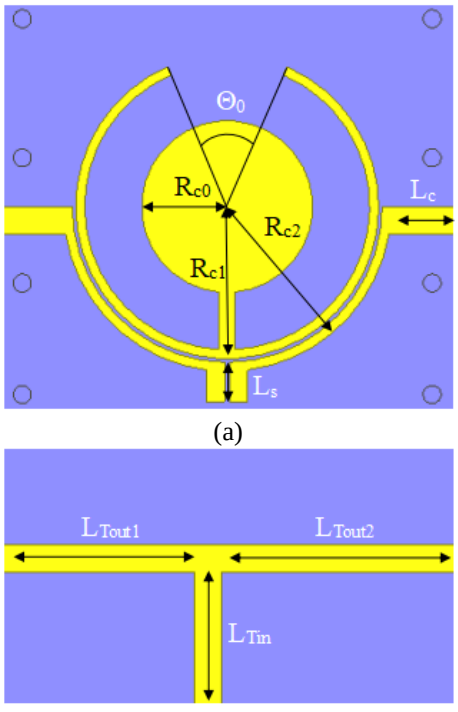

Fig. 3. Configurations of the diplexer components: (a) microstrip resonator and (b) T-junction.

After the two individual channels are designed, the T-junction is carefully designed and optimized for connecting the two sub-channels with I/O ports, and one stub could be considered as an open circuit to another.

The grounded planar dual-mode open-loop microstrip resonators in each channel have been demonstrated in the previous literature [6], and are utilized to design microstrip resonators with low Q-factor. The limited and relatively low unloaded quality factor is a part of the significant problems restricting the performance of filters. It is a known fact that coaxial resonators have greater quality factors than microstrip resonators. To obtain higher Q-factor and the selectivity of filter with the full use of the vertical space above the planar circuit, we introduced a copper rod into the shielding cavity for generating triple-mode resonance. As shown in Fig. 3 (a), the planar microstrip part consists of input and output coupling lines with dual-mode circular open-loop resonators. The characteristic impedance of the input/ output lines are selected as 50Ω, and the length of source-load coupling line is L_s. The dual-mode filter is comprised of a half-wavelength resonator with a circular open stub placed in its center. The radius of the inner circular stub is R_{c0}, the radius of the open-loop resonator is R_{c1}, and the radius of the feeder is R_{c2}. From Fig. 3 (b), the T-junction with three stubs which connect the input port with two separate channels, the length of the stubs is L_{Tin}, L_{Tout1} and L_{Tout2} respectively. The layout of the proposed hybrid bandpass filter is shown in Fig. 4, while the radius of the centered copper rod is R_1, and the distance from the bottom of the rod to the planar microstrip circuit is H_1. The length, width, height, and thickness of the shielding cavity are L_1, W_1, H_0, and W_2, respectively. By welding the copper rod inside the shielding cavity to produce additional transmission zero and transmission pole, thereby enhancing out-of-band suppression and effectively improves the anti-jamming ability.

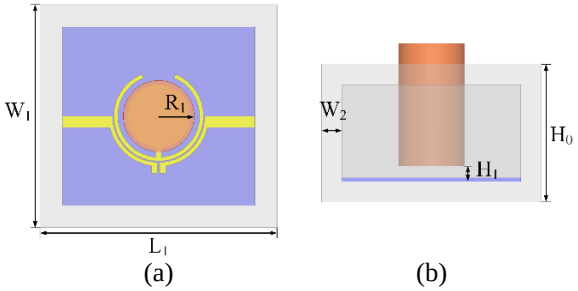

Fig. 4. Layout of the proposed hybrid bandpass filter: (a) top view and (b) orthographic view.

Design of the proposed hybrid diplexer follows the following steps:

Step1: Based on the odd and even mode theory analysis, the initial dimensions of the dual-mode microstrip bandpass filters which operate at 2.4 GHz and 3.5 GHz are determined, respectively. For each microstrip filter, two transmission zeros in the higher

frequency stopband of the filter are determined by the half-wavelength resonator with a circular stub. By changing the radius of the inner circular stub and increasing the length of source-load coupling feeders, the two transmission zeros in the higher frequency stopband can be adequately controlled. The first transmission zero moves to a higher frequency as the radius increases. The second transmission zero moves to a lower frequency as the coupling length decreases.

Step2: To improve the ability of out-of-band suppression and to improve the anti-jamming performance, we adopt the hybrid structure of a shielding cavity with a copper rod to generate the third resonant mode. By controlling the distance between the copper rod to the planar circuit, the frequency responses of the transmission zero in the lower stopband and the pole in the passband can be tuned to obtain the best triple-mode frequency response.

Step3: Optimizing the T-junction to connect both the triple-order bandpass filters to form the desired diplexer. For each stub of the two output ports, one stub could be considered as an open circuit to another.

To address the above scenario, we take the hybrid filter of Channel II with a central operating frequency of 3.45 GHz as the prototype model. Its coupling topology is shown in Fig. 1. Modes 1 and 3 are the even and odd modes of the planar dual-band microstrip resonator, while Mode 2 is formed by the coaxial shielding cavity. The coupling schemes can be analyzed from its coupling matrix [7]:

$$M = \begin{bmatrix} 0 & 0.4696 & 0.4575 & 0.7696 & -0.0145 \\ 0.4696 & -1.435 & 0 & 0 & 0.4696 \\ 0.4575 & 0 & 1.4029 & 0 & 0.4575 \\ 0.7696 & 0 & 0 & -0.0544 & -0.7696 \\ -0.0145 & 0.4696 & 0.4575 & -0.7696 & 0 \end{bmatrix}.$$

Since the proposed triple mode hybrid resonator exhibits symmetry, the coupling matrix is agreed with $M_{S1}=M_{1L}$, $M_{S2}=M_{2L}$, and $M_{S3}=-M_{3L}$. An additional transmission zero is implemented by the source-load coupling on the planar resonators. Although the cross-couplings are not precisely equal to zero, the number of cross-couplings is minimal that considered negligible when compared with the main couplings, which makes it easier to represent the coupling matrix. The generalized coupling matrix of the proposed hybrid filter of 3.45GHz is designed by synthesis method.

The geometric dimensions of the exampled 3.45GHz Channel with coaxial shielding cavity is derived as R_1=4.3mm, W_1=30mm, L_1=32mm, W_2=3mm, and H_0=20mm. Meanwhile, parameters of planar microstrip resonator are R_{c0}=4.3mm, R_{c1}=6.05mm, R_{c2}=6.75mm with Θ_0=22.4 deg. Figure 5 presents the frequency responses of the shielding cavity with or without the copper rod.

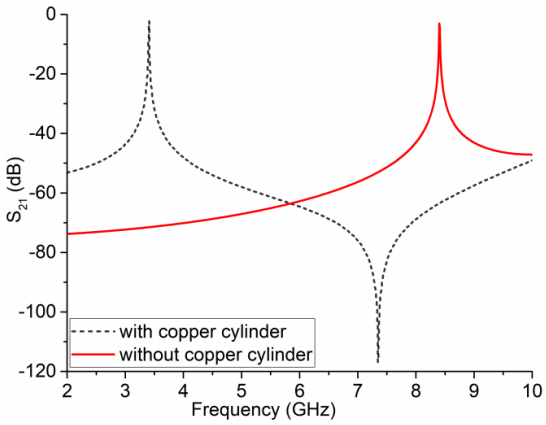

Fig. 5. Frequency responses of shielding cavity with or without copper cylinder.

Without the copper rod, the cavity resonates at the fundamental frequency of the TE_{101} mode (which operates at 8.36 GHz), by introducing the copper rod into the shielding cavity, the resonant frequency shifts to the lower band. Figure 6 exhibits the variation of resonant frequencies and unloaded Q factors with H_1 and R_1, when H_1 equals to 2.2 mm, and the resonant frequency is 3.41 GHz.

With the increase of H_1, the resonant frequency of the shielding cavity moves upward, and the Q_factor increases. With the additions of R_1, the resonant frequency moves to reduce, and the Q-factor decrease. However, with larger values of R_1, the influences on the resonant frequency and Q_factor decrease. For different resonance center frequencies, it is necessary to select the optimal values of H_1 and R_1 to obtain the best Q value by simulation. As a result, the proposed hybrid structure exhibits a higher unloaded Q-factor than the conventional microstrip resonators.

To verify the design concepts above, we designed and fabricated two hybrid cavity-microstrip bandpass filters on substrates, with the dielectric constant of 2.2 and a thickness of 0.508mm, operating at 2.40 GHz and 3.45 GHz respectively. The simulated and measured results are illustrated in Fig. 7 and Fig. 8, the simulated and measured results of the designed filters are shown with appropriate agreements.

After obtained the two filters with desired frequency responses, the T-junction is correctly designed for channel connection with the input/output ports. The specifications for both resonators and T-junction which constituted the exampled 2.4/3.45GHz diplexer are listed in Table 1, the width of the microstrip lines for both input and output lines are 1.54mm (the width of 50Ω microstrip line). The distance between the feeders to the resonators is 0.2mm, and the width of both feeders and the connection line between the circular stub and resonators are equal to 0.5mm. This designed diplexer occupies an overall size

of $0.9\lambda_0 \times 0.24\lambda_0 \times 0.216\lambda_0$, where λ_0 is the wavelength in free space at the center frequency of the lower channel.

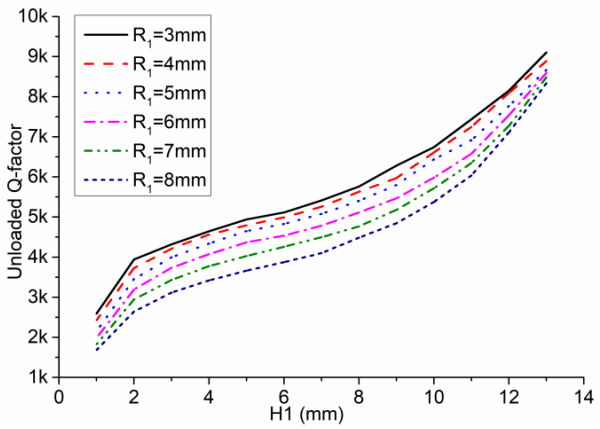

(a)

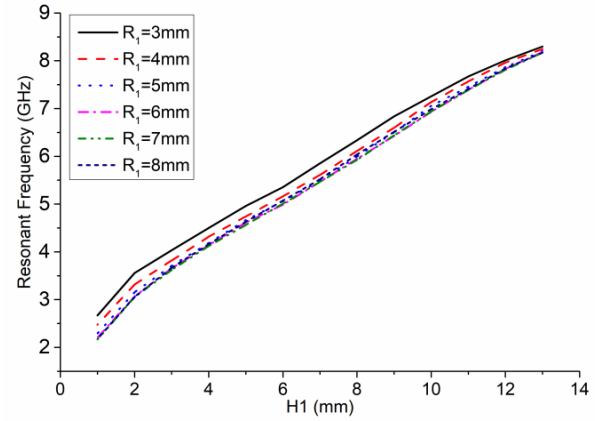

(b)

Fig. 6. Resonant frequency (a) and unloaded Q-factors (b) with the variations on H_1 and R_1.

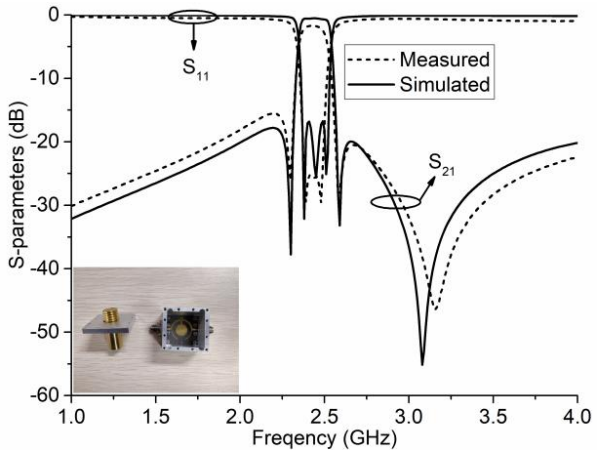

Fig. 7. Simulated and measured results of the proposed triple mode filter in Channel I.

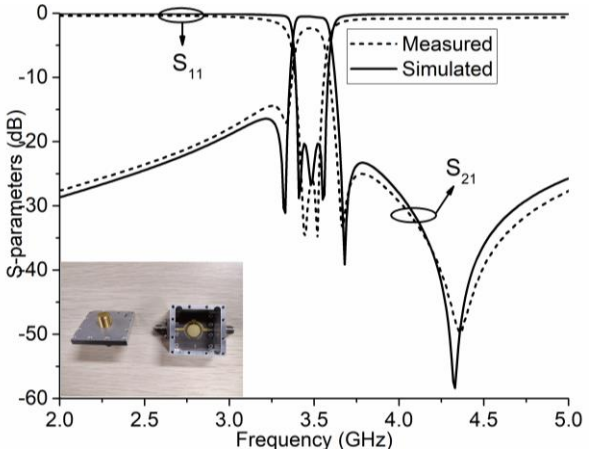

Fig. 8. Simulated and measured results of the proposed triple mode filter in Channel II.

Table 1: Specifications for the components of the diplexer

	R_{c0} (mm)	R_{c1}	R_{c2}	L_c	L_s	Θ_0 (deg)
Channel 1	4.8	8.5	9.2	4.3	2.2	23.2
Channel 2	4.3	6.05	6.75	6.75	1.4	22.4
	L_{Tin}(mm)		L_{Tout1}		L_{Tout2}	
T-junction	13.46		15		32	
	R_1	H_0	H_1	W_1	W_2	L_1
Cavity 1	6	27	2.1	30	3	32
Cavity 2	4.3	20	2.2	30	3	32

III. MEASUREMENT OF THE DIPLEXER

Based on the above analysis, the proposed hybrid cavity-microstrip structure is experimentally designed. The configuration for the 2.4/3.45GHz diplexer is shown in Fig. 2. The diplexer comprised of two individual triple-mode hybrid resonators connecting with a T-junction. Shielding cavities for each channel are fabricated by aluminum with an embedded copper cylinder. The planar microstrip circuits are fabricated on Taconic TLY-5 substrate with a relative dielectric constant of 2.2 and a thickness of 0.508mm. A photograph of the hybrid diplexer is shown in Fig. 9. And the simulated and measured results are presented in Fig. 10.

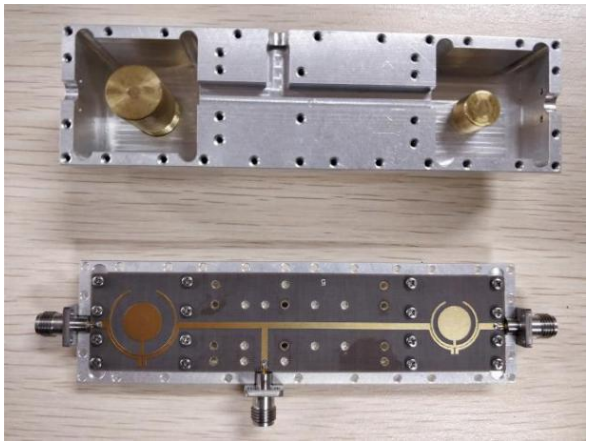

Fig. 9. Photograph of the proposed diplexer.

The measured frequencies of the two channels are centered at 2.40 GHz and 3.45 GHz with the corresponding 3-dB bandwidth of 8.3% and 5.8%. And the insertion losses of the two channels are 1.45 dB and 1.61 dB individually, which might comprise additional losses from surface mounted adapter (SMA) connectors. Measurement return losses are always better than 16 dB and 20 dB in the lower passband and higher passband. Three transmission zeros are generated to enhance the selectivity of each channel. The isolation between the two channels is better than 32 dB from 1 to 5 GHz. We hypothesized that the slight discrepancies between the measured and simulated results perhaps because of the connections with the test fixture and the unexpectedly tolerances from fabrication. Table 2 summarized comparisons between diplexers from reported in Section I and the proposed diplexer, since the heights of the airbox were not given in [1], [3] and [4], the values of height (the third parameter) in Table 2 are estimated from simulation conditions does not include the thickness of shielding cavities(five times as the thickness of the substrate).

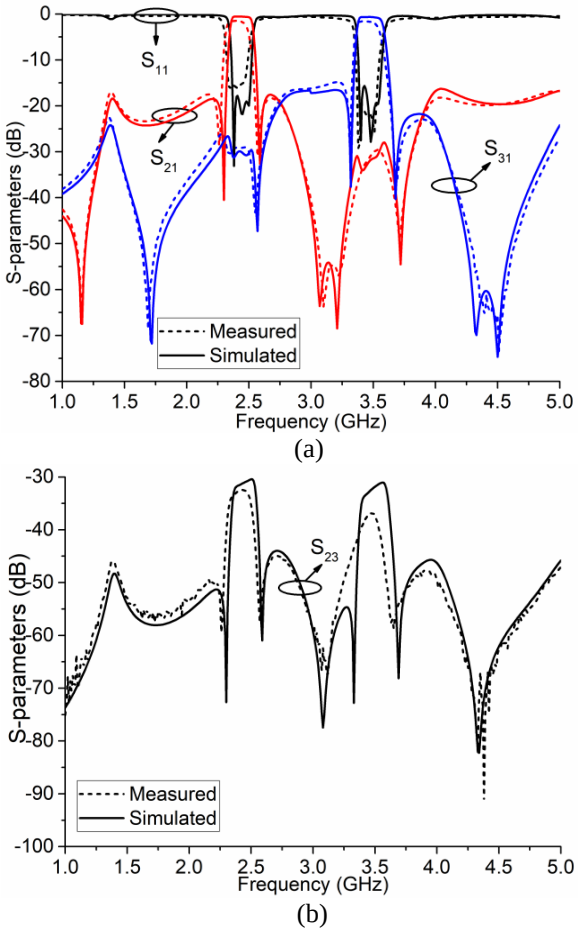

Fig. 10. Comparisons of simulated and measured results for: (a) S11, S21 and S31 and (b) S23 of the proposed diplexer.

Table 2: Comparisons with other reported literatures

Reference	CF (GHz)	Structure	Order	IL (dB)	Isolation (dB)	Size
[1]	1.80/2.38	Microstrip	3	1.38/1.44	>25	$0.12\lambda_g \times 0.23\lambda_g \times 0.022\lambda_g$
[2]	1.95/2.14	Microstrip	2	1.64/1.59	>30	$0.17\lambda_g \times 0.35\lambda_g \times 0.027\lambda_g$
[3]	2.55/2.66	Dielectric	3	0.63/1.10	>18	$1.02\lambda_0 \times 0.51\lambda_0 \times 0.52\lambda_0$
[4]	4.66/5.80	SIW	2	1.60/2.30	>32	$0.27\lambda_0 \times 0.217\lambda_0 \times 0.008\lambda_0$
This work	2.40/3.45	Hybrid	3	1.45/1.61	>32	$0.9\lambda_0 \times 0.24\lambda_0 \times 0.216\lambda_0$ ($1.18\lambda_g \times 0.316\lambda_g \times 0.284\lambda_g$)

IV. CONCLUSION

A hybrid cavity-microstrip diplexer with multiple-controllable TZs is proposed and demonstrated in this paper. Two triple-mode bandpass filters with high Q-factor and high selectivity are obtained by utilizing the proposed hybrid structure. In addition to the planar microstrip dual-mode resonator, the third resonant mode is produced by the couplings between the planar circuits and shielding cavity with a copper rod, significantly improves the frequency selectivity and the isolation between channels. The correctness of the design is verified by the prototype test; the measurement agrees well with simulated results. With the merits of low insertion loss, high selectivity and high isolation, which provides a good choice of modern multi-service and multi-band communication applications.

REFERENCES

[1] T. Yang, P. Chi, and T. Itoh, "Compact quarter-wave resonator and its applications to miniaturized diplexer and triplexer," *IEEE Transactions on Microwave Theory and Techniques*, vol. 59, no. 2, pp. 260-269, Feb. 2011.

[2] Q. Duan, K. Song, F. Chen, and Y. Fan, "Compact wide-stopband diplexer using dual mode resonators," *Electronics Letters*, vol. 51, no. 14, pp. 1085-1087, July 9, 2015.

[3] S. Wong, Z. Zhang, S. Feng, F. Chen, L. Zhu, and Q. Chu, "Triple-mode dielectric resonator diplexer for base-station applications," *IEEE Transactions on Microwave Theory and Techniques*, vol. 63, no. 12, pp. 3947-3953, Dec. 2015.

[4] Y. Dong and T. Itoh, "Substrate integrated waveguide loaded by complementary split-ring resonators for miniaturized diplexer design," *IEEE Microwave and Wireless Components Letters*, vol. 21, no. 1, pp. 10-12, Jan. 2011.

[5] H. J. Tang, W. Hong, J. Chen, G. Q. Luo, and K. Wu, "Development of millimeter-wave planar diplexers based on complementary characters of dual-mode substrate integrated waveguide filters with circular and elliptic cavities," *IEEE Transactions on Microwave Theory and Techniques*, vol. 55, no. 4, pp. 776-782, Apr. 2007.

[6] X. Zhang, Z. Yu, and J. Xu, "Design of microstrip dual-mode filters based on source-load coupling," *IEEE Microwave and Wireless Components Letters*, vol. 18, no. 10, pp. 677-679, Oct. 2008.

[7] J. R. Cameron, "General coupling matrix synthesis methods for Chebyshev filtering functions," *IEEE Transactions on Microwave Theory and Techniques*, vol. 47, no. 4, pp. 433-442, 1999.

Jiao Shu was born in Jiangsu, China. He received his B.S. degree from Nanjing University of Posts and Telecommunications in 2012. He received Master degree from Loyola Marymount University in 2013 in U.S. Since September 2014, he is a Ph.D. student at Nanjing University of Posts and Telecommunications. His interests involve RF/microwave devices, such as antennas and filters.

Yerong Zhang was born in Anhui, China. He received his Ph.D from University of Electronic Science and Technology of China in 1996. He is a Professor with NUPT. In recent years, his main research fields are mobile communication network planning and optimization, wireless communication and electromagnetic compatibility, electromagnetic scattering and imaging, and numerical calculation of electromagnetic theory.

A Dual Band Circularly Polarized Rectenna for RF Energy Harvesting Applications

Osama M. Dardeer [1,2], Hala A. Elsadek [2], Esmat A. Abdallah [2], and Hadia M. Elhennawy [1]

[1] Electronics and Electrical Communication Engineering Department
Ain Shams University, Cairo, Egypt
osamadardeer@eri.sci.eg, helhennawy@ieee.org

[2] Microstrip Department
Electronics Research Institute, Dokki, Giza, Egypt
hhelsadek92@gmail.com, esmataa2@hotmail.com

Abstract ─ This paper presents a dual band rectenna for RF energy harvesting applications. The receiving slot antenna has a single feed configuration with a coplanar waveguide (CPW) structure. A grounded-L strip is employed for circular polarized (CP) radiation. A stepped impedance matching stub is used to enhance the coupling between the feed line, inverted L-strip, and the slot. An asymmetric U-shaped strip is embedded near the upper right corner of the slot as a perturbed element. This asymmetric U-shaped strip is a key component to excite the required phase perturbation to produce a CP radiation. The antenna operates in the WiFi frequency bands of 2.45 GHz (IEEE 802.11b&g) and 5 GHz (IEEE 802.11a/h/j/n/ac/ax WLAN system). A dual band voltage doubler rectifier has been designed and implemented for RF to DC conversion. The impedance matching network for this rectifier is based on a Π-model dual band impedance transformer that is optimized to match two unequal complex loads at two operational frequencies.

Index Terms ─ Circular polarized antenna, dual band, rectenna, rectifier, RF energy harvesting, Π-model impedance transformer.

I. INTRODUCTION

The concept of allowing energy to flow between two points in space is a promising scheme in order to measure several physical quantities and benefit from these measures using suitable sensing devices, which will be powered by Wireless Power Transfer (WPT) scheme. This will increase the number of devices that can be powered simultaneously without the need for wired connections or even bulky batteries [1]. The power is transmitted in RF and then collected by a receiving antenna and converted to DC power using rectifier. This DC energy can be used as a source for low power devices or stored in storage devices as super capacitors, for example. The combination between antenna and a rectifier is called a rectenna. Each harvesting node must contain a rectenna to capture the RF energy transmitted in space.

The rectenna is the key element in RF energy harvesting system. Circular polarized (CP) rectennas can be used due to the ability to obtain constant DC power at random polarization angles. In order to avoid the 3-dB polarization mismatch loss, Sun and Geyi in [2] proposed a dual linearly polarized receiving antenna and consequently dual feeding ports are required. In recent literature, different rectenna designs have been published for RF energy harvesting applications. These rectennas can operate in single band [2], dual band [3-7], and multiband [8-10]. Higher power conversion efficiency (PCE) can be obtained in narrow single band rectennas, but the amount of harvested RF power is low. On the other hand, multi-band rectennas suffer from lower PCE, but more harvested power. The challenge is to maximize the PCE for dual band or multi-band rectennas at the specific operating frequencies. Other trend is to present a broadband operation [11] in order to accumulate more RF power from different frequency bands.

In this paper, a dual band rectenna operating at 2.45 GHz ISM band and WLAN 5 GHz is proposed. The rectenna consists of a dual band CP slot antenna with coplanar waveguide (CPW) feed, and a dual band voltage doubler full wave rectifier. Each part of the rectenna is designed and tested separately, and then assembled in order to evaluate the overall performance. Both of the antenna and the rectifier have been fabricated on the standard FR4 substrate for cost reduction and ease of integration with the rest of the sensing circuitry. This paper is organized as follows: the design of the receiving antenna is presented in Section II. The design of the rectifier circuit is given in Section III. Section IV introduces the rectenna system performance, while Section V gives the conclusion.

Submitted On: December 31, 2018
Accepted On: May 7, 2019

II. RECEIVING ANTENNA DESIGN

The geometry of the proposed dual-band CP slot antenna with coplanar waveguide (CPW) feed is illustrated in Fig. 1. The antenna is fabricated on a square FR4 substrate with a dielectric constant of 4.3, thickness (h) of 1.6 mm, and loss tangent of 0.025. The antenna is fed by CPW line at the center of the structure. The CPW line has a 50 ohms characteristic impedance with a width W_f and a gap g_f. The size of the antenna is 54x54 mm^2. A ring is formed by folding the ground plane, then a rectangular slot is subtracted from this ground to present the main radiating element of the proposed antenna. The slot dimensions are 30x34 mm^2 which is designed to operate at 2.45 GHz. The A and L are optimized with A/L ratio of 1.588 in this study. The other dimensions of the antenna are listed in Table 1.

It is evident to note that there is a protruded tuning stub which is wider than the feed line. It may be considered as a stepped impedance section that greatly enhances the coupling between the feed line, inverted L-strip, and the slot. It also perturbs the magnetic current distribution in the slot so that the 3-dB axial ratio band would be adjusted. An inverted-L strip at the upper left corner of the slot contributes to the circular polarized radiation of the antenna [12]. This grounded L strip should be square (14 mm x 14 mm) in order to enhance the axial ratio bandwidth for the lower resonant frequency.

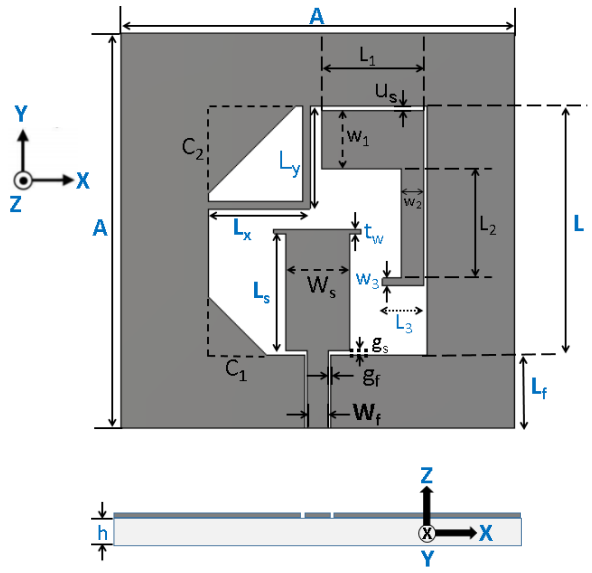

Fig. 1. Geometry of the proposed dual band CP slot antenna with CPW feed.

Two chamfered corners are used in the slot. The 1st one is at the lower left corner of the slot which helps to realize circular polarization at the higher frequencies. The 2nd one is located at the upper left corner of the slot and its dimension is optimized to be 12 mm, which is close to the size of the inverted-L strip and this greatly enhances the circular polarized radiation at the 2.45 GHz resonant frequency. An asymmetric U-shaped strip is embedded near the upper right corner of the slot as a perturbed element. This asymmetric U-shaped strip is a key component to excite the required phase perturbation to produce a CP radiation [13]. It also generates the dual band operation of the antenna.

Table 1: Dimensions of the proposed antenna (unit: mm)

A	54	w_f	3
L	34	w_s	8.74
L_f	10	t_w	0.6
L_s	16	w_1	8
L_1	14	w_2	3
L_2	15	w_3	1
L_3	5.6	g_f	0.3
L_x	14	g_s	0.59
L_y	14	u_s	0.5
C_1	8	C_2	12

The extensive simulation trials illustrate that the inverted-L strip and the assymmetric U-shaped strip are key components to excite the required perturbation for a circular polarized radiation creation. There is a tradeoff between obtaining good impedance bandwidth ($|S_{11}|<$ −10 dB) and good axial ratio bandwidth (AR< 3 dB). Therefore, optimization is used in order to achieve good performance in both the reflection coefficients and ARs. In order to design the proposed dual band CP slot antenna, the design optimization procedure is as follows:

1) Determine antenna size A and slot size L to adjust half wavelength resonator at 2.45 GHz.
2) Adjust the inverted-L strip and associated chamfered corner C2 for axial ratio bandwidth (ARBW) at the lower band.
3) Adjust the asymmetric U-shaped strip and associated chamfered corner C1 for impedance matching and ARBW at the higher band.
4) Perform impedance matching tuning using the protroded stub with its stepped impedance structure.
5) Slightly optimize the dimensions of the proposed antenna to achieve the desired dual band CP performance.

The antenna prototype is shown in Fig. 2. The reflection coefficients are obtained by simulation and measurement using Computer Simulation Technology Microwave Studio (CST MS) ver. 2017 and Agilent 8719ES vector network analyzer, respectively to validate the design. Two frequency bands of operation at 2.45 GHz and 5 GHz are observed in Fig. 3. The achieved frequency bands (for $|S_{11}|$ < -10 dB) are 1.73-2.64 GHz (with bandwidth of 910 MHz) for the IEEE 802.11b&g WLAN system, and 4.83-5.19 GHz (with bandwidth of

360 MHz) for the IEEE 802.11a/h/j/n/ac/ax WLAN system. The 2nd operating band covers different channels in the 5 GHz WLAN. These channels, according to the standard spectrum, are 7, 8, 9, 11, 12, 16, 34, 36, 38, 40, 42, 44, 183, 184, 185, 187, 188, 189, 192, and 196 [14].

Fig. 2. Photograph of the fabricated antenna.

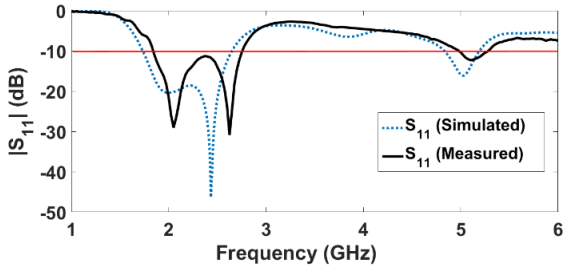

Fig. 3. Reflection coefficient of the proposed antenna.

The AR results also demonstrate the two operational bands at 2.45 GHz and at 5 GHz, respectively, as illustrated in Fig. 4. The achieved frequency bands (for AR < 3 dB) are 2.29-2.458 GHz (with bandwidth of 170 MHz) in the lower band, and 4.88-5.95 GHz (with bandwidth of 1.07 GHz) in the upper band. The measured values of the antenna axial ratio are 1.458 dB and 1.205 dB at 2.45 GHz and 5 GHz, respectively.

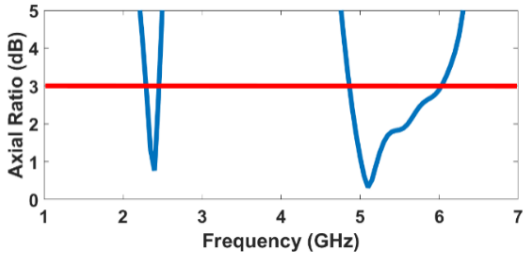

Fig. 4. Simulated axial ratio of the proposed antenna.

The designed antenna radiation patterns are examined by numerical simulations. The 3-D radiation pattern is shown in Fig. 5. In addition, measurement and simulation results for both the E-plane and H-plane radiation characteristics are illustrated in Fig. 6. The antenna radiates in both front and back directions since all metal patches are printed on the top of the substrate. Also, at higher frequencies, the radiation patterns exhibit more rapid variations. The antenna gain variation is illustrated in Fig. 7. At 2.45 GHz, the achieved gain, directivity, and radiation efficiency are 3.74 dBi, 4.035 dBi, and 93.4%, respectively. At 5 GHz, the achieved gain, directivity, and radiation efficiency are 3.32 dBi, 4.09 dBi, and 83.7%, respectively.

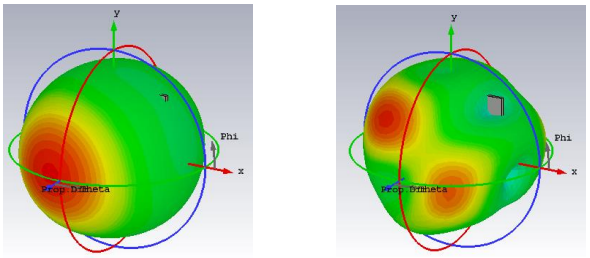

(a) (b)

Fig. 5. 3-D radiation patterns of the proposed antenna at: (a) 2.45 GHz and (b) 5 GHz.

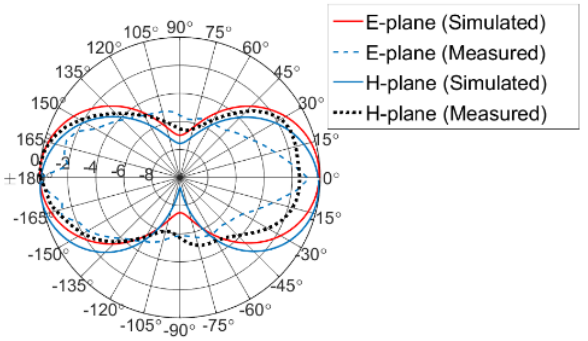

(a)

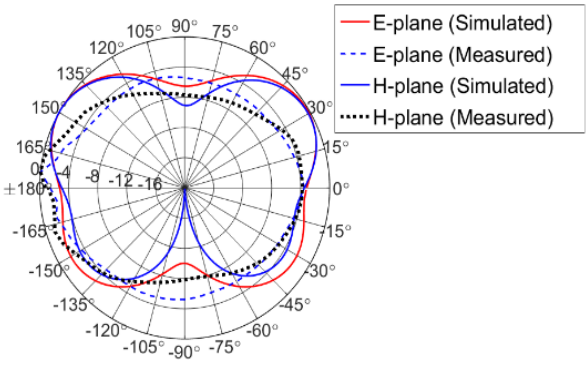

(b)

Fig. 6. Normalized radiation patterns of the proposed antenna at: (a) 2.45 GHz and (b) 5 GHz.

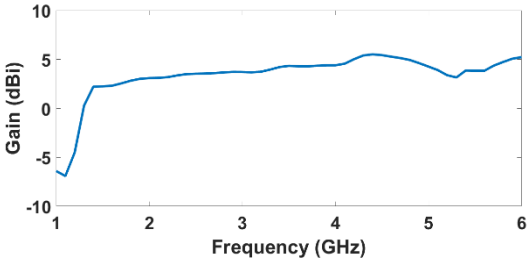

Fig. 7. Gain of the proposed antenna.

III. RECTIFYING CIRCUIT DESIGN

The structure of the rectifier consists of an impedance matching network, conversion circuit, and a resistive load. This can be illustarted from the block diagram of rectenna structure, shown in Fig. 8. The role of the impedance matching network is to maximize the power transfer from the receiving antenna to the conversion circuit. Then, the process of converting AC to DC signal is done. The topology of the conversion circuit used in this paper is the voltage doubler full wave rectification circuit and the schottky diode HSMS-2860 is selected to be the rectifying device. Figure 9 illustrates the equivalent circuit model of the Schottky diode HSMS-2860. The most important component in the design of a rectifying circuit is the diode. Spice model parameters are taken from [15]. The diode turn on voltage V_T is 0.4 V and the reverse breakdown voltage V_{br} is 7 V. The series resistance R_s is 6 ohm and there is a variable junction resistance R_j in parallel with a junction capacitance C_j of 0.18 pF. The diode packaging leads to the emergence of the parasitic phenomenon that can be considered by a parasitic inductor of 2 nH and a parasitic capacitance of 0.08 pF.

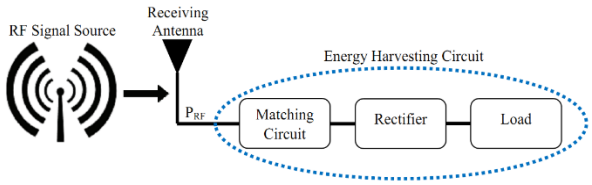

Fig. 8. Block diagram of rectenna structure.

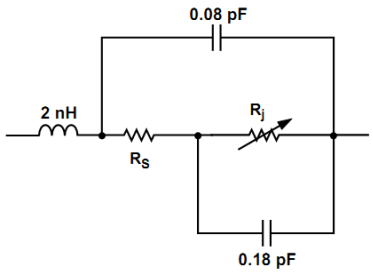

Fig. 9. Equivalent circuit model of the Schottky diode HSMS-2860 [13].

Before designing the impedance matching network, the input impedance of the voltage doubler circuit has to be calculated. This process has been done using the Advanced Design System (ADS) simulator and the real and imaginary parts of the input impedance at 0 dBm are illustrated in Fig. 10. At 2.45 GHz, the input impedance is 1.046–j102.68 Ω, while at 5 GHz, the impedance is 1.142–j34.1 Ω.

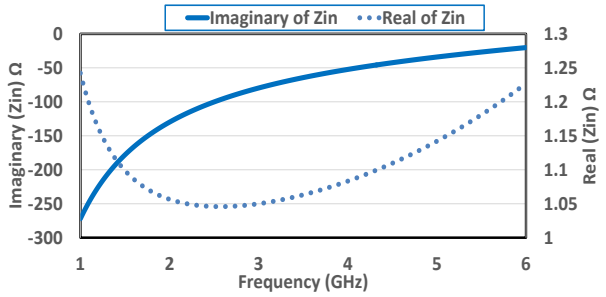

Fig. 10. Complex input impedance of the voltage doubler circuit at 0 dBm.

The impedance matching network is designed in order to match the receiving antenna with the rectifier at these two frequencies of operation, hence reduces power losses. Generally, lumped elements and distributed elements can be used for this purpose. In this paper, distributed elements are used in the form of Π-section configuration in order to achieve impedance matching at the two frequencies of operation. The lumped elements are not preferred due to their parasitics above 1 GHz and the limited available commercial values of these inductors and capacitors. According to [16], the Π section model has been used as a dual band impedance matching transformer for unequal complex impedance loads. The reflection coefficient of the matching network is shown in Fig. 11 and this proves the capability of the dual frequency matching circuit.

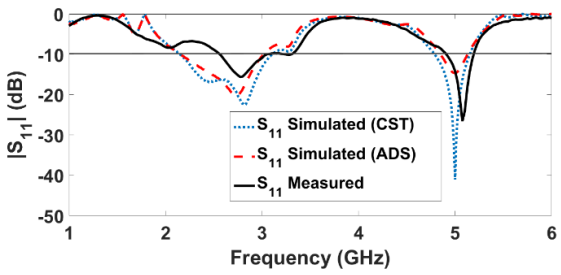

Fig. 11. Reflection coefficient of the matching network.

The geometry of the proposed dual band rectifier is illustrated in Fig. 12. The dimensions of the rectifier are 64 x 28.8 mm^2. The distance between the voltage doubler circuit and the matching network is implemented in the form of a meander line for size reduction. Also, the tuning

stub is printed as an L-shaped stub for miniaturization. The characteristic impedance Z_c and the electrical length θ_c of the sections constituting the Π-model structure are initially calculated according to [16]. Then, the corresponding dimensions are optimized using ADS simulator, and the final dimensions are shown in Fig. 12.

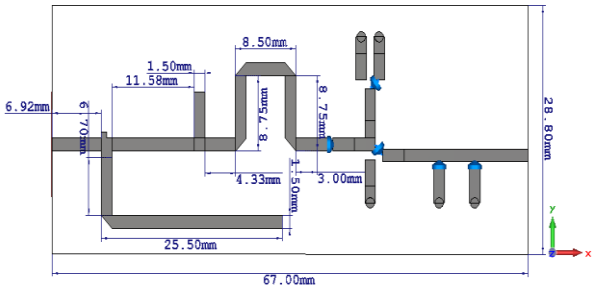

Fig. 12. Geometry of the proposed dual band rectifier.

Figure 13 illustrates the ADS simulation for both the voltage doubler circuit and the Π–model impedance matching circuit. The rectifier is fabricated on FR4 substrate with a dielectric constant of 4.3, thickness (h) of 0.8 mm, and loss tangent of 0.025. The total size of the rectifier is 64 x 28.8 x 0.8 mm^3. Figure 14 shows the photograph of the fabricated rectifier.

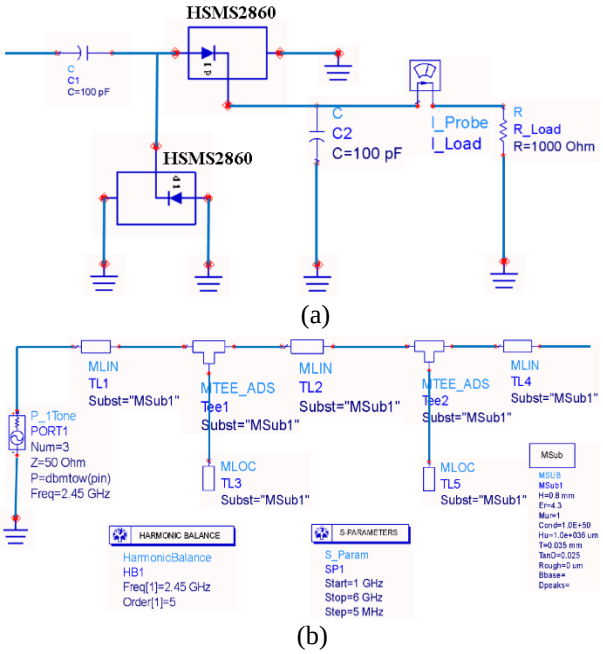

Fig. 13. ADS simulation for: (a) voltage doubler circuit, and (b) Π-model impedance matching circuit.

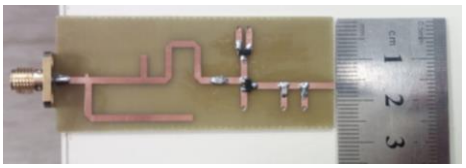

Fig. 14. Photograph of the fabricated rectifier.

Figure 15 shows the simulated and measured output voltage of the dual band rectifier as a function of the input power level when it is varied from -25 dBm to 15 dBm, and the load resistance is fixed at 1KΩ. For example, at 0 dBm, the simulated DC output voltage is 0.352 V at 2.45 GHz while it is 0.175 V at 5 GHz. The measured values are lower than the simulated ones. In addition, the power conversion efficiency is depicted in Fig. 16 for the dual frequency bands.

Different factors affect the conversion efficiency such as the diode turn on voltage, breackdown voltage, operating frequency, series resistance, and the load resistance [1]. The maximum simulated power conversion efficiency reaches 35.4% at 2.45 GHz and 20.9% at 5 GHz, at input power of 15 dBm. This may be due to the fact that the series resistance and the junction capacitance filter out much power as the frequency increases. Of course, the measured values are lower than the simulated ones.

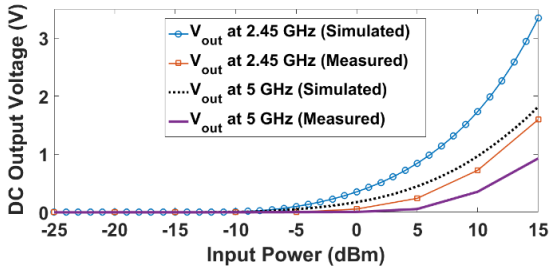

Fig. 15. Output voltage of the dual band rectifier.

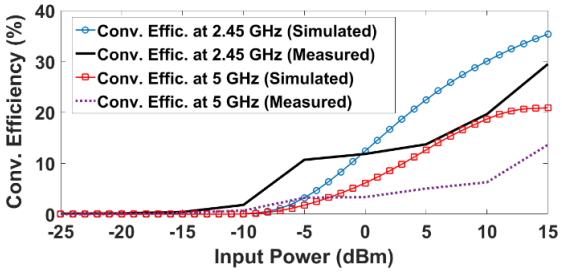

Fig. 16. Power conversion efficiency of the dual band rectifier.

IV. RECTENNA SYSTEM PERFORMANCE

The receiving antenna and rectifier are designed and evaluated separately. Then, they are assembled in order to complete the rectenna prototype which is fabricated and measured, as shown in Fig. 17. A 50 Ω adapter (SMA male-to-male) is used to connect the antenna to the rectifier since the antenna has copper metals on the top only due to the coplanar waveguide feeding, but the rectifier has top and bottom metal layers.

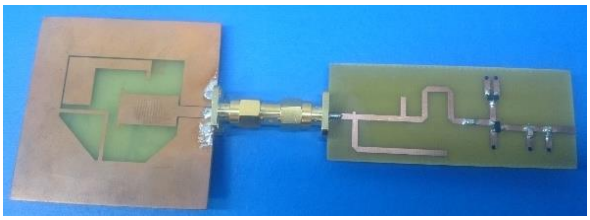

Fig. 17. Photograph of the fabricated rectenna.

The received RF power of antenna, P_{RF}, is measured by spectrum analyzer and the output voltage of rectenna (V_{out}) is measured by a voltmeter. The power conversion efficiency of rectenna $\eta_{RF\text{-}DC}$ is defined as the ratio of the DC power P_{DC} and the RF power P_{RF}:

$$\eta_{RF-DC} = \frac{P_{DC}}{P_{RF}} x100\% = \frac{1}{P_{RF}} x \frac{V_{out}^2}{R_{load}} x100\%. \quad (1)$$

The maximum measured conversion efficiency of the rectenna reaches 26.53% at 2.45 GHz and 12.74% at 5 GHz for an input power level of 15 dBm, as illustrated in Fig. 18. Table 2 shows the comparison between our designed rectenna and other designs reported previously in literature.

It can be seen that proposed design has advantages in the antenna impedance bandwidth and reduced dimensions compared to the circular polarized rectennas [7]. Compared to [11], compact size is achieved in the proposed rectenna. The proposed CP rectenna provides acceptable conversion efficiency as shown in the table and it is worth to note that the linear polarized rectenna cannot achieve constant DC power even if the received RF harvested signal has arbitrary polarization. This is a critical limit in most situations [3].

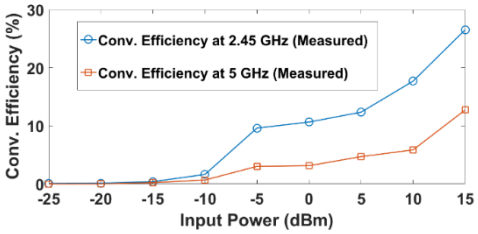

Fig. 18. Power conversion efficiency of the dual band rectenna.

Table 2: Comparison of the proposed rectenna and the related designs reported previously

Ref.	Freq. (GHz)	Ant. Dimensions (mm^3)	Max. Gain (dBi)	I/P Power Level for Peak $\eta_{RF\text{-}DC}$ (dBm)	Max. $\eta_{RF\text{-}DC}$ (%)	Polarization
[3]	2.39—2.52 and 5.65—5.85	44x41x1.6	5.53	10	45	Linear
[7]	0.908—0.922 and 2.35—2.5	120x120x8.67	6.14	0 to 5	39	Circular
[11]	0.88—8.45	100x100x1.6	8.7	-5 to 0	51.8	Linear
This work	1.73—2.64 and 4.83—5.19	54x54x1.6	5.51	5 to 10	35.4	Circular

V. CONCLUSION

This paper presented a dual band rectenna operating at the two WLAN frequency bands 2.45 GHz and 5 GHz. The receiving slot antenna is a dual band CP CPW feed with only one feeding port. The antenna dimensions are 54 × 54 × 1.6 mm^3 with the metal deposited only on one side of the substrate. The proposed antenna –10 dB bandwidth extended from 1.73 GHz to 2.64 GHz for the 1st band and from 4.83 GHz to 5.19 GHz for the 2nd band. The ARBW (for AR < 3 dB) extended from 2.29 to 2.458 GHz (with bandwidth of 170 MHz), and from 4.88 to 5.95 GHz (with bandwidth of 1.07 GHz) for 1st and 2nd bands, respectively. A dual band voltage doubler rectifier has been designed based on a Π-model impedance transformer for dual band operation. The rectifier dimensions are 64 x 28.8 x 0.8 mm^3. The prototypes of the proposed antenna and rectifier were fabricated and measured. Good agreement was found between measured and simulated reflection coefficients. The proposed rectenna is integrated. PCE is measured at different input power levels. An efficiency of 26.53% and 12.74% are achieved at 2.45 and 5 GHz frequencies, respectively. The proposed rectenna has an advantage of obtaining constant DC power at random polarization angles which

makes it suitable for ambient RF energy harvesting applications for powering wireless sensors in various IoT applications.

ACKNOWLEDGMENT

This work is funded by the National Telecom. Regulatory Authority (NTRA), Ministry of Communications and Information Technology (MCIT), Egypt.

REFERENCES

[1] C. R. Valenta and G. D. Durgin, "Harvesting wireless power: Survey of energy-harvester conversion efficiency in far-field, wireless power transfer systems," *IEEE Microw. Mag.*, vol. 15, no. 4, pp. 108-120, June 2014.

[2] H. Sun and W. Geyi, "A new rectenna with all-polarization-receiving capability for wireless power transmission," *IEEE Antennas and Wireless Propagation Letters*, vol. 15, pp. 814-817, 2016.

[3] O. Amjad, S. W. Munir, Ş. T. İmeci, and A. Ö. Ercan, "Design and implementation of dual band microstrip patch antenna for WLAN energy harvesting system," *Applied Computational Electromagnetics Society Journal*, vol. 33, no. 7, pp. 746-751, July 2018.

[4] A. Khemar, A. Kacha, H. Takhedmit, and G. Abib, "Design and experiments of a dual-band rectenna for ambient RF energy harvesting in urban environments," *IET Microwaves, Antennas & Propagation*, vol. 12, no. 1, pp. 49-55, 2018.

[5] K. Dey, T. Dey, R. Hussain, and A. Eroglu, "Design of dual band rectifiers for energy harvesting applications," *2018 International Applied Computational Electromagnetics Society Symposium (ACES)*, Denver, CO, 2018, pp. 1-2.

[6] M. Mattsson, C. I. Kolitsidas, and B. L. G. Jonsson, "Dual-band dual polarized full-wave rectenna based on differential field sampling," *IEEE Antennas and Wireless Propagation Letters*, vol. 17, no. 6, pp. 956-959, June 2018.

[7] A. M. Jie, N. Nasimuddin, M. F. Karim, and K. T. Chandrasekaran, "A dual-band efficient circularly polarized rectenna for RF energy harvesting systems," *Int. J. RF Microw. Comput. Aided Eng.*, vol. 29, pp. 1-11, Jan. 2019.

[8] E. Liu, X. Yang, and L. Li, "Triple-band GCPW rectifier for harvesting EM energy," *2017 International Applied Computational Electromagnetics Society Symposium (ACES)*, Suzhou, 2017, pp. 1-2.

[9] S. Chandravanshi, S. S. Sarma, and M. J. Akhtar, "Design of triple band differential rectenna for RF energy harvesting," *IEEE Transactions on Antennas and Propagation*, vol. 66, no. 6, pp. 2716-2726, June 2018.

[10] N. Singh, B. K. Kanaujia, M. T. Beg, Mainuddin, T. Khan, and S. Kumar, "A dual polarized multi-band rectenna for RF energy harvesting," *AEU - International Journal of Electronics and Communications*, vol. 93, pp. 123-131, 2018.

[11] X. Bai, J. Zhang, L. Xu, and B. Zhao, "A broadband CPW fractal antenna for RF energy harvesting," *Applied Computational Electromagnetics Society Journal*, vol. 33, no. 5, pp. 482-487, May 2018.

[12] M. Shokri, S. Asiaban, and Z. Amiri, "Study, design and fabrication of a CPW fed compact monopole antenna with circular polarization for ultra wide band systems application," *Applied Computational Electromagnetics Society Journal*, vol. 32, no. 9, pp. 749-753, Sept. 2017.

[13] W. C. Weng, J. Y. Sze, and C. F. Chen, "A dual-broadband circularly polarized slot antenna for WLAN applications," *IEEE Transactions on Antennas and Propagation*, vol. 62, no. 5, pp. 2837-2841, May 2014.

[14] En.wikipedia.org. List of WLAN channels. [Online] Available at: https://en.wikipedia.org/wiki/List_of_ WLAN_chan nels [Accessed 1 July 2018].

[15] Hewlett-Packard Co., "Surface mount microwave schottky detector diodes," 5968-4188E datasheet, 1999.

[16] O. Manoochehri, A. Asoodeh, and K. Forooraghi, "Π-Model dual-band impedance transformer for unequal complex impedance loads," *IEEE Microwave and Wireless Components Letters*, vol. 25, no. 4, pp. 238-240, Apr. 2015.

A Novel Low Temperature Process for Microwave Dielectric Ceramics Metallization

Jau-Jr Lin [1*], Cheng-I Lin [1], Tune-Hune Kao [2], and Meng-Chi Huang [2]

[1] Department of Electrical Engineering
National Changhua University of Education, Changhua County, 500, Taiwan, R.O.C.
*jaujrlin@cc.ncue.edu.tw

[2] Mechanical and System Research Laboratories
Industrial Technology and Research Institute, Hsinchu County 310, Taiwan, R.O.C.

Abstract ─ This research proposes a novel low temperature process for microwave dielectric ceramics metallization with laser patterning and electroless copper plating. The process temperature of the proposed process is less than 50 °C, which is much lower than typical metallization technology, such as Low Temperature Co-fired Ceramics (LTCC) and Direct Bond Copper (DBC). Compared with LTCC and DBC, the proposed low temperature process can significantly reduce energy consumption, cut cost for cooling equipment, and offer smaller metal pattern variations. The measurement results demonstrate the line width error and the line position precision are all within ±50 μm. Moreover, this proposed process produces no short circuit or incomplete metallization in the walls of the holes. The measurement and simulation results demonstrate the manufactured samples meet the bandpass filter design specifications. Therefore, the proposed low temperature process is practical and adequate for producing microwave dielectric ceramics.

Index Terms ─ Ceramic laser metallization, laser engraving, microwave dielectric ceramics.

I. INTRODUCTION

Microwave dielectric ceramics are the base material of important elements like filters, oscillators, antennas, and dielectric guides for mobile communications and consumer electronics products [1-6]. With the advance of mobile communications (4G, B4G and 5G), radio LAN (local area network), and GPS technologies in recent years, microwave elements based on microwave dielectric ceramics are being used more extensively and their demand has increased greatly. Therefore, the recent research is paying greater attention to fabricating microwave dielectric ceramics with less energy and manpower.

Conventional ceramic metallization technologies, such as Low Temperature Co-fired Ceramic (LTCC) and Direct Bonded Copper (DBC), are widely used nowadays. LTCC can fabricate three-dimensional ceramic modules with low dielectric loss and embedded silver electrodes [1, 2, 5]. Figure 1 illustrates the flow chart of the LTCC fabrication process. The ceramic tapes are blanked and then punched to create via holes. The next step is the via filling to form electrical interconnects between layers. Afterwards, screen printing or a photo image is used for metal patterning on each layer. The final steps are layer lamination and co-firing bellow 950 °C [1, 2, 5]. The dielectric constant, dissipation factor, and microwave resonance frequency of microwave components fabricated by LTCC are strongly correlated to the process temperature.

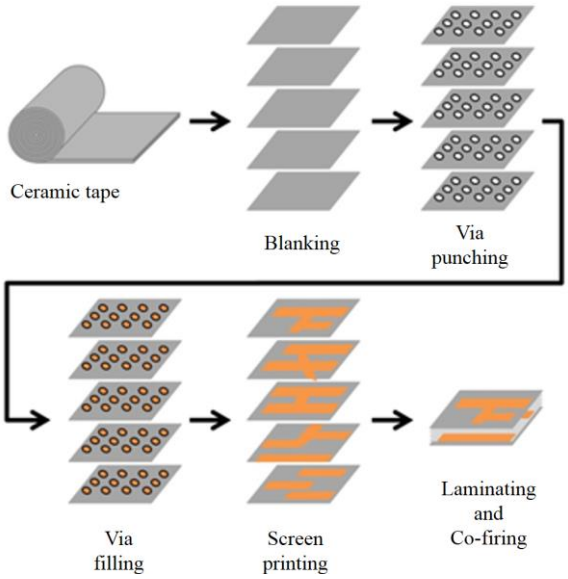

Fig. 1. The flow chart of the LTCC fabrication process.

Submitted On: December 2, 2018
Accepted On: August 11, 2019

DBC is the direct bonding process of copper and ceramics. The advantages of a DBC substrate are that copper metallization is relatively thick, and thermal expansion of the substrate near the surface is close to that of copper. Thus, copper and ceramic bonding strengths are high [7]. The oxygen concentration influences the bonding temperature of copper and substrate, such that when the oxygen concentration is 1.4%, the bonding temperature is a minimum 1065 °C [8].

For conventional ceramic metallization technologies, such as LTCC and DBC, screen printing or a photo image is utilized to generate the designated metal pattern. A silver paste or a copper paste is then employed. The whole ceramic substrate is sintered at a high temperature of 800-950 °C for more than one hour. In order to remove the polymer inside the silver paste or the copper paste, the whole ceramic substrate must be sintered at high temperatures for a long time to obtain good metal electrical properties. The entire process needs high energy and time consumption. Moreover, for the high-temperature sintering process, the metal pattern dimensions and position might show a deviation of 5-14% in error and might produce the aforementioned silver paste sticking or blockage, which causes short circuits or incomplete metallization in via holes. This will directly cause a resonant frequency offset of microwave dielectric ceramics. Due to undesired process variations, people need to inspect and calibrate individual devices one by one after the fabrication process, which requires much more time and labor to do.

A novel low temperature process for microwave dielectric ceramics metallization with laser patterning [9, 10] and electroless copper plating was therefore proposed to overcome those problems caused by the high temperature processes. This proposed process has several advantages over conventional LTCC process: lower energy consumption, less metal pattern dimension deviation, and no short circuit or incomplete metallization in via holes. The structure of the microwave dielectric ceramic and the detail of fabrication process are described and explained in the following sections.

II. MICROWAVE DIELECTRIC CERAMICS

In the design stage, once specifications of the ceramic filter are given and finalized, the HFSS software is used for a preliminary simulation. The HFSS simulation setup is shown in Fig. 2. Figure 2 (a) shows the overall simulation set-up. Figure 2 (b) shows the details of the metal pattern and cavities. After the simulation results meet the filter specifications, the next step will be the fabrication process.

The microwave dielectric ceramic shown in Fig. 2 functions as a bandpass filter [3, 4, 6]. The equivalent circuit is shown in Fig. 3. The four resonant cavities in Fig. 2 can be modeled as the four LC parallel resonance circuits [3, 4, 6]. Here, L_x and C_x {x=1, 2, 3, 4} are the equivalent circuit for the four resonant cavities, shown in Fig. 3; C_{ij} {i,j = 0~5} represent the coupling capacitors between cavities and metal plates [3, 4, 6].

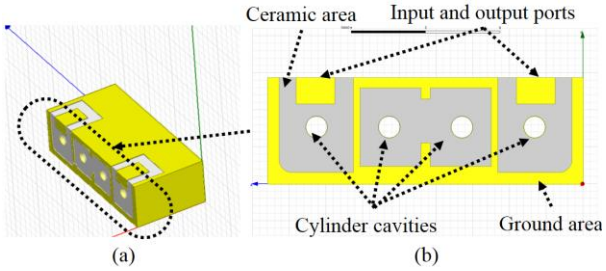

Fig. 2. HFSS simulation set-up.

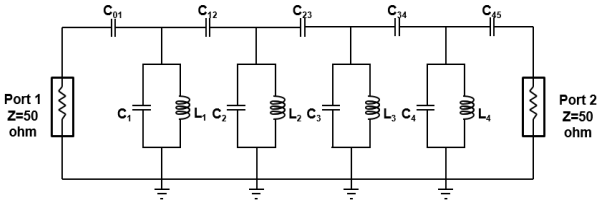

Fig. 3. Equivalent circuit of the filter.

From [11], the *ABCD* matrix of C_{ij} {i,j = 0~5} in Fig. 3 could be represented as equation (1), while the *ABCD* matrix of L_x and C_x {x=1, 2, 3, 4} in Fig. 3 can be represented as equation (2). The total *ABCD* matrix is shown as equation (3) and can be transformed into the S matrix to obtain the reflection coefficients (S_{11} and S_{22}) and transmission coefficients (S_{21} and S_{12}):

$$\begin{bmatrix} A & B \\ C & D \end{bmatrix}_{C_{ij}} = \begin{bmatrix} 1 & \dfrac{1}{j\omega C_{ij}} \\ 0 & 1 \end{bmatrix}, \tag{1}$$

$$\begin{bmatrix} A & B \\ C & D \end{bmatrix}_{C_x \| L_x} = \begin{bmatrix} 1 & 0 \\ \dfrac{1}{j\omega L_x} + j\omega C_x & 1 \end{bmatrix}, \tag{2}$$

$$\begin{bmatrix} A & B \\ C & D \end{bmatrix}_{Total} = \begin{bmatrix} A & B \\ C & D \end{bmatrix}_{C_{01}} \begin{bmatrix} A & B \\ C & D \end{bmatrix}_{C_1 \| L_1} \begin{bmatrix} A & B \\ C & D \end{bmatrix}_{C_{12}} \cdots \begin{bmatrix} A & B \\ C & D \end{bmatrix}_{C_4 \| L_4} \begin{bmatrix} A & B \\ C & D \end{bmatrix}_{C_{45}}. \tag{3}$$

The geometric model of the microwave dielectric ceramic for the fabrication process is shown in Fig. 4, which is drawn by SolidWorks. There are four cylinder cavities for controlling the resonant frequency. The golden color areas are the designated metal patterns. There are two strip metal areas for the input and output ports. The other metal areas are for ground areas. The white area is the bare ceramic area. The overall dimension is about

8 x 3 x 4 mm^3.

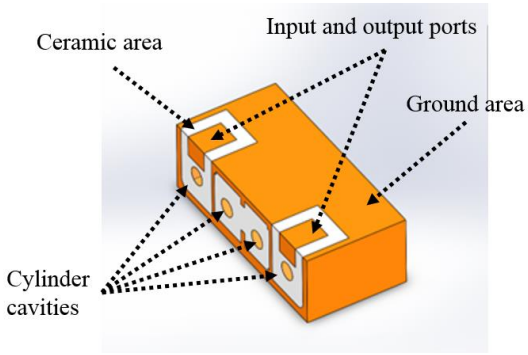

Fig. 4. The test structure of the microwave dielectric ceramic.

III. PROPOSED FABRICATION PROCESS

The concept of the proposed low temperature process for microwave dielectric ceramics metallization is shown in Fig. 5. First, the ceramic substrate is trimmed to the desired dimension. The resonant cavities are created by punching. Second, the designated metal patterns are formed by applying ceramic laser metallization technology [9, 10]. By controlling the duration of electroless copper plating, the desired metal thickness can be obtained. Smart laser trimming [10] is utilized to trim the metal thickness on the surface of cavities to optimize the frequency response of the ceramic filter.

This research uses a perovskite-based ceramic as the substrate and applies the chemical deposition to form the metal patterns. Figure 6 shows the details of the ceramic metallization process. The component $CaTiO_3$ is dissolved out of the ceramic by using an oxidative etching solution; e.g., phosphoric acid and HCl. Micro-pores are formed on the surfaces of ceramic and cavities. After this step, one can visually observe that the solution color is relatively yellow, as shown in Fig. 7 (a). According to the analysis of the dissolved etching solution, the solution contains Ca/Ti, proving that the etching solution roughens the surface. The ceramic is then kept in an activator for 10 minutes, as shown in Fig. 7 (b). The activator contains Sn and Pd ions, making the Sn and Pd ions adhere to the ceramic surface. It is kept in the cleaning agent for three minutes, as shown in Fig. 7 (c), with the purpose of cleaning off the Sn particles and leaving the Sn ions on the ceramic surface. Finally, the ceramic is put in a chemical copper solution, as shown in Fig. 7 (d). The chemical copper solution is heated with a water barrier for 1 hour, the temperature is adjusted between 40~50 °C, and the deposition rate is around 5~7 μm/hr.

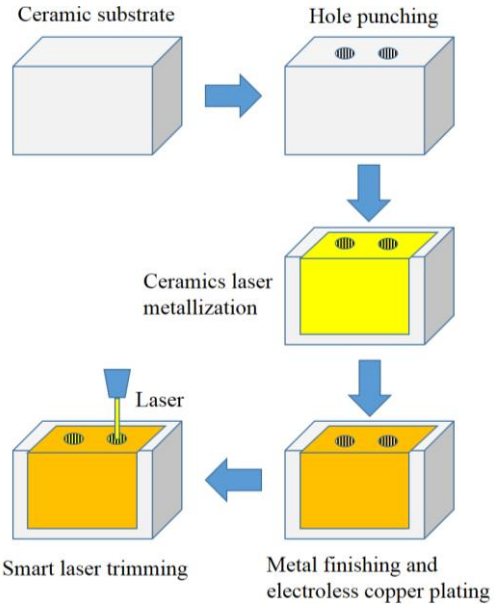

Fig. 5. Fabrication flow chart of the low temperature process for microwave dielectric ceramics metallization.

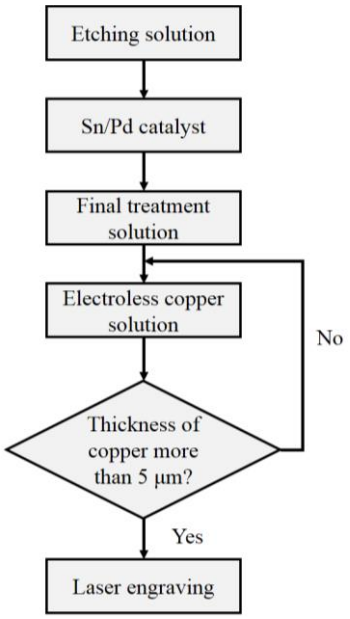

Fig. 6. The ceramic metallization process.

The laser engraving process is described here. First, the 3D geometric shape of the ceramic is built in a SolidWorks drawing software environment. The pattern to be processed by laser is then drawn, as shown in Fig. 2. The *.step file is exported to a computer, and the ceramic height is adjusted to the laser processing height,

which is provided with a fixture and ceramic 3D model to make the computer correspond to the actual object. Next, the laser processing range is defined. Finally, the appropriate laser parameters are adjusted, such as wattage, frequency, speed, and times, so as to reduce the difference between the geometric model size and the size of laser engraving. The image registration is executed to remove the copper layer.

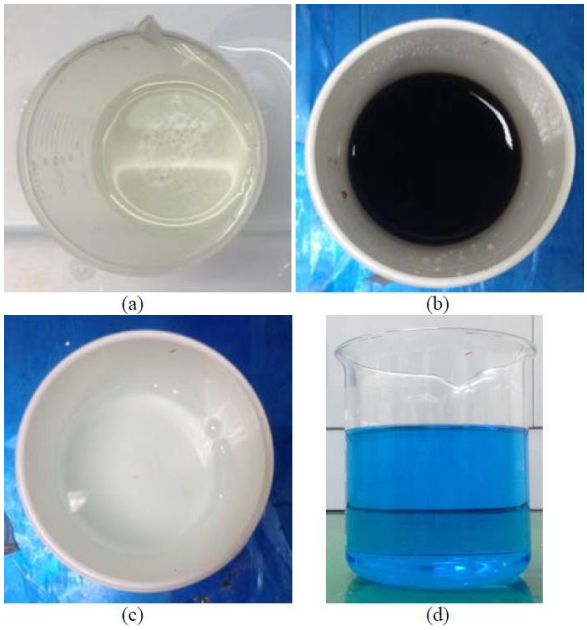

Fig. 7. (a) Etching solution, (b) activator, (c) cleaning fluid, and (d) chemically deposited copper solution.

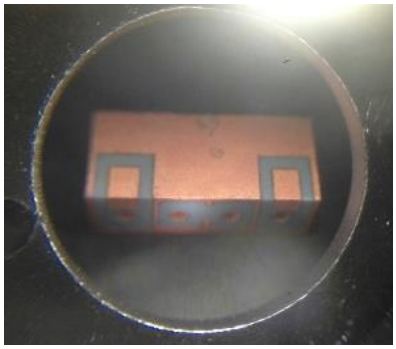

Fig. 8. Photo of the finished product.

IV. EXPERIMENTAL RESULTS AND DISCUSSION

The finished product after forming the chemically deposited copper and laser engraving is shown in Fig. 8. The picture is taken under the microscope. Table 1 shows the error of line width after the proposed fabrication process. From Table 1, the line width errors are within ±50 μm, which are small and consistent through the three samples. Table 2 presents the error of the line's relative position. Once again, the error of the relative position of lines between the design and a final product are within ±50 μm and consistent through three samples. According to the comparison between the pattern and the laser engraving formed size, the line width and the relative position of the line are within ±50 μm; as the screen plate is heated and used many times after, the error could be larger than 100 μm [12].

Table 1: Line width errors between the original design and a final product

Line Width (μm)	Sample1 (μm)	Error (μm)	Sample2 (μm)	Error (μm)	Sample3 (μm)	Error (μm)
520	530	+10	533	+13	535	+15
310	324	+14	334	+24	335	+25
288.5	290	+1.5	297	+8.5	281	-7.5
260	281	+21	284	+24	281	+21
250	249	-1	246	-4	259	+9
180	195	+15	204	+24	191	+11
150	156	+6	139	-11	148	-2
120	121	+1	109	-11	114	-6

Table 2: The error of the relative position of lines between design and a final product

Relative Position of Lines (μm)	Sample1 (μm)	Error (μm)	Sample2 (μm)	Error (μm)	Sample3 (μm)	Error (μm)
1136	1111	-25	1120	-16	1129	-7
810	791	-19	793	-17	793	-17
750	719	-31	725	-25	719	-31
667	645	-22	648	-19	638	-29
630	603	-27	599	-31	604	-26
540	515	-25	511	-29	507	-33
460	426	-34	432	-28	441	-19

Figures 9 and 10 show the $|S_{11}|$ and $|S_{21}|$ comparisons among measurement data of the proposed process and the LTCC with screen printing process along with HFSS simulation results, respectively. As mentioned earlier, this ceramic filter structure is symmetric, and so here we only show the $|S_{11}|$ and $|S_{21}|$ data. According to the comparison among the S-parameters of the proposed process, the LTCC with screen printing process and the HFSS simulation results, the three of them have similar frequency bands and dB values. The measurement and simulation results demonstrate that the fabricated ceramic filter meets the specification requirements. Thus, the proposed low temperature process is practical and adequate for the microwave dielectric ceramics metallization applications.

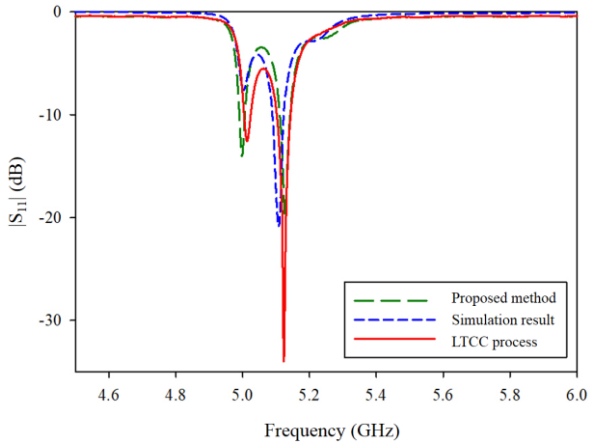

Fig. 9. $|S_{11}|$ comparisons among measurement data of the proposed process and screen printing process and the HFSS simulation results.

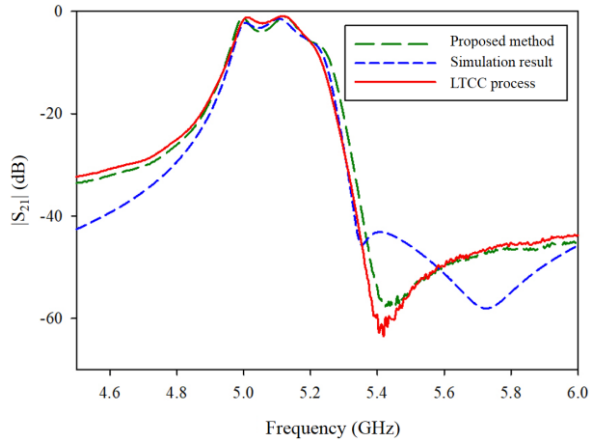

Fig. 10. $|S_{21}|$ comparisons among measurement data of the proposed process and screen printing process and the HFSS simulation results.

Table 3: The comparison of process temperature during metallization among three methods: DBC, LTCC, and the proposed process

	LTCC [2]	DBC [7]	Proposed Process
Process temperature	900~1000 °C	1065 °C	< 50 °C

Table 3 shows the proposed method has the lowest process temperature among three methods. The entire process temperature of the proposed method is below 50 °C, which means that energy is saved significantly. Silver paste may stick to the screen due to re-use, and it will cause an error between the design and final product of more than 100 μm. The proposed method, which applies an electroless copper plating process, can avoid the silver paste stuck problem. Table 4 shows that the laser engraving has a smaller line width of 60 μm than the LTCC with screen printing process and the line width error and relative position error are also within ± 50 μm.

Table 4: The accuracy of proposed process and the LTCC with screen printing process

	LTCC with Screen Printing Process	Proposed Process
Minimum line width	100 μm	60 μm
Line width error	±100 μm	±50 μm
Relative position of lines	±100 μm	±50 μm

VI. CONCLUSION

This research uses a perovskite-based ceramic to metallize microwave dielectric ceramics through chemically deposited copper. The temperature in the overall manufacturing process of the chemically deposited copper is below 50 °C. In comparison to other process methods, e.g., LTCC and DBC manufacturing processes, this technique can reduce the energy consumption effectively and greatly cut the cost of cooling equipment. In addition, the laser engraving forming technique can control the line width and relative position of the line more accurately. When screen printing is used repeatedly, the stuck silver paste exhibits dimensional discrepancy, leading to error signals. In addition, the metal may block up or incompletely adhere to the silver paste sintering pores; when each batch completed has to be checked, the labor cost increases. This study presents that the combination of chemically deposited copper and laser engraving can avoid the aforementioned silver paste sticking or blockage, and thus there is no short circuit or incomplete metallization in via holes. It can also effectively save energy and time when fabricating the appropriate microwave elements. The measurement and simulation results demonstrate that the fabricated ceramic filter meets the specification requirements. Thus, the proposed low temperature process is practical and adequate for the microwave dielectric ceramics applications.

ACKNOWLEDGMENT

This research is supported by Mechanical and Mechatronics Systems Research Laboratories, Industrial Technology Research Institute (ITRI), Taiwan under Grant No. H301AR3400 and by the Ministry of Science and Technology, Taiwan, R.O.C. under Grant No. MOST 107-2221-E-018-002-. We are also grateful to the National Center for High-performance Computing (NCHC) for computer time and facilities.

REFERENCES

[1] R. R. Tummala, "Ceramic and glass-ceramic packaging in the 1990s," *Journal of the American Ceramic Society*, vol. 74, no. 5, pp. 895-908, 1991.

[2] M. T. Sebastian and H. Jantunen, "Low loss dielectric materials for LTCC applications: A review," *International Materials Reviews*, vol. 53, no. 2, pp. 57-90, 2008.

[3] C. Tang, C. Shen, and P. Hsieh, "Design of low-temperature co-fired ceramic bandpass filters with modified coupled inductors," *IEEE Transactions on Microwave Theory and Techniques*, vol. 57, no. 1, pp. 172-179, 2009.

[4] M. Hoft and T. Shimamura, "Design of symmetric trisection filters for compact low-temperature co-fired ceramic realization," *IEEE Transactions on Microwave Theory and Techniques*, vol. 58, no. 1, pp. 165-175, 2010.

[5] S. B. Narang and S. Bahel, "Low loss dielectric ceramics for microwave applications: a review," *Journal of Ceramic Processing Research*, vol. 11, no. 3, pp. 316-321, 2010.

[6] J. Xu, X. Luo, L. Z. Cao, and R. S. Chen, "Optimization of coaxial dielectric resonator filter with aggressive space mapping," in *2012 Asia Pacific Microwave Conference Proceedings*, pp. 229-231, 2012.

[7] J. Schulz-Harder, "Advantages and new development of direct bonded copper substrates," *Microelectronics Reliability*, vol. 43, no. 3, pp. 359-365, 2003.

[8] T. Joyeux, J. Jarrige, J. Labbe, J. Lecompte, and T. Alexandre, "Oxygen influence on wetting and bonding between copper and aluminum nitride," *Key Engineering Materials*, vol. 206, pp. 535-538, 2002.

[9] W. Li, M. Huang, T. Kao, W. Chung, and M. Chou, "Novel LIM (laser induced metallization) technologies of ITRI applied to WWAN/LTE 2-port antenna array for smart handset applications," in *2014 International Symposium on Antennas and Propagation Conference Proceedings*, 2014.

[10] C. Yang, M. Chou, T. Kao, and M. Huang, "Applications of three dimensional laser induced metallization technology with polymer coating," in *2018 13th International Congress Molded Interconnect Devices (MID)*, 2018.

[11] D. M. Pozar, *Microwave Engineering*. John Wiley & Sons, 2009.

[12] J. Kita, A. Dziedzic, L. J. Golonka, and T. Zawada, "Laser treatment of LTCC for 3D structures and elements fabrication," *Microelectronics International*,vol. 19, no. 3, pp. 14-18, 2002.

Jau-Jr Lin received a B.S. degree from National Cheng Kung University, Taiwan in 1997, and a M.S. degree from National Chiao Tung University, Taiwan in 1999. He received a Ph.D. degree from the Department of Electrical and Computer Engineering, University of Florida, Gainesville, FL, U.S.A. in 2007. From 2007 to 2010, he was at Freescale Semiconductor Inc., Tempe, AZ, U.S.A., working on silicon-based millimeter-wave transmitters and millimeter-wave packages in 60-GHz wireless communication systems and 77/79-GHz automotive radar systems. From 2010 to 2012, he worked for Richwave Technology Corporation, Hsinchu, Taiwan as a Technical Section Manager, developing low-power wireless transceivers. In 2012, he joined the Department of Electrical Engineering at National Changhua University of Education, Changhua, Taiwan as an Assistant Professor, where his research interests are wireless communication systems, EM wave propagation, power systems, radar systems, RF circuits and antenna designs.

Coupling of 3D Analytical Calculation and PSO for the Identification of Magnet Parameters used in Magnetic Separation

M. Ouili [1], R. Mehasni [1], M. Feliachi [2], H. Allag [3], H. R. E. H. Bouchekara [4], G. Berthiau [2], and M. E. H. Latreche [1]

[1] Laboratoire d'électrotechnique de Constantine (LEC)
Université des frères Mentouri Constantine 1, Route Ain Elbey, 25000 Constantine, Algérie
mehdi.ouili@lec-umc.org, mehasni@yahoo.fr, meh_latreche@univ-constantine2.dz

[2] Laboratoire IREENA
Université de Nantes, CRTT, BP 406, Boulevard de l'université, 4460, Saint Nazaire cedex, France
mouloud.feliachi@univ-nantes.fr, gerard.berthiau@univ-nantes.fr

[3] Laboratoire de génie électrique de Jijel (L2EI)
Université de Jijel, 18000 Jijel, Algérie
allag_hic@yahoo.fr

[4] Department of Electrical Engineering, Hafr Al-Batin University, Hafr Al-Batin 31991, Saudi Arabia
Bouchekara.houssem@gmail.com

Abstract — In this work, the identification of the residual magnetic flux density of NdFeB permanent magnet, used in a drum magnetic separator, is performed. This identification problem has been formulated as an inverse optimization problem and solved using the Particle Swarm Optimization (PSO) method. For fast calculations, flux densities are computed using a 3D analytical method and the obtained results are compared with measurements.

Index Terms — 3D analytical solution, inverse problem, magnetic separation, parameters identification, Particle Swarm Optimization, permanent magnet.

I. INTRODUCTION

In magnetic separation applications, the efficiency of the separation depends strongly upon the configuration of the applied magnetic field [1-4]. To design a reliable magnetic separator both the geometrical and magnetic specifications of the field generator must be accurately known.

The identification problem in physics devices is largely treated. In [5] the authors presented a simultaneous identification and control of adaptive torque of permanent magnet synchronous machines. In [6] a multiple object positioning and identification method based on the magnetic tracking system was proposed for tracking of minimally invasive medical devices inside human body, such as wireless capsule endoscope. In electrical machine domain, an inverse problem coupled with an analytical model was used for the identification of demagnetization faults in axial flux permanent magnet synchronous machines [7]. Zhe et al. [8] proposed an identification procedure for an Active Magnetic Bearing System (AMBS), which makes it possible to estimate the unknown parameters and to establish the model of transfer function matrix of the AMB system.

The aim of this paper is the identification of the three components of the residual magnetic flux density $\vec{B}_r(B_{rx}, B_{ry}, B_{rz})$ of an NdFeB permanent magnet constituting a rectangular bar with size $1.2\times1\times10\text{cm}^3$ used to realize a drum magnetic separator (see Fig. 1). For that, an inverse optimization problem is formulated and then solved where the objective function is the Mean Squared Error (MSE) between measured and computed values of the magnetic flux density in three different locations in the permanent magnet.

In the field of electromagnetics, several optimization methods have been used to solve different problems as reported in [9-17]. In this paper, the Particle Swarm Optimization (PSO) method has been used to solve the defined problem and the Most Valuable Player Algorithm (MVPA) is used for comparison purposes.

An experimental setup has been developed to measure the magnetic flux density of the permanent magnet. This last one has a parallelepiped shape and a rigid magnetization, this allows to use a 3D (in Cartesian coordinates) analytical integration method [18-19]. Such a solution is more accurate and faster than numerical ones which will make the optimization process faster.

Submitted On: February 6, 2019
Accepted On: May 12, 2019

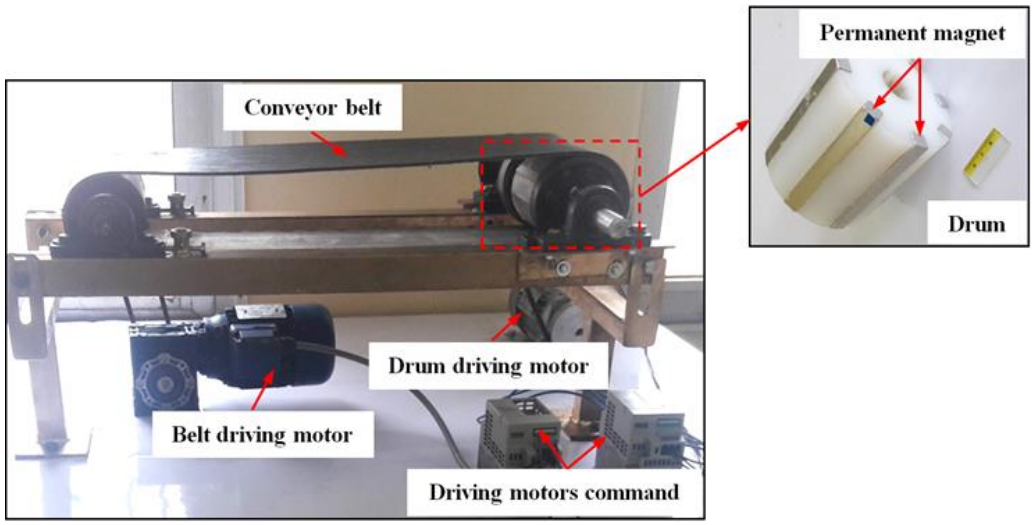

Fig. 1. Experimental setup of the magnetic drum separator.

II. GENERATED MAGNETIC FIELD AND LOCATION OF MEASUREMENT FOR OPTIMIZATION

To know the accurate configuration of the magnetic field generated by the used permanent magnet, measurements have been performed. For this, we have realized and used the experimental test bench presented in Fig. 2.

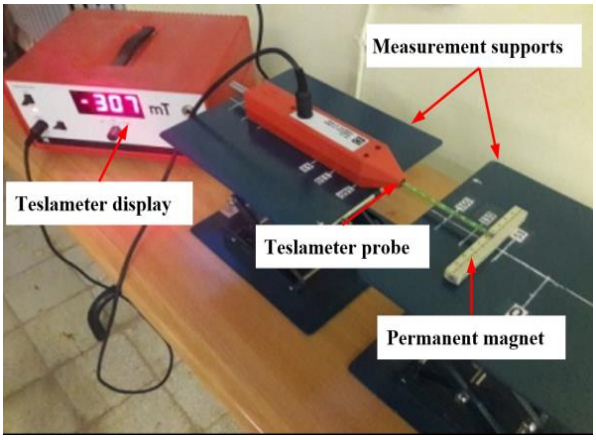

Fig. 2. Experimental setup for measuring the magnetic field.

To define the number of measuring locations required for the optimization process, we have measured and analyzed the magnetic flux density on all the faces of the permanent magnet. To show the nature of the variations of the magnetic flux density on the magnet surfaces, we present the variation of the measured magnetic flux density along the length of two lines situated in significant surfaces oriented in the $\vec{y}$ and $\vec{z}$ directions (see Fig. 3). The line 2 is chosen near the corner of the permanent magnet because along the middle line of this surface the magnetic flux density (B_y) is zero.

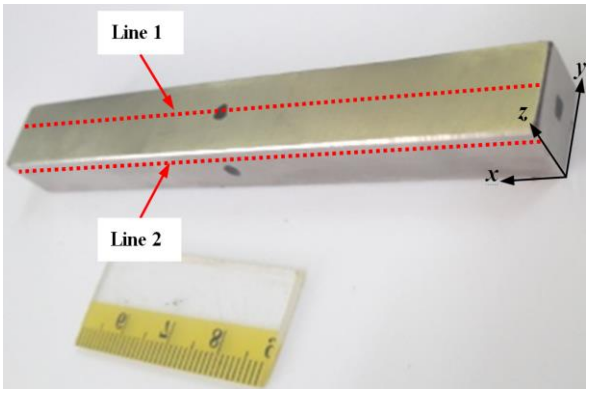

Fig. 3. Lines where the variation of the magnetic flux density is measured.

As shown in Fig. 4 (a), the magnetic flux density is almost constant along the length of the considered line of the significant surfaces of the permanent magnet except at the borders. Using this result along with the fact that each two opposite surfaces of the permanent magnet have opposite magnetic polarities, measuring locations for the optimization are reduced to only three locations located at the center of the three surfaces (see Fig. 4 (b).

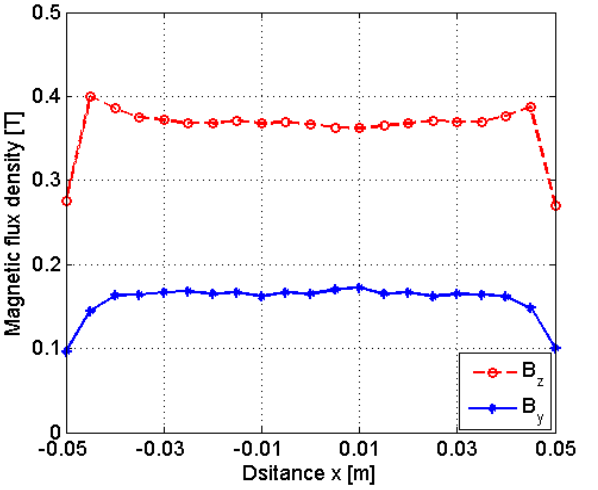

(a)

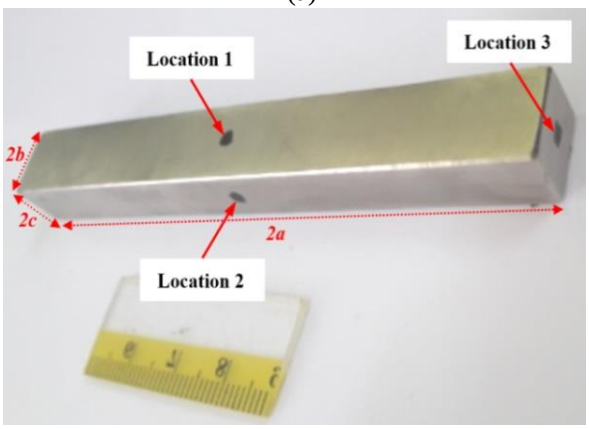

(b)

Fig. 4. (a) Variation of the magnetic flux density along the considered lines, and (b) the three measuring locations for the optimization process.

III. PROBLEM FORMULATION

As aforesaid, the identification problem treated in this paper has been formulated as an inverse optimization problem where the design variables are the three components of the residual magnetic flux density B_{rx}, B_{ry} and B_{rz} of the permanent magnet bar and the objective function is MSE between measured and computed values at three different locations. The objective function can be expressed as follows [20]:

$$F = \frac{1}{2}\sum_{i=1}^{3}\left(B_{mi} - B_{ci}\right)^2, \tag{1}$$

where B_{mi} and B_{ci} are respectively the measured and computed values at the locations $i\ (i = 1, 2, 3)$. In (1), the computed values B_{ci} are function of the three researched parameters $B_{ci} = f\left(B_{rx}, B_{ry}, B_{rz}\right)$.

To compute the quantities B_{ci} we have used the 3D analytical solution given by [21-22]:

$$\begin{bmatrix} B_x \\ B_y \\ B_z \end{bmatrix} = \frac{1}{4\pi}\sum_{i=0}^{1}\sum_{j=0}^{1}\sum_{k=0}^{1}(-1)^{i+j+k}\begin{bmatrix} tg^{-1}\left(\frac{VW}{rU}\right) & \ln(r-W) & \ln(r-V) \\ \ln(r-W) & tg^{-1}\left(\frac{WU}{rV}\right) & \ln(r-U) \\ \ln(r-V) & \ln(r-U) & tg^{-1}\left(\frac{UV}{rW}\right) \end{bmatrix}\begin{bmatrix} B_{rx} \\ B_{ry} \\ B_{rz} \end{bmatrix}. \tag{2}$$

The intermediary variables U, V and W are given by [21-22]:

$$\begin{cases} U = x - (-1)^i a,\ V = y - (-1)^j b,\ W = z - (-1)^k c \\ r = \sqrt{U^2 + V^2 + W^2} \end{cases}. \tag{3}$$

The steps followed to obtain expression (2) are developed in the Appendix.

It is worth to mention that, the choice of three locations to measure the magnetic flux density (the perpendicular component at each face) has considerably reduced the computational time for the optimization process.

IV. OPTIMIZATION METHOD AND OBTAINED RESULTS

To minimize the objective function, the PSO method has been applied [23]. It is a population-based stochastic algorithm and one of the global optimization methods, it simulates the migration and aggregation of animals, such as birds, fishes and bees when they seek for food. The basic form of the PSO algorithm is based on the evolution or movement of a population (called a swarm) of candidate solutions (called particles) in the search space. Each one of these particles has its position, velocity and a fitness value that is determined by an optimization function. The optimization is performed in terms of the objective function where each particle knows its best position obtained individually so far and is called the Personal Best (P_{pbest}). In the same way, the other particles know what is the best position obtained collectively so far and is called the Global Best (P_{gbest}). Each particle updates its velocity and position at each iteration by using the mathematical models given by [24].

$$v_m(t+1) = \omega\, v_m(t) + c_1 r_1\left(P_{pbest}(t) - x_m(t)\right) + c_2 r_2\left(P_{gbest}(t) - x_m(t)\right), \tag{4}$$

$$x_m(t+1) = x_m(t) + v_m(t+1), \tag{5}$$

where m is the particle number, v and x are the particle velocity and position, respectively, c_1 is the cognitive coefficient, c_2 is the social coefficient, r is a random values in the interval [0, 1] and ω is the inertia weight who ensures that the particle swarm can search from the whole search space in the early iterations and converge in later iterations. The PSO method used in this paper is implemented according to the pseudo code given in Algorithm 1 [25].

Algorithm 1: Pseudocode of the PSO method

Input: Problem Size; Population Size
Output: P_{gbest}
Population ← ∅
P_{gbest} ← ∅
  for i=1: population Size
    $P_{velocity}$ ← Random Velocity
    $P_{position}$ ← Random Position
    P_{pbest} ← $P_{position}$
    if cost(P_{pbest}) ≤ cost(P_{gbest})
      P_{gbest} ← P_{pbest}
    end
  end
  while (Stop condition)
    for each P ∈ Population
    $P_{velocity}$ ←Update Velocity($P_{velocity}$, P_{gbest}, P_{pbest})
    $P_{position}$ ← Update Position($P_{position}$, $P_{velocity}$)
    if cost($P_{position}$) ≤ cost(P_{pbest})
      P_{pbest} ← $P_{position}$
      if cost(P_{pbest}) ≤ cost(P_{gbest})
        P_{gbest} ← P_{pbest}
      end
    end
    end
  end
return P_{gbest}

In this paper, he PSO method has been programmed using the commercial MATLAB software and run on a computer with Intel(R) Xeon(R) CPU E5-1620 v2 @ 3.70 GHz Processor and 8.00 GO-RAM under professional windows 7 environment. The stopping criterion was chosen as $\varepsilon = 1\times10^{-9}$ so that the iteration stopped when $F \le \varepsilon$. The tuning parameters used for the PSO algorithm are listed in Table 1.

Table 1: PSO tuning parameters

Parameters	Values
Population Size	40
Cognitive coefficient c_1	-0.6504
Social coefficient both c_2	2.2073
Inertia weight ω	-0.4349
Range of the researched parameters	[-1.3 1.3]

The optimal design variables found after 27 iterations are displayed in Table 2.

Table 2: Optimal values found after 27 iterations

Parameters	Values
B_{rx}(T)	-2.27×10^{-5}
B_{ry}(T)	1.39×10^{-5}
B_{rz}(T)	1.1066
F	1.94×10^{-10}
$t(s)$	0.1989

The results of Table 2 show that the dominant component of the residual flux density is B_{rz} which signifies that the magnetization of the permanent magnet is oriented in the z-axis direction. To verify the obtained results, we have computed the magnetic flux density along the lines of Fig. 3. The comparison between the computed and measured values is presented in Fig. 5.

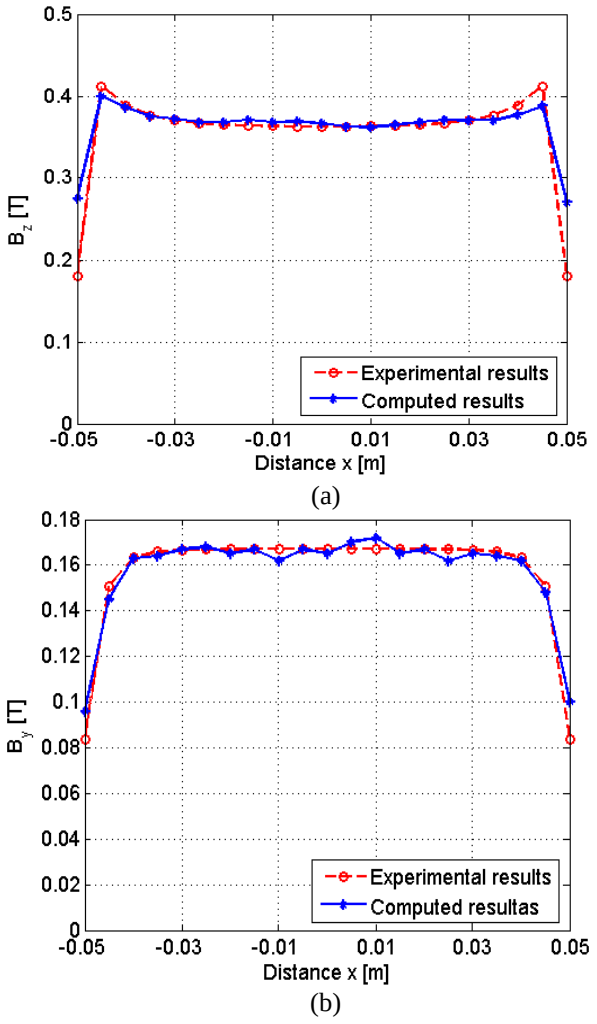

Fig. 5. Variation of the magnetic flux density related to the identified parameters. (a) Variation along the length of the line 1, and (b) variation along the length of the line 2.

Figure 5 shows that the measured and computed results are very close, which validates the reliability of the developed computing codes and the obtained results.

For a global verification of the achieved optimization, we have compared the results obtained by the PSO with those obtained by the Multi Valuable Player Algorithm (MVPA) method.

The MVPA is a recently developed algorithm inspired from sport [16]. It is a very competitive algorithm compared with other optimization algorithms as proved in [26] and [27]. The pseudo code of the MVPA is given in Algorithm 2 and the main steps are detailed bellow. Like other population-based metaheuristics, the MVPA starts by generating a population of players inside the search space following a random distribution. These players are regrouped into teams (line 3). Then the algorithm will iterate 'MaxNFix' times trying to evolve the population to find the optimal solution. In each iteration, a loop on all teams selects a first team called TEAMi. The players of this team compete to determine to best player (Franchise Player) of this team and the population is updated accordingly (line 8). This first phase is called the 'individual competition phase'. In the second competition phases called 'team competition phase', a second team called TEAMj is randomly selected among the leagues' teams. TEAMi and TEAMj play against each other to determine the wining team. The population is updated according to the outcome of this matchup (lines 9-13). Once the competition phase is completed the players are checked to see if there is any player outside the search space. In such case, this player is brought back to the search space (line 14). In order to improve the performance of the MVPA three steps have to be performed which are 'application of greediness', 'application of elitism' and 'remove duplicates'. In the first step, a player is updated only if his new fitness is better than the old one. In the second step, some of the worst players are replaced by some of the best players. In the third step duplicate players are removed and changed by new ones.

In the pseudocode of the MVPA, the inputs are the function (ObjFunction), the number of design variables (ProblmSize), the number of players which is equivalent to the population size (PlayersSize), the number of teams in the league (TeamsSize) and the maximum number of fixtures which is equivalent to the maximum number of iterations (MaxNfix). The output of the algorithm is the leage's MVP which is the best solution obtained.

To estimate the speed of convergence of the two applied methods, Fig. 6 plots the evolution of the objective function versus the number of iterations.

Algorithm 2: Pseudocode of the MVPA method

1 **Inputs:** ObjFunction (objective function), ProblemSize (dimension of the problem), PlayersSize (number of players), TeamsSize (number of teams) and MaxNFix (maximum number of fixtures)
2 **Output**: MVP
3 Initialization
4 **for** fixture=1:MaxNFix
5 **for** i=1:TeamsSize
6 $\mathrm{TEAM_i}$ =Select the team number i from the league's teams
7 $\mathrm{TEAM_j}$ = Randomly select another team j from the league's teams where j≠i
8 $\mathrm{TEAM_i} = \mathrm{TEAM_i} + \mathrm{rand} \times (\mathrm{FranchisePlayer_i} - \mathrm{TEAM_i}) + 2 \times \mathrm{rand} \times (\mathrm{MVP} - \mathrm{TEAM_i})$
9 **if** $\mathrm{TEAM_i}$wins against $\mathrm{TEAM_j}$
10 $\mathrm{TEAM_i} = \mathrm{TEAM_i} + \mathrm{rand} \times (\mathrm{TEAM_i} - \mathrm{FranchisePlayer_j})$
11 **else**
12 $\mathrm{TEAM_i} = \mathrm{TEAM_i} + \mathrm{rand} \times (\mathrm{FranchisePlayer_j} - \mathrm{TEAM_i})$
13 **end**
14 Check if there are players outside the search space
15 **end**
16 Application of greediness
17 Application of elitism
18 Remove duplicates
19 **end for**

A comparison between the results obtained by PSO and those obtained by MVPA method is shown in Table 3.

Table 3: Optimal values of the researched parameters obtained by the two methods

Parameters	**PSO**	**MVPA**
B_{rx} (T)	-2.27×10^{-5}	-1.07×10^{-4}
B_{ry} (T)	1.39×10^{-5}	-1.34×10^{-4}
B_{rz} (T)	1.1066	1.1069
F	1.94×10^{-10}	7.67×10^{-10}
t (s)	0.1989	0.2505
Iteration's number	27	15

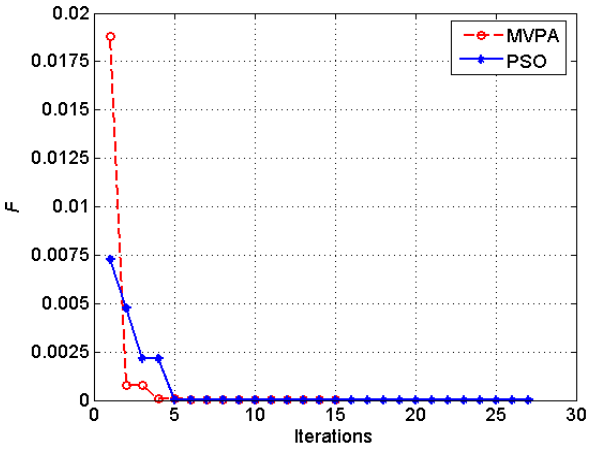

Fig. 6. Evolutions of the objective function as a function of computing iterations.

The comparison between the obtained results of the Table 3 and Fig. 6 show that the two applied optimization methods have given the same values of the three researched parameters corresponding to the three components of the residual magnetic flux density.

The obtained results show clearly that the MVPA converges quickly but the PSO algorithm performs better in terms of running time.

V. CONCLUSION

In this work, developed for a magnetic separation study, a methodology for NdFeB permanent magnet parameters identification based on the resolution of an inverse problem has been presented. In such methodology, the PSO method is combined with 3D analytical solution, which has given a good accuracy and a low processing cost. The results of the analytical solution have been validated by comparison with measurements. For a global verification of the achieved optimization, we have compared the obtained results by the PSO with those obtained by the Multi Valuable Player Algorithm (MVPA) method. The comparison shows that the two applied methods have given the same optimal results. However, the PSO method presents better performances in terms of running time.

ACKNOWLEDGMENT

This work was supported by the Inductics-Net of the ATRST agency and the DGRSDT Direction, Algerian section.

APPENDIX

Analytical calculation of magnetic flux density created by a magnet

Based on the conventional equivalent magnetic charge method, for parallel uniform magnetized magnet in *z* direction, the magnetization effect can be represented by two parallel magnetic charge surfaces (Colombian approach) on the sides of the permanent magnet which their normal is collinear with the supposed magnetization direction [28].

An assumed rigid and uniform magnetization can be replaced by a distribution of magnetic poles. The density of such poles distribution is defined by [29]:

$$\sigma = \vec{M}.\vec{n} = \frac{\vec{B}_r}{\mu_0}.\vec{n}. \tag{6}$$

Let us consider the rectangular surface $2a \times 2b$ having a uniform pole density σ (Fig. 7).

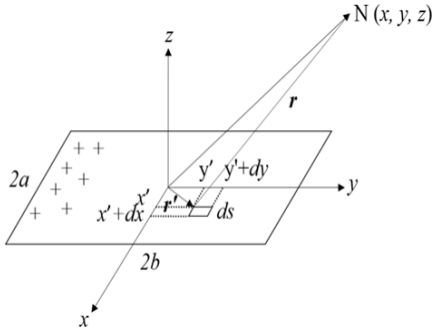

Fig. 7. Geometrical illustration for the potential and the magnetic field calculation.

The magnetic scalar potential *V* in a point N is given by [21-22]:

$$V = \frac{1}{4\pi} \iint_S \frac{M.ds}{\|\vec{r}-\vec{r}'\|}. \tag{7}$$

Depending on the residual magnetic flux density, the expression (7) can be written as:

$$V = \frac{1}{4\pi\mu_0} \iint_S \frac{B_r.ds}{\|\vec{r}-\vec{r}'\|}. \tag{8}$$

In Cartesian coordinates system, (8) can be written as:

$$V = \frac{B_r}{4\pi\mu_0} \int_{-b}^{b} dy' \int_{-a}^{a} \frac{1}{\sqrt{(x'-x)^2+(y'-y)^2+z^2}} dx'. \tag{9}$$

After two analytical integrations, we obtain:

$$V = \frac{B_r}{4\pi\mu_0} \sum_{i=0}^{1} \sum_{j=0}^{1} (-1)^{i+j} \left(-U\ln(r-V) - V\ln(r-U) - W.tg^{-1}\left(\frac{UV}{rW}\right) \right), \tag{10}$$

$$\begin{cases} U = x-(-1)^i a \ , \ V = y-(-1)^j b \ , \ W = z \\ r = \sqrt{U^2+V^2+W^2} \end{cases}. \tag{11}$$

The magnetic field can be calculated by deriving the scalar potential expression, which leads to:

$$\vec{H} = \frac{Br}{4\pi\mu_0} \sum_{i=0}^{1} \sum_{j=0}^{1} (-1)^{i+j} \begin{pmatrix} \ln(r-V) \\ \ln(r-U) \\ tg^{-1}\left(\frac{UV}{Wr}\right) \end{pmatrix}. \tag{12}$$

So, the magnetic flux density is given by:

$$\vec{B} = \frac{B_r}{4\pi} \sum_{i=0}^{1} \sum_{j=0}^{1} (-1)^{i+j} \begin{pmatrix} \ln(r-V) \\ \ln(r-U) \\ tg^{-1}\left(\frac{UV}{Wr}\right) \end{pmatrix}. \quad (13)$$

For a cubical magnet in which the magnetization is collinear with *z* direction, (see Fig. 8), the magnetic flux density can be determined from the upper and the lower charged surfaces.

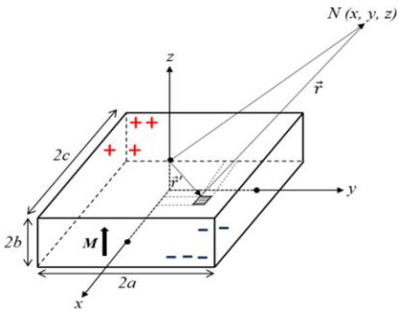

Fig. 8. Magnetic field created by a cuboidal permanent magnet.

In this case, comparing also to (equation 13), the magnetic flux density will be:

$$\vec{B} = \frac{Br}{4\pi} \sum_{i=0}^{1} \sum_{j=0}^{1} \sum_{k=0}^{1} (-1)^{i+j+k} \begin{pmatrix} \ln(r-V) \\ \ln(r-U) \\ tg^{-1}\left(\frac{UV}{Wr}\right) \end{pmatrix}. \quad (14)$$

The intermediary variables become:

$$\begin{cases} U = x-(-1)^i a\,,\ V = y-(-1)^j b\,,\ W = z-(-1)^k c \\ r = \sqrt{U^{\,2}+V^{\,2}+W^{\,2}} \end{cases}. \quad (15)$$

For a permanent magnet magnetization oriented randomly in space, the global magnetization is the superposition of the three components as shown in Fig. 9:

$$\vec{M} = M_x\vec{i} + M_y\vec{j} + M_z\vec{k}. \quad (16)$$

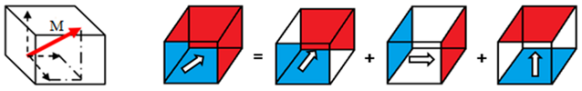

Fig. 9. Decomposition of a randomly oriented magnetization in a permanent magnet [22].

Then, the computation of the total components of is deduced as follows:

$$\vec{B} = \vec{B}_x + \vec{B}_y + \vec{B}_z, \quad (17)$$

According to the result given by *z* axis-oriented magnetization (7 to 13), the total *B* resulting from the inclined magnetization is given by a simple permutation of analytic formulas for the two other directions of magnetization (*x* axis and *y* axis). So, we can write:

$$\vec{B} = \frac{1}{4\pi} \sum_{i=0}^{1} \sum_{j=0}^{1} \sum_{k=0}^{1} (-1)^{i+j+k} \begin{bmatrix} B_{rx} tg^{-1}\left(\frac{WV}{rU}\right) + B_{ry}\ln(r-W) + B_{rz}\ln(r-V) \\ B_{rx}\ln(r-W) + B_{ry} tg^{-1}\left(\frac{WU}{rV}\right) + B_{rz}\ln(r-U) \\ B_{rx}\ln(r-V) + B_{ry}\ln(r-U) + B_{rz} tg^{-1}\left(\frac{VU}{rW}\right) \end{bmatrix}, \quad (18)$$

In other manner, we can write the magnetic flux density components as:

$$\begin{bmatrix} B_x \\ B_y \\ B_z \end{bmatrix} = \frac{1}{4\pi} \sum_{i=0}^{1} \sum_{j=0}^{1} \sum_{k=0}^{1} (-1)^{i+j+k} \begin{bmatrix} tg^{-1}\left(\frac{VW}{rU}\right) & \ln(r-W) & \ln(r-V) \\ \ln(r-W) & tg^{-1}\left(\frac{WU}{rV}\right) & \ln(r-U) \\ \ln(r-V) & \ln(r-U) & tg^{-1}\left(\frac{UV}{rW}\right) \end{bmatrix} \begin{bmatrix} B_{rx} \\ B_{ry} \\ B_{rz} \end{bmatrix}, \quad (19)$$

REFERENCES

[1] X. Zheng, N. Guo, R. Cui, et al., "Magnetic field simulation and experimental tests of special cross-sectional shape matrices for high gradient magnetic separation," *IEEE Transactions on Magnetics*, vol. 53, no 3, pp. 1-10, 2017.

[2] R. Mehasni, M. E. H. Latreche, and M. Feliachi, "Effect of the magnetic dipole-dipole interaction on the capture efficiency in open gradient magnetic separation," *IEEE Trans on Magnetics*, vol. 43, no. 8, Aug. 2007.

[3] A. Belounis, R. Mehasni, M. Ouili, and M. E. H. Latreche, "Optimization of the capture element for an OGMS based on the 3d computation of the magnetic particle behavior," *International Journal of Electromagnetic and Mechanics*, vol. 48, no. 4, pp. 387-397, 2015.

[4] F. Mishima, Y. Akiyama, and S. Nishijima, "Fundamental study on magnetic separator using oxygen dissolved perfluorocarbon," *IEEE Transactions on Applied Superconductivity*, vol. 24, no. 3, pp. 1-5, 2014.

[5] D. M. Reed, S. Jingand, and H. F. Hofmann, "Simultaneous identification and adaptive torque control of permanent magnet synchronous machines," *IEEE Transactions on Control Systems Technology*, vol. 25, no. 4, pp. 1372-1383, 2017.

[6] S. Song, C. Hu, and M. Q. Meng, "Multiple objects positioning and identification method based on magnetic localization system," *IEEE Transactions on Magnetics*, vol. 52, Oct. 2016.

[7] J. De Bisschop, A. Abdallah, P. Sergeant, and L. Dupré, "Identification of demagnetization faults in axial flux permanent magnet synchronous machines using an inverse problem coupled with

an analytical model," *IEEE Transactions on Magnetics*, vol. 50, no. 11, Nov. 2014.

[8] S. Zhe, H. Ying, Z. Jinging, S. Zhengang, Z. Lei, and Y. Suyuan, "Identification of active magnetic bearing system with a flexible rotor," *Elsivier, Mechanical Systems And Signal Processing*, vol. 49, no. 2, pp. 302-316, Dec. 2014.

[9] H. Boudjefdjouf, H. R. H. Bouchekara, F. de Paulis, et al., "Wire fault diagnosis based on time-domain reflectometry and backtracking search optimization algorithm," *Applied Computational Electromagnetics Society Journal*, vol. 31, no. 4, 2016.

[10] J. Pzolghadr, Y. Cai, and N. Ojaroudi, "UWB slot antenna with band-notched property with time domain modelling based on genetic algorithm optimization," *Applied Computational Electromagnetics Society Journal*, vol. 31, no. 8, 2016.

[11] R. Carlos, K. Tine, and G. Alejandro, "Identification of a proton-exchange membrane fuel cell's model parameters by means of an evolution strategy," *IEEE Transactions on Industrial Informatics*, vol. 11, no. 2, July 2014.

[12] S.-Y. Kuo and Y.-H. Chou, "Entanglement-enhanced quantum-inspired Tabu search algorithm for function optimization," *IEEE Access*, vol. 5, pp. 13236-13252, 2017.

[13] F. Campelo, F. G. Guimarães, H. Igarashi, J. A. Ramírez, and S. Noguchi, "A modified immune network algorithm for multimodal electromagnetic problems," *IEEE Transactions on Magnetics*, vol. 42, no. 4, pp. 1111-1114, Apr. 2006.

[14] F.-P. Xiang, E.-P. Li, X.-C. Wei, and J.-M. Jin, "A particle swarm optimization-based approach for predicting maximum radiated emission from PCBS with dominant radiators," *IEEE Trans on Electromagnetic Compatibility*, vol. 57, pp. 1197-1205, 2015.

[15] L. D. S. Coelho, L. D. Afonso, and P. Alotto, "A modified imperialist competitive algorithm for optimization in electromagnetics," *IEEE Transactions on Magnetics*, vol. 48, no. 2, pp. 579-582, 2012.

[16] H. R. E. H. Bouchekara, "Most valuable player algorithm: A novel optimization algorithm inspired from sport," *Operational Research*, pp. 1-57, May 10, 2017.

[17] H. R. H. Bouchekara, M. Nahas, and H. M. Kaouach, "Optimal design of electromagnetic devices using the league championship algorithm," *Applied Computational Electromagnetics Society Journal*, vol. 32, no. 6, 2017.

[18] A. Azzouza, H. Allag, J.-P. Yonnet, and P. Tixador, "3-D new calculation principle of levitation force between permanent magnet and hard type-II superconductor using integral approach," *IEEE Trans. Magn.*, vol. 53, no. 11, 2017.

[19] H. Allag, J.-P. Yonnet, H. R. H. Bouchekara, et al., "Coulombian model for 3d analytical calculation of the torque exerted on cuboidal permanent magnets with arbitrary oriented polarizations," *Applied Computational Electromagnetics Society Journal*, vol. 30, no. 4, 2015.

[20] M. Hadef, M. R. Mekideche, and H. Allag, "Relative magnetic permeability identification of the permanent magnets of a synchronous motor using inverse problem," *International Review of Electrical Engineering (IREE)*, vol. 2, no. 2, pp. 103-109, 2007.

[21] A. Gilles and J.-P. Yonnet, "3D analytical calculation of the forces exerted between two cuboidal magnets," *IEEE Trans on Magnetics*, vol. mag-20, no. 5, Sep. 1984.

[22] H. Allag, J.-P. Yonnet, and M. E. H. Latreche, "3D analytical calculation of forces between linear Halbach-type permanent magnet arrays," *8th International Symposium on. IEEE*, pp. 1-6, 2009.

[23] J.-H. Lee, J.-W. Kim, J.-Y. Song, et al., "Distance-based intelligent particle swarm optimization for optimal design of permanent magnet synchronous machine," *IEEE Trans on Magnetics*, vol. 53, no. 6, 2017.

[24] C. Zhang, Z. Chen, Q. Mei, et al., "Application of particle swarm optimization combined with response surface methodology to transverse flux permanent magnet motor optimization," *IEEE Trans on Magnetics*, vol. 53, no. 12, pp. 1-7, 2017.

[25] J. Brownlee, "Clever algorithms: nature-inspired programming recipes," *Jason Brownlee*, 2011.

[26] B. Alatas, "Sports inspired computational intelligence algorithms for global optimization," *Artificial Intelligence. Rev*., 2017.

[27] H. R. E. Bouchekara, A. Orlandi, M. Al-Qdah, and F. de Paulis, "Most valuable player algorithm for circular antenna arrays optimization to maximum sidelobe levels reduction," *IEEE Transactions on Electromagnetic Compatibility*, vol. 60, no. 6, 2018.

[28] H. Zhang, B. Kouet, and L. Li, "Analytical calculation of the 3D magnetic field created by non-periodic permanent magnet arrays," in *Electrical Machines and Systems (ICEMS) 2011 International Conference on. IEEE*, pp. 1-4, 2011.

[29] F. J. Maarten, J. J. H. Paulides, and E. Ilhan, "Relative permeability in a 3d analytical surface charge model of permanent magnets," *IEEE Trans. on Magnetics*, vol. 49, no. 5, May 2013.

Mehdi Ouili was born in Constantine, Algeria, in 1987. He received the B.S. and M.S. degrees in Electrical Engineering from the University of Constantine, Algeria in 2010 and 2013 respectively. He is currently working toward the Ph.D. degree at the Department of Electrical Engineering, in the same University, member of the LEC laboratory. His current research interests include magnetic separation process.

Rabia Mehasni was born in Grarem, Algeria, in 1970. He received the Ph.D. in Electrical Engineering from the University of Constantine, Algeria in 2007. He is with the Department of Electrical Engineering, University of Constantine since 2000. He is currently Research Director at the LEC Laboratory. He has published in the field of magnetic separation. His research interests are in the field of numerical methods and modeling techniques to approach the multidisciplinary problems.

Mouloud Feliachi is native of Biskra in Algeria. He is an Engineer of the "Ecole Nationale Polytechnique" of Algiers (1976), a Ph.D. of the "Conservatoire National des Arts et Métiers" of Paris (1981) and "Docteur d'Etat Es-Sciences Physiques" of the "Institut National Polytechnique" of Grenoble (1986), all in Electrical Engineering. In 1987, he worked as an Engineer for the Leroy Somer company in Orléans. In 1988, he joined the University of Nantes (Institut Universitaire de Technologie - Saint-Nazaire) where he is Professor. He was Scientific Director of LRTI-Lab and Head of the Modeling and Simulation team in GE44-Lab. He is currently leading a Franch-Algerian thematic network of research in Inductics, within IREENA Lab. His research interests are in hybrid analytical and numerical modeling of low frequency electromagnetic phenomena with emphasis on multi-physics and eddy current non-destructive testing and evaluation.

Hichem Allag received the diploma of Engineer in Electrical Engineering from the University of Jijel (Algeria) and the magister from University of Constantine in respectively 2000 and 2002. He was qualified as Assistant Professor in Jijel University in 2003. From 2007 to 2010, he prepared and received the Ph.D. in the University of Joseph Fourier in France. He is currently Professor in University of Jijel, Director of Electrotechnic and Industrial Electronic Laboratory, Head of Department of Fundamental Sciences and Technology. His scientific researches include computational electromagnetic and control applications.

Houssem R.E.H. Bouchekara is an Associate Professor at the Electrical Engineering Department of University of Hafr Al Batin. He has received his B.S. in Electrical Engineering from University Mentouri Constantine, Algeria, in 2004. He has received his Master in Electronic Systems and Electrical Engineering from Polytechnic School of the University of Nantes, France, 2005. He received his Ph.D. in Electrical Engineering from Grenoble Institute of Technology, France, in 2008. His research interest includes: optimization techniques, magnetic refrigeration, electromagnetics, electric machines and Power systems.

Gerard Berthiau received the M.S. and Engineer degrees in Scientific Computingfrom Conservatoire National Arts et Metiersin 1991, Ph.D. degree in Electronics from Ecole Centrale Parisin 1994 and the "Habilitation a Diriger les Recherches" at the University of Nantes in 2007. He is currently a Full Professor in the Department of Physics at the Institute of Technology of Saint-Nazaire, Nantes University, France. His current research interests include electromagnetic field computation and physical properties characterization for non destructive testing particularly for composite materials, inverse problems and optimization techniques.

Mohamed El Hadi Latreche is a Professor in the Electrical Engineering Department of the University Mentouri of Constantine, in Algeria. He is a researcher in LEC Laboratory of Constantine and his research area is the electromagnetic field and numerical calculations, with a focus on electromagnetic induction phenomena, and optimization structures. He has published more than 20 academic articles and participated in more than 50 scientific conferences.

Optimized Semi-implicit Methods for Modeling Cardiac Propagation

Riasat Khan [1] and Kwong T. Ng [2]

[1] Department of Electrical and Computer Engineering
North South University, Dhaka, Bangladesh
riasat.khan@northsouth.edu

[2] Department of Electrical and Computer Engineering
New Mexico State University, Las Cruces, NM 88003, USA
ngnsr@nmsu.edu

Abstract ― Computer simulation of cardiac electrophysiology is now considered a powerful tool for exploring the causes of cardiac arrhythmias. Cardiac electric propagation has been studied using the monodomain model to describe wave propagation of action potential in the heart. The governing nonlinear reaction-diffusion partial differential equation is solved with the semi-implicit (implicit-explicit) method that does not have the stability limit of the explicit time-stepping scheme. Both first order and second order semi-implicit techniques for temporal discretization are considered in this paper. Second order finite difference technique is used to discretize the spatial derivatives. An explicit finite difference scheme with 512×512 nodes and 0.1 μs time step is used as the benchmark for error calculation. APPSPACK, a parallel pattern search optimization software, is used to obtain the optimal semi-implicit parameters that give the lowest root-mean-square error. Results are presented for the semi-implicit techniques with or without the operator split or protective zone method. They demonstrate that the optimized second order semi-implicit method gives the best overall performance.

Index Term ― Derivative-free optimization method, monodomain model, operator split method, pattern search algorithm, semi-implicit scheme.

I. INTRODUCTION

The complex bidomain model is arguably the most comprehensive mathematical model for simulating electrical activities in the heart [1]. According to this model, the cardiac tissue is considered as two overlapping continuous domains, representing the interstitial and intracellular regions illustrated in Fig. 1. An electric potential, known as the transmembrane potential or action potential, is produced between these two domains when an electrical stimulus is applied. With the propagation of this action potential across the cardiac tissue, an electric field is generated at the surface of the human body, giving rise to the electrogram. The bidomain model consists of coupled nonlinear reaction-diffusion and elliptical equations. Disregarding the interstitial region transforms the bidomain model into a simplified monodomain model, also known as the reaction-diffusion or cable model, which involves a single nonlinear reaction-diffusion equation [2]. The simplification of the bidomain model leads to a significantly less intensive computational solution, and recently Potse et al. showed that the discrepancy in simulated action potential propagation between the two models is negligible [3]. This confirms the use of the monodomain model as a preliminary step to develop new numerical techniques.

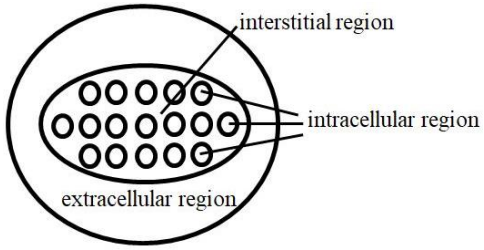

Fig. 1. Illustration of the intracellular, interstitial, and extracellular region.

The cardiac monodomain equation consists of a temporal derivative, a spatial Laplacian, and nonlinear ionic current terms. The central finite difference technique with second-order accuracy has been used to approximate the Laplacian. The ionic current introduces nonlinearity and is represented as a complex nonlinear function of the action potential. The temporal derivative has been commonly discretized with the explicit method [1], though it has a stability constraint that seriously limits the time step size. In this work, temporal discretization is achieved with the semi-implicit or implicit-explicit scheme, in which the implicit method is used for the

Submitted On: July 28, 2018
Accepted On: September 13, 2019

spatial Laplacian but the explicit method is employed for the ionic current. This mixed approach eliminates the stability limit of the explicit method, while avoiding the expensive solution of a nonlinear matrix equation required in a fully implicit method. Both first and second order semi-implicit techniques with one and two discretization coefficients, respectively, have been implemented.

A major objective of this study is to find the above coefficients that give the best results, i.e., the lowest root-mean-square (RMS) error potential. The pattern search algorithm has been applied to find these optimal parameters by using the asynchronous parallel pattern search package, APPSPACK. APPSPACK uses derivative-free optimization to minimize the objective function by changing the design variables [4]. To our knowledge, this is the first time a second order technique or parameter optimization is considered in semi-implicit finite difference modeling of cardiac propagation.

II. CARDIAC MONODOMAIN MODEL

The monodomain model is a mathematical model that describes the flow of electrical current in the heart. The governing monodomain equation is given by:

$$\frac{\partial V_m}{\partial t} = \frac{1}{C_m}\{\frac{1}{\beta}[\nabla\cdot(\bar{\bar{\sigma}}_i \nabla V_m) + I_{si}] - \Sigma I_{ion}\}, \qquad (1)$$

where V_m is the action potential, i.e., the difference between the intracellular and interstitial potentials, C_m is the cell membrane capacitance per unit area, β is the membrane area per unit volume, and $\bar{\bar{\sigma}}_i$ denotes the intracellular conductivity tensor. I_{si} is the intracellular source current that initiates the activation, and ΣI_{ion} represents the total ionic current through the membrane.

In this study, the ionic current ΣI_{ion} is obtained as the sum of six different types of ionic currents using the Luo-Rudy model [5]. The Luo-Rudy model is a comprehensive ionic current model that is capable of reproducing electrocardiograms similar to those recorded from patients.

III. SEMI-IMPLICIT MONODOMAIN FORMULATION

Both the first and second order semi-implicit methods have been derived from the formulation proposed by Ascher et al. [6] for partial differential equations. The update equation for the first order semi-implicit temporal discretization is given by:

$$\underbrace{\{[I] - \underbrace{\frac{\theta\Delta t}{C_m\beta}[D_o]\}}_{[A]}\underbrace{\bar{V}_m^{n+1}}_{\bar{x}}}_{} = \underbrace{\bar{V}_m^n + \frac{(1-\theta)\Delta t}{C_m\beta}[D_o]\bar{V}_m^n + \Delta t[\frac{1}{C_m\beta}\bar{I}_{si}^{n+1} - \frac{1}{C_m}\overline{\Sigma I}_{ion}^n]}_{\bar{b}}, \quad (2)$$

where $[I]$ is the identity matrix, $0 \le \theta \le 1$ is the discretization coefficient, Δt is the time step size, n is the time step index, the bar designates a vector containing all the nodal values of the corresponding quantity, and $[D_o]\bar{V}_m$ represents the finite difference approximation of the Laplacian. Equation (2) represents a matrix equation, which is solved with the Jacobi preconditioned conjugate gradient iterative technique.

The second order semi-implicit discretization of the monodomain equation can be derived as:

$$\underbrace{\{(\theta+\frac{1}{2})[I] - \underbrace{\frac{\Delta t\,(\theta+\frac{c}{2})}{C_m\beta}[D_o]\}}_{[A]}\underbrace{\bar{V}_m^{n+1}}_{\bar{x}}}_{} = \underbrace{2\theta\bar{V}_m^n - \left(\theta-\frac{1}{2}\right)\bar{V}_m^{n-1} + \frac{\Delta t}{C_m\beta}\left[(1-\theta-c)[D_o]\bar{V}_m^n + \frac{c}{2}[D_0]\bar{V}_m^{n-1}\right] + \underbrace{\frac{\Delta t}{C_m}\left[[(1+\theta)\overline{\Sigma I}_{ion}^n - \theta\overline{\Sigma I}_{ion}^{n-1}]\right]}_{\bar{b}} + \frac{\Delta t}{C_m\beta}\bar{I}_{si}^{n+1}}_{}. \qquad (3)$$

where θ and c are second order semi-implicit temporal discretization coefficients.

A. Pattern search algorithm

The pattern search algorithm [4] is used to implement the optimization of the temporal coefficients in (2) and (3). The algorithm is based on the univariate or cyclic coordinate descent method, which uses the design variables, θ and c in the present case, as coordinate directions [7]. The search direction is computed by cycling through the n design variables, yielding n iterations for each direction search cycle. As the monodomain equation involves the nonlinear ionic current, the pattern search produces a zigzag pattern as it approaches the solution. To alleviate the zigzag path's effect, the pattern search algorithm has been set to use $n+1$ iterations for each direction search cycle. This minor modification assembles a linear combination of the previous n search directions and the optimum value of the step size for that direction in the additional iteration step.

An asynchronous parallel pattern search package, APPSPACK, is used to implement the pattern search algorithm and obtain the optimum semi-implicit coefficients [8]. Developed at Sandia National Laboratories, APPSPACK minimizes an objective function with an unconstrained or bound-constrained input;

$$\min_{l\le x\le u} f(x) = \sqrt{\frac{\sum_{n=1}^{N}(V_m^{BM} - V_m^{calculated})^2}{N}}. \qquad (4)$$

In the above equation, the bound of x is an n-dimensional vector, where l and u are its lower and upper bound. The objective function is obtained as the RMS difference between the simulated action potential, $V_m^{calculated}$, and the benchmark solution, V_m^{BM}. The bounded constraints of the design variables are set to be $0 \le \theta \le 1$ and $0 \le c \le 1$. The optimum solution is obtained with an asynchronous parallel set search that satisfies the bounded constraints by choosing appropriate search directions.

B. Operator split and protective zone method

In the operator split method, the update of unknown V_m is divided into multiple steps and the time derivative is considered as the sum of several components [9]. For the semi-implicit operator split method, the update of the Laplacian and ionic current terms are performed in alternate steps with different time steps sizes Δt and Δt_i, respectively. As the ionic current involves nonlinearity and relatively fast temporal variation, it is updated with smaller time steps, i.e., $\Delta t_i < \Delta t$. In the protective zone method, the ionic current in the operator split scheme is updated with smaller time steps only when the action potential has the fastest rate of change. The operator split as well as the protective zone method was found to improve computational efficiency [10].

IV. RESULTS AND DISCUSSION

The dimensions of the cardiac tissue are 0.5 cm in x (horizontal) direction, and 0.1667 cm in y (vertical) direction and the anisotropic tissue conductivities are 0.174 and 0.0193 S/m in x and y directions, respectively. A point stimulation current pulse located at the left bottom corner of the tissue and constant in time, with duration of 1 ms, is used to excite a propagating action potential. The three different grid sizes considered are 36, 72 and 144 nodes in each direction, and a period of 12 ms is simulated. The optimization iteration stops when the variation in RMS error between the calculated and benchmark solution is less than 0.001.

A. Methods without operator split or protective zone

The optimal θ and c values (θ_{opt} and c_{opt}) have been obtained for the three different grid sizes and Δt = 0.05 ms and 0.01 ms for the first and second order semi-implicit method. Note that for the first order method, θ = 0 and 0.5 correspond to the explicit and Crank-Nicolson method, respectively. As shown in Table 1, for the first order method, θ_{opt} varies from approximately 0 to 1. For the second order method, c_{opt} is approximately zero for all the cases, but θ_{opt} varies from 0.0820 to 0.443. The RMS error decreases by 1.76–4.18 times when Δt is varied from 0.05 to 0.01 ms, depending on the order and grid size. As expected, the error decreases when the grid size is increased, e.g., for Δt = 0.01 ms, it decreases by a factor of 2.21 and 3.02 for the first and second order method, respectively, when the grid size is changed from 36^2 to 144^2. Compared to the first order method, the second order method reduces the error by 14.2–35.7%. The use of optimized parameters also allows us to achieve accuracies higher than those obtained with the common numerical schemes, with little impact on the solution time. For example, with a 144^2 grid and Δt = 0.01 ms, the error for the optimized first order method is 16.4% and 19.1% lower than that for the explicit and Crank-Nicolson method, respectively.

Table 1: RMS error and optimum coefficients for first and second order method without operator split or protective zone

Grid Size, Δt	First Order	Second Order
36^2, 0.05 ms	25.1 mV at θ_{opt} = 0.998	21.6 mV at θ_{opt} = 0.227 & c_{opt} = 0.0500
72^2, 0.05 ms	22.2 mV at θ_{opt} = 1.00	17.6 mV at θ_{opt} = 0.385 & c_{opt} = 0.00
144^2, 0.05 ms	21.9 mV at θ_{opt} = 1.00	17.0 mV at θ_{opt} = 0.443 & c_{opt} = 0.0100
36^2, 0.01 ms	13.9 mV at θ_{opt} = 1.00	12.3 mV at θ_{opt} = 0.0820 & c_{opt} = 0.00
72^2, 0.01 ms	7.32 mV at θ_{opt} = 0.00200	5.43 mV at θ_{opt} = 0.210 & c_{opt} = 0.00100
144^2, 0.01 ms	6.31 mV at θ_{opt} = 0.324	4.06 mV at θ_{opt} = 0.370 & c_{opt} = 0.00400

B. Methods with operator split

The operator split scheme has been implemented such that Δt_i for ionic current is five times smaller than Δt for the Laplacian term. Table 2 demonstrates the RMS error and optimum θ and c values for operator split method with different grid sizes and time steps. The operator split improves the accuracy significantly, reducing the error by 5.91–11.3 times. However, the solution time also increases by a factor of 5.79–8.38. For the first order method, θ_{opt} varies from 0.00 to 0.583. For the second order method, θ_{opt} varies from 0.287 to 0.500 while c_{opt} is still nearly zero. Except for the 36^2 grid with the larger Δt = 0.05 ms, θ_{opt} and c_{opt} values are close to those for the Crank-Nicolson Adams-Bashforth method (θ = 0.5, c = 0). When Δt is varied from 0.05 to 0.01 ms, the error reduces by a factor of 2.05–5.05. At the same time, the error reduces by an average of 6.99% when second order instead of first order method is used. It should be noted that increasing the grid size or decreasing the time step, while reducing the error, also increases the solution time correspondingly. Changing from first order to second order method, however, has a negligible effect on the solution time. Furthermore, the use of optimized coefficients can again lead to error minimization, e.g., for a 36^2 grid and Δt = 0.05 ms, the error for the optimized second order method is 20.6% lower than that for the Crank-Nicolson Adams-Bashforth technique.

C. Protective zone method

In the protective zone method, the ionic current is updated with a smaller time step if $\left|\frac{\partial V_m}{\partial t}\right| > 0$. While this only causes an insignificant increase in the error, it reduces the solution time of the operator split approach by a factor of 2.23–2.57. According to Table 3, the effects of the different parameters with protective zone method follow the same trend seen previously in results obtained without the protective zone scheme.

Table 2: RMS error and optimum coefficients for first and second order method with operator split

Grid Size, Δt	First Order	Second Order
36^2, 0.05 ms	3.38 mV at $\theta_{opt} = 0.285$	3.41 mV at $\theta_{opt} = 0.287$ & $c_{opt} = 0.00700$
72^2, 0.05 ms	3.28 mV at $\theta_{opt} = 0.483$	2.83 mV at $\theta_{opt} = 0.460$ & $c_{opt} = 0.0750$
144^2, 0.05 ms	3.32 mV at $\theta_{opt} = 0.583$	2.87 mV at $\theta_{opt} = 0.461$ & $c_{opt} = 0.0600$
36^2, 0.01 ms	1.65 mV at $\theta_{opt} = 0.00$	1.59 mV at $\theta_{opt} = 0.497$ & $c_{opt} = 0.00200$
72^2, 0.01 ms	0.650 mV at $\theta_{opt} = 0.527$	0.604 mV at $\theta_{opt} = 0.500$ & $c_{opt} = 0.0685$
144^2, 0.01 ms	0.693 mV at $\theta_{opt} = 0.516$	0.658 mV at $\theta_{opt} = 0.500$ & $c_{opt} = 0.0507$

Table 3: RMS error and optimum coefficients for first and second order method with protective zone

Grid Size, Δt	First Order	Second Order
36^2, 0.05 ms	3.42 mV at $\theta_{opt} = 0.270$	3.50 mV at $\theta_{opt} = 0.530$ & $c_{opt} = 0.0730$
72^2, 0.05 ms	3.29 mV at $\theta_{opt} = 0.527$	2.95 mV at $\theta_{opt} = 0.462$ & $c_{opt} = 0.0100$
144^2, 0.05 ms	3.34 mV at $\theta_{opt} = 0.566$	2.87 mV at $\theta_{opt} = 0.455$ & $c_{opt} = 0.0500$
36^2, 0.01 ms	1.63 mV at $\theta_{opt} = 0.0460$	1.69 mV at $\theta_{opt} = 0.625$ & $c_{opt} = 0.418$
72^2, 0.01 ms	0.656 mV at $\theta_{opt} = 0.268$	0.728 mV at $\theta_{opt} = 0.510$ & $c_{opt} = 0.0370$
144^2, 0.01 ms	0.701 mV at $\theta_{opt} = 0.445$	0.658 mV at $\theta_{opt} = 0.500$ & $c_{opt} = 0.0519$

V. CONCLUSION

Optimization of the temporal discretization coefficients for semi-implicit finite difference modeling of cardiac propagation has been implemented with a pattern search algorithm. The proposed second order semi-implicit technique provides higher computational efficiency than the first order method used in previous studies. The operator split and protective zone schemes developed for the first order method also work for the second order method, which allows an effective tradeoff between accuracy and solution time. Moreover, the optimized coefficients result in error minimization with negligible effect on the solution time. The optimized c coefficient is close to zero for all the cases, while the other optimal coefficients show varying degrees of dependence on grid size and time step. The computational cost in finding these optimized coefficients can be amortized over the repeated simulations in physiological studies that use the same coefficients. Future research may involve the extension of the current study to higher order semi-implicit schemes and three-dimensional realistic cardiac geometries.

REFERENCES

[1] C. S. Henriquez and W. Ying, *The Bidomain Model of Cardiac Tissue: From Microscale to Macroscale*. Springer, Boston, 2001.

[2] S. L. Cloherty, N. H. Lovell, S. Dokos, and B. G. Celler, "A 2D monodomain model of rabbit sinoatrial node," *23rd Annual International Conference of the IEEE Engineering in Medicine and Biology Society*, Istanbul, pp. 44-47, 2001.

[3] M. Potse, B. Dube, J. Richer, A. Vinet, and R. M. Gulrajani, "A comparison of monodomain and bidomain reaction-diffusion models for action potential propagation in the human heart," *IEEE Tran. on Biomed. Eng.*, vol. 53, pp. 2425-2435, 2006.

[4] A. R. Conn, K. Scheinberg, and L. N. Vicente, *Introduction to Derivative-Free Optimization*. SIAM, Philadelphia, 2009.

[5] C. H. Luo and Y. Rudy, "A model of the ventricular cardiac action potential, depolarization, repolarization, and their interaction," *Circulation Research*, vol. 68, pp. 1501-1526, 1991.

[6] U. M. Ascher, S. J. Ruuth, and B. T. R. Wetton, "Implicit-Explicit methods for time-dependent partial differential equations," *SIAM J. Numeric. Anal.*, vol. 32, pp. 797-823, 1995.

[7] A. Onose and B. Dumitrescu, "Adaptive cyclic and randomized coordinate descent for the sparse total least squares problem," *23rd European Signal Processing Conference (EUSIPCO)*, Nice, pp. 1696-1700, 2015.

[8] G. A. Gray and T. G. Kolda, "Algorithm 856: APPSPACK 4.0: Asynchronous parallel pattern search for derivative-free optimization," *ACM Trans. Math. Softw.*, vol. 32, pp. 485-507, 2006.

[9] S. Krishnamoorthi, M. Sarkar, and W. S. Klug, "Numerical quadrature and operator splitting in finite element methods for cardiac electrophysiology," *International Journal for Numerical Methods in Biomedical Engineering*, vol. 29, pp. 1243-1266, 2013.

[10] R. Khan and K. T. Ng, "Higher order finite difference modeling of cardiac propagation," *IEEE International Conference on Bioinformatics and Biomedicine (BIBM)*, Kansas City, MO, pp. 1945-1951, 2017.